Andrey E. Krauklis

Environmental Aging of Constituent Materials in Fiber-Reinforced Polymer Composites

Andrejs Krauklis, Member of the Royal Society of Chemistry (MRSC)

NTNU
Norwegian University of
Science and Technology

NTNU

Andrey E. Krauklis

Environmental Aging of Constituent Materials in Fiber-Reinforced Polymer Composites

Andrejs Krauklis, Member of the Royal Society of Chemistry (MRSC)

Thesis for the Degree of Philosophiae Doctor

Trondheim, August 2019

Norwegian University of Science and Technology
Faculty of Engineering
Department of Mechanical and Industrial Engineering

NTNU
Norwegian University of
Science and Technology

"What is the goal of the life? It's to create yourself a soul. For me, … an art... more than an industry. And it's the search of the human soul... Have mind. Have power. Have ambition. I wanted to do something like that. Why not?" **Alejandro Jodorowsky**, in *Jodorowsky's Dune*.

"I have learned to be content with whatever I have. I know what it is to have little, and I know what it is to have plenty. In any and all circumstances I have learned the secret of being well-fed and of going hungry, of having plenty and of being in need." **Saint Paul**, in *Philippians 4:11-12*.

"Consider the lilies of the field, how they grow; they neither toil nor spin, yet I tell you, even Solomon in all his glory was not clothed like one of these." **Jesus**, in *Matthew 6:28-30*.

"The really fine things of life are not things at all." **Anonymous**, Springfield, Illinois, USA, *1948*.

Nevertheless, …

"Life has three rules: Paradox, Humor, and Change." **Dan Millman**, in *Way of the Peaceful Warrior*.

"We may like to think of ourselves as civilized, but that civilization is in large part bestowed by material wealth. Without this stuff, we would quickly be confronted by the same basic struggle for survival that animals are faced with… Materials are a reflection of who we are, a multi-scale expression of our human need and desires." **Mark Andrew Miodownik, MBE**, in *Stuff Matters: Exploring the Marvelous Materials That Shape Our Man-Made World*.

But…

"I eat too much. I drink too much. A greedy, selfish such-n-such. But when I wrap my turban on. My mind is clear. I'm 'Baba Lon'." **Lon Milo DuQuette**, in *Ask Baba Lon: Answers to Questions of Life and Magick*.

… and finally, there is some seriously complicated matter ahead…

"Do you have the patience to wait until your mud settles and the water is clear?" **Lao Tzu**, in *Tao Te Ching*.

Ora et labora…

PREFACE

This thesis has been submitted to the Norwegian University of Science and Technology (NTNU) for partial fulfilment of the requirements for the degree of Philosophiæ Doctor (Ph.D.). The research has been carried out at the Department of Mechanical and Industrial Engineering (MTP), known as the Department of Engineering Design and Materials (IPM) at the time of commencing the Ph.D. research work, under supervision of Prof. Andreas Thorsten Echtermeyer and co-supervisor Assoc. Prof. Nils-Petter Vedvik over a period from August 2016 to April 2019. Some work has been conducted by the author at Rudolfs Cimdins Riga Biomaterials Innovation and Development Centre (RBIAC) and the University of Latvia in Riga.

ABSTRACT

Fiber-reinforced polymer (FRP) composites have seen a rapid rise in use in the past 50 years due to their high strength, stiffness, relatively light weight and relatively high corrosion resistance, especially when compared with more traditional structural materials such as steel and aluminum. Composite materials are widely used in structural applications in marine, offshore and oil & gas industries. A typical design lifetime of offshore FRP structures is 25 or more years in direct contact with water leading to some deterioration of the material properties. Knowing and forecasting the extent of the material property deterioration in water is of great interest for designers and users of the offshore FRP structures. The environmental durability becomes a limiting factor in the use of composites for structural applications, since the superior material properties are compromised by the uncertainty of the material interaction with the environment.

Each of the composite constituents (matrix, fibers and sizing-rich interphase) is affected differently by interaction with water molecules. It is therefore of high importance to understand the degradation severity and mechanisms of each of the constituent material due to aging in water. The materials studied are amine-cured epoxy matrix, R-glass fibers and the epoxysilane-based sizing-rich composite interphase, which, combined, constitute the fiber-reinforced composite laminate. Degradation mechanisms for each constituent material were identified, and novel tools, i.e. models and methods, were developed for prediction of long-term properties of composite materials and its constituents. These practical tools are to be of assistance in partially substituting the rigorous physical testing procedures in the state-of-the-art situation. Prediction of long-term properties of composites should significantly reduce costs associated with extensive testing and should already allow a partial transition towards the multiscale modeling approach.

Brief description of the results

A spectroscopic method for true water content determination and monitoring in polymers and composites was developed.

Aging mechanisms and changes in the chemical structure of the amine-based epoxy were investigated. No chain scission (hydrolysis or oxidation-induced) was present, whilst thermo-oxidation and leaching occurred. Four unique reactive sites responsible for thermo-oxidation were found. The only mechanism that was important for the strength reduction of the studied polymer was swelling. Mechanical properties of the epoxy could be regained upon redrying the material to the initial water content. An analytical method for predicting anisotropic swelling in composites from the swelling of the epoxy was developed and explained.

Aging of glass fibers occurred in two distinct phases: a short-term non-steady-state (Phase I) and long-term steady-state (Phase II). Phase I was very complex and involved many competing processes in parallel, such as ion exchange, gel formation and dissolution. Phase II was dissolution-dominated. A chemical kinetic model termed the Dissolving Cylinder Zero-Order Kinetic (DCZOK) model was developed for predicting mass loss and a decreasing radius of glass fibers at various environmental conditions.

The sizing-rich composite interphase was degrading due to hydrolysis, resulting in the formation of the interphase flaws. These flaws could further develop into fiber/matrix debondings, matrix cracks and splitting along the fibers. The internal volume created by the flaws and cracks could then be filled with water leading to the observed mass increase of a typical composite.

All known environmental aging mechanisms of the studied composite constituents were systematized and a phenomenologically complete mass balance was presented. Using the mass balance, it was possible to deduce the dissolution kinetics of the sizing rich-composite interphase.

ACKNOWLEDGEMENTS

By Oksana Vladimirovna Golubova

Andrey Eduardovich Krauklis
Trondheim, Norway
July 2019

x

CONTENTS

CHAPTER 1

INTRODUCTION

Parts of the Ph.D. thesis are copied from the appended Papers I-VIII (Appendices A-H).

1.1. BACKGROUND

Composites & environmental durability

Fiber-reinforced polymer (FRP) composites have seen a rapid rise in use in the past 50 years due to their high strength, stiffness, relatively light weight and high corrosion resistance, especially when compared with more traditional structural materials such as steel and aluminum [1]. The reason for such superior performance is the synergistic interaction between the constituent materials inside the composite [1]. There are three constituents in an FRP, namely a polymer matrix, a fibrous reinforcement and a multi-component coating on the surface of the fibers – the sizing. During the manufacture of FRPs, the sizing results in the formation of a sizing-rich composite interphase between the reinforcing fibers and the matrix polymer, chemically and physically bonding fibers and the polymer together [2]. Epoxy, glass fibers and epoxysilane/epoxy sizing are the constituents studied in this work.

FRP laminates are used for structural applications in marine, offshore and oil & gas industries due to their light weight and corrosion resistance [3–5]. Composites offshore have been implemented in such applications as risers, tethers, repair patches and ship hulls [6–11]. In these applications, FRPs get continuously exposed to water and humid environments for decades, a typical design lifetime being around 25 years or more [7].

Exposure of composite to aqueous and humid environments leads to aging, negatively impacting the mechanical properties of FRPs [12–18]. Understanding and quantifying the water-induced aging is especially important for glass fiber-reinforced composites since the glass fibers are hygroscopic [19]. The environmental durability is one of the limiting factors in the structural applications [20], since the superior strength and stiffness of composite materials are often compromised by the uncertainty of the material interaction with the environment [21]. Durability is a primary issue because environmental factors such as moisture, temperature and stress to which the material is exposed can degrade the properties of the constituent phases. Environmental aging is especially important at higher temperatures, since the aging is then accelerated. Furthermore, constituents are affected by environmental aging differently from each other [22]. Thus, understanding the mechanisms and kinetics of environmental aging of individual constituents is of high importance for the composite environmental durability. Since water uptake in composites is governed by diffusion [23] and water concentration has a crucial role in environmental aging [24], of importance is also the development of a method that allows determination of the true water content inside the FRPs.

Matrix polymer & environmental aging

Epoxy polymers are a common thermoset matrix material known for their relatively high strength, stiffness, low volatility, chemical resistance, and low shrinkage on curing [25–27]. Epoxies are two-component systems consisting of an epoxy compound and a hardener (also known as a curing agent), which react to form the cured polymer matrix network [28]. The epoxy family covers a large diversity of polymer networks defined by the type of the epoxy compound and hardener employed. All these variations lead to a different polymer matrix formed, and affect its physical and chemical properties

1

[28,29]. DGEBA-based epoxies, such as in this work, are the most widely used epoxy polymers in structural applications and constitute more than 75% of epoxy resins sold worldwide [30]. In this work, the epoxy material system contains two epoxy compounds (DGEBA and HDDGE) and two hardeners (IPDA and POPA). After the curing reaction, a three-dimensional amine epoxy matrix is obtained [31].

When the epoxy matrix is exposed to aqueous or humid environments, water molecules can migrate into the polymer and may affect its properties [5,25,32,33]. Highly crosslinked amine-cured epoxy polymers are hydrophilic and their mechanical properties can significantly deteriorate upon water uptake [26,34,35]. It is well established that water uptake is an important factor in performance and durability of epoxy-based composites which undergo plasticization and swelling stresses [36].

Hygrothermal process may induce both reversible and irreversible changes in the epoxy [20,37]. Irreversible changes persist even after redrying the material [32]. Irreversible damage in epoxies may occur due to susceptibility of the polymer to hydrolysis/chain-scission, residual curing, leaching and oxidation. For some epoxy systems, water at elevated temperatures can attack the crosslinked network, causing chain scission and leaching [4]. For the studied epoxy, residual curing and hydrolysis/chain scission did not occur [3,38], while leaching and oxidation did, but did not exhibit any significant effect on the mechanical properties of the studied epoxy [38].

The main effect of water on the mechanical property deterioration of the epoxy polymer was hygroscopic swelling [38]. Swelling is a specific response accompanying moisture diffusion in polymers and polymer-based composites [4]. Susceptibility of polymers to swelling results in a two-fold effect on FRPs: on the one hand, it causes a decrease in mechanical strength of the polymeric matrix [38], while on the other, it results in swelling stresses when the hygroscopic swelling is restrained [39]. The degradation of the tensile strength can be attributed to the plasticization/swelling and deterioration of the polymer (ultimate tensile strength of some epoxies may decrease even by 40% due to hygroscopic swelling) [20,33,40]. While some authors report significant fatigue life reduction of epoxies due to swelling, others do not observe noticeable changes after water absorption [32]. For the studied epoxy, both static and fatigue strength dropped by about 20% due to hygroscopic swelling [38].

More details and key findings on environmental aging of the epoxy, including mechanisms and deterioration of the mechanical properties can be found in Chapter 3 and in Papers I-IV (Appendices A-D).

Fiber reinforcement & environmental aging

Glass fibers (GFs) are often used as reinforcement in structural composite materials. Furthermore, the most common fibrous reinforcement material is glass [41]. GFs are produced from raw materials, which are virtually unlimited in supply [41] and possess such desirable reinforcement material properties as high hardness, strength and stiffness [41,42]. Various types of GFs exist such as E, ECR, R and S-glass, listed in the order of increasing mechanical strength [43]. Another common reinforcement material, carbon fibers, is known to be inert in water, while the glass fibers degrade strongly in aqueous environments [44,45]. Thus, concerning environmental aging, it is more relevant to expand knowledge base on the water-induced degradation of glass fibers.

The fact that even water may corrode glass fibers has been known for many years [45]. Glass fibers are hydrophilic and are susceptible to degradation when exposed to water environments [46]. Hydrolytic degradation of glass fibers can significantly reduce mechanical strength and leads to corrosion-induced defects [44]. The degradation of glass fibers due to environmental attack can severely affect the performance of GFRPs [47]. Humid and water environments act primarily to reduce the fiber strength caused by the growth of flaws, such as surface cracks [45,47]. Unprotected glass fibers exposed to water lose their strength relatively quickly, especially so if they are mechanically loaded [48,49].

The long-term environmental degradation of glass materials has been previously studied mainly with respect to nuclear waste applications [50,51]. Most of the existing works on glass dissolution have been performed with bulk silicate glass, and fibers are not studied often [52]. Recently, there has been an increasing interest in environmental aging of FRPs, where R-glass and E-glass are often used as

reinforcement [3,24,52-55]. Even so, very few studies exist on the kinetics of GF dissolution (mostly on E-glass) [56,57]. Most studies on environmental degradation of composites are concerned directly with deterioration of the mechanical properties, and the mechanistic origin and the kinetics of chemical degradation tend to be overlooked [54,55]. However, a few studies exist that explain general mechanisms of environmental degradation of glass materials using various approaches that are based on surface reactions, chemical affinity and diffusion [46,58-62]. Yet again, dissolution experiments in existing studies are mainly performed with bulk silicate glasses, and glass fibers are not studied often [52].

However, a few studies on the kinetics of glass fiber dissolution exist. For instance, Mišíková et al have studied the E-glass fiber leaching kinetics in distilled water at different temperatures [56]. Bashir et al studied the kinetics of the dissolution of E-glass fibers in alkaline solutions by immersing single fibers and measuring the diameter change [57]. Recently, Krauklis and Echtermeyer presented an analytical model termed Dissolving Cylinder Zero-Order Kinetic (DCZOK) that predicts glass dissolution kinetics during long-term hygrothermal aging of glass fiber bundles and fiber-reinforced composites at various environmental conditions [24,52,43]. The model is able to predict the mass loss and fiber radius reduction kinetics during dissolution [24,52]. The dissolution of glass fibers inside composites is slowed down compared to glass fiber bundles and is addressed in the analytical model [24].

In the short-term (Phase I, up to about a week in contact with water [43,52]), hydrolytic degradation involves such competing processes as ion exchange, gel formation and dissolution [50,52,63]. In the long-term (Phase II), hydrolytic degradation is governed by the glass dissolution mechanism and follows zero-order reaction kinetics [50,52]. Such kinetics depend on the glass surface area in contact with water, which is proportional to the fiber radius. As the dissolution continues, the radius decreases resulting in the mass loss deceleration [52]. Elements that are released during degradation of R-glass are Na, K, Ca, Mg, Fe, Al, Si and Cl [52]. The total mass of all ions released is the cumulative mass loss [52]. The total mass loss is what manifests in the radius reduction [52].

During glass-water interaction, several chemical reactions may occur, shown in Chemical Reactions (a)-(k), after [43,50,52,63-66]:

$$(\equiv Si - ONa) + H_2O \rightarrow (\equiv Si - OH) + OH^- + Na^+ \tag{a}$$

$$(\equiv Si - OK) + H_2O \rightarrow (\equiv Si - OH) + OH^- + K^+ \tag{b}$$

$$(\equiv Si - O)_2Ca + H_2O \rightarrow 2(\equiv Si - OH) + 2OH^- + Ca^{2+} \tag{c}$$

$$(\equiv Si - O)_2Mg + H_2O \rightarrow 2(\equiv Si - OH) + 2OH^- + Mg^{2+} \tag{d}$$

$$(\equiv Si - O - Al =) + H_2O \leftrightarrow (\equiv Si - OH) + (= Al - OH) \tag{e}$$

$$(\equiv Si - O)_2Fe + H_2O \rightarrow 2(\equiv Si - OH) + 2OH^- + Fe^{2+} \tag{f}$$

$$(\equiv Si - O)_3Fe + H_2O \rightarrow 3(\equiv Si - OH) + 3OH^- + Fe^{3+} \tag{g}$$

$$(\equiv Si - O - Si \equiv) + OH^- \leftrightarrow (\equiv Si - OH) + (\equiv Si - O^-) \tag{h}$$

$$(\equiv Si - O^-) + H_2O \leftrightarrow (\equiv Si - OH) + OH^- \tag{i}$$

$$SiO_2 + 2H_2O \leftrightarrow H_4SiO_4 \tag{j}$$

$$MeCl_x \xrightarrow{H_2O} (Me^{x+}) + xCl^- \tag{k}$$
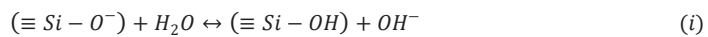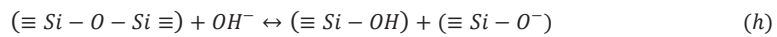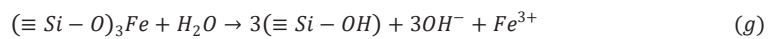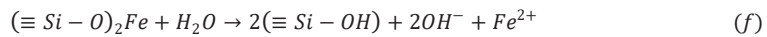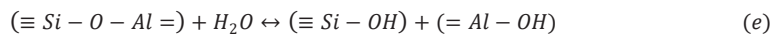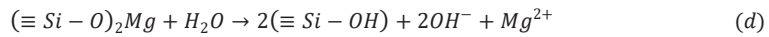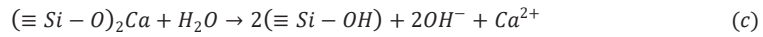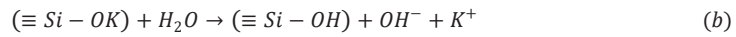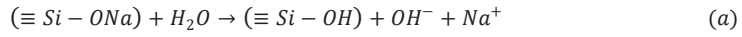
Chemical reaction (j) can also be written as a combination of subsequent reactions (l) and (m), meaning that initially H_2SiO_3 is formed, which dissociates weakly and further reacts with water to form silicic acid:

$$SiO_2 + H_2O \leftrightarrow H_2SiO_3 \qquad\qquad (l)$$

$$H_2SiO_3 + H_2O \leftrightarrow H_4SiO_4 \qquad\qquad (m)$$

As shown in the Chemical reactions (a)-(k), various competing reactions happen simultaneously. Initially these reactions happen at independent rates (short-term non-steady-state), later one process becomes limiting and dominates the behaviour (long-term steady-state). Therefore, the degradation process should be divided into two respective stages as was described earlier.

More details and key findings on environmental aging of glass fibers, including analytical models of chemical kinetics, can be found in Chapter 3 and in Papers V-VII (Appendices E-G).

Sizing-rich composite interphase & environmental aging

The composite interphase is of vital importance since the mechanical properties of composite materials are often determined by whether the mechanical stresses can be efficiently transferred from the matrix to the reinforcing fibers [19,67,68]. The quality of the interfacial interaction is strongly dependent on the adhesional contact and the presence of flaws in the interphase [69]. It is generally agreed that the composite interphase is often the mechanical weak link and a potential source for the initiation of defects in fiber-reinforced composite structures [19].

Water and humid environments negatively impact the mechanical properties of FRPs partially because of a loss of the interfacial bonding [11-14,19]. Flaws in the interphase can be introduced due to the interaction with water uptaken from the environment [69]. The removal of the sizing material can also lead to a microcrack initiation at the surface of glass fibers, and that various sizing components can be extracted by water, resulting in the loss of the material [70-74]. It is therefore of high importance to understand the environmental aging mechanism and kinetics of a sizing-rich composite interphase.

What complicates the situation is that the sizing, which forms the interphase, has a proprietary composition. Commercial glass fibers are often supplied with only one or two sizing-related details. The first being an indication of the chemical compatibility of the sizing with the matrix polymer, e.g. epoxy, as in this case. The second is a value for the loss on ignition (LOI), which indicates the amount of sizing [75]. The key functions of the sizing are (1) to protect the glass fibers during handling and production, (2) to ensure a high level of stress transfer capability across the fiber-matrix interphase and (3) to protect the composite matrix interphase against environmental degradation [11].

It is known that the W2020 sizing consists of about five various chemicals [76,77]. Furthermore, it is known, that the sizing contains an organofunctional silane commonly referred to as a coupling agent [78-80]. This class of chemicals can be considered the most important in the glass fiber sizing, as it is the main component that promotes adhesion and stress-transfer between the polymer matrix and the fiber [11].

The structure of the sizing-rich composite interphase is very complex [11], as the sizing itself is heterogeneous and not uniform [11,81]. Furthermore, it has been observed by various researchers, that sizing is coated on fibers in "islands", "islets" or in patches, meaning that fiber surface is only partially covered by the sizing, also giving some roughness to the surface [11,82-87]. Mai et al investigated silane-based sizings using AFM and concluded that sized fibers are rougher than the desized fibers [87]. Also, similar conclusions were drawn by a few other researchers [69,81]. Similar results have been observed in this work, using Brunauer-Emmett-Teller (BET) theory for specific surface area determination.

The composite interphase can be visualized as a matrix polymer/poly(siloxane)/glass fiber model (shown in Figure 1.1) [19].
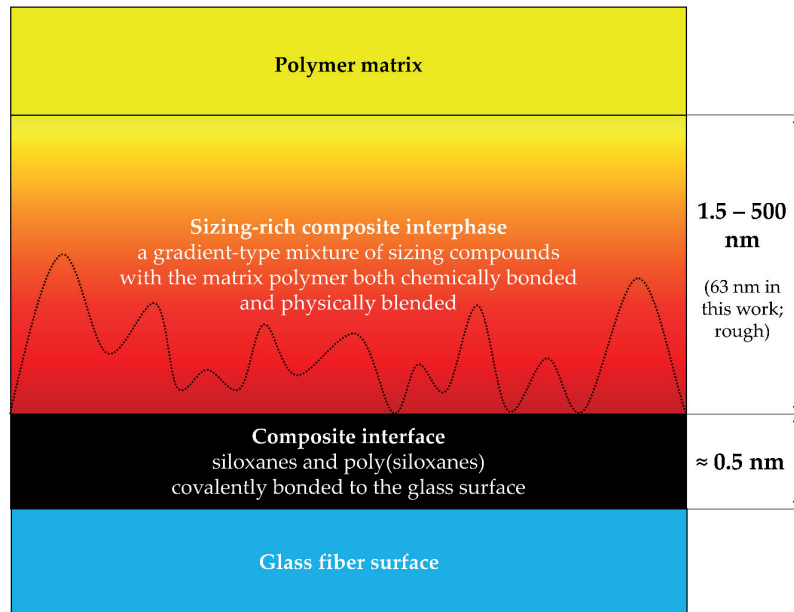
Figure 1.1. The concept of a polymer-siloxane-glass interphase, after [19]. The dotted line indicates that the sizing is rough [69,81,87].

The siloxanes and poly(siloxanes) form covalent bonds with the glass fiber surface, resulting in a two-dimensional interface, the thickness of which is governed by the length of the chemical bonds, and is of an ångstrøm-scale (one tenth of a nanometer) [19]. A composite interphase is a gradient-type blend of the sizing compounds and the bulk matrix polymer, usually being about a micrometer in thickness [11,19,32,88,89]. It was observed, that an interfacial failure occurs at 0.5 – 4 nm from the glass surface in glass/epoxysilane/epoxy interphase, indicating that the interphase region, rather than the two-dimensional interface is the weak link [19].

There are no direct measurement methods to study the environmental aging of the composite interphase. It is not known yet how to quantify the interphase loss in the composite due to aging. Furthermore, it has been noted by Riaño et al that modeling techniques to study the composite interphase are becoming of high interest to the scientific community and industry [90]. Recently, Krauklis, Gagani and Echtermeyer proposed a phenomenological mass balance approach for the hygrothermal aging of fiber-reinforced composites and systematized and quantified known aging mechanisms of composite microconstituents (Paper VIII) [22]. Mass balance allowed deducing the kinetics of the hydrolytic degradation of the sizing-rich composite interphase [22].

More details and key findings on environmental aging of the composite interphase and chemical kinetics of its dissolution can be found in Chapter 3 and in Paper VIII (Appendix H).

True water content of the matrix and the composite

Composites uptake water from their surroundings. Water uptake is governed by water diffusion and depends on the thickness of the composite structure and the temperature of the environment [23,91-95]. More details on prediction of water uptake and diffusion for the same GFRP material as in this work can be found in papers by Gagani et al, for various composite structures both with and without voids [23].

For polymers, experimental techniques such as differential scanning calorimetry (DSC), ultraviolet (UV) reflection spectroscopy, attenuated total reflection Fourier transform infrared spectroscopy (ATR-FTIR) and Fourier transform near-infrared spectroscopy (FT-NIR) have been reported [35,96-101]. It has also been reported that NIR spectroscopy, e.g. FT-NIR, is a promising technique for the water content monitoring for various materials, in part due to recent improvements of NIR spectrometers [102-104]. NIR spectroscopy has long been used in such fields as medicine, food and polymers [102,105,106].

The only widely known method for determination of water content in composites is a gravimetric method, which provides information of weight gain upon water uptake, or the weight loss upon drying [53]. However, gravimetric curves for composites are not straightforward to interpret, since alongside typical Fickian water uptake there are also aging processes occurring inside the composite [22]. Another significant drawback of the gravimetric method is the necessity to know the mass of the absolutely dry material, which in some cases requires extremely long drying times. Furthermore, it is not possible to obtain such data precisely due to humidity of the ambient air, unless perfectly dry conditions can be ensured during drying and weight gain measurements. In order to understand water-induced aging on the mechanistic microlevel, the absolute or true water content has to be known. Otherwise, an error is introduced when linking property deterioration due to water influence and the concentration of water inside the material. Therefore, an alternative NIR spectroscopic method for measuring and monitoring true water content in epoxy polymers and fiber-reinforced composites was developed [53]. More details on the method can be found in Chapter 3 and in Paper I (Appendix A).

Hygroscopic swelling of the matrix and the composite

Since for the studied epoxy matrix, only mechanism of swelling is important for the strength reduction [38], it is important to quantitively link hygroscopic swelling with the true water content.

Unlike the polymer itself, in FRPs, the matrix is constricted by fibers, and as a result, this affects the swelling behavior. What complicates the phenomenon even more is the orthotropic nature of swelling of composites—fibers, such as glass or carbon, do not swell, while the polymer matrix does [5,39]. Such incompatible swelling behavior in FRPs leads to swelling stresses at the interfaces, which may lead to microcrack formation, especially under transient conditions (non-uniform moisture content distribution) [5,107]. Hygroscopic swelling may affect the mechanical properties of FRPs significantly [4,38,53,108]. Thus, it is important to know not only the true water content, but also the swelling behavior, in order to properly characterize the FRP material property change, i.e., strength or modulus, resulting from moisture absorption [109]. Linear strain increases linearly with increasing water concentration for both composites and polymers [108,110]. For orthotropic laminates, three Coefficients of Hygroscopic Expansion (CHEs; $\beta_x, \beta_y, \beta_z$) are needed in order to predict swelling [109].

Quantification of the orthotropic CHEs can be performed experimentally using samples with different fiber orientations. However, it is a time-consuming and tedious process that also tends to involve quite high experimental scatters. The industrial interest lies in the reduction of testing time and testing-related expenses. Thus, a modeling approach to swelling of FRPs due to the effects of water (and also other liquids, such as oil) is of interest [111].

Various studies have been performed on swelling of FRPs [21,39,108,112-119] and, more recently, on hygroscopic swelling in textile composites [120,121]. The works available in the literature have addressed several aspects of hygroscopic swelling in composites, from the nature of swelling in polymeric matrix [5,13,39,122], to the influence of swelling on the fluid diffusion in polymers [108,111,117,123,124], to the development of micromechanical models to predict transverse swelling [112,120,121].

An interesting opportunity is the possibility to predict the orthotropic swelling constants (CHEs) of the composite from the CHE of the matrix polymer, which is isotropic. The matrix properties are easy to measure. Furthermore, they also may be found in literature for various polymers [122,125]. However, in some cases, the interfacial effects may not be negligible [126], many of the moisture-related properties of composites are known to be traceable to those of the matrix material [53,108]. Swelling

strains of a composite and a matrix polymer should also be related to each other through a proper analysis [108,127]. Since swelling in polymers does not follow the ideal mixing law [4], i.e., the volume increase of the polymer is not equal to the volume of the absorbed water, and it is necessary to perform swelling experiments for the matrix polymer itself, or to find polymer CHE in the literature [122,125].

Recently, Krauklis et al have shown that orthotropic hygroscopic swelling of fiber-reinforced composites can be analytically predicted from the swelling of the matrix polymer using a model based on linear elasticity [109]. More details on the model can be found in Chapter 3 and in Paper IV (Appendix D).

1.2. MOTIVATION

The current situation shows that there is a lack of efficient tools for reliably predicting changes in properties of composite materials and their constituents due to environmental aging, as well as the processes involved are not fully understood, i.e. the degradation processes at the microconstituent level taking place and their respective mechanisms [128]. Thus, an interaction of composite constituents with the environment was investigated, and novel tools were developed in order to predict environmental aging.

1.3. OBJECTIVES AND SCOPE

The aim of this work is to identify the environmental aging mechanisms of composite microconstituent materials, to study the severity of such aging on the mechanical properties, and to develop novel tools for the prediction of changes in composite properties due to environmental aging. The microconstituents of the composites were studied in order to evaluate the water-induced degradation. This resulted in the development of the tools, i.e. analytical models and methods, for prediction of microconstituent and composite properties in offshore applications. The developed tools allow an efficient alternative to the state-of-the-art procedures based on physical testing, which is much more time-consuming than the use of analytical models. Prediction of long-term properties of composites should significantly reduce costs associated with extensive testing and should already allow a partial transition towards the multiscale modeling approach.

The reached goals and contribution to the state-of-the-art are the following:
- Providing a true water content determination method for polymers and composites.
- Providing a better understanding of environmental aging mechanisms in fiber-reinforced composites and microconstituents and its effect on mechanical properties of such materials.
- Providing practical tools, i.e. models and methods, for quantitative prediction of both short-term and long-term water-induced changes in the microconstituent materials and composites. The tools are to be of assistance in substituting the rigorous physical testing procedures in the state-of-the-art situation.

In order to achieve these goals, the following objectives were fulfilled:
- To obtain the water saturation levels and to develop a method for determination and monitoring of the true water content in composites and microconstituents.
- To study the interaction of composite microconstituents as well as composite material itself with the affecting environment, i.e. water. Collected data involves both the mechanical side and the chemical/physico-chemical side of the processes involved.
- To study the material degradation when exposed to environmental aging and evaluate how the properties of the material are affected.

- Based on environmental aging experiments, to propose and develop analytical models in order to predict changes in properties of the composite microconstituents due to exposure to such environments.

1.4. THESIS STRUCTURE

The thesis is made as a compendium of eight scientific articles together with five additional chapters. Chapter 1 introduces the reader to the scientific problem that is to be addressed and provides motivation for the research described in this work, the objectives and a description of the scientific papers. Chapter 2 gives a detailed description of the materials and methods used. Chapter 3 provides a summary of the results. Chapter 4 outlines the main conclusions. Chapter 5 describes the recommendations for the future work. The eight scientific articles are incorporated in the Appendices A-H of the thesis.

Publications included in the Ph.D. thesis (Appendices A-H):

(I) Krauklis, A.E.; Gagani, A.I.; Echtermeyer, A.T. Near-Infrared Spectroscopic Method for Monitoring Water Content in Epoxy Resins and Fiber-Reinforced Composites. *Materials* (Switzerland) **2018**, 11(4), 586-599. DOI: 10.3390/MA11040586.

(II) Krauklis, A.E.; Echtermeyer, A.T. Mechanism of Yellowing: Carbonyl Formation During Hygrothermal Aging in a Common Amine Epoxy. *Polymers* (Switzerland) **2018**, 10(9), 1017-1031. DOI: 10.3390/POLYM10091017.

(III) Krauklis, A.E.; Gagani, A.I.; Echtermeyer, A.T. Hygrothermal Aging of Amine Epoxy: Reversible Static and Fatigue Properties. *Open Engineering* (Poland) **2018**, 8(1), 447-454. DOI: 10.1515/ENG-2018-0050.

(IV) Krauklis, A.E.; Gagani, A.I.; Echtermeyer, A.T. Prediction of Orthotropic Hygroscopic Swelling of Fiber-Reinforced Composites from Isotropic Swelling of Matrix Polymer. *Journal of Composites Science* (Switzerland) **2019**, 3(1), 10-23. DOI: 10.3390/JCS3010010.

(V) Krauklis, A.E.; Echtermeyer, A.T. Long-Term Dissolution of Glass Fibers in Water Described by Dissolving Cylinder Zero-Order Kinetic Model: Mass Loss and Radius Reduction. *Open Chemistry* (Poland) **2018**, 16(1), 1189-1199. DOI: 10.1515/CHEM-2018-0133.

(VI) Krauklis, A.E.; Echtermeyer, A.T. Dissolving Cylinder Zero-Order Kinetic Model for Predicting Hygrothermal Aging of Glass Fiber Bundles and Fiber-Reinforced Composites. In *4th International Glass Fiber Symposium*; Gries, Th.; Pico, D.; Lüking, A.; Becker, Th., Eds.; Mainz, G: Aachen, Germany, **2018**; pp. 66–72. ISBN: 978-3-95886-249-4.

(VII) Krauklis, A.E.; Gagani, A.I.; Vegere, K.; Kalnina, I.; Klavins, M.; Echtermeyer, A.T. Dissolution Kinetics of R-Glass Fibres: Influence of Water Acidity, Temperature and Stress Corrosion. *Fibers* (Switzerland) **2019**, 7(3), 22-40, in a *Special Issue: Advances in Glass Fibers*. DOI: 10.3390/fib7030022.

(VIII) Krauklis, A.E.; Gagani, A.I.; Echtermeyer, A.T. Long-Term Hydrolytic Degradation of the Sizing-Rich Composite Interphase. *Coatings* (Switzerland) **2019**, 9(4), 263-286. DOI: 10.3390/coatings9040263.
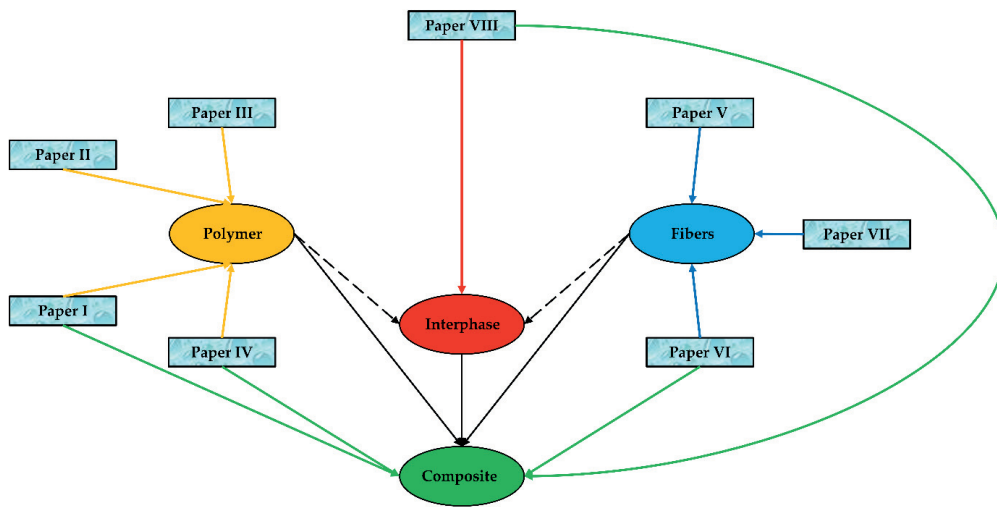
Figure 1.2. Schematic relationship of the papers and composite constituent materials in the thesis.

The relationship between the articles and the studied materials is represented by a simple diagram in Figure 1.2. Black lines represent the relationship between the constituents and the composite material itself. Black dotted lines signify that the interphase exists only when the polymer and matrix are combined, thus only in the composite. Colored lines show which publications correspond to which constituent material and the composite itself. Yellow, red, blue and green lines correspond to works on polymer, interphase, fibers and composite, respectively.

Papers I-IV cover the polymeric matrix material (amine-cured DGEBA-based epoxy). Paper I presents a method of true water content determination in a polymer matrix. Paper II identifies hygrothermal aging mechanisms and changes in the chemical structure of the polymer. Paper III identifies the influence of hygrothermal aging on the mechanical properties of the polymer and shows that only mechanism of swelling is important for the strength reduction. It shows how severely swelling affects static tensile strength and fatigue properties of the epoxy, and how these properties can be regained upon redrying to the initial water content, indicating reversibility. Paper IV shows how water uptake quantitively manifests in hygroscopic swelling of the polymer.

Papers V-VII cover the reinforcement material (R-glass fibers). Paper V identifies hygrothermal aging mechanisms in glass. The paper describes long-term aging of R-glass fibers in water and presents a chemical kinetic model called a Dissolving Cylinder Zero-Order Kinetic (DCZOK) model. The model can be used for quantitative predictions of the mass loss and fiber radius reduction due to glass dissolution in water. Paper VI shows the protective effect of sizing against the dissolution of R-glass fibers. Paper VII describes such environmental effects as pH, temperature and stress corrosion on the dissolution of glass fibers. The paper reports activation energies and kinetic constants for various environmental conditions, as well as the extended DCZOK model that takes into account the environmental effects.

Paper VIII covers the composite interphase. The paper shows how, by identifying all the aging mechanisms and using a mass balance approach, it is possible to deduce the environmental aging of the interphase material. The kinetics and the mechanism of hydrolytic aging are described.

Papers I, IV, VI and VIII also cover the composite material directly. Paper I presents a method of true water content determination and monitoring in a composite material. Paper IV shows how hygroscopic swelling can be quantitively predicted in composite from swelling of a polymer, since fibers do not swell. Paper VI extends the use of the DCZOK model to the composites. Paper VIII

summarizes environmental aging mechanisms of GFRPs using a phenomenological mass balance approach and describes long-term gravimetric (mass gain and loss) behavior of the composite. Furthermore, it provides a link between the water uptake of a composite and the hydrolytic damage of the interphase.

The contribution of the author and the co-authors is as follows:

A.E. Krauklis formulated the objectives and defined the test program, designed and assembled the customized rigs in Paper VII. Produced the test specimens, developed test methods in all the Papers (I-VIII), carried out most experiments and analytical modeling tasks, analyzed and interpreted the data and wrote all the Papers (I-VIII).

A.I. Gagani produced some of the composite test specimens, carried out FEA simulations and helped with analytical modeling in Paper IV, has helped with experimental work in Paper III and with writing literature review in Paper VII.

E. Sæter produced some of the composite test specimens and helped with experimental work in Paper VIII.

I. Kalnina helped with experimental work in Paper VII.

K. Vegere helped with organizing collaboration with Riga Technical University that allowed some parts of the experimental testing in Papers II and VII.

M. Klavins contributed with suggestions and comments on Paper VII and helped with organizing collaboration with Latvian University that allowed some parts of the experimental testing in Paper VII.

A.T. Echtermeyer contributed with intellectual discussions, guidance, suggestions and comments to all papers.

Relevant publications not included in the Ph.D. thesis:

(IX) Echtermeyer, A.T.; Gagani, A.I.; Krauklis, A.E.; Mazan, T. Multiscale Modelling of Environmental Degradation—First Steps. In *Durability of Composites in a Marine Environment 2. Solid Mechanics and Its Applications*; Davies, P.; Rajapakse, Y.D.S., Eds.; Springer: Cham, Switzerland, **2018**; Volume 245, pp. 135-149. ISBN: 978-3-319-65145-3.

(X) Gagani, A.I.; Krauklis, A.E.; Echtermeyer, A.T. Anisotropic fluid diffusion in carbon fiber reinforced composite rods: Experimental, analytical and numerical study. *Marine Structures* (Netherlands) **2018**, 59, 47-59. DOI: 10.1016/j.marstruc.2018.01.003.

(XI) Gagani, A.I.; Krauklis, A.E.; Echtermeyer, A.T. Orthotropic fluid diffusion in composite marine structures. Experimental procedure, analytical and numerical modelling of plates, rods and pipes. *Composites: Part A* (United Kingdom) **2018**, 115, 196-205. DOI: 10.1016/j.compositesa.2018.09.026.

(XII) Gagani, A.I.; Monsås, A.B.; Krauklis, A.E.; Echtermeyer, A.T. The effect of temperature and water immersion on the interlaminar shear fatigue of glass fiber epoxy composites using the I-beam method. *Composites Science and Technology* (Netherlands) **2019**, 181, 107703-107712. DOI: 10.1016/j.compscitech.2019.107703.

(XIII) Gagani, A.I.; Krauklis, A.E.; Sæter, E.; Vedvik, N.P.; Echtermeyer, A.T. A Novel Method for Testing and Determining ILSS for Marine Composites. *Composite Structures* (Netherlands) **2019**, 220, 431-440. DOI: 10.1016/j.compstruct.2019.04.040.

Scientific conferences:

(I) Echtermeyer, A.T.; Gagani, A.I.; Krauklis, A.E. Long-term degradation of composite laminates in offshore applications described by a multi-scale approach. *36th International Conference on Ocean, Offshore and Arctic Engineering Conference OMAE 17*. Trondheim, Norway, **2017**.

(II) Gagani, A.I.; Krauklis, A.E.; Echtermeyer, A.T. 3D microscale finite element anisotropic model for predicting diffusion in GF/epoxy composites. *20th International Conference on Composite Structures ICCS20*. Paris, France, **2017**.

(III) Echtermeyer, A.T.; Gagani, A.I.; Krauklis, A.E. Effect of anisotropic diffusion of water on the long-term degradation of composite laminates inside metal end fittings. *Oil & Gas Non-Metallics 2017*. London, United Kingdom, **2017**.

(IV) Gagani, A.I.; Krauklis, A.E.; Echtermeyer, A.T. Fluid diffusion in fiber reinforced composites in the presence of cracks and delamination. *International Conference on Composite Structures ICCS21*. Bologna, Italy, **2018**.

(V) Krauklis, A.E.; Gagani, A.I.; Echtermeyer, A.T. Hygrothermal Aging of Fiber-Reinforced Composites: Introduction to Phenomenological Perspective and Mass Balance Approach. *International Conference on Composite Structures ICCS21*. Bologna, Italy, **2018**.

(VI) Krauklis, A.E.; Echtermeyer, A.T. Dissolving Cylinder Zero-Order Kinetic Model for Predicting Hygrothermal Aging of Glass Fiber Bundles and Fiber-Reinforced Composites. *Fourth International Glass Fiber Symposium IGS 2018*. Aachen, Germany, **2018**.

(VII) Echtermeyer, A.T.; Gagani, A.I.; Krauklis, A.E.; Moslemian, R. Long Term Fatigue Degradation – Superposition of Dry and Wet Properties. *Twenty-second International Conference on Composite Materials ICCM22*. Melbourne, Australia, **2019**.

CHAPTER 2

METHODOLOGY

2.1. MATERIALS

Matrix polymer: amine-cured epoxy

The epoxy resin and amine hardener were supplied by Hexion. Amine-cured epoxy was prepared by mixing reagents Epikote Resin RIMR135™ and Epikure Curing Agent RIMH137™ stoichiometrically, in a ratio of 100:30 by weight. The mixture was degassed in a vacuum chamber for 30 minutes to remove bubbles. The density of the polymer (ρ_m) was 1.1 g/cm³.

Resin and hardener system consisted of the following compounds by composition: 63 wt% Bisphenol A diglycidyl ether (DGEBA; CAS 1675-54-3; number average molecular weight ≤ 700); 14 wt% 1,6-hexanediol diglycidyl ether (HDDGE; CAS 16096-31-4); 14 wt% poly(oxypropylene)diamine (POPA; CAS 9046-10-0; molecular weight 230); and 9 wt% isophorondiamine (IPDA; CAS 2855-13-2). Chemical structures of these compounds are shown in Figure 2.1.
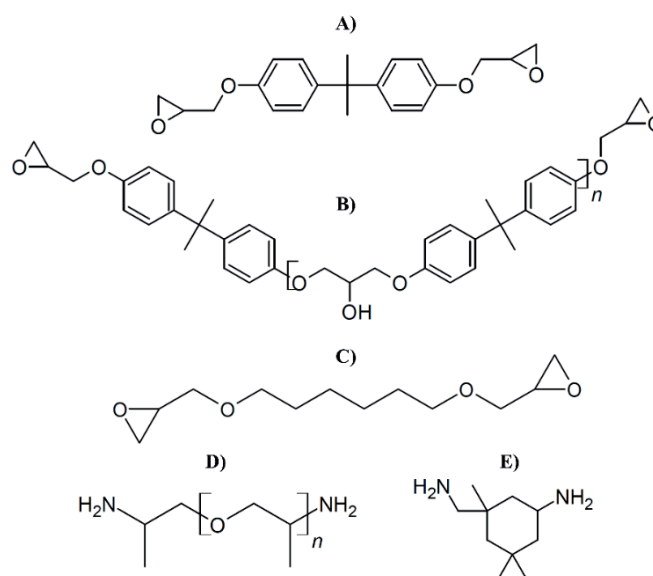
Figure 2.1. Molecular structures of epoxy and hardener components: (A) DGEBA monomer; (B) DGEBA oligomer (n = 1–2); (C) HDDGE; (D) POPA; (E) IPDA.

The dogbone and rectangular sample steel molds, shown in Figure 2.2, were prepared using computer numerical control (CNC) machining for casting the epoxy into the required geometry.
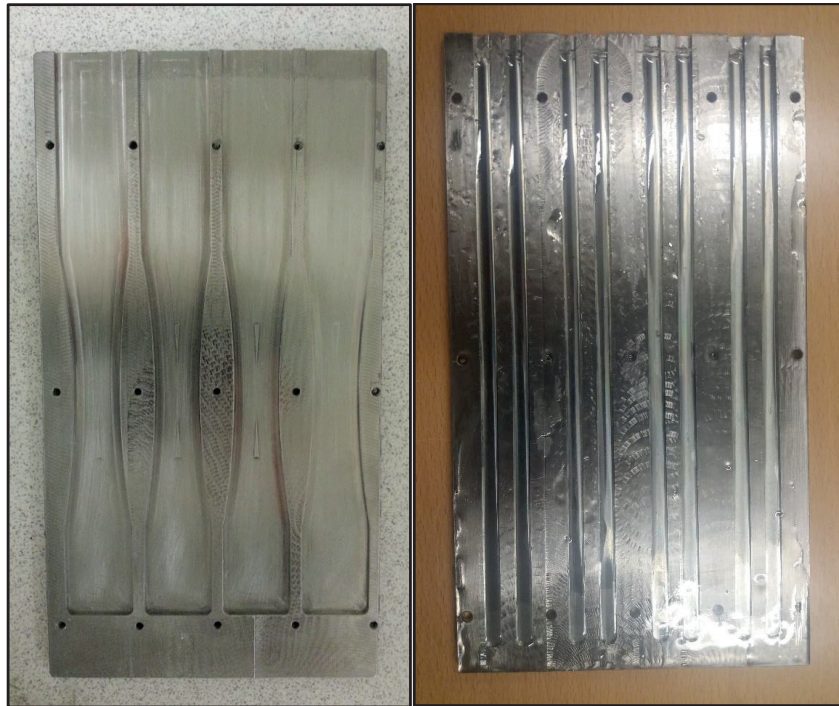
Figure 2.2. Steel molds for casting epoxy (left) dogbones and (right) rectangular samples.

Degassed resin was cast into the respective mold, followed by curing at room temperature for 24 hours and post-curing in an air oven at 80 °C for 16 hours. Full cure was achieved [3]. After samples were post-cured, the polymer samples were removed from the mold's grooves and cut into the desired length with a vertical bandsaw. Sample preparation was followed by grinding with sandpaper (FEPA P60, grain size 269 μm). The resin molds allowed making rectangular DMTA (40 mm x 7 mm x 2 mm) and dogbone-shaped (200 mm x 30 mm x 2 mm with 20 mm width in the narrowest part) specimens according to ISO 6721 and ISO 527 [129,130]. In both cases, the prepared molds allowed sufficient width control within a tolerance of 5%. In order to get samples to the right thickness and enable sufficient thickness control, a metal holder for grinding was prepared and used, as shown in Figure 2.3.

The desired thickness was obtained using grinding and polishing machine Jean Wirtz PHOENIX 2000 and SiC grinding discs (FEPA P500, grain size 30 μm). Exicator grease was used to enable sufficient adhesion of the sample with the holder. The sufficient thickness control, correct length and width were ensured within a 5% tolerance. Dogbone-shaped epoxy samples used in static tension and fatigue tests were prepared in a similar way.

The geometry of dogbone specimens equipped with Tokyo Sokki Kenkyujo strain gauges (gauge length of 6 mm) are shown in Figure 2.4. The specified dimensions from ISO 6721 and ISO 527 [129,130] were achieved within 5% tolerance. The placement of strain gauges as shown in Figure 2.4 allowed to measure strains in both the direction of the applied load and the direction normal to it, thus enabling the calculation of Poisson's ratio.
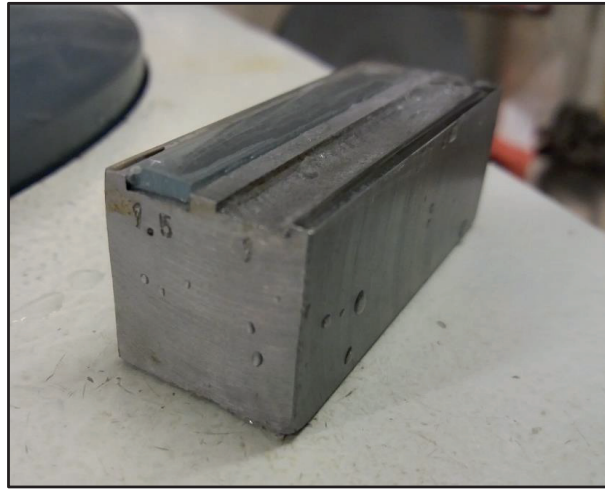
Figure 2.3. Steel sample holder for grinding rectangular epoxy samples.
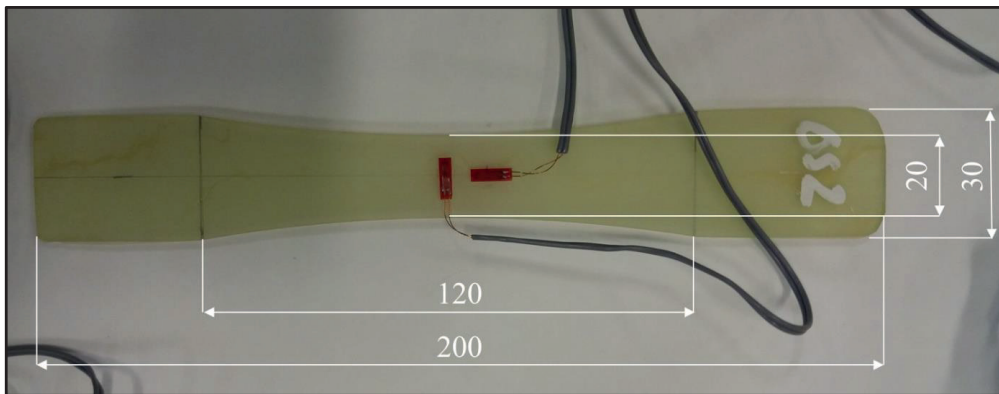
Figure 2.4. Geometry of dogbone specimens used for static tensile and fatigue tests. The placement of strain gauges is indicated.

Reinforcement material: R-glass fibers

A typical glass fiber used for marine and oil & gas applications was selected. Boron-free and fluorine-free high strength, high modulus 3B HiPer-Tex™ W2020 R-glass fiber bundles and stitch-bonded mats were used. These are classified as high-strength, high modulus R-glass (defined by an international standard ISO 2078 [131]). The material was the same in both cases (bundles and mats) and possessed the same properties. An average fiber diameter was 17 ± 2 μm [132]. The density of glass (ρ_f) was 2.54 g/cm³ [132]. A single bundle had about 4098 fibers [52]. The specific surface area of glass fibers was determined to be 0.09 m²/g from geometrical considerations as a product of number, circumference and length of the fibers [52]. Specific surface area determined with Brunauer-Emmett-Teller (BET) of sized and bare glass fibers was 0.180 and 0.084 m²/g, respectively [22]. Bare glass fibers were obtained by desizing glass fibers via heat cleaning. It should also be noted, that the heat cleaning might have had an effect on the density and the chemical nature of the surface layer of glass fibers, which could affect the initial dissolution of the desized glass fibers (this would affect ONLY the bare fibers). R-glass fiber bundles were used for dissolution experiments and fiber bundle tensile tests, while R-glass fiber mats

15

were used for making the laminates. A typical glass fiber Young's modulus value was taken from literature (72.4 GPa) [47]. This value was used throughout this work. However, later it was found that the modulus of the studied R-glass was slightly higher (86 – 89 GPa), according to the most recent datasheet by 3B [133]. This, however, did not affect the results significantly and did not change the conclusions at all. All fibers used throughout this work were sized, unless otherwise stated, and are shown in Figures 2.5 and 2.6.
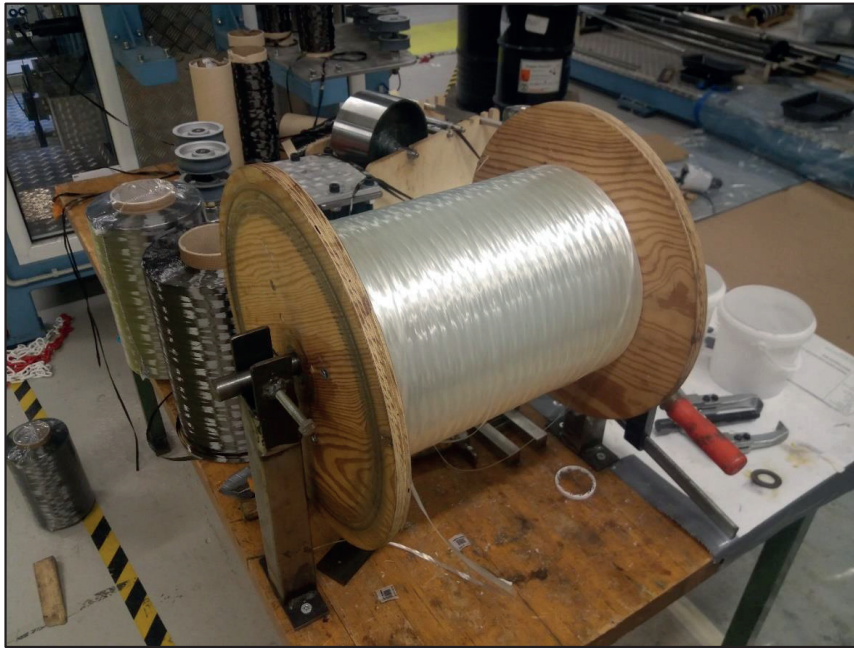
Figure 2.5. R-glass fiber bundles.
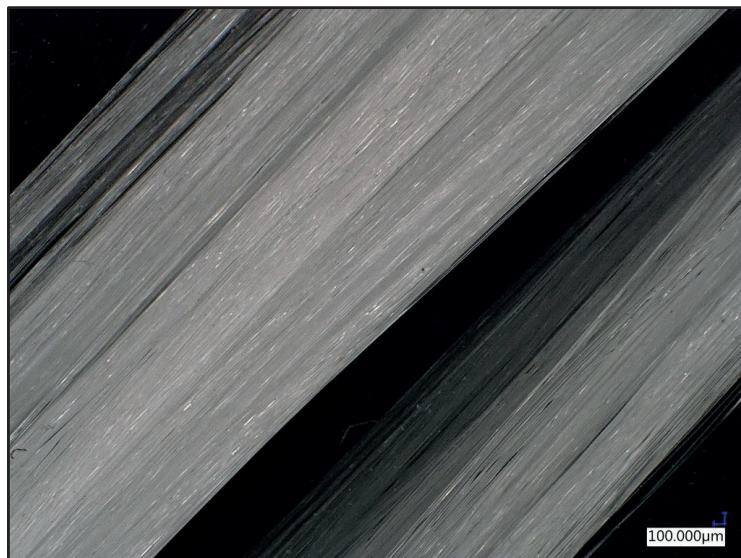
Figure 2.6. Micrograph of R-glass fiber bundles taken with a digital microscope Keyence VHX6000.

16

Sizing & the sizing-rich composite interphase

The sizing is a multi-component coating that results in the formation of the composite interphase during the manufacture of GFRPs [11]. This microconstituent has a proprietary composition. However, it is known that typical sizings consist of about five various chemicals [76,77]. Furthermore, it is known, that the sizing contains an organofunctional silane commonly referred to as a coupling agent [78-80]. This class of chemicals can be considered the most important in the glass fiber sizing, as it is the main component that promotes adhesion and stress-transfer between the polymer matrix and the fiber [11]. It also provides improvements in interphase strength and hygrothermal resistance of the composite interphase [80,133]. The silane coupling agents have the general structure [X-Si(-O-R)$_3$] where R is a methyl or ethyl group and X is a reactive group in respect to the polymer. When applied to fibers, it is first hydrolysed to a silanol in presence of water. It is unstable and further condenses onto the fibers by producing a siloxane network, which then partially becomes covalently bonded to the glass fiber surface. During the composite manufacture, the X reactive groups of the silane may still be available to react with the thermosetting polymer, leading to a strong network bridging between the fiber and the matrix polymer [11]. The most common coupling agents are silane compounds [70]. According to a size formulation patent review by Thomason and specifically a patent EP2540683A1 by Piret, Masson and Luc of 3B, the coupling agent in the studied W2020 sizing was an epoxysilane [76,77]. Usually sizings contain about 10 wt% of the coupling agent [88].

The composition of the sizing also consists of a number of multi-purpose components, such as a film former which, holds the filaments together in a strand and protects the filaments from damage through fiber-fiber contact. Film formers are as closely compatible to the polymer matrix as possible. Epoxies, such as in this case [70], are very common film formers [78]. Usually sizings contain about 70-80 wt% of the film former [88].

The sizing may also contain cationic or non-ionic lubricants, that reduce fiber-fiber abrasion, or other additives, such as antistatic agents, emulsifiers, chopping aids, wetting agents or surfactants, and antioxidants [11].

The exact composition of the sizing used in this study was not known, but based on technical details on the given R-glass fibers elsewhere [70], it is assumed that the sizing is based on the general characteristics described above. The results obtained are compatible with this assumption.

Glass fiber-reinforced composite laminates

Composite laminates were prepared via vacuum-assisted resin transfer molding (VARTM) using the same curing and post-curing procedure as for the polymer. The constituent glass fibers and matrix polymer materials were the same, as described before. The composite laminates were cut into rectangular bars and subsequently into composite plates with dimensions 20 mm x 20 mm x 1 mm (Papers I, IV and VI) and 50 mm x 50 mm x 1.5 mm (Paper VIII) with fibers oriented parallel (C1 plates) and normal (C3 plates) to the large face of the plate, respectively, as shown in Figure 2.7. The thickness was adjusted within 5% tolerance using grinding and polishing machine Jean Wirtz PHOENIX 2000 and SiC discs (FEPA P500, grain size 30 μm). The specified dimensions were achieved within 5% tolerance.
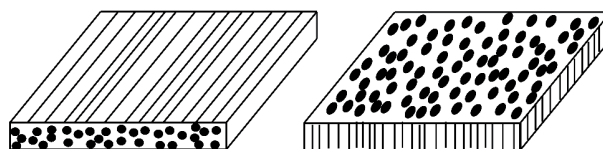
Figure 2.7. Composite plate configurations: (left) C1 and (right) C3.

Reagents and other chemicals

The distilled water (resistivity 0.5-1.0 MΩ·cm) was used for conditioning of the epoxy, glass fibers and composite samples. It was produced using the water purification system Aquatron A4000. The pH of the distilled water was 5.650 ± 0.010, being lower than neutral due to dissolved CO_2 from atmosphere in equilibrium.

IUPAC standard buffer solutions made by Radiometer analytical were used for studying the effect of pH on kinetics of GF and GFRP dissolution. The solutions of pH 1.679 ± 0.010, 4.005 ± 0.010, 5.650 ± 0.010, 7.000 ± 0.010 and 10.012 ± 0.010 were used. All of the samples were put dry into the water solutions, meaning that they were all saturated at respective pH and temperature.

2.2. EXPERIMENTAL METHODS

This section describes experimental methods used for investigating the mechanisms of environmental aging of composite and constituent materials, and their severity. In additional modeling techniques that were employed are described briefly.

2.2.1. Material Characterization and Testing

Determination of fiber fractions in composites

Fiber volume fractions were obtained by density measurements (Papers I, IV and VI) and burnoff tests (Paper VIII).

The polymer and composite plates were exposed to water. The density of matrix polymer (ρ_m) and glass fiber (ρ_f) was 1.1 g/cm³ and 2.54 g/cm³, respectively. The density of the composite ($\rho_{composite}$) was determined to be 1.97 g/cm³ by measuring mass and dimensions of a large composite block (Papers I, IV and VI). The volume and mass fractions of matrix polymer were calculated using the following equations, respectively:

$$V_f = \frac{\rho_{composite} - \rho_m}{\rho_f - \rho_m}$$

$$m_f = \frac{\rho_f \cdot V_f}{\rho_m \cdot (1 - V_f) + \rho_f \cdot V_f}$$

For the composite laminate in Papers I, IV and VI, the volume and mass fraction of the fibers were V_f = 0.606 and m_f = 0.780, respectively. The void content was very low (less than 0.02 %) and could be neglected.

In Paper VIII another laminate was used made out of the same constituents. The fiber volume fraction of the composite was V_f = 0.595 and was determined using the burn-off test, after the ASTM Standard D3171 [135]. The void volume fraction of the composite was 0.44 % and was measured by image analysis of optical microscope images, as was described elsewhere [23].

Determination of number of fibers & glass fiber surface area

The amount of glass fibers n in samples was calculated from density and geometrical considerations, using the following equation:

$$n = \frac{m_0}{\rho_{glass}\pi l r_0^2}$$

where l is the length of fibers; ρ_{glass} is the density of the glass; m_0 is the initial mass of a fiber bundle sample; r_0 is the initial fiber radius. The number of fibers per bundle was determined to be about 4098.

External surface area of glass fibers was evaluated from geometrical considerations as a product of number, circumference and length of fibers. The specific surface area of a studied sample can be calculated using the following equation:

$$S_0^{specific} = \frac{S_0}{m_0} = \frac{2\pi n l r_0}{m_0}$$

Specific surface area $S_0^{specific}$ was determined to be 0.09 m²/g glass. Additionally, Brunauer-Emmett-Teller (BET) tests were performed in order to determine specific surface area of sized and bare glass fibers. Specific surface area determined with Brunauer-Emmett-Teller (BET) of sized and bare glass fibers was 0.180 and 0.084 m²/g, respectively [22].

Loss on ignition & sizing amount determination

The Loss On Ignition (LOI) value of the fiber bundles was determined according to the standard practice ASTM D4963 [75]. This technique allows measurement of the weight loss of a sized glass sample. Since the weight loss is due to the burning off of the sizing, the method can be used to determine the amount of sizing on the fiber [11]. According to the LOI measurements the sizing was 0.64 wt% of the fibers. The temperature during the LOI measurement was about 565 °C applied for about 5 – 5.5 hours.

The obtained LOI is consistent with literature. LOI of most glass fiber reinforcement products is below 1.2 wt% [11]. For instance, Zinck and Gerard [136] also studied an silane-based sizing which had a similar LOI value of 0.77 wt%.

Weight measurements of the wet samples

Samples were weighed using analytical scales Mettler Toledo AG204 (± 0.1 mg). The surface layers of the samples immersed in water were dried using a soft and dry paper cloth, enabling to account for only the absorbed water inside the samples. The water bath and the scale were in the same room in vicinity of each other, which enabled performing weight measurements very quickly. We did not experience problems related to weight instability. Furthermore, using a set of samples provided statistical confidence in the weight gain results.

Conditioning and drying of polymer and composite samples

Conditioning in water was performed for polymer and composite plates using a batch system. A heated distilled water (60 ± 1 °C) bath was used. Samples were weighed using analytical scales Mettler Toledo AG204 (± 0.1 mg). Polymer and composite samples were conditioned at least until saturation with water was achieved. Up to and at the saturation point, the samples were taken out of the water bath, weighed and analyzed with an FTIR spectrophotometer. FTIR spectra at different water contents allowed to determine the true water content in polymer and composites and lead to the development of a novel spectroscopic water content monitoring method for composites (Paper I).

The drying of saturated polymer samples was performed in a drying cabinet ESAB PK-410 at 60 ± 1 °C in air atmosphere, with natural convection and relative humidity of 13 RH%. After that, samples were reconditioned at ambient conditions in the air to regain its their initial water content.

The water uptake and drying curve for polymer is shown in Figure 2.8, indicating the three sets of samples (dry, saturated and redried) used for mechanical testing (Paper III) and for determination of aging mechanisms (Paper II).
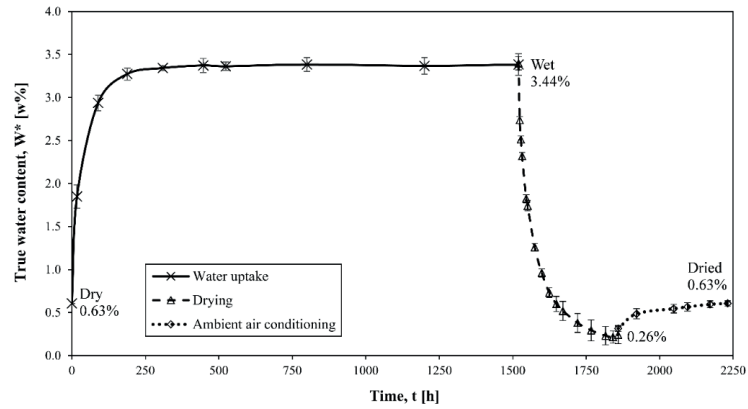
Figure 2.8. Water uptake and drying curves for epoxy polymer indicating true water content in dry, saturated and redried samples.

Transmission FT-NIR spectroscopy & true water content determination

Polymer and composite characterization with different water contents was performed using Fourier transform infrared spectroscopy (FTIR) in the near-infrared range (NIR). FT-NIR was used in order to develop a true water content determination method for polymer and composites (Paper I).

Near-infrared spectra were obtained using the Fourier transform spectrophotometer Foss NIRSystems 6500 operated in transmission mode, shown in Figure 2.9. An optical fiber probe and a spectral analysis software Foss Vision were used.

Figure 2.9. Epoxy sample analyzed with transmission FT-NIR spectroscopy (left) and FT-NIR spectrometer (right).

Spectra were taken in Vis-NIR wavenumber range of 4000–25000 cm⁻¹, using 32 scans per spectrum with a resolution of 4 cm⁻¹. FT-NIR spectroscopy was used to determine that the initial and redried polymer samples had the same water content.

HR-ICP-MS & glass dissolution experiments from fiber bundles and composites

HR-ICP-MS was used to determine dissolution of R-glass fibers from bundles and composites (Papers V-VII). Unlike the polymer, glass does not absorb water, but rather loses mass due to dissolution.

Dissolution experiments in water were performed for glass fiber bundles and fiber-reinforced composite plates using a batch system. Samples for dissolution study were weighed using analytical scales Mettler Toledo AG204 (± 0.1 mg) before the experiments. The samples were placed in inert closed vessels filled with 50 mL of distilled water or pH buffer solutions. The tight sealing of samples was ensured. The water-tight vessels, with samples and water solutions (or buffer solutions with pH levels of 1.679, 4.005, 5.650, 7.000 and 10.012; with an accuracy of ± 0.010) in them, were placed in the water bath. The water´s temperature (25, 40, 60, 80 °C) in the bath was controlled via PID-controlled heating, giving an accuracy of ± 1 °C. Two-stage heating system was used in order to ensure that there is no contact of the sample water with other potential ion release sources, such as the heating element itself.

The concentration of the dissolved ions in the water from the vessels was analyzed in time via High Resolution Inductively Coupled Plasma Mass Spectrometry (HR-ICP-MS) providing glass dissolution kinetics. Experimentally, the total mass loss of glass material was measured as a sum of all ions' release quantified with HR-ICP-MS cumulatively over time. Analyses were performed using a double focusing magnetic sector field HR-ICP-MS Thermo-Scientific Finnigan ELEMENT 2, equipped with a sample introduction system ESI/Elemental Scientific PrepFAST and a pre-treatment/digestion Milestone UltraClave. Acidification of samples was performed using ultra-pure grade HNO₃ in order to avoid adsorption of ions to the wall of the sample vials.

Infinite water availability conditions were ensured by using fresh distilled water for each separate measurement.

The benefit of HR-ICP-MS versus gravimetric analysis is that it allows measuring dissolution kinetics of each separate ions as well as the total mass loss [52]. The data obtained from the HR-ICP-MS experiments are in the form of mass concentration at each time point (non-cumulative) c (g/L) and need to be converted to the $m_{dissolved}$ form by using the following equation:

$$m_{dissolved} = V_{water} \int_0^t c \, dt$$

where V_{water} is the volume of a water sample in the HR-ICP-MS measurement. V_{water} used for experiments was 50 mL. This equation is valid for each individual ion release and for the total mass loss.

For studying the influence of external loads on dissolution kinetics, a stress corrosion rig was designed, built and used during the experiments. The experimental rig is shown in Figure 2.10, and design schematics of the stress corrosion setup are shown in Figure 2.11.

Figure 2.10. Glass fiber stress corrosion experimental setup.

The principle is that glass fibers are inside an inert cylinder pushed by an inert rod, which transfers the stress from the weights to the fibers. The water samples for HR-ICP-MS analyses are taken from the main cylinder, where distilled water is in contact with stressed glass fibers. The temperature was PID-controlled using two-stage heating system, ensuring temperature of 60 ± 1 °C. Polymeric spheres, seen in Figure 2.10, were used to reduce the evaporation rate of the heating water.
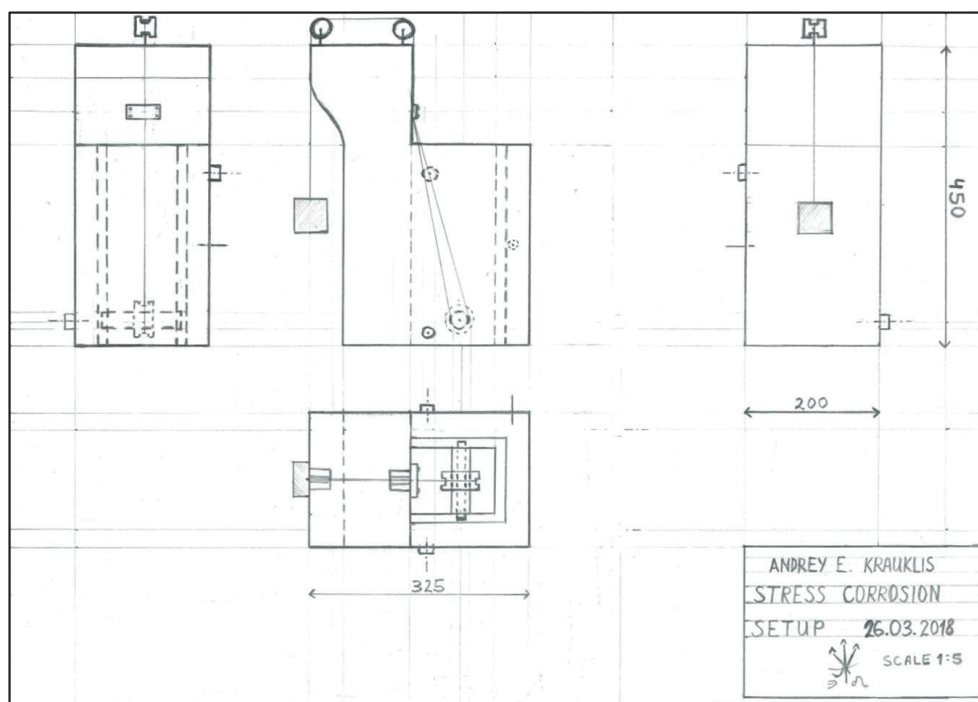
Figure 2.11. Design schematics of the stress corrosion rig for glass fiber bundles, indicating also the placement of fibers and weights.

pH measurements & HR-ICP-MS for studying leaching from the epoxy

HR-ICP-MS and pH measurements were used to determine leaching from the epoxy polymer (Paper II).

Leaching experiments in water were performed for polymer plates using a batch system. Samples were weighed using analytical scales Mettler Toledo AG204 (± 0.1 mg) before the experiments. The samples were placed in inert closed vessels filled with 50 mL of distilled water. The tight sealing of samples was ensured. The water-tight vessels, with samples and distilled water in them, were placed in the water bath. The water's temperature (60 °C) in the bath was controlled via PID-controlled heating, giving an accuracy of ± 1 °C. Two-stage heating system was used.

The concentration of the dissolved compounds in the water from the vessels was analyzed in time via high resolution inductively coupled plasma mass spectrometry (HR-ICP-MS) providing leaching kinetics. Experimentally, the total mass loss of glass material was measured as a sum of all elements' release quantified with HR-ICP-MS cumulatively over time, similarly as was done in glass dissolution experiments.

pH measurements were performed using standard pH-meter Radiometer analytical MeterLab PHM210 (pH ± 0.01). IUPAC standard buffer solutions produced by Radiometer analytical were used for calibration of the pH meter. The pH was determined for each sample, resulting in the pH kinetics curves, that indicate the change of H_3O^+ concentration in water due to leaching. After pH was determined, the samples were acidified using ultra-pure grade HNO_3 and further analyzed with HR-ICP-MS. HR-ICP-MS analyses were performed using a double focusing magnetic sector field HR-ICP-MS Thermo-Scientific Finnigan ELEMENT 2, equipped with a sample introduction system ESI/Elemental Scientific PrepFAST and a pre-treatment/digestion Milestone UltraClave.

Optical microscopy, glass fiber radius reduction & polymer and composite swelling measurements

Optical microscopy was performed using a digital microscope Hirox RH-2000 equipped with lens MXB-2500REZ with a magnification of 140 and resolution of 1.06 μm. Microscopy was used for measuring changes in glass fiber radius after various immersion times in water (Paper V) and for determination of hygroscopic swelling of polymer and composite plates (Paper IV).

Changes in the length and width of the polymer and composites plates were measured using the edge dimensions of the plates. The strains and swelling coefficients were obtained using the following equations for matrix polymer and composites, respectively:

$$\varepsilon_m = \frac{l - l_0}{l_0} = \beta_m W$$

$$\varepsilon_i = \frac{l - l_0}{l_0} = \beta_i W_m$$

where i stands for x, y and z for respective swelling directions. Composite C1 was used to obtain swelling coefficients in the direction parallel to fibers (β_x) and transverse to fibers (β_y), while composite C3 also provided transverse-to-fibers swelling (β_z) which was similar to and consistent with β_y.

SEM & EDX

Scanning electron microscopy (SEM) and energy-dispersive X-ray spectroscopy (EDX) experiments were performed using Tescan Mira/LMU in a backscattered electron regime, with working voltage of 15 kV. SEM and EDX was used to study the changes in polymer due to environmental aging (Paper II).

ATR-FT-IR spectroscopy

Fourier transform infrared (FT-IR) spectra were recorded using Varian Scimitar 800 FT-IR in the Attenuated Total Reflectance (ATR) mode via Pike technologies GladiATR™ mode. Spectra were obtained at 4 cm^{-1} resolution, co-adding 50 scans over a range of wavenumbers from 400 to 4000 cm^{-1}. ATR-FT-IR was used to compare spectra of the polymer before and after environmental aging in order to deduce aging-induced changes in the chemical structure (Paper II).

DMTA & glass transition temperature determination

Dynamic Mechanical Thermal Analysis (DMTA) tests, for determination of glass transition temperature T_g, storage and loss moduli for dry and saturated polymer samples, were conducted using a Netzsch GABO Eplexor qualimeter, equipped with a 1.5 kN load cell operated in displacement control with a constant static strain of 0.4%, and a cyclic strain of 0.1% applied with a frequency of 1 Hz (Papers II and III). The temperature sweep range was from 20 up to 120 °C, with a heating rate of 1 °C/min. The glass transition temperature T_g was determined using DMTA as the crossing of tangents to the inflection points in the storage modulus curves, after standard practice ISO 6721-11 [32,129]. The setup and the sample placement are shown in Figure 2.12.
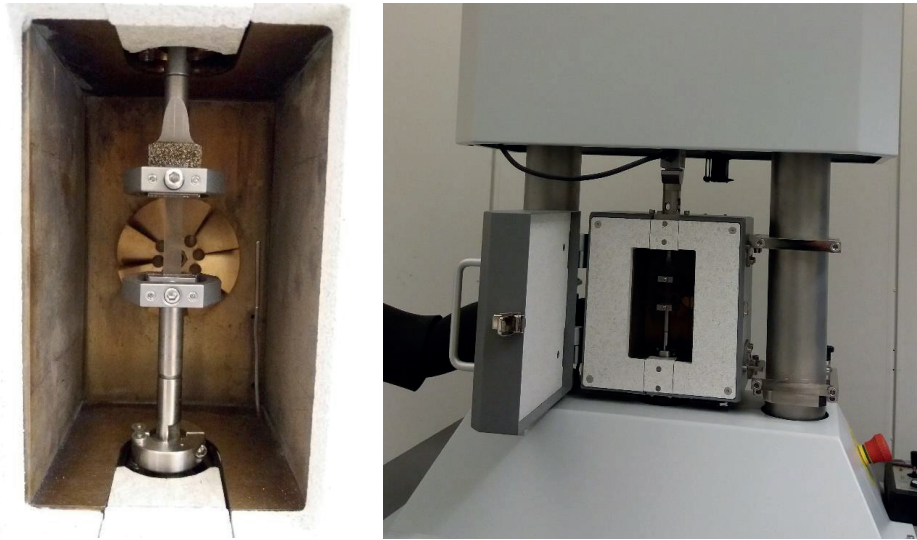
Figure 2.12. Placement of the specimen (left) and the DMTA machine (right).

Uniaxial tensile testing

To evaluate the effect of the true water content on the ultimate tensile strength (UTS), Young's modulus and Poisson's ratio of the dry, saturated and redried epoxy polymer, tensile tests were conducted using the servo hydraulic test machine Instron Model 1342, shown in Figure 2.13. Dogbone-shaped epoxy samples were used in order to determine tensile strength; the rate was set to 1 mm/min of controlled displacement (Paper III). The temperature during the tests was about 23 °C (room temperature). Tensile tests were performed with 4 specimens for each configuration (dry, wet and dried). Average values and experimental scatter were reported for ultimate tensile strength, Young's modulus and Poisson's ratio for each group.

Uniaxial tension-tension fatigue testing

To evaluate the effect of water content on the fatigue behavior of the dry, saturated and redried epoxy polymer, tension-tension fatigue tests were conducted using a servo hydraulic test machine Instron Model 1342, shown in Figure 2.13. Dogbone-shaped epoxy samples were used in order to obtain S-N curves (Paper III). The testing frequency was chosen in order to keep a constant strain rate of 0.05%/min. The temperature during the tests was about 23 °C (room temperature). Tests were performed at R ratio of 0.1. In fatigue, between 11 and 13 dogbone specimens were used for obtaining S-N curves for each case (dry, wet and dried).

Figure 2.13. Placement and failure of the specimen in the test machine.

2.3. MODELING

2.3.1. Numerical Modeling (FEA)

FEA is used in this work to validate the analytical prediction of the hygroscopic swelling of the fiber-reinforced composite plates in Paper IV. The commercial FEA software package Abaqus was used in all FEA simulation experiments. The detailed description of the FEA approach is given in Paper IV (Appendix D).

2.3.2. Analytical Modeling

Analytical models are described shortly in the key findings of the thesis (Chapter 3) and in more detail in respective papers. Paper I (Appendix A) describes a model for the true water content determination in polymer and composites. Paper IV (Appendix D) describes a model for prediction of orthotropic hygroscopic swelling of composites from isotropic swelling of a polymer matrix. Papers V-VII (Appendices E-G) describe a model of glass dissolution prediction of fiber bundles and composites at various environmental conditions. Paper VIII (Appendix H) describes a phenomenological mass balance model for composites in water and predicts the kinetics of the composite interphase hydrolysis.

CHAPTER 3

KEY FINDINGS

3.1. TRUE WATER CONTENT DETERMINATION AND MONITORING IN POLYMERS AND COMPOSITES (PAPER I)

It is common to report water content without accounting for moisture initially present in the material. In reality, some water is already present in the polymer uptaken from the air, which has a certain humidity. The true water content shows the amount of water with respect to the absolutely dry material and is defined as:

$$W^*(t) \equiv \frac{m_{water}(t)}{m_{absolutely\,dry}} \cdot 100\% = \left(\frac{m(t) - m_{absolutely\,dry}}{m_{absolutely\,dry}} \right) \cdot 100\%$$

where W^* is the true water content (wt%); m_{water} is the mass of water (g); $m_{absolutely\,dry}$ is the mass of an absolutely dry specimen (with null water content; g); m is the mass of a specimen with some water taken up (g).

A benefit of using a spectroscopic method over the conventional gravimetric analysis is the possibility of deducing the mass of an absolutely dry material and the true water content, which is an important indicator of water content-dependent properties, i.e. strength, stiffness and fatigue property changes due to water content. Theoretically, it is possible to obtain mass of the absolutely dry material with conventional drying, but usually this requires extremely long drying times. Furthermore, it is not possible to obtain such data precisely due to humidity of the ambient air, unless perfectly dry air can be ensured during drying and weight gain measurements. These technical problems can be easily avoided by using a spectroscopic method.

The true water content at initial conditions was already 0.63 wt% for the studied epoxy. These conditions are what would usually be denoted as a 'dry' material. Thus, the initial water content is significant and should not be neglected. The provided method allows determining and quantifying it. The true water content at saturation with water was 3.44 wt%. For a composite, equilibrium true water content value (scaled by polymer mass fraction) was only slightly higher (3.56 wt%) than that of the polymer itself. The difference was attributed to the sizing-rich interphase also absorbing water.

A detailed Fourier Transform Near-Infrared (FT-NIR) spectroscopic method for estimating and monitoring true water content in epoxy resins and fiber-reinforced composites was developed using the maxima of the absorbance band at about 5200 cm⁻¹ in the Near-Infrared (NIR) combination mode region correlated with the true water content. Based on extensive measurements of epoxy polymer and composite samples of varying water content and thickness, regression was performed, and the quantitative absorbance dependence on water content in the materials was successfully established. The model equations for monitoring water content in epoxy resin and composite material samples were obtained and experimentally validated. The model was related to the Beer–Lambert law and explained in such terms. The details of the method were reported, allowing the use of the method in practical applications.

Model in short

Based on the Beer–Lambert law, absorbance (*A*) is dependent on the molar attenuation coefficient (ε), concentration (*c*) and the path length (*l*) [137]:

$$A = log_{10}\left(\frac{I_0}{I}\right) = \varepsilon c l$$

In this case, the concentration term is the true water content (W^*), and the path length is the thickness of the sample (δ). Thus, the Beer–Lambert law can be expressed as:

$$A = \varepsilon^* W^* \delta = \frac{K_{slope}}{\delta} W^* \delta$$

where ε^* is the attenuation coefficient (wt%$^{-1}$mm^{-1}) and K_{slope} is the attenuation coefficient for a specific sample thickness (wt%$^{-1}$), for more details see the method described in Paper I (Appendix A).

The method was extended to glass fiber-reinforced composite materials. The true water content of the polymer matrix in the composite can be calculated as:

$$W^*_{resin} = \frac{m_{comp}(t) - \left(1 - m_{f_{resin_{initial}}}\right) \cdot m_{comp_{initial}} - m_{resin_{absolutely\,dry}}}{m_{resin_{absolutely\,dry}}} \cdot 100\%$$

where W^*_{resin} is the true water content (wt%); m_{comp} is the mass of a composite specimen with some water taken up (g); $m_{comp_{initial}}$ is the initial mass of a composite specimen (g); $m_{f_{resin_{initial}}}$ is the initial mass fraction of the epoxy in the composite (g/g); $m_{resin_{absolutely\,dry}}$ is the mass of an absolutely dry epoxy (with null water content; g).

Calculated W^*_{resin} is then to be used for predicting the water content in the composite:

$$A = K_{slope}\, W^*_{resin}$$

Since composite materials have components of different absorbance, there is a necessity to correct for the summary absorbance of the components via the baseline shift. In order to do so, an additional parameter is required: a ratio, termed *Peak Factor*, of the maximum absorbance for the composite ($A_{peak_{comp}}$) and the polymer ($A_{peak_{resin}}$) at water saturation:

$$Peak\ Factor \equiv \frac{A_{peak_{comp}}}{A_{peak_{resin}}}$$

The final water content monitoring equation for the composite system:

$$A_{peak_{comp}} = \varepsilon^* \cdot Peak\ Factor \cdot \delta \cdot W^*_{resin} = K_{slope} \cdot Peak\ Factor \cdot W^*_{resin}$$

Paper I (Appendix A) describes a model for the true water content determination in polymers and composites in more detail.

3.2. CHANGES IN THE CHEMICAL STRUCTURE OF THE MATRIX POLYMER DUE TO HYGROTHERMAL AGING (PAPER II)

The hygrothermal aging may involve both reversible and irreversible processes [20,37]. Irreversible changes are those that persist even after redrying the material to its initial water content [32]. The epoxy yellows irreversibly, indicating that the mechanistic origin of the color change lies among irreversible degradation pathways. Morphology was found to be unaffected. Changes in the chemical structure of the epoxy were studied and the mechanism of yellowing was identified. Experimental evidence in this work was obtained using a combination of FT-NIR, ATR-FT-IR, EDX, HR-ICP-MS, pH measurements, optical microscopy, SEM, and DMTA.

Irreversible aging mechanisms, which have been reported in the literature to occur during hygrothermal influence on general epoxies are [4,32,37,138]:

1. Hydrolysis (involves chain scission)
2. Thermo-oxidation (might involve chain scission, backbone modifications or crosslinking)
3. Photo-oxidation (might involve chain scission, backbone modifications or crosslinking)
4. Residual curing (additional crosslinking)
5. Leaching (initially present additives, impurities or degradation products)

In this work, photo-oxidative effects were avoided by conducting experiments in the absence of high-intensity light sources [139,140]. For the studied material, no chain scission (hydrolysis or oxidation-induced) occurred [38]. To avoid residual curing, the material was fully cured. Based on this, hydrolysis, photo-oxidation, and residual curing were excluded, whilst thermo-oxidation and leaching occurred and were investigated further. Compounds involved in leaching were identified to be epichlorohydrin and inorganic impurities but were found to be unrelated to yellowing. It was found, that yellowing occurred due to the thermo-oxidative carbonyl formation in the epoxy carbon-carbon backbone via nucleophilic radical attack.

"Weak points" for radical attack in the epoxy network were identified and are shown in Figure 3.1. In the network, 12 unique sites potentially involved in thermo-oxidation were found. Furthermore, 8 of these sites were excluded based on experimental evidence and literature [28,31,141-146]. Sites marked in green were the identified main reactive sites (δ⁺DGEBA-II, δ⁺POPA-I, δ⁺HDDGE-III, and δ⁺HDDGE-IV).
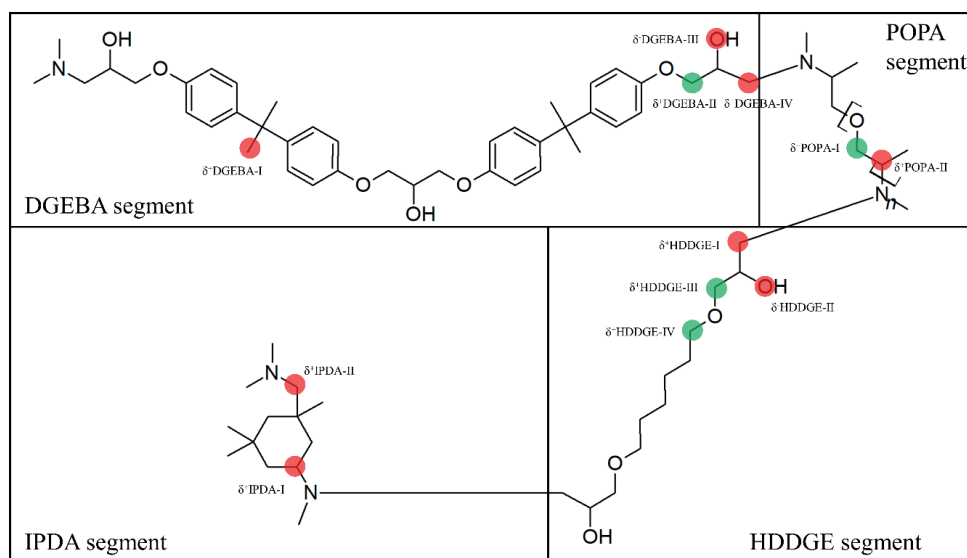
Figure 3.1. Chemical structure of the studied DGEBA/HDDGE/IPDA/POPA amine epoxy network (mixing ratios are not considered). Marked sites represent "weak points" for radical attack in the network. Sites marked in red are excluded based on experimental evidence and literature. Sites marked in green are the main reactive sites.

Four of these unique reactive sites were involved in thermo-oxidation. One reactive site was involved in minor thermo-oxidative crosslinking of the HDDGE segments, as shown in Scheme 1. The other three sites were linked to carbonyl formation. Noteworthy that all three sites involved in carbonyl formation had similar structures, containing highly reactive polyoxypropylene and *i*-propanol moieties.

Respective reactions were proposed. A crosslinking mechanism of HDDGE segments was proposed in Scheme 1, involving sites δ⁺HDDGE-IV. This reaction is analogous to thermo-oxidative crosslinking of DGEBU, after [143].
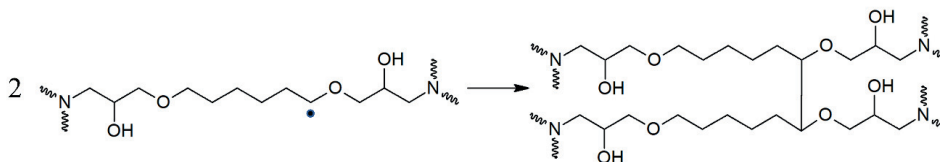
Scheme 1. Crosslinking reaction of the HDDGE segments via reactive sites δ⁺HDDGE-IV.

δ⁺POPA-I site as a polyoxypropylene moiety-containing segment is very susceptible to radical attack under oxidation, due to low stability of the tertiary C-H bond and the destabilizing effect of the neighboring ether group [31,147]. The proposed carbonyl formation reaction on this site is shown in Scheme 2.
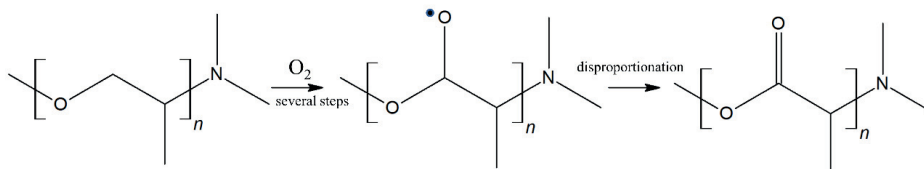
Scheme 2. Carbonyl formation involving polyoxypropylene moiety on reactive site δ⁺POPA-I.

The δ⁺DGEBA-II and δ⁺HDDGE-III sites as *i*-propanol moiety-containing segments are also highly susceptible to oxidation [144,148]. The carbonyl formation on these two sites follows the same reaction, as shown in Scheme 3 [144].
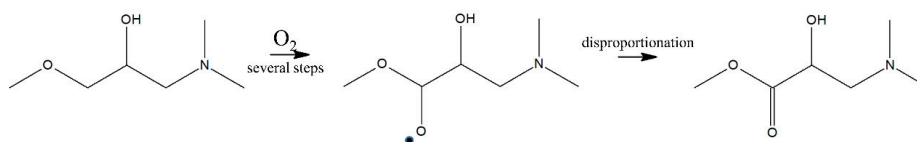
Scheme 3. Carbonyl formation reaction involving *i*-propanol moiety on reactive sites δ⁺DGEBA-II and δ⁺HDDGE-III.

T_g is a useful parameter revealing chemical changes for polymers [149]. The T_g of a redried epoxy (84.7 °C) was slightly higher than for the initial material (81.7 °C), indicating that no chain scission occurred [141,147]. A likely reason of a T_g increase was a combination of polymer relaxation [32], anti-plasticizing effect of leaching, and a minor crosslinking [141,143] of the HDDGE segments (Scheme 1).

It is speculated that yellowing could be prevented or delayed by adding phenolic antioxidants, such as hindered phenols.

3.3. REVERSIBILITY OF THE MECHANICAL PROPERTIES OF THE MATRIX POLYMER UPON RE-DRYING (PAPER III)

Exposure of the epoxy to water caused the material to swell. In order to investigate the influence of water on the mechanical properties of the epoxy, static tensile and tension fatigue tests were performed.

Swelling/plasticization is the only hygrothermal process that significantly affects mechanical properties of the studied polymer. It was found, that mechanical properties of the studied epoxy are reversible upon re-drying the material to its initial water content. The material regains its initial strength, Poisson's ratio, Young's modulus and fatigue performance after re-drying to its initial water content. Thus, swelling/plasticization was fully reversible for the studied epoxy.

When epoxy was saturated with water, the ultimate tensile strength (UTS) decreased from the initial 66.4 ± 3.0 MPa down to 48.5 ± 3.3 MPa, resulting in a relative decrease of about 20% due to swelling/plasticization by water. The results of fatigue tests indicated that the S-N curve of a wet epoxy also shifted by 20% without a change in slope. The S-N curves of dry and dried material were identical, further proving the reversibility in mechanical properties.

Furthermore, it is shown experimentally that the tension fatigue S-N curve of a wet epoxy resin can be estimated by shifting the S-N curve of a dry material proportionally to a reduction in static tensile strength due to swelling/plasticization.

Results show that Poisson's ratio increases for saturated epoxy but returns to the initial values after drying to the initial water content, indicating that this effect is reversible. An increase in Poisson's ratio of epoxy due to absorbed water is consistent with literature [150]. Such increase in Poisson's ratio is likely due to the absorbed almost incompressible water or the reduction of glass transition temperature (T_g) due to the plasticizing action [150,151]. The T_g of dry, saturated and re-dried epoxy was 81.7, 59.1 and 84.7 °C, respectively.

The strain to failure increased from initial 3.71 ± 0.10% to wet 4.78 ± 0.51%. It was a brittle fracture, and shattering often occurred for dry and re-dried specimens, while there was no shattering for the saturated epoxy. On the micro level failure is believed to occur due to a combination of crosslink bond breakage and disentanglement of macromolecular chains.

3.4. PREDICTION OF HYGROSCOPIC SWELLING OF THE COMPOSITE FROM SWELLING OF THE MATRIX POLYMER (PAPER IV)

Swelling in fiber-reinforced composites is anisotropic. For orthotropic laminates, three CHEs ($\beta_x, \beta_y, \beta_z$) are needed in order to predict swelling. Quantification of the orthotropic CHEs can be performed experimentally using samples with different fiber orientations. However, it is a time-consuming and tedious process that also tends to involve quite high experimental scatters. Thus, an analytical tool based on linear elasticity was developed that predicts the orthotropic swelling constants (CHEs) of the composite from the CHE of the matrix polymer, which is isotropic. The matrix properties are easy to measure. Furthermore, they also may be found in literature for various polymers [122,125]. The method has an advantage that it is simple-to-use in practice and requires only a swelling coefficient of the matrix polymer, elastic constants of matrix and fibers and a known fiber volume fraction of the composite.

Hygroscopic strains were measured after various times of exposure to water for both matrix polymer and composite samples, and CHEs were obtained in each direction experimentally. Linear strain behavior has been observed experimentally with increasing moisture concentration for both composites and polymers, in agreement with [108,110]. Swelling behavior in the fiber direction (β_x) was constrained by the non-swelling fibers and was close to null, while swelling in the transverse directions (β_y, β_z) was found to occur freely – similar to the unconstrained polymer.

CHEs are systematized in Table 3.1. Numerical FEA and analytical prediction as well as experimental results are shown in Table 3.1 and Figure 3.2.

Good agreement was obtained and was reported between experimental swelling data, analytical and numerical results for composite laminates. To the best knowledge of the author, this is the first micromechanical model that predicts the anisotropic swelling of composites from isotropic swelling of the polymer.

During the review of the dissertation, it was pointed out that the modulus of the studied R-glass should be slightly higher than was used in the calculations (a typical glass fiber modulus was used). This, however, did not affect the transverse swelling predictions and did not change the conclusions. As for the axial swelling, conclusions were also unaffected, but a slightly lower analytical axial CHE (β_x) was obtained (0.029 instead of 0.036).

Table 3.1. Coefficients of hygroscopic expansion. Experimental scatter is reported with one standard deviation for the coefficient of hygroscopic expansion (CHE). * indicates an input parameter for the models. ‡ indicates a value for a typical E-glass fiber.

CHE	Experimental	Analytical	Numerical
β_m	0.332 ± 0.021	0.332*	0.332*
β_x	0.060 ± 0.018	0.029 (0.036 ‡)	0.044
β_Y	0.569 ± 0.066	0.546	0.552
β_z	0.576 ± 0.059	0.546	0.573
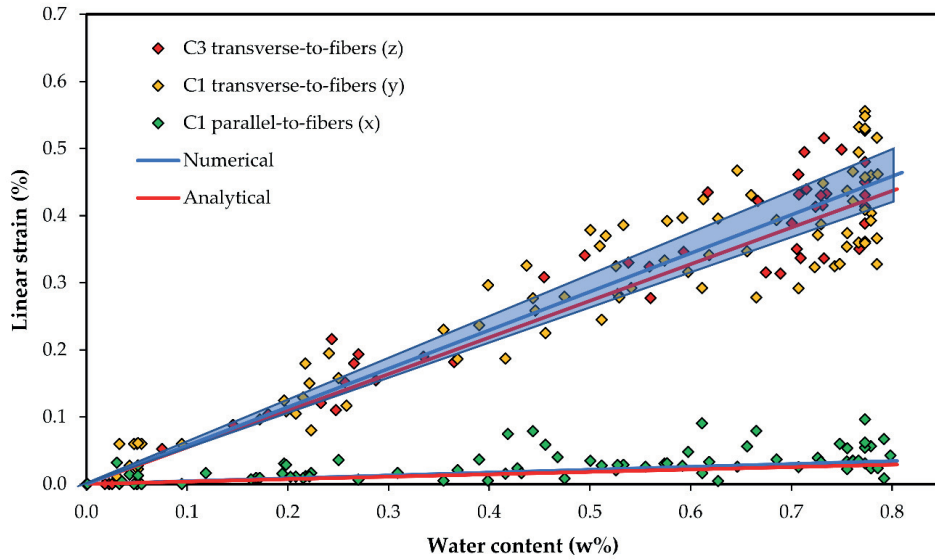
Figure 3.2. Numerical and analytical fit of swelling with the experimental data for composites. Analytical results are shown in red lines; global averaged out numerical results are shown in blue lines, while a numerical scatter is shown with blue sectors indicating scatter on the local scale due to various fiber arrangements.

Brief description of the model

Composite transverse swelling strains (directions y and z) can be predicted as a serial connection of fiber and matrix:

$$\varepsilon_y = V_f \varepsilon_f + (1 - V_f) \varepsilon_m$$

where ε_y is the composite transverse swelling strain, V_f the fiber volume fraction, ε_f is the fiber swelling strain and ε_m is the matrix swelling strain. For many engineering reinforcements (carbon fibers, glass fibers, etc.) the swelling is null, $\varepsilon_f = 0$. In these cases:

$$\varepsilon_y = (1 - V_f) \varepsilon_m$$

The transverse swelling coefficient is defined in the following equation [47]:

$$\beta_y = \frac{\varepsilon_y}{W_c} = \frac{(1 - V_f)\varepsilon_m}{W_c} = (1 - V_f)\frac{W}{W_c}\beta_m$$

where W is the moisture content in the matrix and W_c the moisture content in the composite.

Composite axial swelling (direction x) can be predicted by employing a parallel connection model of fiber and matrix. The swelling of the matrix in this case is strongly constrained by the stiffness of the fibers. The constrained swelling strain in the matrix ε_m generates a stress equal to:

$$\sigma_m = E_m \varepsilon_m$$

where σ_m is the stress in the matrix and E_m is the stiffness of the matrix.

The load transferred from the matrix to the fibers, L can be estimated as:

$$L = \sigma_m A_m = \sigma_m A(1 - V_f) = \sigma_f A_f = \sigma_f A V_f$$

where A is the cubic cell lateral surface area (in the $x - z$ plane), $A_m = A(1 - V_f)$ is the matrix part of the cubic cell lateral surface area and $A_f = A V_f$ is the fiber part of the cubic cell lateral surface area.

The stress transferred to the fiber, σ_f:

$$\sigma_f = \sigma_m \frac{1 - V_f}{V_f}$$

Finally, the composite axial strain, ε_x, can be predicted as equal to the fiber axial strain, ε_f, as the axial swelling of the cubic cell is governed by its behaviour:

$$\varepsilon_x = \varepsilon_f = \frac{\sigma_f}{E_f} = \frac{\sigma_m}{E_f}\frac{1 - V_f}{V_f}$$

where E_f is the fiber stiffness.

The axial swelling coefficient is defined as, after [47]:

$$\beta_x = \frac{\varepsilon_x}{W_c} = \frac{\sigma_m}{W_c E_f}\frac{1 - V_f}{V_f} = \frac{E_m \varepsilon_m}{W_c E_f}\frac{1 - V_f}{V_f} = \frac{E_m \beta_m}{E_f}\frac{W}{W_c}\frac{1 - V_f}{V_f}$$

Paper IV (Appendix D) describes a model for prediction of orthotropic hygroscopic swelling of composites from isotropic swelling of a polymer matrix in more detail.

3.5. PREDICTION OF MASS LOSS AND RADIUS REDUCTION OF GLASS FIBERS DUE TO DISSOLUTION IN WATER (PAPER V)

The long-term (3194 hours) dissolution of R-glass fibers in water was studied experimentally. An analytical model termed Dissolving Cylinder Zero-Order Kinetic (DCZOK) model was developed and successfully used to describe the kinetics of mass loss and fiber radius reduction during the dissolution in water. Experimentally mass loss was obtained using HR-ICP-MS for separate released ions.

The model differentiates between the complex short-term and dissolution-dominated long-term processes. Furthermore, the novelty of the model is the ability to describe both dissolution and radius reduction kinetics without the necessity for introducing additional terms such as conversion factor. The model is able to predict both mass loss and radius reduction kinetics using the same four parameters: initial fiber radius (r_0), rate constants for both short-term degradation (K_0^I) and steady-state degradation (K_0^{II}) and the time when steady-state kinetics are reached (t_{st}). All parameters can be easily determined from initial radius measurements and mass loss evolution in time.
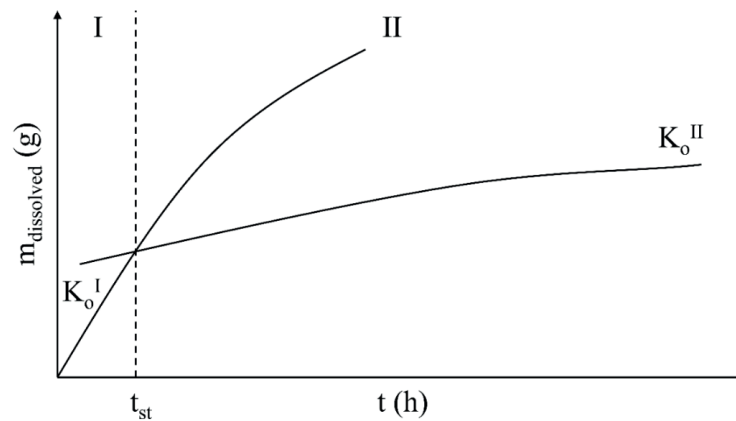
Figure 3.3. Separation of mass loss or cumulative ion release curves into (Phase I) short-term non-steady-state and (Phase II) long-term steady-state regions.

The methodology was provided offering the guidelines on how to obtain the required parameters in order to use the model in practice. The developed model is useful for both predicting the time evolution of fiber radius reduction and material mass loss.

Elements released during degradation were determined to be Na, K, Ca, Mg, Fe, Al, Si and Cl. The total material loss and release of each separate ion was modeled using the developed kinetic equations, and rate constants were obtained and reported. Si contribution to the total mass loss was the largest (56.1 wt%) and governed the dissolution process. Ca and Mg are released at approximately similar rates to each other and contributed 14.3 and 15.1 wt% to the total mass loss, respectively, while all other elements contributed less than 7 wt% individually, as shown in Figure 3.4. It was speculated that in the steady-state some equilibrium composition of glass (different from the bulk composition) is obtained in the outer layers that are contact with water, allowing elements to dissolve at some limiting rate and proportionally to their content in the outer layers of the glass.

The rate constants K_0^I and K_0^{II} for the glass dissolution and individual ions' release are systematized in Table 3.2. Rate constants are often given in relation to the surface area of a material, thus describing dissolution behavior from a unit of the material's surface area [61]. Obtained values are reasonable (similar order of magnitude) compared with dissolution rates of other glass fibers, after [152].

The kinetics of radius reduction were reported. The radius reduction was found to be linear with time. However, the induction period before the linear regime, as was also observed elsewhere [57], which can be explained with the complexity of the short-term non-steady-state process and, to the best knowledge of the author, was not explained before. The rate constant and the density of the glass described the rate (proportionality) of the dissolution.
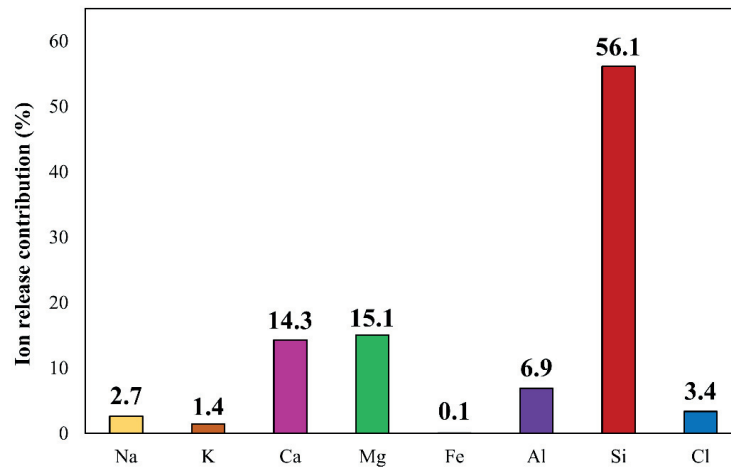
Figure 3.4. Comparison of ion release rates in the steady-state (values have been calculated from the rate constants in the steady-state).

Table 3.2. Rate constants of glass dissolution and individual ions' release (t_{st} = 166 hours).

	K_0^I (g/m²·s)	K_0^{II} (g/m²·s)
Na	$6.80 \cdot 10^{-11}$	$1.80 \cdot 10^{-11}$
K	$4.85 \cdot 10^{-11}$	$9.80 \cdot 10^{-12}$
Ca	$8.72 \cdot 10^{-10}$	$9.70 \cdot 10^{-11}$
Mg	$4.85 \cdot 10^{-10}$	$1.02 \cdot 10^{-10}$
Fe	$2.20 \cdot 10^{-12}$	$4.40 \cdot 10^{-13}$
Al	$1.45 \cdot 10^{-10}$	$4.68 \cdot 10^{-11}$
Si	$1.10 \cdot 10^{-9}$	$3.80 \cdot 10^{-10}$
Cl	$7.80 \cdot 10^{-11}$	$2.28 \cdot 10^{-11}$
Glass (all ions)	$3.00 \cdot 10^{-9}$	$6.68 \cdot 10^{-10}$

Radius reduction predicted by the model after 3194 hours was only 0.0036 μm (0.04 % radius loss). The full dissolution of the studied R-glass fibers would take about 1025 years. The radius loss after 25 years, a typical design lifetime, would be 2.45 %. These values are for 60 °C. For lower temperatures, the radius reduction would be even less [50,51,63].

The model is similar in concept to an older solid-state model called the contracting cylinder [153] or shrinking cylinder [57], which relates the evolution of conversion to time. The model presented in this work differentiates between the complex short-term (Phase I) and dissolution-dominated long-term (Phase II) stages. Furthermore, DCZOK model describes both mass loss and radius reduction kinetics due to glass dissolution without the necessity for introducing additional terms such as a conversion factor.
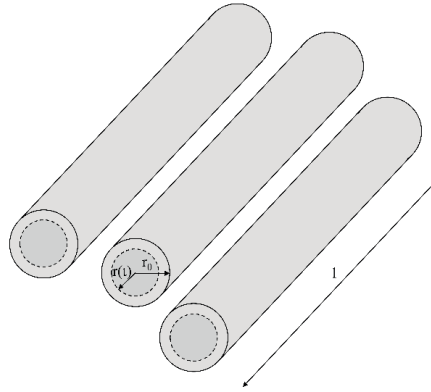
Figure 3.5. Schematic representation of a fiber bundle and geometrical dimensions.

Experimentally $m_{dissolved}$ was measured as a sum of all ions' release quantified with HR-ICP-MS cumulatively over time. A schematic representation of a fiber bundle and important dimensions for the model are shown in Figure 3.5. The number of fibers is n (-); the initial radius of the fibers is r_0 (m); the length of fibers is l (m).

The model involves the following assumptions. As a simplification, this model is deterministic and all fibers are assumed to have the same initial radius, which is r_0; and the cross-sectional surface area at the end of the fibers is assumed to be negligible in calculations of the surface area. The length of the long fibers l is assumed to be constant during the whole dissolution process. During the whole degradation process, the density of the glass material stays constant (ρ_{glass}).

Dissolution is a surface reaction. The rate of the dissolution is dependent on the constant describing the rate of the reaction (K_0), the glass surface area exposed to water (S). In infinite water availability conditions, the surface reaction can be well-described with zero-order kinetics [57,153], which can then be represented by a following differential equation:

$$\frac{\partial m}{\partial t} = K_0 S$$

where m (g) is a total cumulative mass dissolved after time t (s), K_0 (g/m²·s) is a zero-order reaction kinetic constant and S (m²) is the glass surface area in contact with water.

As the reaction proceeds, the radius of the fibers is reduced and the total surface area (S) is decreased, thus leading to a decrease in the rate of mass loss. The overall ion release rate decreases proportionally to the decrease in total surface area or a decrease in fiber radius.

The volume of a single fiber is $\pi r^2 l$, where l is the cylinder length and r is the cylinder radius. For n fibers, the volume is $n\pi r^2 l$ and mass is $\rho_{glass} n\pi r^2 l$. The surface area of a single fiber is $2\pi r l$. For n fibers it is $2n\pi r l$. Substituting mass and surface area expressed in such terms into the following equation:

$$\frac{\partial r^2}{\partial t} = \frac{2K_0}{\rho_{glass}} r$$

The final mass loss kinetic model equation in differential form is obtained:

$$\frac{\partial m}{\partial t} = 2n\pi l \left(r_0 K_0 - \frac{K_0^2}{\rho_{glass}} t \right)$$

The final model equations combining approximated non-steady-state short-term and physical steady-state long-term dissolution kinetics are proposed. The complete radius reduction DCZOK model:

$$\begin{cases} t \leq t_{st}: & r = r_0 - \dfrac{K_0^I}{\rho_{glass}} t \\ t > t_{st}: & r = r_{t_{st}} - \dfrac{K_0^{II}}{\rho_{glass}} (t - t_{st}) \end{cases}$$

The complete mass loss DCZOK model:

$$\begin{cases} t \leq t_{st}: & m_{dissolved} = n\pi l \left(2r_0 K_0^I t - \dfrac{K_0^{I\,2}}{\rho_{glass}} t^2 \right) \\ t > t_{st}: & m_{dissolved} = m_{dissolved_{t_{st}}} + n\pi l \left(2r_{t_{st}} K_0^{II} (t - t_{st}) - \dfrac{K_0^{II\,2}}{\rho_{glass}} (t - t_{st})^2 \right) \end{cases}$$

where K_0^I and K_0^{II} are the rate constants (g/m²·s) for the short-term non-steady-state and long-term steady-state regions, respectively; $r_{t_{st}}$(m) and $m_{dissolved_{t_{st}}}$(g) are the fiber radius and lost mass after time t_{st} (s), when steady-state is reached.

Paper V (Appendix E) describes a model for prediction of glass dissolution of fiber bundles in more detail. Also note, that in this Section 3.5 and in Paper V (Appendix E), rate constants K_0 include the protective effect of the sizing (ξ_{sizing}), and are further treated as apparent dissolution rate constants $K_0^*{}_{sized\ fibers}$, as is described in Papers VI and VII (Appendices F-G).

3.6. PREDICTION OF MASS LOSS OF GLASS FIBERS INSIDE THE COMPOSITE DUE TO HYGROTHERMAL AGING (PAPER VI)

An analytical model for prediction of long-term dissolution of glass fibers termed Dissolving Cylinder Zero-Order Kinetic (DCZOK) model was extended for thin fiber-reinforced composite plates and was presented and explained. The model describes mass loss kinetics during hygrothermal aging of desized and sized R-glass fiber bundles and R-glass fiber-reinforced composite plates with various fiber orientations. Effects of sizing, availability of water and accumulation of degradation products were discussed. The model predicts the mass loss during hygrothermal aging of bare and sized glass fiber bundles and fiber-reinforced composites.

The sizing slowed down glass dissolution of fiber bundles dramatically. The protective effect of sizing ξ_{sizing} (0.165) on glass fiber dissolution was found to be about six times.

Compared to dissolution of sized fiber bundles, the long-term dissolution of glass from composites was slowed down by 36.84% and 65.26% depending on fiber orientation. Slower dissolution from composites compared to unprotected desized glass was explained with the effect of sizing, limited water availability and due to silica degradation product accumulation inside the composite.

A method to decouple water availability and accumulation terms was proposed by using measurements for composite samples with different fiber orientations.

Apparent glass dissolution rate constants were obtained from experimental long-term dissolution kinetics data for Si loss from sizeless and sized glass fiber bundles as well as for composite plates. Obtained rate constants are reported in Table 3.3. The goodness of fit with experimental data is represented by determination coefficients R^2.

Table 3.3. Long-term dissolution of R-glass fiber bundles and reinforced composite plates.

	K_0^* (g Si/m²·s)	R^2
Sizeless Fiber Bundle	$2.30 \cdot 10^{-9}$	0.9576
Sized Fiber Bundle	$3.80 \cdot 10^{-10}$	0.9781
Composite Plate C1	$1.32 \cdot 10^{-10}$	0.9953
Composite Plate C3	$2.40 \cdot 10^{-10}$	0.9923

Brief description of the model

The model presented here is a general case of the DCZOK model presented in Paper V (Appendix E). The rate of the dissolution is dependent on the zero-order reaction kinetic constant (K_0), the glass surface area exposed to water (S), presence of sizing (ξ_{sizing}), the availability of water (C_{H_2O}) and the order of the reaction (n_{order}). In addition, as the aging proceeds, degradation products are accumulated in the composites and slow down the rate of the reaction. Since the long-term reaction is governed by Si dissolution [52], the silica hydrolysis products are what causes the deceleration of glass dissolution inside the composites. In the model, the accumulation term is accounted for as a driving force term, that shows that rate of the mass loss is proportional to the difference between saturation ($C_{SiO_2}^{eq}$) and current concentration (C_{SiO_2}) of degradation products in the composite and the order (m_{order}). The global model (general case) can then be mathematically expressed as the following equation:

$$\frac{\partial m}{\partial t} = K_0 \xi_{sizing} S C_{H_2O}^{n_{order}} \left(C_{SiO_2}^{eq} - C_{SiO_2} \right)^{m_{order}} = K_0^* S$$

where m is a total cumulative mass dissolved after time t; K_0^* is an apparent reaction kinetic constant that can be obtained from regression of experimental data. While K_0 is a material property, K_0^* incorporates effects of sizing, water availability and degradation product accumulation.

For sized fibers, effect of sizing (ξ_{sizing}) should be accounted for. The model simplifies to:

$$\frac{\partial m}{\partial t} = K_0 \xi_{sizing} S = K_{0\,sized\,fibers}^* S$$

For bare (desized) fibers the model simplifies to:

$$\frac{\partial m}{\partial t} = K_0 S = K_{0\,sizeless\,fibers}^* S$$

Paper VI (Appendix F) describes a model for prediction of glass dissolution prediction of sized, desized fiber bundles and composites in more detail.

3.7. PREDICTION OF GLASS FIBER DISSOLUTION AT VARIOUS ENVIRONMENTAL CONDITIONS (PAPER VII)

The long-term dissolution of R-glass fibers in water was studied experimentally at various environmental conditions, such as varying pH levels, temperature and under the effect of stress corrosion. Experimentally mass loss was obtained using HR-ICP-MS for separate released ions.

The analytical model termed Dissolving Cylinder Zero-Order Kinetic (DCZOK) model was successfully used to explain the long-term glass dissolution experiments of R-glass fibers at various environmental conditions. The kinetic constants were obtained for various pH and temperature conditions as well as for different stress levels. The protective effect of sizing was accounted for in this model [24]. The obtained rate constants are systematized in Tables 3.4, 3.5 and 3.6 for the effect of pH, temperature and stress, respectively. Obtained values are comparable with dissolution rates of other glass fibers studied in the literature [24,52,152].

Temperature showed an Arrhenius-type influence on the kinetics, increasing rate of dissolution exponentially with increasing temperature:

$$K_0 = Ae^{-\frac{E_A(pH,\sigma)}{RT}}$$

where A is the pre-exponential factor (g/(m²·s)); R is the gas constant being 8.314 J/(mol·K); T is the absolute temperature (K); E_A is the activation energy (J/mol). Both pH and stress corrosion are thought to affect the activation energy term in the Arrhenius equation [154,155].

Activation energy of the steady-state glass dissolution was obtained and reported at pH 5.65 and no stress (53.46 and 34.84 kJ/mol for Si and total glass dissolution, respectively). Obtained values are consistent with values reported in literature, being slightly lower than for E-glass (58–79 kJ/mol in alkaline solutions [57]). Activation energy for Si dissolution of various silica-based materials may be around 60 kJ/mol [156]. The steady-state (Phase II) was achieved after about a week.

Table 3.4. The glass dissolution rate constants obtained via regression of the experimental data of R-glass fiber bundles using DCZOK model for Si and total mass loss at 60 °C and various pH.

pH	$K_{0_{Si}}^{I}$ (g/(m²·s))	$K_{0_{Si}}^{II}$ (g/(m²·s))	$K_{0_{total}}^{I}$ (g/(m²·s))	$K_{0_{total}}^{II}$ (g/(m²·s))
1.679 ± 0.010	(3.10±0.44)·10⁻⁷	(1.25±0.09)·10⁻⁷	(1.70±0.19)·10⁻⁶	(1.16±0.08)·10⁻⁶
4.005 ± 0.010	(2.59±0.33)·10⁻⁸	(1.70±0.11)·10⁻⁸	(8.48±1.21)·10⁻⁸	(6.24±0.36)·10⁻⁸
5.650 ± 0.010	(6.67±1.03)·10⁻⁹	(2.30±0.16)·10⁻⁹	(1.82±0.29)·10⁻⁸	(4.05±0.29)·10⁻⁹
7.000 ± 0.010	(3.64±0.53)·10⁻⁸	(2.55±0.19)·10⁻⁸	(5.46±0.82)·10⁻⁸	(4.85±0.38)·10⁻⁸
10.012 ± 0.010	(8.97±1.27)·10⁻⁸	(4.56±0.32)·10⁻⁸	(1.39±0.16)·10⁻⁷	(1.11±0.07)·10⁻⁷

The activation energy of glass dissolution was affected by pH. The influence of pH is complicated and may be described by a parabolic polynomial function – the activation energy peaks at pH 5.65 and decreases towards more basic, as well as more acidic conditions. In comparison with neutral conditions, basic and acidic aqueous environments showed an increase in dissolution rates, affecting the lifetime of glass fibers negatively. GFRPs should not be used in strongly acidic conditions. This is in agreement with an observation in another study, stating that many GFRPs fail catastrophically after a critical time when exposed to acids [47]. The steady-state (Phase II) was achieved after about a week.

Table 3.5. The glass dissolution rate constants obtained via regression of the experimental data using DCZOK model for Si and total mass loss at pH 5.65 and various temperatures.

T (°C)	$K^I_{0_{Si}}$ (g/(m²·s))	$K^{II}_{0_{Si}}$ (g/(m²·s))	$K^I_{0_{total}}$(g/(m²·s))	$K^{II}_{0_{total}}$(g/(m²·s))
25 ± 1	$(1.46\pm0.23)\cdot10^{-9}$	$(2.60\pm0.18)\cdot10^{-10}$	$(1.04\pm0.12)\cdot10^{-8}$	$(1.42\pm0.11)\cdot10^{-9}$
40 ± 1	$(2.62\pm0.37)\cdot10^{-9}$	$(1.08\pm0.08)\cdot10^{-9}$	$(1.37\pm0.19)\cdot10^{-8}$	$(2.72\pm0.19)\cdot10^{-9}$
60 ± 1	$(6.67\pm1.03)\cdot10^{-9}$	$(2.30\pm0.16)\cdot10^{-9}$	$(1.82\pm0.29)\cdot10^{-8}$	$(4.05\pm0.29)\cdot10^{-9}$
80 ± 1	$(2.19\pm0.31)\cdot10^{-8}$	$(8.91\pm0.73)\cdot10^{-9}$	$(4.24\pm0.59)\cdot10^{-8}$	$(1.47\pm0.11)\cdot10^{-8}$

The activation energy of glass dissolution is affected by stress corrosion. The activation energy decreases linearly as the stress increases. The steady-state (Phase II) was achieved after about 5 days (120 h), sooner than in all unstressed cases, indicating that stress may slightly accelerate the transition towards the steady-state dissolution.

Table 3.6. The glass dissolution rate constants obtained via regression of the experimental data using DCZOK model for Si and total mass loss at 60 °C and pH 5.65 at various stress levels.

σ (MPa)	$K^I_{0_{Si}}$ (g/(m²·s))	$K^{II}_{0_{Si}}$ (g/(m²·s))	$K^I_{0_{total}}$ (g/(m²·s))	$K^{II}_{0_{total}}$ (g/(m²·s))
0.0	$(6.67\pm1.03)\cdot10^{-9}$	$(2.30\pm0.16)\cdot10^{-9}$	$(1.82\pm0.29)\cdot10^{-8}$	$(4.05\pm0.29)\cdot10^{-9}$
0.2	$(7.27\pm1.15)\cdot10^{-9}$	$(2.38\pm0.21)\cdot10^{-9}$	$(2.08\pm0.42)\cdot10^{-8}$	$(4.12\pm0.33)\cdot10^{-9}$
26.4	$(7.45\pm1.03)\cdot10^{-9}$	$(2.58\pm0.19)\cdot10^{-9}$	$(2.04\pm0.33)\cdot10^{-8}$	$(4.35\pm0.35)\cdot10^{-9}$
42.2	$(8.30\pm1.33)\cdot10^{-9}$	$(3.47\pm0.25)\cdot10^{-9}$	$(2.01\pm0.41)\cdot10^{-8}$	$(5.56\pm0.44)\cdot10^{-9}$
52.7	$(9.21\pm1.33)\cdot10^{-9}$	$(4.73\pm0.33)\cdot10^{-9}$	$(1.65\pm0.44)\cdot10^{-8}$	$(8.12\pm0.67)\cdot10^{-9}$

The increase in stress reduces the activation energy of dissolution linearly and accelerates the glass dissolution rates exponentially.

Brief description of the model

For the sized fiber bundles, the mass loss kinetic DCZOK model equation in differential form is the following [52]:

$$\frac{\partial m}{\partial t} = 2n\pi l \left(r_0 K_0 \xi_{sizing} - \frac{K_0^2 \xi_{sizing}^2}{\rho_{glass}} t \right)$$

where n is the number of fibers (-); l is the length of fibers (m); r_0 is the initial fiber radius (m), and ρ_{glass} is the density of glass (g/m³).

pH, temperature and stress corrosion affect the material-environment energy-activated interactions, thus affecting the dissolution rate constants K_0:

$$K_0 = f(pH, T, \sigma)$$

where pH is the acidity of the environment (-), T is its temperature (K), and σ is stress (MPa).

The DCZOK model was expanded to account for the environmental conditions (pH, T, σ):

$$\frac{\partial m}{\partial t} = 2n\pi l \left(r_0 K_0 \xi_{sizing} - \frac{\left(K_0 \xi_{sizing}\right)^2}{\rho_{glass}} t \right) = 2n\pi l \left(r_0 A e^{-\frac{E_A(pH,\sigma)}{RT}} \xi_{sizing} - \frac{\left(A e^{-\frac{E_A(pH,\sigma)}{RT}} \xi_{sizing}\right)^2}{\rho_{glass}} t \right)$$

where m is a total cumulative mass dissolved after time t; K_0 is a material/environment interaction property; ξ_{sizing} is the protective effect of sizing; pH is the acidity of the environment (-), T is its temperature (K); σ is stress (MPa); n is the number of fibers (-); l the length of fibers (m); r_0 is the initial fiber radius (m); ρ_{glass} is the density of glass (g/m³); A is the pre-exponential factor (g/(m²·s)); R is the gas constant being 8.314 J/(mol·K); T is the absolute temperature (K); E_A is the activation energy (J/mol).

In this equation, K_0 and ξ_{sizing} are the time-independent parameters, whereas S changes with time. As the dissolution proceeds, the radius of the fibers is reduced and the total surface area S is decreased, thus leading to a decrease in the dissolution rate. For each ion, individual K_0^I and K_0^{II} values have to be obtained, while t_{st} and r_0 for each individual ion release are the same and are equivalent to that for the total mass loss [52]. K_0^I and K_0^{II} are the dissolution rate constants (g/(m²·s)) for the short-term non-steady-state (Phase I) and long-term steady-state regions (Phase II), respectively.

The model involves the following assumptions. As a simplification, this model is deterministic and all fibers are assumed to have the same initial radius r_0; the cross-sectional surface area at the end of the fibers is assumed to be negligible in calculations of the surface area; the length of the long fibers l is assumed to be constant during the whole dissolution process. During the whole degradation process, the density of the glass material is assumed constant ρ_{glass}. The effect of sizing ξ_{sizing} is assumed to be independent of environmental conditions and time [24,52]. For free fiber bundles (not embedded in the composite) the conditions of infinite availability of water are ensured by using large volumes of water, thus making the rate of reaction independent of the water concentration [24,52].

The model can also predict fiber radius reduction kinetics during the dissolution using the same four parameters, that can be determined experimentally [52]. The DCZOK model can be used to describe dissolution for each element separately as well as for the total mass loss.

Paper VII (Appendix G) describes a model for prediction of glass dissolution prediction of sized fiber bundles at various environmental conditions in more detail.

3.8. Long-Term Aging of the Sizing-Rich Composite Interphase (Paper VIII)

Composite plates of two configurations C1 and C3, as was shown in Figure 2.7, were conditioned for a period of about a year in a heated bath with distilled water (60 ± 1 °C). The C1 was representative of a typical composite, whereas C3 was unusual with a short fiber-matrix interface length and the interphases being connected to the large sample´s surface.

In water, the sizing-rich composite interphase was exposed to hydrolytic degradation. Glass fiber composites absorb water with time and the mass of the composites increase subsequently. When measuring diffusivity and saturation level of water according to ASTM D5229 testing is stopped when the mass increase with time stops [157], i.e. it is reaching a plateau, in this case at about 200 hours. If the water uptake experiments are stopped as suggested by ASTM, then the long-term behavior is not captured, as shown in Figure 3.6. However, continuing the tests exposing the laminates to water for longer, the mass of a typical composite C1 increases again, measured up to 9 months. This observation is also consistent with the results of another study on long-term water uptake by composite plates [158]. This additional water uptake was found to be due to the hydrolytic degradation of the sizing-rich fiber matrix interphase.
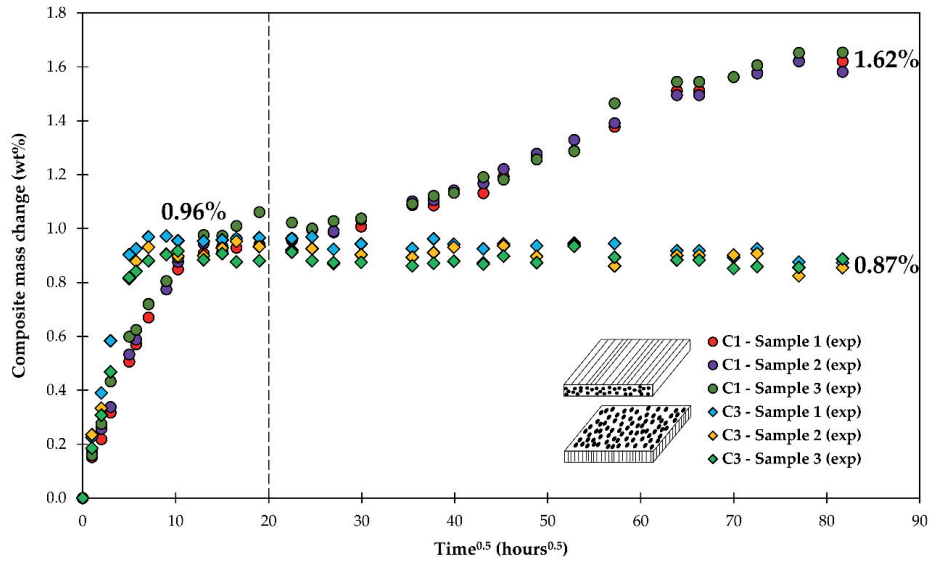
Figure 3.6. Long-term water uptake by composite laminates. Dashed line corresponds to a time when a test following standard practice ASTM D5229 would be stopped [157].

Due to water-induced dissolution interphase flaws were formed, as shown schematically in Figure 3.7, which developed further into matrix cracks, observed in micrographs in Figure 3.8. The internal volume created by the flaws and cracks can be filled with water leading to the observed mass increase. The microscopically measured size of the flaws matches the order of magnitude of the volume required for obtaining the measured additional mass increase.
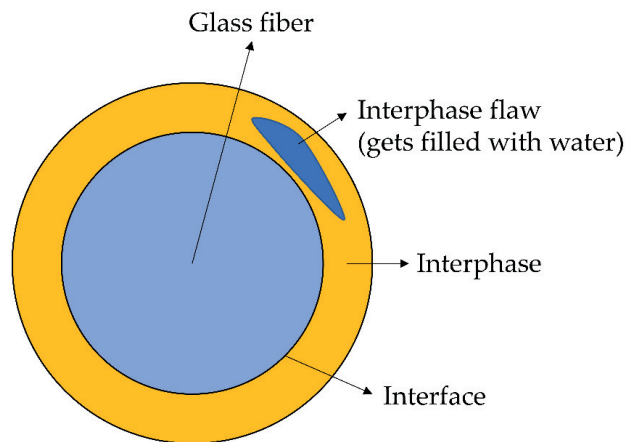
Figure 3.7. Interphase flaw is formed and gets filled with water.
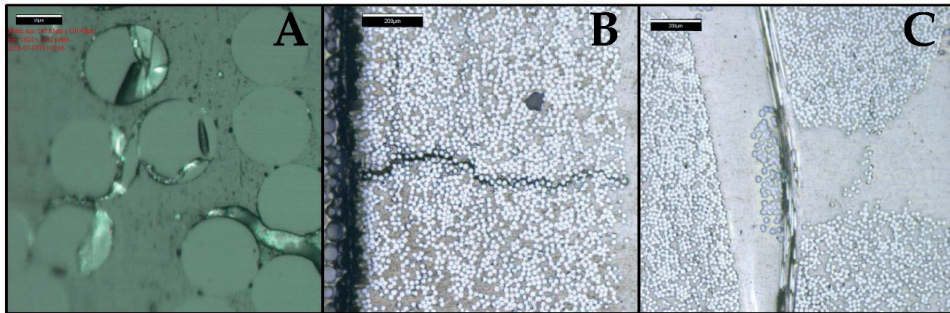
Figure 3.8. Micrograph of a composite sample exposed to water for 6673 hours at 60 °C. The micrograph indicates the (A) Fiber matrix debondings; (B) Matrix transverse cracks, (C) Splitting along the fibers.

Three damage mechanisms were observed in the micrographs:

1. Fiber matrix debondings, shown in Figure 3.8(A).
2. Matrix transverse cracks, shown in Figure 3.8(B). These cracks seem to be inside the bundle. This location may be also a result of the weakening of the fiber matrix interphase, which was covered in point 1.
3. Splitting along the fibers, shown in Figure 3.8(C).

Fiber matrix debonding appears to be the first failure mechanism, caused by hydrolysis of the interphase. When these debondings accumulate creating a weakened local region they can easily combine into a longer "matrix crack" due to a release of curing, thermal and swelling stresses, resulting in a crack formation. The reason for the observed splitting along fibers is less clear. It could be related to the matrix cracks, but it could also be caused by the fibers used for stitching the reinforcing mat. All these flaws (cracks) create volume that can be filled with water and increases the mass of the composite.

When C3 specimens were conditioned in water their mass increased during the first 200 hours similar to C1. Continuing the test for longer times lead, however, to a mass loss, seen in Figure 3.6. For these specimens the flaws created by the fiber matrix interphase hydrolysis were open towards the surface of the test specimen, since the interphase length (and fiber length) was so short, 1.5 mm. The reaction products of the hydrolysis could migrate into the surrounding water bath leading to a mass drop. This mass loss allowed determining the product of the dissolution rate constant and the surface area of the interphase.

The small specimens tested here would degrade the entire interphase within 22 to 30 years at 60 °C. The calculation is based on a full mechanistic mass balance approach considering all the composite´s constituents: water uptake and leaching of the matrix, dissolution of the glass fibers and dissolution of the composite interphase. These processes were modeled using a combination of Fickian diffusion and zero-order kinetics. The mass loss due to long-term gravimetric behavior of composite C3 was successfully modeled, because the C3 samples did not have a significant accumulation of the degradation products.

Based on long-term test data from the literature tested for close to 10 years it seems that typical composites, such as C1, will initially absorb extra water in the flaws and cracks created by interphase hydrolysis. Eventually these cracks will create a network that is connected to the surface of the composite laminate. When this network is formed reaction products can leave the laminate and the mass will be reduced similarly to C3.

Damage caused by the hydrolytic aging of the sizing-rich composite interphase very likely leads to a decrease in interfacial strength. For instance, Gagani et al [159] and Rocha et al [32] have reported the composite interphase-related deterioration of the mechanical properties due to aging in water. It is

likely that the formation of the interphase flaws described in this work is the mechanistic origin of the interfacial strength deterioration of composites.

Paper VIII (Appendix H) covers hydrolysis of the composite interphase, but the same approach should be applicable for all other environmental agents and solvents (in general, solvolysis).

Brief description of the model

The combination of the phenomenological perspective and mass balance approach provide a useful tool for analyzing mass uptake/loss processes in composites during hygrothermal aging by breaking down a complex process into constituent-related processes. The processes that affect weight gain or loss of composites are summarized in Table 3.7. The proposed model equation should be a phenomenological full representation of the interaction between the composite material and the water environment.

Table 3.7. Summary of the processes during hygrothermal aging of composites that affect the mass balance.

Process	Sign	Reference
Water uptake of the polymer matrix	+	[23]
Water uptake by the composite interphase	+	[53]
Water uptake by the voids	+	[11,23,160]
Thermo-oxidation of the polymer matrix	+	[3]
Leaching from polymer matrix	-	[3]
Glass fiber dissolution	-	[24,43,52]
Sizing-rich interphase dissolution	-	[22]

Gravimetric measurements determine the sample′s mass over time during conditioning in water. The mass consists of the following terms:

$$m_{gravimetric}(t) = m_{dry} + m_{water\ uptake}(t) + m_{oxidation}(t) - m_{leaching}(t) - m_{glass\ dissolution}(t) - m_{interphase\ dissolution}(t)$$

The dissolution of the interphase is then simply given by:

$$m_{interphase\ dissolution}(t) = m_{dry} + m_{water\ uptake}(t) + m_{oxidation}(t) - m_{leaching}(t) - m_{glass\ dissolution}(t) - m_{gravimetric}(t)$$

The water uptake and leaching can be calculated using the Fickian diffusion [23,157]:

$$M_\infty = \frac{M_\infty^m(\nu_m + \nu_i)\rho_m + M_\infty^v \nu_v \rho_{water}}{\nu_f \rho_f + (\nu_m + \nu_i)\rho_m}$$

$$M(t) = M_\infty \left[1 - e^{-7.3\left(\frac{Dt}{h^2}\right)^{0.75}}\right]$$

where ρ_m is the matrix density, ρ_f is the fiber density, ρ_{water} is the water density, ν_f is the fiber volume fraction, ν_m is the matrix volume fraction, ν_i is the interphase volume fraction, ν_v is the void volume fraction ($\nu_f + \nu_m + \nu_i + \nu_v = 1$), M_∞^m is the matrix saturation water content (3.44 wt%) and M_∞^v is the

void saturation water content (100 wt%). $M(t)$ is the water content, M_∞ is the water saturation content, t is time, h is the thickness and D is the diffusivity in the thickness direction of the plate.

Figure 3.9. Experimental composite C3 plate mass change during the conditioning in water, shown over a square root of time. Water uptake and mass balance are modeled.

The dissolution kinetics of glass and the interphase can be calculated using zero-order kinetics. The full Dissolving Cylinder Zero-Order Kinetics (DCZOK) model is the following [52]:

$$
\begin{cases}
t \leq t_{st}: & m_{dissolved} = n\pi l \left(2r_0 K_0^{*\,I} t - \dfrac{K_0^{*\,I\,2}}{\rho_f} t^2 \right) \\[2ex]
t > t_{st}: & m_{dissolved} = m_{dissolved_{t_{st}}} + n\pi l \left(2r_{t_{st}} K_0^{*\,II}(t - t_{st}) - \dfrac{K_0^{*\,II\,2}}{\rho_f} (t - t_{st})^2 \right)
\end{cases}
$$

where n is the number of fibers; l is the length of fibers; r_0 is the initial fiber radius; ρ_{glass} is the density of glass ; $K_0^{*\,I}$ and $K_0^{*\,II}$ are the apparent dissolution rate constants for the short-term non-steady-state (Phase I) and long-term steady-state (Phase II) regions, respectively; $r_{t_{st}}$ and $m_{dissolved_{t_{st}}}$ are the fiber radius and lost mass after time t_{st} (s), when steady-state is reached.

Paper VIII (Appendix H) describes a model for prediction of the hydrolytic degradation kinetics of the composite interphase in more detail.

45

CHAPTER 4

CONCLUSIONS

The microconstituents of the composites were studied in order to evaluate the water-induced degradation. Environmental aging mechanisms of composite microconstituent materials (epoxy, glass fibers and sizing) were successfully identified. Models and methods were developed for studying and predicting the changes in constituent and composite materials' properties due to the environmental aging. The severity of hygrothermal aging on the mechanical properties was also obtained and explained for epoxy, whereas deterioration of interfacial strength for the same material system was covered together with Dr. Abedin I. Gagani from the same group at NTNU elsewhere [159].

A spectroscopic method of the true water content determination in the matrix and in composites was developed. The true water content at saturation was 3.44 wt%, whereas at initial conditions it was already 0.63 wt% for the studied epoxy. These initial conditions are what would usually be denoted as a 'dry' material. Thus, the initial water content is significant and should not be neglected.

Mechanical properties and chemical structure of the epoxy and the effect of water environment was studied. For the studied amine-based epoxy, mechanical properties were affected (negatively) only via plasticization/swelling mechanism in the presence of water. This negative effect was fully reversible upon redrying the material to its initial water content. Changes in chemical structure involved thermo-oxidation, which took a few distinct pathways: minor thermo-oxidative crosslinking and carbonyl formation in the carbon-carbon backbone of the polymer. The carbonyl formation caused the material to yellow irreversibly. In addition, small molecular size compounds, that were initially present in the polymer, were diffusing out into the water due to leaching. Thermo-oxidation and leaching did not show any significant effect on the deterioration of mechanical performance of the epoxy.

Since swelling was found to be the only mechanism that affects the mechanical properties of the studied epoxy polymer significantly, an analytical model for the prediction of hygroscopic swelling in fiber-reinforced composites from the isotropic swelling data of the matrix polymer was developed.

For the studied R-glass, long-term dissolution experiments were performed, and the dissolution behavior was obtained. Environmental aging occurred in two distinct phases: short-term non-steady-state (Phase I) and long-term steady-state (Phase II). The first one involved many subprocesses occurring in parallel, but relatively quickly transitioned into the second phase, in about a week's time. This means that Phase II is of most interest for the long-term degradation. In Phase II, the degradation was dominated by glass dissolution and was successfully modeled using the Dissolving Cylinder Zero-Order Kinetics (DCZOK) model at various environmental conditions (pH, temperature and stress corrosion). In addition, glass fiber dissolution from thin composites was successfully modeled using the DCZOK model.

The sizing-rich composite interphase degrades due to hydrolysis, resulting in the formation of the interphase flaws. These flaws may further develop into fiber/matrix debondings, matrix cracks and splitting along the fibers, as was observed in micrographs. The internal volume created by the flaws and cracks can be filled with water leading to the observed mass increase. Based on the combination of experimental evidence of about a year and long-term test data from the literature [158] tested for close to 10 years it seems that typical composites will initially absorb extra water in the flaws and cracks created by interphase hydrolysis. Eventually these cracks will create a network that is connected to the surface of the composite laminate. When this network is formed reaction products can leave the laminate and the mass will be reduced continuously.

Another important aspect that has to be noted is that when measuring diffusivity and saturation level of water according to ASTM D5229 testing is stopped when the mass increase with time stops [157], i.e. it is reaching a plateau. However, the water uptake keeps increasing after that due to the

hydrolytic degradation of the sizing-rich fiber matrix interphase. If the water uptake experiments are stopped as suggested by ASTM, then the long-term behavior is not captured.

A phenomenological mass balance model was developed and successfully used in order to obtain the dissolution kinetics of the sizing-rich composite interphase.

The thesis provides a better understanding of environmental aging mechanisms of the constituents in fiber-reinforced composites and its effect on mechanical properties of such materials. Based on environmental aging experiments, novel analytical models were proposed and developed in order to predict changes in properties of the composite microconstituents due to exposure to such environments. These practical tools, i.e. models and methods, were provided for quantitative prediction of water-induced changes in the microconstituent materials and composites. The tools are to be of assistance in partially substituting the rigorous physical testing procedures in the state-of-the-art situation. Prediction of long-term properties of composites should significantly reduce costs associated with extensive testing and should already allow a partial transition towards the multiscale modeling approach.

CHAPTER 5

FUTURE WORK

This thesis addresses the problem of environmental aging of composites and their constituents. Nevertheless, there are related aspects and research topics that were only touched upon or not fully investigated. For industry a couple of aspects would be of high interest:

- The application and validation of the proposed methodology to study environmental aging of composites with different matrix, fiber and sizing materials.
- The application and validation of the proposed methodology to study aging via exposure to oil or composite pipe and riser rinsing with methanol.

The questions for further work include:

- Water-induced and temperature effects on the viscoelastic behavior, i.e. creep, of matrix polymers and their prediction in composites.

- The developed true water determination method described in Paper I (Appendix A) is potentially useful also for other polymers and composite systems with different fiber or resin fractions, as well as for diffusant media other than water. However, there is one significant drawback of the method at the moment that it has its limitations for thick and non-transparent composite samples. Thus, a combination of methods or the improvement of the current method is recommended. Other spectroscopic methods such as Raman, while not as sensitive to water, and reflectance FTIR, while mostly providing information about the surface of the material, might also be considered in developing water monitoring methods, especially in cases when composites are non-transparent to the IR light.

- Other common epoxies and matrix polymers should be studied using a similar approach to Paper II (Appendix B) also shown in Figure 5.1. This should be done in order to see whether there are other aging mechanisms in other matrix polymers, i.e. hydrolysis, as expected for example, for the anhydride-based epoxy. The proposed approach which was followed in Paper II is shown schematically in Figure 5.1.

- Other common matrix polymers should be studied analogously as in Paper III (Appendix C). Similar research would be of high interest to thermoplastic-based composites, e.g. using highly crosslinked polypropylene (HXPP) or polyamides (PA6, PA11, PA12). The methodology described here should be applicable to other matrix materials. It is expected that mechanical properties of HXPP should be reversible, whereas polyamides are expected to age irreversibly due to chemical degradation. Hydrolytic degradation kinetics of polyamides and the effect of such aging on mechanical properties of these common thermoplastic matrix materials was studied in detail by Mazan et al [161,162]. They have reported that the hydrolysis induced chain scission and chemicrystalization were the two main mechanisms of property change [162]. Furthermore, they were able to model mechanical deterioration behavior of PA11. For the studied epoxy it was shown experimentally that the tension fatigue S-N curve of a wet epoxy resin can be estimated by shifting the S-N curve of a dry material proportionally to a reduction in static tensile strength due to hygrothermal effects. This observation and its

universality should be investigated also for other polymers that do not degrade chemically, e.g. not affected by hydrolysis or chain scission.

- The imperfections of the fiber–matrix interface are neglected in the analytical model for hygroscopic swelling prediction for composites, described in a Paper IV (Appendix D). A good agreement between experimental, numerical and analytical results indicated that this effect is negligible for the material system studied. For a more advanced model, there should be additional studies concerning this aspect.
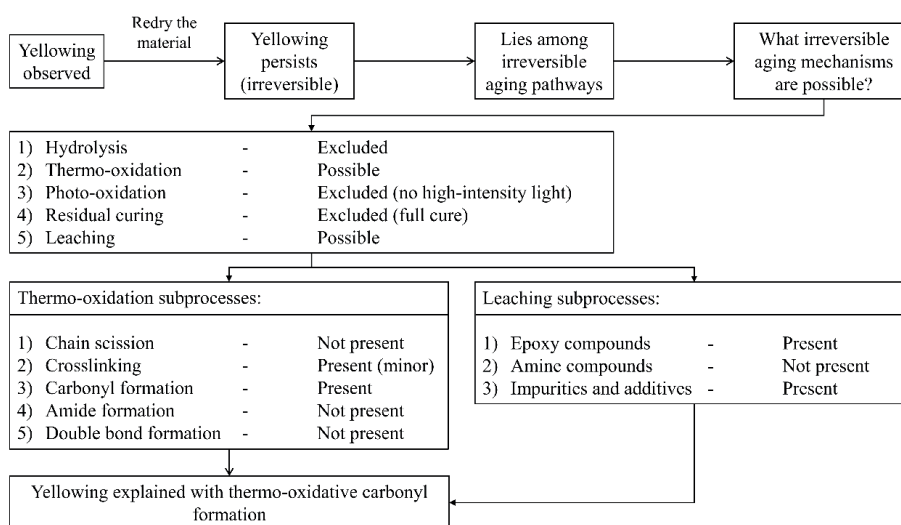
Figure 5.1. Schematic representation of the logic during investigation of the changes in the chemical structure of the polymer due to aging.

- Aging of R-glass fibers was studied in this work. However, there should be no limitations to apply the Dissolving Cylinder Zero-Order Kinetics (DCZOK) model to other types of glass fibers. Validation of the model with various types of glass fibers such as E, ECR, S is advised. The model should be applicable to other types of glass since SiO_2 is the major component in virtually all types of glass [57], but it would be beneficial to validate this model experimentally with other types of glass fibers.

- The influence of pH, temperature and stress corrosion on the rate constants and dissolution activation energies was obtained in Paper VII (Appendix G), however influence of each parameter was studied one at a time. Thus, a suggestion for future work includes a cross-parametric study for pH, temperature and stress corrosion in order to deduce a general analytical solution for the environmental influence on the activation energy of dissolution, and to study whether there is any coupled effect. The DCZOK model should also be extendable to include the effect of ionic strength.

- Validating the DCZOK model for seawater conditions (about 1.84 – 12.62 mg SiO_2/kg water; pH of seawater 7.8) would be highly beneficial, especially for the marine and offshore industries, since the real-life structures most often operate in the seawater environment. When GFs are used in seawater, the dissolution of glass occurs slower due to the presence of silica in the seawater, which is in seawater from the contact with sand and minerals [163-166]. The

approach in distilled water is conservative with regards to seawater, meaning that structures implementing glass fibers designed for distilled water conditions should not encounter penalties to their service time in the seawater.

- Silica degradation products are large and are likely unable to escape thick composite structures. It is recommended to perform diffusion studies and determine diffusivity of the degradation products inside the composites. In order to study the transport of SiO_2 through the matrix, a permeability experiment using the polymer membrane should be performed, where on one side of the membrane would be SiO_2-saturated water, while on the other side, there would be distilled SiO_2-free water. This would allow to determine the permeability and diffusivity of the silica degradation products in the polymer material used as a matrix in the composite. Furthermore, tests with fiber bundles not embedded in the composite immersed in the SiO_2-saturated water should be performed to see whether the fiber dissolution stops completely. Furthermore, the thickness of the composite may have an influence on the accumulation of the degradation products inside the composites. It should be harder for degradation products to leave the thicker composite. This would mean that the effect of degradation product accumulation should be better protecting the thicker GFRP structures from glass dissolution. Additional research is needed to test this hypothesis.

- It would be interesting to combine the fiber dissolution study with a fiber strength study to obtain some indication of how fiber mass loss affects fiber (and composite) performance. By modeling the dissolution kinetics of glass, it should be possible to predict the long-term deterioration of mechanical properties of the glass fibers due to hydrolytic crack growth. Micromechanical models to predict the crack growth of the glass fibers have been previously proposed by Wierderhorn and Bolz [167] for stress-corrosion and Sekine and Beaumont [168] for glass corrosion in acids. However, to the best knowledge, the link from the dissolution chemistry-based kinetic models to the crack growth models has not been done yet, even though it has been proposed by Charles back in 1958 [169]. The DCZOK model is seen as a potential chemical kinetics component for modeling such hydrolytic crack growth in glass fibers. This aspect should be further investigated.

ABBREVIATIONS & SYMBOLS

Abbreviations:

ATR-FT-IR	Attenuated Total Reflectance Fourier Transform Infrared Spectroscopy
BET	Brunauer-Emmett-Teller theory
C1	Composite plate with fibers oriented parallel to the plate face
C3	Composite plate with fibers oriented normal to the plate face
DCZOK	Dissolving Cylinder Zero-Order Kinetic model
DGEBA	Bisphenol A diglycidyl ether
DMTA	Dynamic Mechanical Testing Analysis
E - glass	"Electrical" glass
ECR - glass	"Electrical/Chemical Resistance" glass
EDX	Energy-Dispersive X-ray spectroscopy
FE	Finite Element
FEA	Finite Element Analysis
FRP	Fiber-Reinforced Polymer, same as fiber-reinforced composite
FT-NIR	Fourier Transform Near Infrared spectroscopy
GF	Glass Fiber
GFRP	Glass Fiber-Reinforced Polymer, same as Glass Fiber-Reinforced Composite
HDDGE	1,6-Hexanediol diglycidyl ether
HR-ICP-MS	High Resolution Inductively Coupled Plasma Mass Spectrometry
IPDA	Isophorondiamine
LOI	Loss On Ignition
PEO	Poly(ethylene oxide)
PDMS	Polydimethylsiloxane
POPA	Poly(oxypropylene)diamine
PPO	Poly(propylene oxide)
R - glass	"Reinforcement" glass
RVE	Representative Volume Element
S - glass	"Strength" glass
SEM	Scanning Electron Microscopy
VARTM	Vacuum-Assisted Resin Transfer Molding

Symbols:

β_m	Hygroscopic swelling coefficient for matrix polymer (-)
β_x	Hygroscopic swelling coefficient for composite in along-the-fiber direction (-)
β_y, β_z	Hygroscopic swelling coefficient for composite in transverse directions (-)
ε	Linear strain (%)
ε_h	Linear hygroscopic strain (%)
ε_m	Linear strain of the polymer matrix (%)
ε_f	Linear strain of the fibers (%)
ε_{max}	Linear strain to failure (%)
ε_x	Linear strain for composite in along-the-fiber direction (%)
$\varepsilon_y, \varepsilon_z$	Linear strain for composite in transverse-to-fiber directions (%)
δ_i	Thickness of the composite interphase (m)
ν_f	Poisson's ratio of glass fibers (-) in: *Paper IV*
ν_f	Volume fraction of the fibers (m^3/m^3)
ν_m	Poisson's ratio of the matrix polymer (-) in: *Papers III & IV*
ν_m	Volume fraction of the matrix polymer (m^3/m^3)
ν_i	Volume fraction of the composite interphase (m^3/m^3)
ν_v	Volume fraction of the voids (m^3/m^3)
$\rho_{composite}$	Density of the composite (g/m^3)
ρ_f	Density of the glass fibers (g/m^3)
ρ_{glass}	Density of the glass (g/m^3), same as ρ_f
ρ_i	Density of the sizing-rich composite interphase (g/m^3)
ρ_m	Density of the matrix polymer (g/m^3)
ρ_{water}	Density of the water (g/m^3)
ξ_{sizing}	Protective effect of sizing against glass dissolution (-)
σ	Stress (MPa)
σ_f	Stress in glass fibers (MPa)
σ_m	Stress in the matrix polymer (MPa)
A	Pre-exponential factor (g/(m^2·s))
A	Cubic cell lateral surface area (-) in: *Paper IV*
A_f	Fiber part of the cubic cell lateral surface area (-)
A_m	Matrix part of the cubic cell lateral surface area (-)
c	Non-cumulative ion mass concentration measured with HR-ICP-MS (g/L)
CHE	Coefficient of Hygroscopic Expansion (-), same as β
D	Through-thickness water diffusivity of the material (mm^2/h)
$D_{leaching}$	Through-thickness leachable compound diffusivity of the material (mm^2/h)
E	Young's modulus (MPa)
E_A	Dissolution activation energy (J/mol)
E_f	Stiffness of glass fibers (MPa)

E_m	Stiffness of the matrix polymer (MPa)
h	Thickness of a material plate (m)
K_0	Glass dissolution rate constant (g/(m²·s))
K_0^I	Glass dissolution rate constant (non-steady-state; Phase I) (g/(m²·s))
K_0^{II}	Glass dissolution rate constant (steady-state; Phase II) (g/(m²·s))
$K_{0_{Si}}^I$	Dissolution rate constant for Si only (non-steady-state) (g/(m²·s))
$K_{0_{Si}}^{II}$	Dissolution rate constant for Si only (steady-state) (g/(m²·s))
$K_{0_{total}}^I$	Dissolution rate constant for glass (non-steady state) (g/(m²·s))
$K_{0_{total}}^{II}$	Dissolution rate constant for glass (steady-state) (g/(m²·s))
K_0^*	Apparent glass dissolution rate constant (g/(m²·s))
K_0^{*I}	Apparent glass dissolution rate constant (non-steady-state; Phase I) (g/(m²·s))
K_0^{*II}	Apparent glass dissolution rate constant (steady-state; Phase II) (g/(m²·s))
K_i^0	Zero-order rate constant of the composite interphase dissolution (g/(m²·s))
l	Length of fibers and the interphase (m)
L_x, L_y, L_z	Dimensions of the RVE (-)
m	Mass of a polymer including moisture (g) in: *Paper I*
$m; m_{dissolved}$	Glass mass loss due to dissolution (g)
$m_{dissolved_{t_{st}}}$	Dissolved glass mass when the steady-state is reached (g)
$m_{absolutely\ dry}$	Mass of an absolutely dry specimen (0 wt% water content) (g)
m_f	Mass fraction of fibers in a composite laminate (g/g)
m_i	Mass of the composite interphase (g)
m_{i_0}	Initial mass of the composite interphase (g)
m_{order}	Order of the degradation product accumulation (-)
m_{Si}	Si mass loss due to dissolution (g)
m_{water}	Mass of moisture uptaken by the specimen (g)
M	Water content of the composite (wt%)
M_∞	Saturation water content of the composite (wt%)
M^m	Water content of the matrix polymer (wt%)
M_∞^m	Saturation water content of the matrix polymer (wt%)
M_∞^v	Saturation water content of the voids (wt%)
$M_{leaching}$	Content of leached compounds from the polymer (wt%)
$M_{leaching}^0$	Initial leachable compound content in the polymer (wt%)
n	Number of fibers (-)
n_{order}	Order of the water availability term (-)
N	Number of cycles before specimen fails in fatigue (-)
pH	Acidity of the environment (-)
r	Fiber radius (m)
r_0	Initial fiber radius (m)
$r_{t_{st}}$	Fiber radius when the steady-state dissolution is reached (m)
R	Universal gas constant (8.314 J/(mol·K))
S	Stress (MPa)

S	Glass fiber surface area (m²)
S_0	Initial glass fiber surface area (m²)
$S_0^{specific}$	Specific glass fiber surface area (m²/g)
S_{glass}	Total glass fiber surface area in a composite plate (m²)
S_i	Surface area of the composite interphase (m²)
S_{i_0}	Initial surface area of the composite interphase (m²)
$S_i^{specific}$	Specific surface area of the composite interphase (m²/g)
t	Time (s)
t_{st}	Time when steady-state dissolution is reached (s)
T	Absolute temperature (K)
T_g	Glass transition temperature (K)
u_x, u_y, u_z	Relative displacements in Finite Element simulations (-)
UTS	Ultimate Tensile Strength (MPa)
V_f	Volume fraction of fibers in a composite laminate (m³/m³)
V_{water}	Volume of a water sample used for the HR-ICP-MS (L)
W	Gravimetric water content (wt%) in: *Paper I*
$W; W^*$	True water content (wt%)
W_c	Moisture content in the composite (wt%)
W_m	Moisture content scaled by polymer matrix fraction of the composite (wt%)
x, y, z	Cartesian coordinate system

BIBLIOGRAPHY

1. Berg, J.; Jones, F.R. The role of sizing resins, coupling agents and their blends on the formation of the interphase in glass fiber composites. *Composites Part A* **1998**, 29, 1261–1272, doi:10.1016/S1359-835X(98)00091-8.

2. Feih, S.; Wei, J.; Kingshott, P.; Sørensen, B.F. The influence of fiber sizing on the strength and fracture toughness of glass fiber composites. *Composites Part A* **2005**, 36, 245–255, doi:10.1016/j.compositesa.2004.06.019.

3. Krauklis, A.; Echtermeyer, A. Mechanism of Yellowing: Carbonyl Formation during Hygrothermal Aging in a Common Amine Epoxy. *Polymers* **2018**, *10*, 1017–1031, doi:10.3390/polym10091017.

4. Xiao, G.Z.; Shanahan, M.E.R. Swelling of DGEBA/DDA epoxy resin during hygrothermal ageing. *Polymer* **1998**, *39*, 3253–3260, doi:10.1016/S0032-3861(97)10060-X.

5. Toscano, A.; Pitarresi, G.; Scafidi, M.; Di Filippo, M.; Spadaro, G.; Alessi, S. Water diffusion and swelling stresses in highly crosslinked epoxy matrices. *Polym. Degrad. Stab.* **2016**, *133*, 255–263, doi:10.1016/j.polymdegradstab.2016.09.004.

6. Grabovac, I.; Whittaker, D. Application of bonded composites in the repair of ships structures—A 15-year service experience. *Compos. Part A* **2009**, *40*, 1381–1398, doi:10.1016/j.compositesa.2008.11.006.

7. McGeorge, D.; Echtermeyer, A.T.; Leong, K.H.; Melve, B.; Robinson, M.; Fischer, K.P. Repair of floating offshore units using bonded fibre composite materials. *Compos. Part A* **2009**, *40*, 1364–1380, doi:10.1016/j.compositesa.2009.01.015.

8. Gustafson, C.G.; Echtermeyer, A. Long-term properties of carbon fibre composite tethers. *Int. J. Fatigue.* **2006**, *28*, 1353–1362, doi:10.1016/j.ijfatigue.2006.02.035.

9. Salama, M.M.; Stjern, G.; Storhaug, T.; Spencer, B.; Echtermeyer, A. *The First Offshore Field Installation for a Composite Riser Join*t.; OTC-14018-MS; Offshore Technology Conference: Houston, TX, USA, **2002**, doi:10.4043/14018-MS.

10. Echtermeyer, A.T.; Gagani, A.I.; Krauklis, A.E.; Mazan, T. Multiscale Modelling of Environmental Degradation—First Steps. In *Durability of Composites in a Marine Environment 2. Solid Mechanics and its Applications*, Davies, P., Rajapakse, Y.D.S., Eds.; Springer: Cham, Switzerland, 2018; Volume 245, pp. 135–149, ISBN: 978-3-319-65145-3.

11. Thomason, J.L. *Glass Fiber Sizings: A Review of the Scientific Literature.* Middletown, DE, USA, **2012**, ISBN:978-0-9573814-1-4.

12. Weitsman, Y. Coupled damage and moisture-transport in fiber-reinforced, polymeric composites. *Int. J. Solids Struct.* **1987**, 23(7), 1003-1025, doi:10.1016/0020-7683(87)90093-X.

13. Weitsman, Y.J.; Elahi, M. Effects of fluids on the deformation, strength and durability of polymeric composites—An overview. *Mech. Time-Depend. Mater.* **2000**, 4, 107–126, doi:10.1023/A:1009838128526.

14. Roy, S. Moisture-Induced Degradation. In *Long-Term Durability of Polymeric Matrix Composites*; Pochiraju, V.K.; Tandon, P.G.; Schoppner, A.G., Eds.; Springer: Boston, MA, USA, **2012**; pp 181-236, ISBN:978-1-4419-9307-6.

15. Apicella, A.; Nicolais, L. Effect of Water on the Properties of Epoxy Matrix and Composite. *Adv. Polym. Sci.* **1985**, 72, 69-77, doi:10.1007/3-540-15546-5_3.

16. Lefebvre, D.R.; Elliker, P.R.; Takahashi, K.M.; Raju, V.R.; Kaplan, M.L. The Critical Humidity Effect in the Adhesion of Epoxy to Glass: Role of Hydrogen Bonding. *J. Adhes. Sci. Technol.* **2000**, 14, 925-937, doi:10.1163/156856100742988.

17. Guermazi, N.; Elleuch, K.; Ayedi, H.F. The Effect of Time and Aging Temperature on Structural and Mechanical Properties of Pipeline Coating. *Mater. Des.* **2009**, 30, 2006-2010, doi:10.1016/j.matdes.2008.09.003.

18. Wu, C.F.; Xu, W.J. Atomistic Simulation Study of Absorbed Water Influence on Structure and Properties of Crosslinked Epoxy Resin. *Polymer* **2007**, 48, 5440-5448, doi:10.1016/j.polymer.2007.06.038.

19. DiBenedetto, A.T. Tailoring of interfaces in glass fiber reinforced polymer composites: a review. *Mater. Sci. Eng. A* **2001**, 302, 74-82, doi:10.1016/S0921-5093(00)01357-5.

20. Wang, M.; Xu, X.; Ji, J.; Yang, Y.; Shen, J.; Ye, M. The hygrothermal aging process and mechanism of the novolac epoxy resin. *Composites Part B* **2016**, 107, 1-8, doi:10.1016/j.compositesb.2016.09.067.

21. Halpin, J.C. *Effects of Environmental Factors on Composite Materials*; Technical report AFML-TR-67–423, Air Force Materials Laboratory: Dayton, OH, USA, **1969**.

22. Krauklis, A.E.; Gagani, A.I.; Echtermeyer, A.T. Long-Term Hydrolytic Degradation of the Sizing-Rich Composite Interphase. *Coatings* **2019**, 9(4), 263-286, doi:10.3390/coatings9040263.

23. Gagani, A.I.; Fan, Y.; Muliana, A.H.; Echtermeyer, A.T. Micromechanical modeling of anisotropic water diffusion in glass fiber epoxy reinforced composites. *J. Compos. Mater.* **2017**, 52(17), 2321-2335, doi:10.1177/0021998317744649.

24. Krauklis, A.E.; Echtermeyer, A.T. Dissolving Cylinder Zero-Order Kinetic Model for Predicting Hygrothermal Aging of Glass Fiber Bundles and Fiber-Reinforced Composites. In *4th International Glass Fiber Symposium*; Gries, Th.; Pico, D.; Lüking, A.; Becker, Th., Eds.; Mainz, G (Verlag): Aachen, Germany, **2018**; pp. 66–72, ISBN:978-3-95886-249-4.

25. Maggana, C.; Pissis, P. Water sorption and diffusion studies in an epoxy resin system. *J. Polym. Sci. Part B* **1999**, 37(11), 1165–1182, doi:10.1002/(SICI)1099-0488(19990601)37:11<1165::AID-POLB11>3.0.CO;2-E.

26. Lee, M.C.; Peppas, N.A. Water transport in epoxy-resins. *Prog. Polym. Sci.* **1993**, 18(5), 947–961, doi:10.1016/0079-6700(93)90022-5.

27. Popineau, S.; Rondeau-Mouro, C.; Sulpice-Gaillet, C.; Shanahan, M.E.R. Free/bound water absorption in an epoxy adhesive. *Polymer* **2005**, 46(24), 10733–10740, doi:10.1016/j.polymer.2005.09.008.

28. Tennent, N.H. Clear and Pigmented Epoxy Resins for Stained Glass Conservation: Light Ageing Studies. *Stud. Conserv.* **1979**, 24, 153–164, doi:10.2307/1505777.

29. Ernault, E.; Richaud, E.; Fayolle, B. Origin of epoxies embrittlement during oxidative ageing. *Polym. Test.* **2017**, 63, 448–454, doi:10.1016/j.polymertesting.2017.09.004.

30. Pham, H.Q.; Marks, M.J. Epoxy resins. In *Ullmann's encyclopedia of industrial chemistry*; **2005**, Wiley-VCH. doi: 10.1002/14356007.a09_547.pub2, ISBN:9783527303854.

31. Mailhot, B.; Morlat-Thérias, S.; Ouahioune, M.; Gardette, J.-L. Study of the Degradation of an Epoxy/Amine Resin, 1 Photo- and Thermo-Chemical Mechanisms. *Macromol. Chem. Phys.* **2005**, 206, 575–584, doi:10.1002/macp.200400395.

32. Rocha, I.B.C.M.; Raijmaekers, S.; Nijssen, R.P.L.; van der Meer, F.P.; Sluys, L.J. Hygrothermal ageing behaviour of a glass/epoxy composite used in wind turbine blades. *J. Compos. Struct.* **2017**, 174, 110–122, doi:10.1016/j.compstruct.2017.04.028.

33. Startsev, V.O.; Lebedev, M.P.; Khrulev, K.A.; Molokov, M.V.; Frolov, A.S.; Nizina, T.A. Effect of outdoor exposure on the moisture diffusion and mechanical properties of epoxy polymers. *Polym. Test.* **2018**, 65, 281–296, doi:10.1016/j.polymertesting.2017.12.007.

34. Li, L.; Yu, Y.; Wu, Q.; Zhan, G.; Li, S. Effect of Chemical Structure on the Water Sorption of Amine-Cured Epoxy Resins. *Corros. Sci.* **2009**, 51, 3000-3006, doi:10.1016/j.corsci.2009.08.029.

35. Wang, J.; Gong, J.; Gong, Z.; Yan, X.; Wang, B.; Wu, Q.; Li, S. Effect of Curing Agent Polarity on Water Absorption and Free Volume in Epoxy Resin Studied by PALS. *Nucl. Instrum. Methods Phys. Res. B* **2010**, 268, 2355-2361, doi:10.1016/j.nimb.2010.04.010.

36. Morel, E.; Bellenger, V.; Verdu, J. Structure-Water Absorption Relationships for Amine-Cured Epoxy Resins. *Polymer* **1985**, 26, 1719-1724, doi:10.1016/0032-3861(85)90292-7.

37. Clancy, T.C.; Frankland, S.J.V.; Hinkley, J.A.; Gates, T.S. Molecular modeling for calculation of mechanical properties of epoxies with moisture ingress. *Polymer* **2009**, 50(12), 2736–2742, doi:10.1016/j.polymer.2009.04.021.

38. Krauklis, A.E.; Gagani, A.I.; Echtermeyer, A.T. Hygrothermal Aging of Amine Epoxy: Reversible Static and Fatigue Properties. *Open Eng.* **2018**, 8, 447–454, doi:10.1515/eng-2018-0050.

39. Ibarra, L.; Chamorro, C. Short fiber–elastomer composites. Effects of matrix and fiber level on swelling and mechanical and dynamic properties. *J. Appl. Polym. Sci.* **1991**, 43, 1805–1819, doi:10.1002/app.1991.070431004.

40. Chen, Y.; Davalos, J.F.; Ray, I.; Kim, H.-Y. Accelerated aging tests for evaluations of durability performance of FRP reinforcing bars for concrete structures. *Compos. Struct.* **2007**, 78(1), 101–111, doi:10.1016/j.compstruct.2005.08.015.

41. Wallenberger, F.T. Commercial and Experimental Glass Fibres. In *Fibreglass and Glass Technology*; Wallenberger, F.T.; Bingham, P.A., Eds.; Springer: US, **2010**; ISBN:978-1-4419-0735-6.

42. Steinmann, W.; Saelhoff, A.-K. Essential Properties of Fibres for Composite Applications. In *Fibrous and Textile Materials for Composite Applications, Textile Science and Clothing Technology*; Rana, S.; Fangueiro, R., Eds.; Springer: Singapore, 2016; ISBN:978-981-10-0232-8.

43. Krauklis, A.E.; Gagani, A.I.; Vegere, K.; Kalnina, I.; Klavins, M.; Echtermeyer, A.T. Dissolution Kinetics of R-Glass Fibres: Influence of Water Acidity, Temperature and Stress Corrosion. *Fibers* **2019**, 7(3), 22-40, in a *Special Issue: Advances in Glass Fibers*, doi:10.3390/fib7030022.

44. Brown, E.N.; Davis, A.K.; Jonnalagadda, K.D.; Sottos, N.R. Effect of surface treatment on the hydrolytic stability of E-glass fiber bundle tensile strength. *Compos. Sci. Technol.* **2005**, 65, 129–136, doi:10.1016/j.compscitech.2004.07.001.

45. Bledzki, A.; Spaude, R.; Ehrenstein, G.W. Corrosion Phenomena in Glass Fibres and Glass Fibre Reinforced Thermosetting Resins. *Compos. Sci. Technol.* **1985**, 23(4), 263-285, doi:10.1016/0266-3538(85)90040-5.

46. Tournié, A.; Ricciardi, P.; Colomban, P. Glass Corrosion Mechanisms: A Multiscale Analysis. *Solid State Ionics* **2008**, 179(38), 2142-2154, doi:10.1016/j.ssi.2008.07.019.

47. Agarwal, B.D.; Broutman, L.J. *Analysis and Performance of Fibre Composites*, 2nd ed.; John Wiley and Sons, Inc.: Hoboken, USA, **1990**; pp. 339-359, ISBN:978-0-471-51152-6.

48. Schutte, C.L. Environmental durability of glass-fiber composites. *Mater. Sci. Eng. R Reports* **1994**, 13, 265-323, doi:10.1016/0927-796X(94)90002-7.

49. Renaud, C.M.; Greenwood, M.E. Effect of glass fibers and environments on long-term durability of GFRP composites, In Proceedings of 9 EFUC Meeting, Wroclaw, Poland, **2005**.

50. Grambow, B.; Müller, R. First-order dissolution rate law and the role of surface layers in glass performance assessment. *J. Nucl. Mater.* **2001**, 298(1-2), 112-124. doi:10.1016/S0022-3115(01)00619-5.

51. Grambow, B. A General Rate Equation for Nuclear Waste Glass Corrosion. *Mat. Res. Soc. Symp. Proc.* **1985**, 44, 15-27, doi:10.1557/PROC-44-15.

52. Krauklis, A.E.; Echtermeyer, A.T. Long-Term Dissolution of Glass Fibers in Water Described by Dissolving Cylinder Zero-Order Kinetic Model: Mass Loss and Radius Reduction. *Open Chem.* **2018**, 16(1), 1189-1199, doi:10.1515/chem-2018-0133.

53. Krauklis, A.E.; Gagani, A.I.; Echtermeyer, A.T. Near-Infrared Spectroscopic Method for Monitoring Water Content in Epoxy Resins and Fiber-Reinforced Composites. *Materials* **2018**, 11(4), 586-599, doi:10.3390/ma11040586.

54. Stamenović, M.R.; Putić, S.S.; Rakin, M.B.; Medjo, B.; Čikara, D. Effect of alkaline and acidic solutions on the tensile properties of glass–polyester pipes. *Mater. Des.* **2011**, 32(4), 2456-2461, doi:10.1016/j.matdes.2010.11.023.

55. Amaro, A.M.; Reis, P.N.B.; Neto, M.A.; Louro C. Effects of alkaline and acid solutions on glass/epoxy composites. *Polym. Degrad. Stab.* **2013**, 98(4), 853-862, doi:10.1016/j.polymdegradstab.2012.12.029.

56. Mišíková, L.; Liška, M.; Galusková, D. CORROSION OF E-GLASS FIBRES IN DISTILLED WATER. *Ceram. Silikaty* **2007**, 51(3), 131-135.

57. Bashir, S.T.; Yang, L.; Liggat, J.J.; Thomason, J.L. Kinetics of dissolution of glass fibre in hot alkaline solution. *J. Mater. Sci.* **2018**, 53(3), 1710-1722. doi:10.1007/s10853-017-1627-z.

58. Delage, F.; Ghaleb, D.; Dussossoy, J.L.; Chevallier, O.; Vernaz, E. A mechanistic model for understanding nuclear waste glass dissolution. *J. Nucl. Mater.* **1992**, 190, 191-197, doi:10.1016/0022-3115(92)90086-Z.

59. Geisler-Wierwille, T.; Nagel, T.J.; Kilburn, M.R.; Janssen, A.; Icenhower, J.; Fonseca, R.O.C.; Grange, M.L.; Nemchin, A.A. The Mechanism of Borosilicate Glass Corrosion Revisited. *Geochim. Cosmochim. Acta* **2015**, 158, 112-129, doi:10.1016/j.gca.2015.02.039.

60. Icenhower, J.; Steefel, C.I. Dissolution Rate of Borosilicate Glass SON68: A Method of Quantification Based upon Interferometry and Implications for Experimental and Natural Weathering Rates of Glass. *Geochim. Cosmochim. Acta* **2015**, 157, 147-163, doi:10.1016/j.gca.2015.02.037.

61. Ma, T.; Jivkov, A.P.; Li, W.; Liang, W.; Wang, Y.; Xu, H.; Han, X. A mechanistic model for long-term nuclear waste glass dissolution integrating chemical affinity and interfacial diffusion barrier. *J. Nucl. Mater.* **2017**, 486, 70-85, doi:10.1016/j.jnucmat.2017.01.001.

62. Geisler, T.; Dohmen, L.; Lenting, C.; Fritzsche, M.B.K. Real-time in situ observations of reaction and transport phenomena during silicate glass corrosion by fluid-cell Raman spectroscopy. *Nature Materials* **2019**, 18, 342-348, doi:10.1038/s41563-019-0293-8.

63. Hunter, F.M.I.; Hoch, A.R.; Heath, T.G.; Baston, G.M.N. *Report RWM005105, AMEC/103498/02 Issue 2: Review of Glass Dissolution Models and Application to UK Glasses*; AMEC: Didcot, Oxfordshire, UK, **2015**.

64. Michalske, T.A.; Freiman, S.W. A Molecular Mechanism for Stress Corrosion in Vitreous Silica. *J. Am. Ceram. Soc.* **1983**, 66, 284–288, doi:10.1111/j.1151-2916.1983.tb15715.x.

65. Iler, R.K. *The Chemistry of Silica: Solubility, Polymerization, Colloid and Surface Properties and Biochemistry of Silica*; Wiley: New York, USA, **1979**; pp. 896, ISBN:978-0-471-02404-0.

66. Putnis, C.V.; Ruiz-Agudo, E. The mineral–water interface: where minerals react with the environment. *Elements* **2013**, 9, 177–182, doi:10.2113/gselements.9.3.177.

67. Dai, Z.; Shi, F.; Zhang, B.; Li, M.; Zhang, Z. Effect of sizing on carbon fiber surface properties and fibers/epoxy interfacial adhesion. *Appl. Surf. Sci.* **2011**, 257, 6980–6985, doi:10.1016/j.apsusc.2011.03.047.

68. Yuan, X.; Zhu, B.; Cai, X.; Liu, J.; Qiao, K.; Yu, J. Optimization of interfacial properties of carbon fiber/epoxy composites via a modified polyacrylate emulsion sizing. *Appl. Surf. Sci.* **2017**, 401, 414-423, doi:10.1016/j.apsusc.2016.12.234.

69. Plonka, R.; Mäder, E.; Gao, S.L.; Bellmann, C.; Dutschk, V.; Zhandarov, S. Adhesion of epoxy/glass fiber composites influenced by aging effects on sizings. *Composites Part A* **2004**, 35, 1207–1216, doi:10.1016/j.compositesa.2004.03.005.

70. Peters, L. Influence of Glass Fibre Sizing and Storage Conditions on Composite Properties. In *Durability of Composites in a Marine Environment 2. Solid Mechanics and Its Applications*; Davies, P.; Rajapakse, Y.D.S., Eds.; Springer: Cham, Switzerland, **2018**; Volume 245, pp. 19-31, ISBN:978-3-319-65145-3.

71. Culler, S.R.; Ishida, H.; Koenig, J.L. *Hydrothermal stability of γ-Aminopropyltriethoxysilane Coupling Agent on Ground Silicon Powder and E-Glass Fibers*; Technical report, Department of Macromolecular Science: Cleveland, OH, USA, **1983**.

72. Wang, D.; Jones, F.R.; Denison, P. TOF SIMS and XPS study of the interaction of hydrolysed γ-aminopropyltriethoxysilane with E-glass surfaces. *J. Adhes. Sci. Technol.* **1992**, 6, 79-98, doi:10.1163/156856192X00070.

73. Wang, D.; Jones, F.R.; Denison, P. Surface analytical study of the interaction between γ-amino propyl triethoxysilane and E-glass surface. Part I Time-of-flight secondary ion mass spectrometry. *J. Mater. Sci.* **1992**, 27, 36-48, doi:10.1007/BF00553834.

74. Wang, D.; Jones, F.R. Surface analytical study of the interaction between γ-amino propyl triethoxysilane and E-glass surface. Part II X-ray photoelectron spectroscopy. *J. Mater. Sci.* **1993**, 28, 2481-2488, doi:10.1007/BF01151683.

75. ASTM D4963/D4963M-2011. Standard Test Method for Ignition Loss of Glass Strands and Fabrics, **2011**.

76. Piret, W.; Mason, N.; Luc, P. European Patent EP2540683A1, Glass fibre sizing composition by 3B-Fibreglass SPRL, **2011**.

77. Thomason, J.L. *Glass Fibre Sizing: A Review of Size Formulation Patents*. Blurb Co: Glasgow, Scotland, UK, **2015**; ISBN:978-0-9573814-3-8.

78. Loewenstein, K.L. *Glass science and technology (Book 6), The manufacturing technology of continuous glass fibres*. Elsevier: Amsterdam, Netherlands, **1993**, ISBN:978-0444893468.

79. Thomason, J.L.; Adzima, L.J. Sizing up the interphase: an insider's guide to the science of sizing. *Composites Part A* **2001**, 32, 313-321, doi:10.1016/S1359-835X(00)00124-X.

80. Plueddemann, E.P. *Silane coupling agents, 2nd edition*. Plenum Press: New York and London, **1991**; ISBN:978-0-306-43473-0.

81. Wolff, V.; Perwuelz, A.; El Achari, A.; Caze, C.; Carlier, E. Determination of surface heterogeneity by contact angle measurements on glass fibres coated with different sizings. *J. Mater. Sci.* **1999**, 34, 3821-3829, doi:10.1023/A:1004604917226.

82. Watson, H.; Mikkola, P.J.; Matisons, J.G.; Rosenholm, J.B. Deposition characteristics of ureido silane ethanol solutions onto E-glass fibres. *Colloids Surf. A* **2000**, 161, 183-192, doi:10.1016/S0927-7757(99)00336-2.

83. Feresenbet, E.; Raghavan, D.; Holmes, G.A. Influence of silane coupling agent composition on the surface characterization of fiber and on fiber-matrix interfacial shear strength. *J. Adhes.* **2003**, 79, 643-665, doi:10.1080/00218460309580.

84. Fagerholm, H.M.; Lindsjö, C.; Rosenholm, J.B.; Rökman, K. Physical characterization of E-glass fibres treated with alkylphenylpoly(oxyethylene)alcohol. *Colloids Surf.* **1992**, 69, 79-86, doi:10.1016/0166-6622(92)80218-Q.

85. Thomason, J.L.; Dwight, D.W. The use of XPS for characterization of glass fibre coatings. *Composites Part A* **1999**, 30, 1401-1413, doi:10.1016/S1359-835X(99)00042-1.

86. Turrión, S.G.; Olmos, D.; González-Benito, J. Complementary characterization by fluorescence and AFM of polyaminosiloxane glass fibers coatings. *Polym. Test.* **2005**, 24, 301-308, doi:10.1016/j.polymertesting.2004.11.006.

87. Mai, K.; Mäder, E.; Mühle, M. Interphase characterization in composites with new non-destructive methods. *Composites Part A* **1998**, 29, 1111-1119, doi:10.1016/S1359-835X(98)00092-X.

88. Joliff, Y.; Belec, L.; Chailan, J.-F. Impact of the interphases on the durability of a composite in humid environment – a short review. *20th International Conference on Composite Structures ICCS20*. Paris, France, **2017**.

89. Kim, J.K.; Sham, M.L.; Wu, J. Nanoscale characterization of interphase in silane treated glass fibre composites. *Composites Part A* **2001**, 32, 607-618, doi:10.1016/S1359-835X(00)00163-9.

90. Riaño, L.; Belec, L.; Chailan, J.-F.; Joliff, Y. Effect of interphase region on the elastic behavior of unidirectional glass-fiber/epoxy composites. *Compos. Struct.* **2018**, 198, 109-116, doi:10.1016/j.compstruct.2018.05.039.

91. Crank, J. *The mathematics of diffusion, 2nd edition*. Clarendon Press: Oxford, United Kingdom, **1975**; ISBN:978-0-19-853411-6.

92. Gagani, A.I.; Krauklis, A.E.; Echtermeyer, A.T. Anisotropic fluid diffusion in carbon fiber reinforced composite rods: Experimental, analytical and numerical study. *Marine Struct.* **2018**, 59, 47-59, doi:10.1016/j.marstruc.2018.01.003.

93. Gagani, A.I.; Krauklis, A.E.; Echtermeyer, A.T. Orthotropic fluid diffusion in composite marine structures. Experimental procedure, analytical and numerical modelling of plates, rods and pipes. *Composites Part A* **2018**, 115, 196-205, doi:10.1016/j.compositesa.2018.09.026.

94. Bonniau, P.; Bunsell, A.R. Water Absorption by Glass Fibre Reinforced Epoxy Resin. In *Composite Structures*; Marshall, I.H., Ed.; Springer: Dordrecht, Netherlands, **1981**; pp. 92–105, ISBN:978-94-009-8122-5.

95. Augl, J.M.; Berger, A.E. *The Effect of Moisture on Carbon Fiber Reinforced Epoxy Composites. 1. Diffusion*; Technical Report NSWC/WOL/TR-76-7, White Oak Laboratory: Silver Spring, Maryland, USA, **1976**.

96. Bertolino, V.; Cavallaro, G.; Lazzara, G.; Merli, M.; Milioto, S.; Parisi, F.; Sciascia, L. Effect of the Biopolymer Charge and the Nanoclay Morphology on Nanocomposite Materials. *Ind. Eng. Chem. Res.* **2016**, 55, 7373-7380, doi:10.1021/acs.iecr.6b01816.

97. Ciprioti, S.V.; Tuffi, R.; Dell'Era, A.; Poggetto, F.D.; Bollino, F. Thermal Behavior and Structural Study of SiO_2/Poly(ε-caprolactone) Hybrids Synthesized via Sol-Gel Method. *Materials* **2018**, 11, 275-285, doi:10.3390/ma11020275.

98. Mijović, J.; Zhang, H. Local Dynamics and Molecular Origin of Polymer Network−Water Interactions as Studied by Broadband Dielectric Relaxation Spectroscopy, FTIR, and Molecular Simulations. *Macromolecules* **2003**, 36, 1279-1288, doi:10.1021/ma021568q.

99. Philippe, L.V.S.; Lyon, S.B.; Sammon, C.; Yarwood, J. Validation of Electrochemical Impedance Measurements for Water Sorption into Epoxy Coatings Using Gravimetry and Infra-Red Spectroscopy. *Corros. Sci.* **2008**, 50, 887-896, doi:10.1016/j.corsci.2007.09.008.

100. Cotugno, S.; Mensitieri, G.; Musto, P.; Sanguigno, L. Molecular Interactions in and Transport Properties of Densely Crosslinked Networks: a Time-Resolved FT-IR Spectroscopy Investigation of the Epoxy/H_2O System. *Macromolecules* **2005**, 38, 801-811, doi:10.1021/ma040008j.

101. Weir, M.D.; Bastide, C.; Sung, C.S.P. Characterization of Interaction of Water in Epoxy by UV Reflection Spectroscopy. *Macromolecules* **2001**, 34, 4923-4926, doi:10.1021/ma0017900.

102. Mijović, J.; Zhang, H. Molecular Dynamics Simulation Study of Motions and Interactions of Water in a Polymer Network. *J. Phys. Chem. B* **2004**, 108, 2557-2563, doi:10.1021/jp036181j.

103. MacQueen, R.C.; Granata, R.D. A Positron Annihilation Lifetime Spectroscopic Study of the Corrosion Protective Properties of Epoxy Coatings. *Prog. Org. Coat.* **1996**, 28, 97-112, doi:10.1016/0300-9440(95)00557-9.

104. Muroga, S.; Hikima, Y.; Ohshima, M. Near-Infrared Spectroscopic Evaluation of the Water Content of Molded Polylactide Under the Effect of Crystallization. *Appl. Spectrosc.* **2017**, 71, 1300-1309, doi:10.1177/0003702816681011.

105. Genkawa, T.; Watari, M.; Nishii, T.; Ozaki, Y. Development of a Near-Infrared/Mid-Infrared Dual-Region Spectrometer for Online Process Analysis. *Appl. Spectrosc.* **2012**, 66, 773-781, doi:10.1366/11-06499.

106. Ozaki, Y. Near-Infrared Spectroscopy – Its Versatility in Analytical Chemistry. *Anal. Sci.* **2012**, 28, 545-563, doi:10.2116/analsci.28.545.

107. Zhou, J. Transient analysis on hygroscopic swelling characterization using sequentially coupled moisture diffusion and hygroscopic stress modeling method. *Microelectron. Reliab.* **2008**, 48, 805–810, doi:10.1016/j.microrel.2008.03.027.

108. Hahn, H.T.; Kim, R.Y. Swelling of Composite Laminates. In *Advanced Composite Materials: Environmental Effects*; ASTM STP 658; American Society for Testing and Materials: Philadelphia, PA, USA, **1978**, pp. 98–120.

109. Krauklis, A.E.; Gagani, A.I.; Echtermeyer, A.T. Prediction of Orthotropic Hygroscopic Swelling of Fiber-Reinforced Composites from Isotropic Swelling of Matrix Polymer. *Journal of Composites Science* **2019**, 3(1), 10-23, doi:10.3390/JCS3010010.

110. Shirangi, M.H.; Michel, B. Mechanism of moisture diffusion, hygroscopic swelling, and adhesion degradation in epoxy molding compounds. In *Moisture Sensitivity of Plastic Packages of IC Devices*, Fan, X.J.; Suhir, E., Eds.; Springer, New York, NY, USA, **2010**; pp. 29–69, ISBN:978-1-4419-5719-1.

111. Obeid, H.; Clément, A.; Fréour, S.; Jacquemin, F.; Casari, P. On the identification of the coefficient of moisture expansion of polyamide-6: Accounting differential swelling strains and plasticization. *Mech. Mater.* **2018**, 118, 1–10, doi:10.1016/j.mechmat.2017.12.002.

112. Cairns, D.S.; Adams, D.F. Moisture and thermal expansion properties of unidirectional composite materials and the epoxy matrix. *J. Reinf. Plast. Compos.* **1983**, 2, 239–255, doi:10.1177/073168448300200403.

113. Ashton, J.E.; Halpin, J.C.; Petit, P.H. *Primer on Composite Materials Analysis*; Technomic Pub. Co.: Stamford, CT, USA, **1969**; ISBN:978-0-8776-2754-8.

114. Schapery, R.A. Thermal expansion coefficients of composite materials based on energy principles. *J. Compos. Mater.* **1968**, 2, 380–404, doi:10.1177/002199836800200308.

115. Coran, A.Y.; Boustany, K.; Hamed, P. Unidirectional fiber-polymer composites: Swelling and modulus anisotropy. *J. Appl. Polym. Sci.* **1971**, 15, 2471–2485, doi:10.1002/app.1971.070151014.

116. Daniels, B.K. Orthotropic swelling and simplified elasticity laws with special reference to cord-reinforced rubber. *J. Appl. Polym. Sci.* **1973**, 17, 2847–2853, doi:10.1002/app.1973.070170921.

117. Fan, Y.; Gomez, A.; Ferraro, S.; Pinto, B.; Muliana, A.; La Saponara, V. Diffusion of water in glass fiber reinforced polymer composites at different temperatures. *J. Compos. Mater.* **2018**, 53, 1097–1110, doi:10.1177/0021998318796155.

118. Jacquemin, F.; Fréour, S.; Guillén, R. Analytical modeling of transient hygro-elastic stress concentration—Application to embedded optical fiber in a non-uniform transient strain field. *Compos. Sci. Technol.* **2006**, 66, 397–406, doi:10.1016/j.compscitech.2005.07.019.

119. Meng, M.; Rizvi, M.J.; Le, H.R.; Grove, S.M. Multi-scale modelling of moisture diffusion coupled with stress distribution in CFRP laminated composites. *Compos. Struct.* **2016**, 138, 295–304, doi:10.1016/j.compstruct.2015.11.028.

120. Sinchuk, Y.; Pannier, Y.; Gueguen, M.; Tandiang, D.; Gigliotti, M. Computed-tomography based modeling and simulation of moisture diffusion and induced swelling in textile composite materials. *Int. J. Solids Struct.* **2018**, 154, 88–96, doi:10.1016/j.ijsolstr.2017.05.045.

121. Sinchuk, Y.; Pannier, Y.; Gueguen, M.; Gigliotti, M. Image-based modeling of moisture-induced swelling nd stress in 2D textile composite materials using a global-local approach. *Proc. Inst. Mech. Eng., Part C: J. Mech. Eng. Sci.* **2018**, 232, 1505–1519, doi:10.1177/0954406217736789.

122. Weitsman, Y.J. *Fluid Effects in Polymers and Polymeric Composites*; Springer: New York, NY, USA, **2012**; ISBN:978-1-4614-1059-1.

123. Sar, B.E.; Fréour, S.; Davies, P.; Jacquemin, F. Accounting for differential swelling in the multi-physics modelling of the diffusive behaviour of polymers. *J. Appl. Math. Mech.* **2014**, 94, 452–460, doi:10.1002/zamm.201200272.

124. Fan, Y.; Gomez, A.; Ferraro, S.; Pinto, B.; Muliana, A.; La Saponara, V. The effects of temperatures and volumetric expansion on the diffusion of fluids through solid polymers. *J. Appl. Polym. Sci.* **2017**, 134, 45151–45165, doi:10.1002/app.45151.

125. Kappert, E.J.; Raaijmakers, M.J.T.; Tempelman, K.; Cuperus, F.P.; Ogieglo, W.; Benes, N.E. Swelling of 9 polymers commonly employed for solvent-resistant nanofiltration membranes: A comprehensive dataset. *J. Membr. Sci.* **2019**, 569, 177–199, doi:10.1016/j.memsci.2018.09.059.

126. Ramirez, F.A.; Carlsson, L.A.; Acha, B.A. Evaluation of water degradation of vinylester and epoxy matrix composites by single fiber and composite tests. *J. Mater. Sci.* **2008**, 43, 5230–5242, doi:10.1007/s10853-008-2766-z.

127. Shirell, C.D.; Halpin, J. Moisture Absorption in Epoxy Composite Materials. In Proceedings of the Composite Materials: Testing and Design (Fourth Conference), ASTM STP617, Valley Forge, PA, USA, 3–4 May **1977**; American Society for Testing and Materials: Philadelphia, PA, USA, pp. 514–528, doi:10.1520/STP26963S.

128. Echtermeyer, A.T. Integrating Durability in Marine Composite Certification. In *Durability of Composites in a Marine Environment*; Davies, P.; Rajapakse, Y.D.S., Eds.; Springer: Dordrecht, The Netherlands, **2014**; pp. 179–194. ISBN:978-94-007-7416-2.

129. International Standard ISO 6721-11:2012(E), Plastics – Determination of dynamic mechanical properties – Part 11: Glass transition temperature, **2012**.

130. International Standard ISO 527-1:2012(E), Plastics – Determination of tensile properties – Part 1: General principles, **2012**.

131. International Standard ISO 2078:1993 (revised in 2014), Textile glass – Yarns – Designation, **2014**.

132. 3B Fibreglass technical data sheet. HiPer-tex W2020 rovings, Belgium, **2012**.

133. 3B Fibreglass data sheet. https://www.3b-fibreglass.com/HiPer-tex (last accessed on 5 July 2019).

134. Emadipour, H.; Chiang, P.; Koenig, J.L. Interfacial strength studies of fibre-reinforced composites. *Res Mechanica* **1982**, 5, 165-176.

135. ASTM D3171/ D3171-15. Standard Test Methods for Constituent Content of Composite Materials, **2015**.

136. Zinck, P.; Gerard, J.F. On the hybrid character of glass fibres surface networks. *J. Mater. Sci.* **2005**, 40(9), 2759-2760, doi:10.1007/s10853-005-2124-3.

137. Swinehart, D.F. The Beer–Lambert Law. *J. Chem. Educ.* **1962**, 39(7), 333-335, doi: 10.1021/ed039p333.

138. Belec, L.; Nguyen, T.H.; Nguyen, D.L.; Chailan, J.F. Comparative effects of humid tropical weathering and artificial ageing on a model composite properties from nano- to macro-scale. *Compos. Part A* **2015**, 68, 235-241, doi:10.1016/j.compositesa.2014.09.028.

139. Down, J.L. The Yellowing of Epoxy Resin Adhesives: Report on High-Intensity Light Aging. *Stud. Conserv.* **1986**, 31, 159–170, doi:10.2307/1506247.

140. Down, J.L. The yellowing of epoxy resin adhesives: Report on natural dark aging. *Stud. Conserv.* **1984**, 29, 63–76, doi:10.2307/1506076.

141. Coutinho, I.; Ramos, A.M.; Lima, A.M.; Fernandes, F.B. Studies of the degradation of epoxy resins used for the conservation of glass. In *Proceedings of the Holding it all together, Ancient and Modern Approaches to Joining, Repair and Consolidation*, London, UK, **2008**, doi:10.13140/RG.2.1.2799.3124.

142. Celina, M.C.; Dayile, A.R.; Quintana, A. A perspective on the inherent oxidation sensitivity of epoxy materials. *Polymer* **2013**, 54, 3290–3296, doi:10.1016/j.polymer.2013.04.042.

143. Ernault, E.; Richaud, E.; Fayolle, B. Thermal-oxidation of epoxy/amine followed by glass transition temperature changes. *Polym. Degrad. Stab.* **2017**, 138, 82–90, doi:10.1016/j.polymdegradstab.2017.02.013.

144. Galant, C.; Fayolle, B.; Kuntz, M.; Verdu, J. Thermal and radio-oxidation of epoxy coatings. *Prog. Org. Coat.* **2010**, 69, 322–329, doi:10.1016/j.porgcoat.2010.07.005.

145. Deng, T.; Liu, Y.; Cui, X.; Yang, Y.; Jia, S.; Wang, Y.; Lu, C.; Li, D.; Cai, R.; Hou, X. Cleavage of C–N bonds in carbon fiber/epoxy resin composites. *Green Chem.* **2015**, 17, 2141–2145, doi:10.1039/C4GC02512A.

146. Li, K.; Wang, K.; Zhan, M.-S.; Xu, W. The change of thermal-mechanical properties and chemical structure of ambient cured DGEBA/TEPA under accelerated thermo-oxidative aging. *Polym. Degrad. Stab.* **2013**, 98, 2340–2346, doi:10.1016/j.polymdegradstab.2013.08.014.

147. Zahra, Y.; Djouani, F.; Fayolle, B.; Kuntz, M.; Verdu, J. Thermo-oxidative aging of epoxy coating systems. *Prog. Org. Coat.* **2014**, 77, 380–387, doi:10.1016/j.porgcoat.2013.10.011.

148. Ernault, E.; Richaud, E.; Fayolle, B. Thermal oxidation of epoxies: Influence of diamine hardener. *Polym. Degrad. Stab.* **2016**, 134, 76–86, doi:10.1016/j.polymdegradstab.2016.09.030.

149. Sauvant-Moynot, V.; Duval, S.; Grenier, J. Innovative pipe coating material and process for high temperature fields. *Oil Gas Sci. Technol.* **2002**, 57, 269–279, doi:10.2516/ogst:2002019.

150. Theocaris, P.S. Influence of plasticizer on Poisson's ratio of epoxy polymers. *Polymer* **1979**, 20, 1149-1154, doi:10.1016/0032-3861(79)90308-2.

151. Fine, R.A.; Millero, F.J. Compressibility of water as a function of temperature and pressure. *J. Chem. Phys.* **1973**, 59(10), 5529-5536, doi:10.1063/1.1679903.

152. Eastes, W.; Potter, R.M.; Hadley, J.G. Estimating in-vitro glass fibre dissolution rate from composition. *Inhal. Toxicol.* **2000**, 12, 269–280, doi:10.1080/089583700196149.

153. Khawam, A.; Flanagan, D.R. Solid-State Kinetic Models: Basics and Mathematical Fundamentals. *J. Phys. Chem. B* **2006**, 110, 17315-17328, doi:10.1021/jp062746a.

154. Michalske, T.A.; Bunker, B.C. A Chemical Kinetics Model for Glass Fracture. *J. Am. Ceram. Soc.* **1993**, 76, 2613–2618, doi:10.1111/j.1151-2916.1993.tb03989.x.

155. Shiue, Y.S.; Matthewson, M.J. Stress dependent activation entropy for dynamic fatigue of pristine silica optical fibres. *J. Appl. Phys.* **2001**, 89, 4787–4793, doi:10.1063/1.1361245.

156. Criscenti, L.J.; Kubicki, J.D.; Brantley, S.L. Silicate Glass and Mineral Dissolution: Calculated Reaction Paths and Activation Energies for Hydrolysis of a Q^3 Si by H_3O^+ Using Ab Initio Methods. *J. Phys. Chem. A* **2006**, 110, 198–206, doi:10.1021/jp044360a.

157. ASTM D5229/D5229M-14. Standard Test Method for Moisture Absorption Properties and Equilibrium Conditioning of Polymer Matrix Composite Materials, ASTM International; West Conshohocken, PA, **2014**.

158. Perreux, D.; Choqueuse, D.; Davies, P. Anomalies in moisture absorption of glass fibre reinforced epoxy tubes. *Composites Part A* **2002**, 33, 147-154, doi: 10.1016/S1359-835X(01)00111-7.

159. Gagani, A.I.; Krauklis, A.E.; Sæter, E.; Vedvik, N.P.; Echtermeyer, A.T. A Novel Method for Testing and Determining ILSS for Marine Composites. *Comp. Struct.* **2019**, 220, 431-440, doi:10.1016/j.compstruct.2019.04.040.

160. Thomason, J.L. The interface region in glass-fibre-reinforced epoxy resin composites: 2. Water absorption, voids and the interface. *Composites* **1995**, 26, 477-485, doi:10.1016/0010-4361(95)96805-G.

161. Mazan, T.; Jørgensen, J.K.; Echtermeyer, A.T. Aging of polyamide 11. Part 2: General multiscale model of the hydrolytic degradation applied to predict the morphology evolution. *J. Appl. Polym. Sci.* **2015**, 132(41), 42630-42639, doi:10.1002/app.42630.

162. Mazan, T.; Jørgensen, J.K.; Echtermeyer, A.T. Aging of polyamide 11. Part 3: Multiscale model predicting the mechanical properties after hydrolytic degradation. *J. Appl. Polym. Sci.* **2015**, 132(46), 42792-42802, doi:10.1002/app.42792.

163. Fournier, R.O.; Rowe, J.J. The solubility of amorphous silica in water at high temperatures and high pressures. *Am. Mineral.* **1977**, 62, 1052-1056.

164. Crundwell, F.K. On the Mechanism of the Dissolution of Quartz and Silica in Aqueous Solutions. *ACS Omega* **2017**, 2(3), 1116–1127, doi:10.1021/acsomega.7b00019.

165. Von Damm, K.L.; Edmond, J.M.; Grant, B.; Measures, C.I.; Walden, B.; Weiss, R.F. Chemistry of submarine hydrothermal solutions at 21°N, East Pacific Rise. *Geochim. Cosmochim. Acta* **1985**, 49, 2197-2220, doi:10.1016/0016-7037(85)90222-4.

166. Holland, H.D. *The chemistry of the atmosphere and oceans*; Wiley: New York, USA, **1978**; pp. 351, ISBN:978-0471035091.

167. Wierderhorn, S.M.; Bolz, L.H. Stress corrosion and static fatigue of glass. *J. Am. Ceram. Soc.* **1970**, 53(10), 543-548, doi:10.1111/j.1151-2916.1970.tb15962.x.

168. Sekine, H.; Beaumont, P.W.R. A physically based micro-mechanical theory and diagrams of macroscopic stress-corrosion cracking in aligned continuous glass-fiber-reinforced polymer laminates. *Compos. Sci. Technol.* **1998**, 58, 1659-1665, doi:10.1016/S0266-3538(97)00236-4.

169. Charles, R.J. Static Fatigue of Glass. II. *J. Appl. Phys.* **1958**, 29, 1554-1560, doi:10.1063/1.1722992.

APPENDICES

Appendix A

Paper I

Krauklis A.E., Gagani A.I., Echtermeyer A.T.

Near-Infrared Spectroscopic Method for Monitoring Water Content in Epoxy Resins and Fiber-Reinforced Composites.

Paper I

Article

Near-Infrared Spectroscopic Method for Monitoring Water Content in Epoxy Resins and Fiber-Reinforced Composites

Andrey E. Krauklis * , Abedin I. Gagani and Andreas T. Echtermeyer

Department of Mechanical and Industrial Engineering (past: Department of Engineering Design and Materials), Norwegian University of Science and Technology, 7491 Trondheim, Norway; abedin.gagani@ntnu.no (A.I.G.); andreas.echtermeyer@ntnu.no (A.T.E.)
* Correspondence: andrejs.krauklis@ntnu.no; Tel.: +371-268-10288

check for updates

Abstract: Monitoring water content and predicting the water-induced drop in strength of fiber-reinforced composites are of great importance for the oil and gas and marine industries. Fourier transform infrared (FTIR) spectroscopic methods are broadly available and often used for process and quality control in industrial applications. A benefit of using such spectroscopic methods over the conventional gravimetric analysis is the possibility to deduce the mass of an absolutely dry material and subsequently the true water content, which is an important indicator of water content-dependent properties. The objective of this study is to develop an efficient and detailed method for estimating the water content in epoxy resins and fiber-reinforced composites. In this study, Fourier transform near-infrared (FT-NIR) spectroscopy was applied to measure the water content of amine-epoxy neat resin. The method was developed and successfully extended to glass fiber-reinforced composite materials. Based on extensive measurements of neat resin and composite samples of varying water content and thickness, regression was performed, and the quantitative absorbance dependence on water content in the material was established. The mass of an absolutely dry resin was identified, and the true water content was obtained. The method was related to the Beer–Lambert law and explained in such terms. A detailed spectroscopic method for measuring water content in resins and fiber-reinforced composites was developed and described.

Keywords: epoxy; composites; water; NIR; spectroscopy

1. Introduction

Epoxy resins are widely used in composite materials (e.g., fiber-reinforced laminates), adhesives and surface coatings due to their relatively high strength, stiffness, low volatility and shrinkage during the curing process, as well as good adhesive properties. However, it is known that highly crosslinked amine-cured epoxy resins are hydrophilic, and their properties can significantly deteriorate upon water uptake [1–3]. It is well established that water uptake is an important factor in the performance and durability of epoxy-based composites, which undergo plasticization and swelling stresses [4].

Composite materials are often exposed to water or humid air environments. This is of special interest for offshore applications, since composites are widely used there due to their relatively light weight and high corrosion resistance, especially when compared to steel. Furthermore, the deep-water applications of composites have to be mentioned such as in, for example, risers and tethers [5]. It has been reported that water environments negatively impact the mechanical properties of such materials [6–12]. It is therefore of high importance to develop a water content monitoring method for such materials exposed to water environments.

Among the methods used for measuring the water content, such experimental techniques as thermogravimetry, differential scanning calorimetry (DSC), ultraviolet (UV) reflection spectroscopy, attenuated total reflection Fourier transform infrared spectroscopy (ATR-FTIR) and Fourier transform near-infrared spectroscopy (FT-NIR) have been reported [3,13–20]. The most common is a gravimetric method, which provides weight gain information upon water uptake or the weight loss upon drying. A significant drawback of the gravimetric method is the necessity to know the mass of the absolutely dry material, which in some cases requires long drying times and a complicated setup to obtain such data. Therefore, an alternative technique for measuring water content in epoxy resins and fiber-reinforced composites is required. NIR spectroscopy, e.g., FT-NIR, is a promising technique for water content monitoring [21–23]. Due to the high transmission of NIR light, its applicability to products with sizes in the mm range is usually possible [21].

It is common to report water content without accounting for moisture initially present in the material. In reality, some water is already present in the resin uptaken from the air, which has a certain humidity. The spectroscopic method provides a way to deduce the amount of water present initially in the material. Combining initial water content with that from water uptake experiments, the true water content is obtained. True water content and its determination are described further in the work. It is important to know the true water content when one has to look at strength, stiffness and fatigue property changes due to water content [24,25]. It was found that true water content at initial conditions is already 0.63% for the studied epoxy. These conditions are what would usually be denoted as a dry material. The true water content at saturation is 3.44%. Thus, the initial water content is significant and should not be neglected. The provided method allows determining and quantifying it.

Recent improvements of NIR spectrometers, resulting in a dramatic increase in their performance, e.g., acceleration of measuring time, have further lowered the threshold for using this method for process monitoring [21,22]. NIR has a broad range of practical applications, both in the laboratory and industry, the evaluation of diffusant content being one of those. For instance, NIR spectroscopy has long been used in such fields as medicine, food and polymers [21,26–28].

Multiple studies of water content evaluation in polymers have been reported. For example, Camacho et al. [26] and Kuda-Malwathumullage et al. [27] constructed NIR spectroscopic models for polyamides (Nylon 6,6), while Muroga et al. developed an NIR model for evaluating the water content of molded polylactide (PLA) under the effect of crystallization [21]. Studies on the determination of the water content of polymer/filler nanocomposites at variable relative humidity have been reported [29,30]. Use of spectroscopic methods for epoxies has also been reported, including use of FT-NIR to study epoxy network interactions with water molecules [15,17,31–34]. However, despite the described benefits of NIR spectroscopy, and specifically FT-NIR, and the mentioned relevant studies on epoxy-water interactions, the authors believe that a sufficiently detailed and simple-in-application method needs to be reported and discussed, allowing one to evaluate the water content in epoxy resin and epoxy-based composite samples of varying thickness and water content. Thus, the objective of this study is to establish such a model and provide the details of the method for its application in practice. Previous work has only been done on polymers, but not on fiber-reinforced composites. Such work on composites is seen as novel and important for industry. It has not been reported anywhere else to the best knowledge of the authors.

2. Experimental Section

2.1. Materials

Amine-cured epoxy: Amine-cured epoxy resin was prepared using reagents Epikote Resin RIMR 135 (Hexion, International: USA/Europe) and Epikure Curing Agent MGS RIMH 137 (Hexion, International: USA/Europe) in a ratio of 100:30 by weight. The mixture was degassed in a vacuum chamber for 0.5 h in order to remove bubbles. The sample mold was prepared using computer numerical control (CNC) machining. Degassed resin was then molded into rectangular-shaped

samples, followed by curing at room temperature for 24 h and post-curing in an air oven (Lehmkuhls Verksteder, Oslo, Norway) at 80 °C for 16 h. After samples were post-cured, the resin was removed from the mold's grooves and cut into the desired length with a vertical bandsaw. After cutting epoxy samples, the precise desired length was obtained by using sandpaper (FEPA P60, grain size 269 μm) to grind the edges. The prepared mold allows sufficient width control within a tolerance of 5%. In order to get samples to the right thickness and enable sufficient thickness control, a metal holder for grinding was prepared and used. The desired thickness was obtained using PHOENIX 2000 (Jean Wirtz, Dusseldorf, Germany) and SiC grinding discs (Struers, Cleveland, OH, USA; FEPA P500, grain size 30 μm). Exicator grease (Riedel-de Haën, Seelze, Germany) was used to enable sufficient adhesion of the sample with the holder. The sufficient thickness control, correct length and width were ensured within a 5% tolerance. Dog bone-shaped epoxy resin samples used in tensile tests were prepared in a similar way.

Composite laminates: Glass fiber-reinforced epoxy composite laminates were prepared using the vacuum-assisted resin transfer molding (VARTM) process. The composite laminate plate was turned into cylinders of a diameter of 20 mm. The cylinders were then cut into discs of a thickness slightly above 2 mm. The thickness was then adjusted to 2 mm within a 5% tolerance via grinding with a super fine sandpaper (FEPA P800, grain size 21.8 μm).

DI water: Deionized water (0.5–1.0 MΩ·cm) was used for water uptake measurements, produced via the water purification system Aquatron A4000 (Cole-Parmer, Vernon Hills, IL, USA).

2.2. Methods

Conditioning of resin and composite samples in water: Water uptake experiments were conducted using a batch system. A heated DI water (60 °C) bath was used for conditioning the samples. Samples were weighed using the analytical scales AG204 (±0.1 mg; Mettler Toledo, Columbus, OH, USA) in order to obtain the mass of the unconditioned samples and placed into the water bath. Samples were conditioned until equilibrium was achieved. Up to and at the saturation point, the samples were taken out of the water bath, weighed and analyzed with an FTIR spectrophotometer in order to obtain spectra at different water contents.

Drying of conditioned resin and composite samples: The drying of saturated samples was performed in a drying cabinet PK-410 (ESAB, London, UK) at 60 °C in air atmosphere with natural convection and relative humidity of 13 RH%.

Determination of resin fraction in composites: The density of neat epoxy resin (ρ_{resin}) and glass fiber (ρ_{glass}) was 1.1 g/cm^3 and 2.54 g/cm^3, respectively. The density of the composite (ρ_{comp}) was determined to be 1.97 g/cm^3 by measuring the mass and dimensions of a large composite block. The volume and mass fractions of neat resin were calculated using Equations (1) and (2), respectively.

$$V_{f_{resin}} = 1 - V_{f_{glass}} = 1 - \frac{\rho_{comp} - \rho_{resin}}{\rho_{glass} - \rho_{resin}} \tag{1}$$

$$m_{f_{resin}} = \frac{\rho_{resin} \cdot V_{f_{resin}}}{\rho_{resin} \cdot V_{f_{resin}} + \rho_{glass} \cdot \left(1 - V_{f_{resin}}\right)} \tag{2}$$

The volume and mass fraction of resin are $V_{f_{resin}} = 0.394$ and $m_{f_{resin}} = 0.220$, respectively.

FT-IR: Sample characterization with different water content was performed using Fourier transform infrared spectroscopy (FTIR) in the near-infrared range. Near-infrared spectra were obtained using the Fourier transform spectrophotometer NIRSystems 6500 (Foss, Eden Prairie, MN, USA) operated in transmission mode; an optical fiber probe and spectral analysis software Vision (Foss, Eden Prairie, MN, USA) were used. Spectra were taken in the Vis-NIR wavenumber range of 4000–25,000 cm^{-1} using 32 scans per spectrum with a resolution of 4 cm^{-1}. A spectrum of the driest (in this case, dried) sample was subtracted from the spectrum of the sample of interest. Then, the line connecting spectrum points at 5400 and 4900 cm^{-1} was constructed. The slope and the intercept of

this line were obtained. Subsequently, baseline correction was performed by subtracting the obtained line from the spectrum of interest.

Tensile tests: To evaluate the effect of water content on the ultimate tensile strength (UTS) of neat epoxy resin, tensile tests were conducted using the servo hydraulic test machine Instron Model 1342 (Instron, International: USA/UK). Dog bone-shaped epoxy resin samples were used in order to determine tensile strength; the rate was set to 1 mm/min of controlled displacement.

3. Results and Discussion

3.1. Water Uptake, Drying and Conditioning in Air Experiments of Neat Resin

The definition of water content in neat resin is described by Equation (3):

$$W(t) \equiv \frac{m(t) - m_{dried}}{m_{dried}} \cdot 100\% \tag{3}$$

where $m(t)$ is the mass of the wet neat resin; m_{dried} is the mass of the resin after drying.

Four samples of neat resin were used to obtain the water uptake and drying curves, as well as conditioning in air at room temperature back to initial water content; average values with standard deviations are reported. The curves are shown in Figure 1.
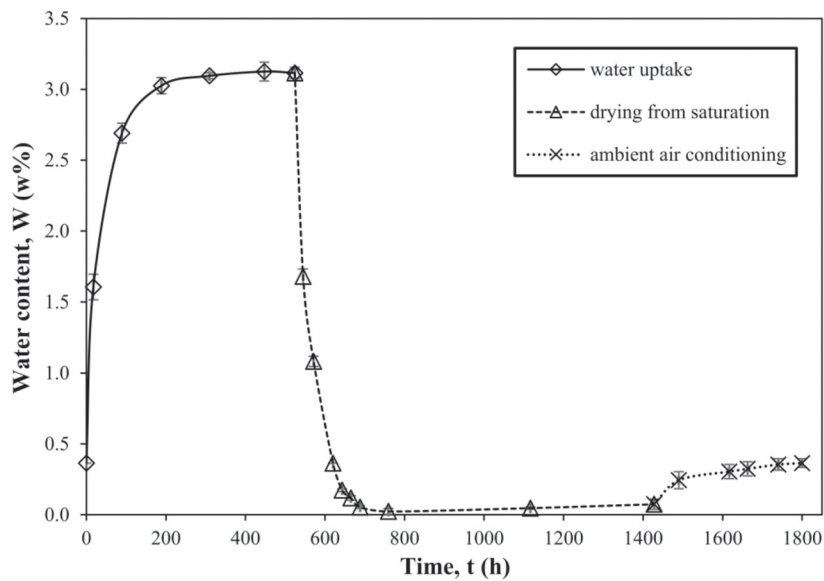
Figure 1. Water uptake, drying and conditioning in air curves of amine-cured epoxy resin.

3.2. Reversible Drop in Ultimate Tensile Strength of Neat Resin with Water Content

The ultimate tensile strength (UTS) was measured (1) for neat resin at initial conditions (in equilibrium with water vapor in ambient conditions), (2) for water-saturated resin and (3) for dried resin air-conditioned back to initial water content. The ultimate tensile strength (UTS) has decreased down to 80% of the initial dry value (from about 60 down to 48 MPa), as shown in Figure 2. Results indicate that the UTS of dried epoxy is comparable to that of the initial, indicating the reversibility of the drop in UTS. This aspect of reversibility is reported in greater detail elsewhere [24].
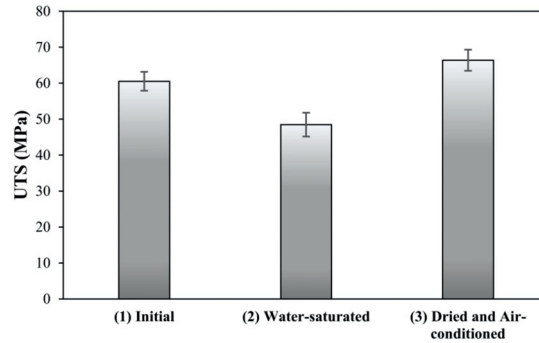
Figure 2. Water-induced drop in ultimate tensile strength (UTS) of amine-cured epoxy resin.

3.3. The Method for Monitoring Water Content in Neat Resin

The spectrum of a dried epoxy sample was obtained and is further denoted as the reference spectrum (the sample with the lowest water content available). The water (diffusant) absorption band's maximum was identified to be at about 5200 cm^{-1}. This band changed depending on the water content, as shown in Figure 3. Based on study by Falk et al. [35], this band corresponds to a combination mode of stretching and bending of the water molecule's OH group. This observation is also consistent with a recent study by Muroga et al. on spectroscopic evaluation of water content in polylactide (PLA) and with a novel work on water monitoring methods in PMMA by Wiedemair et al. [21,36]. Thus, this absorption band is chosen to monitor the water content of the epoxy resin. The wavenumber of the water absorption band shifts to lower values as the water content increases. True water content and the corresponding wavenumber values at the absorption peak are reported in Table 1.
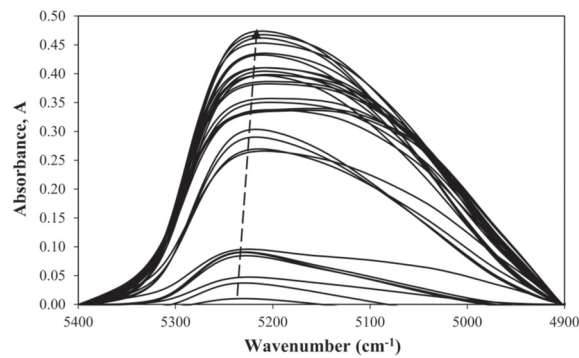
Figure 3. Difference of spectra with respect to the dried epoxy of the water absorbance band in epoxy resin samples of varying water content. The baseline corresponds to the driest sample (in this case, dried).

Table 1. True water content and the corresponding wavenumber values at the absorption peak.

True Water Content, W* (%)	Wavenumber (cm^{-1})
0.26	5230
0.61	5225
1.68	5219
1.88	5214
2.84	5214
2.94	5208
3.34	5208

The absorbance at the maximum of the water absorption band was quantified in the identified range. Absorbance values of the water band are comparable to those reported for studying water content in other polymeric systems [15,21]. The linear regression analysis (linear least square method) was then performed to obtain the equation $A = f(W)$. Based on 40 measurements, for the studied neat resin, the regression equation (Equation (4)) was obtained ($R^2 = 0.9466$):

$$A = 0.1248W + 0.0330 = K_{slope}^0 W + \beta \tag{4}$$

where 0.0330 is the intercept β and is due to the undried water content. Since the slope is the same for the undried water content $W_{undried\ water}$ as for the determined water content W, the relationship can be rewritten in the form of Equation (5).

$$A = K_{slope}^0 (W + W_{undried\ water}) \tag{5}$$

When W is equal to zero, absorbance is present because the samples are not fully dried. Thus, the intercept $W_{undried\ water}$ is due to the presence of water that was not removed during the drying process. This allows one to determine the amount of water present in the sample after drying, as shown by Equation (6), and to deduce how much water was in samples at equilibrium at ambient conditions if needed. Furthermore, this allows one to determine the mass of the absolutely dry material.

$$W_{undried\ water} = \frac{\beta}{K_{slope}^0} \tag{6}$$

In this case, the undried water content $W_{undried\ water}$ is equal to 0.26%, meaning that even after drying, there is still a significant amount of water present, which is supported by the observable water band in the IR spectra of dried samples. In order to calculate the mass of the absolutely dry neat resin $m_{absolutely\ dry}$ (Equation (8)), Equations (3) and (5) are used.

$$A = K_{slope}^0 \left(\frac{m(t) - m_{dried}}{m_{dried}} \cdot 100\% + \frac{W_{undried\ water} m_{dried}}{m_{dried}} \right) \tag{7}$$

$$m_{absolutely\ dry} = \left(1 - \frac{W_{undried\ water}}{100} \right) m_{dried} \tag{8}$$

This leads to a definition of the true water content. The true water content shows the amount of water with respect to the absolutely dry material and is defined as in Equation (9).

$$W^*(t) \equiv \frac{m_{water}(t)}{m_{absolutely\ dry}} \cdot 100\% = \left(\frac{m(t) - m_{absolutely\ dry}}{m_{absolutely\ dry}} \right) \cdot 100\% \tag{9}$$

The water content monitoring equation then can be written in the form of Equation (10).

$$A = K_{slope} W^* \tag{10}$$

The water content is then recalculated to obtain the true water content W^* as defined by Equation (9). The linear regression for $A = f(W^*)$ gives a similar slope (K_{slope} is equal to 0.1247) with a zero intercept to the initial result of $A = f(W)$ (K_{slope}^0 is equal to 0.1248). The determination coefficient is $R^2 = 0.9466$, which indicates that this model equation accounts for 89.61% of the variation in absorbance band maximum values in the dataset. The remaining 10.39% of variation not explained by the equation is expected to be due to the sample thickness having a tolerance of 5%, as well as some possible drying in air during the collection of spectra, since spectra are taken in ambient conditions at room temperature in air atmosphere. Such low variation even within a 5% thickness tolerance of samples indicates this method as being precise and efficient for monitoring water content of neat resin. Thus, this method

can be used as an indicator of the water concentration-dependent drop of the mechanical properties of the material.

3.4. Extension of the Method to Samples of Varying Thickness

Based on the Beer–Lambert law (Equation (11)), absorbance is dependent on the molar attenuation (absorption) coefficient (ε), concentration (c) and the path length (l).

$$A = \log_{10}\left(\frac{I_0}{I}\right) = \varepsilon c l \tag{11}$$

In our case, the concentration term is the true water content (W^*), and the path length is the thickness of the sample (δ). Thus, the Beer–Lambert law in our case can be expressed as Equation (12).

$$A = \varepsilon^* W^* \delta \tag{12}$$

Note that in this case, attenuation coefficient ε^* is not the same as a conventional molar attenuation coefficient ε, since the concentration term used is of true water content (W^*) and not of the molar concentration (c); thus, in order to avoid misunderstanding, in this work, the proportionality coefficient will be denoted as ε^*. However, calculation of the molar attenuation coefficient will be shown later in this work, as well. In practice, mass concentrations are easier to imagine and work with. However, conventionally, attenuation coefficients are given in molar units. Thus, a way to convert between mass and molar concentrations is provided.

Since the model is as shown in Equation (10), the thickness effect (path length) is contained in the slope term of the model equation (Equation (9)); thus, the slope term can be divided into the attenuation coefficient and the thickness. The new slope term is the attenuation coefficient and is obtained as shown in Equation (13).

$$\varepsilon^* = \frac{K_{slope}}{\delta} \tag{13}$$

In the case of resin, the water content monitoring equation (Equation (9)) then becomes Equation (12). The model in Equation (12) is validated by using water-saturated resin samples of varying thickness, e.g., by setting term W^* to a constant value, thus proving the linear dependence of absorbance on sample thickness (path length), as shown in Figure 4. The determination coefficient is $R^2 = 0.8480$.
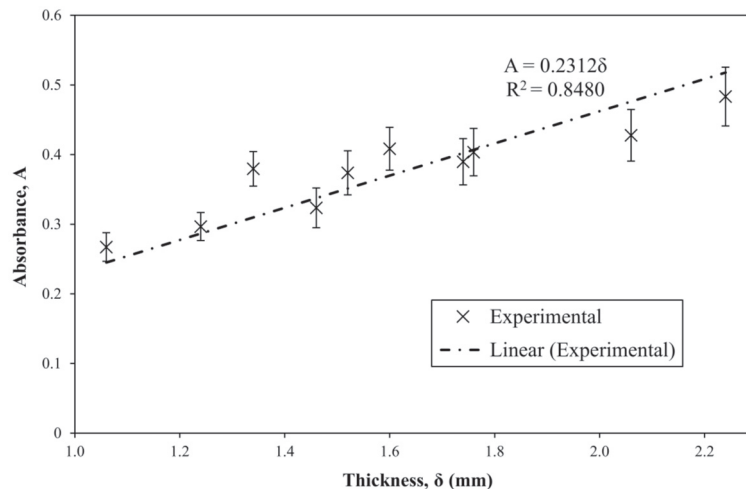

Figure 4. Linear dependence of absorbance on the sample thickness of water-saturated neat resin.

Based on the linear dependence of absorbance on sample thickness, for saturated samples $\varepsilon^* W_{max}^*$ equals 0.2312, and the attenuation coefficient is then $0.0672 \pm 0.0034\%^{-1} \cdot mm^{-1}$ ($R^2 = 0.8480$). Using model equation (Equation (10)), it is known that $\varepsilon^* \delta_{2\ mm}$ equals 0.1247. From this, taking into account a 5% thickness tolerance, the attenuation coefficient is $0.0624 \pm 0.0031\%^{-1} \cdot mm^{-1}$. The values are within the standard deviation. Since the attenuation coefficient ε^* in our case has units of $\%^{-1} \cdot mm^{-1}$, in order to obtain the molar attenuation coefficient ε, calculation of water molar concentration is required. Using the definition of true water content (Equation (9)), the relationship between the molar concentration of the diffusant (water) and the true water content can be written as Equation (14).

$$c(t) \left[\frac{mol}{L} \right] = \frac{\left[\frac{\frac{W^*(t)\ [\%]}{100} \cdot m_{absolutely\ dry}[g]}{M_{water} \left[\frac{g}{mol} \right]} \right]}{a \cdot b \cdot \delta\ [\text{mm}^3] \cdot 10^{-6} \left[\frac{L}{\text{mm}^3} \right]} \tag{14}$$

where a and b are length and width of the sample in mm, respectively.

Since thickness is the path length ($l = \delta$) and $\varepsilon c l = \varepsilon^* W^* \delta$ (Equations (11) and (12)), the molar attenuation coefficient can then be obtained from Equation (15).

$$\varepsilon = \frac{\varepsilon^* W^*}{c} \tag{15}$$

Since $\varepsilon^* W^*$ is found to be equal to $0.2312\ \text{mm}^{-1}$ for the resin of interest at full saturation ($W_{max}^* = 3.44\%$) for a sample of 2 mm in thickness, using Equation (14), the molar concentration is 2.29 ± 0.12 M, and using Equation (15), the molar attenuation coefficient ε is equal to $1.01 \pm 0.06\ \frac{L}{mol \cdot cm}$. The low value of the molar attenuation coefficient is explained by the fact that resin media has a relatively high light attenuation itself. Note that molar attenuation coefficient for water in epoxy media ε is obtained using the difference spectra with respect to the spectrum of the dried neat resin.

The authors have assessed the method in the thickness range from 1.06–2.24 mm. The authors expect that the method is applicable also to thinner samples. Extrapolation to samples thicker than 2.24 mm is not completely certain.

3.5. Extension of the Method to Composite Systems

In order to extend the method of monitoring water content to fiber-reinforced composites, the mass fraction of resin has to be known. For the studied glass-fiber reinforced composites, the resin mass fraction for samples at initial conditions ($m_{f_{resin_{initial}}}$) was determined as described earlier and is 0.2198. The resin mass fraction is used in order to deduce diffusant uptake by resin from the composite spectra. The proposed equation for monitoring the true water content due to exposure of composites to water media is represented by Equation (16).

$$A = \varepsilon^* W_{resin}^* \delta = K_{slope}\ W_{resin}^* \tag{16}$$

The definition of the water content in the composite material is described by Equation (17).

$$W_{comp} \equiv \frac{m(t) - m_{comp_{dried}}}{m_{comp_{dried}}} \cdot 100\% \tag{17}$$

The true water content of composites is defined by Equation (18).

$$W_{comp}^* \equiv \frac{m_{comp}(t) - m_{comp_{absolutely\ dry}}}{m_{comp_{absolutely\ dry}}} \cdot 100\% \tag{18}$$

An assumption is required that fiber is always dry (not absorbing water) and neglecting the influence of the sizing, since the mass of sizing is negligible compared to resin mass. This is, however,

not always fully true and is a convenient assumption. The mass of the composite is then as shown in Equation (19).

$$m_{comp_{dried}} = m_{resin_{dried}} + m_{fiber} \tag{19}$$

In order to prove that the assumption is valid in this case, that the increase in fiber or sizing mass is negligible due to water uptake, the water uptake using prepared composite discs was performed and scaled by the factor of the resin mass fraction of the composite. The comparison of the neat resin and the scaled composite water uptake graphs is represented in Figure 5.
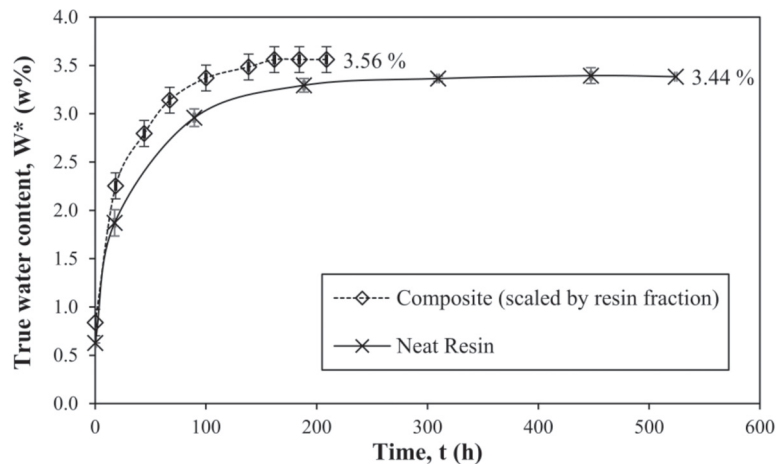

Figure 5. True water content curves of neat resin and glass fiber-reinforced composite (scaled by the resin mass fraction).

The shape of the kinetic curve is sample geometry-dependent and is slightly different in this case, as seen in Figure 5. However, the equilibrium water uptake value is a material property and can be used for the comparison. As seen in Figure 5, the equilibrium true water content value for a composite (scaled by resin mass fraction) is only slightly higher than that for the neat resin, resulting in a difference of 0.12% in true water content between average values. The difference can be explained due to the sizing also absorbing water. The authors believe that an increase of the true water content (at equilibrium) for the composite compared to the epoxy is increased due to the interactions of epoxy/fibers via the formation of the interphase. It is likely that what is measured is a sum of water content in both resin and the interphase. It has been reported that the interphase might be responsible for increased water uptake [37].

Thus, the assumption that only resin uptakes water is not completely true, but considering the relatively low difference, this is a reasonable approximation. Another aspect that might be causing the difference in the equilibrium water uptake value could also be the presence of voids in the composite, which is usually greater than in the neat resin due to the specifics of the impregnation process.

Use of such and approximation should be assessed in the case of other fiber-resin systems, since sizing can have a varying influence on the water uptake in different systems. For instance, in the case of carbon fiber-vinylester composites, it has been reported that the sizing affects the equilibrium water uptake of the composite significantly [37]. Thus, it has to be noted that the extension of the method might have limitations for certain composite systems.

Since the mass of water comes into the resin mass term, the mass fraction of resin is dependent on the water content and is defined as in Equation (20).

$$m_{f_{resin}}(t) \equiv \frac{m_{resin}(t)}{m_{resin}(t) + m_{fiber}} = \frac{m_{resin_{absolutely\ dry}} + m_{water}(t)}{m_{resin_{absolutely\ dry}} + m_{water}(t) + m_{fiber}} \tag{20}$$

In order to obtain the absolutely dry mass of the composite material, the set of Equations (21)–(23) is used.

$$m_{f_{resin_{dried}}} = \frac{m_{comp_{dried}} - \left(1 - m_{f_{resin_{initial}}}\right) \cdot m_{comp_{initial}}}{m_{comp_{dried}}} \tag{21}$$

$$m_{resin_{absolutely\ dry}} = m_{f_{resin_{dried}}} \cdot m_{comp_{dried}} \cdot \left(1 - \frac{W_{undried\ water}}{100}\right) \tag{22}$$

$$m_{comp_{absolutely\ dry}} = m_{resin_{absolutely\ dry}} + \left(1 - m_{f_{resin_{initial}}}\right) \cdot m_{comp_{initial}} \tag{23}$$

The true water content of the resin component in the composite can be calculated using Equation (24).

$$W_{resin}^* = \frac{m_{comp}(t) - \left(1 - m_{f_{resin_{initial}}}\right) \cdot m_{comp_{initial}} - m_{resin_{absolutely\ dry}}}{m_{resin_{absolutely\ dry}}} \cdot 100\% \tag{24}$$

Calculated W_{resin}^* is then to be used for predicting the water content, using Equation (25), analogous to the monitoring equation for neat resin (Equation (10)).

$$A = K_{slope}\ W_{resin}^* \tag{25}$$

In order to use the composite spectra for predicting W_{resin}^*, a factor for scaling from composites down to resin is required. Since composite materials have components of different absorbance, a normalization procedure is required. The composite absorbs light much more than the neat resin. There is a necessity to correct for the summary absorbance of the components via the baseline shift. In order to do so conveniently, two parameters need to be determined for the developed absorbance band maximum-based model: the maximum absorbance of the neat resin ($A_{peak_{resin}}$) and of the composite ($A_{peak_{comp}}$) at water saturation (at water uptake equilibrium values). These values are obtained using the difference spectra for respective fully-saturated materials as described earlier. In this case, the obtained values are $A_{peak_{resin}} = 0.47$ and $A_{peak_{comp}} = 0.044$. Note that due to the higher absorbance of the composite material, the absorbance of the water band deduced from the difference spectra is one order of magnitude lower than for the neat resin. In order to extend the model from neat resin to composites, we introduce the scaling factor, which is denoted as *Peak Factor* and defined as shown in Equation (26). In our case, it is equal to 0.094.

$$Peak\ Factor \equiv \frac{A_{peak_{comp}}}{A_{peak_{resin}}} \tag{26}$$

The final water content monitoring equation for the composite system can then be written in the form of Equation (27) if the effect of thickness is known and in the form of Equation (28) if the effect of thickness is not known.

$$A_{peak_{comp}} = \varepsilon^* \cdot Peak\ Factor \cdot \delta \cdot W_{resin}^* \tag{27}$$

$$A_{peak_{comp}} = K_{slope} \cdot Peak\ Factor \cdot W_{resin}^* \tag{28}$$

For the particular composite system of interest (glass fiber-reinforced amine-cured epoxy), the water monitoring equation is represented by Equation (29).

$$A_{peak_{comp}} = 0.012 \cdot W_{resin}^* \tag{29}$$

The model was validated by the experimental data using composite discs with a varying water content. The experimental data and predicted values (Equation (29)) are shown in Figure 6.
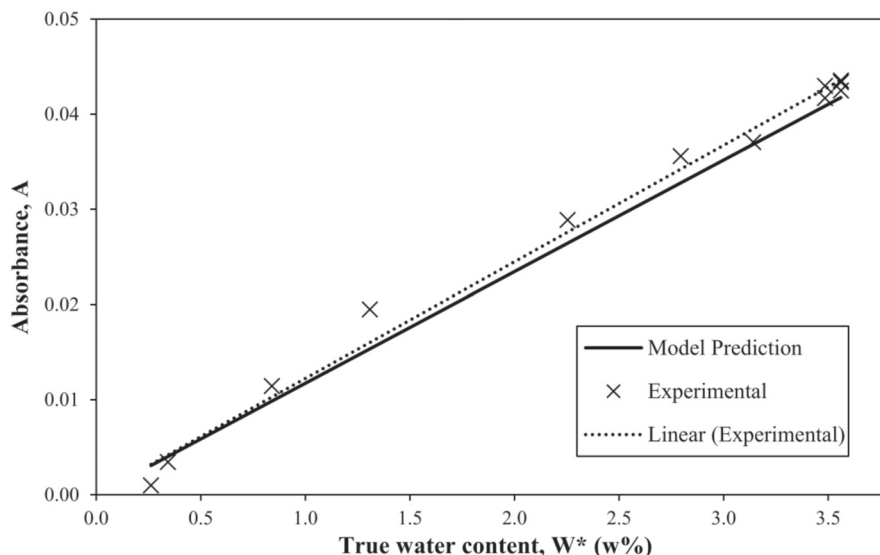

Figure 6. Validation of the water monitoring model extended to composites.

The fit between the final model and experimental data for composites resulted in a determination coefficient R^2 of 0.9329, meaning that the developed model accounts for 87.03% of the variation in the absorbance band's maximum values in the dataset. The best linear regression fit ($R^2 = 0.9908$) has only a slightly higher slope than the model, as shown in Figure 6.

3.6. Final Remarks on the Results

The developed method is potentially useful also for other polymers and composite systems with different fiber or resin fractions, as well as for diffusant media other than water. The developed method is based on the physics behind the Beer–Lambert law and can be used for samples of varying thickness. It should be noted, however, that the method has its limitations. If the sample is too thick or non-transparent in the studied radiation wavelength range, the method is not applicable, e.g., monitoring of carbon fiber-composite materials is expected to be limited.

The method can be used as an indicator of water-induced property changes in polymers and composites. While the drop in ultimate tensile strength (UTS) of the neat resin is reversible for the studied amine-cured epoxy resin, some types of fibers, such as glass fibers, are susceptible to irreversible degradation. Thus, in composites, the decline of UTS is not only water-concentration dependent, but also time-dependent. In cases when the material stays in the water environment during its working conditions, the driving force is always directed towards the drier interior of the material. In such cases, spectroscopic water content monitoring can provide valuable information about the interaction time of composite constituents (matrix, fibers, sizing) with the diffusant.

In practice, when the water content distribution in a composite structure is of interest, use of a transmittance FTIR is very limited. In order to become applicable for such cases, the following scenario is proposed. A replica of the structure parts, alongside the actual structure, should be immersed in water media at the same conditions. These replica parts then can be cut into samples of the thickness applicable for the method and analyzed. While destructive and requiring additional

expenses, the method can be a useful indicator of long-term water content and distribution in the composite structures, where such destructive tests might be required only once in tens of years.

Other spectroscopic methods such as Raman, while not as sensitive to water, and reflectance FTIR, while mostly providing information about the surface of the material, might also be considered in developing water monitoring methods, especially in cases when composites are non-transparent to the IR radiation.

4. Conclusions

In this study, a detailed method for estimating and monitoring water content in epoxy resins and fiber-reinforced composites was developed using the maxima of the absorbance band at about 5200 cm^{-1} in the NIR combination mode region correlated with the true water content. The method provides a benefit over the conventional gravimetric analysis providing the possibility to deduce the mass of an absolutely dry material and subsequently the true water content, which is an important indicator of water content-dependent properties. Based on extensive measurements of neat resin and composite samples of varying water content and thickness, regression was performed, and the quantitative absorbance dependence on water content in the materials was successfully established. The model equations for monitoring water content in epoxy resin and composite material samples were obtained and experimentally validated. The model was related to the Beer–Lambert law and explained in such terms. The details of the method were reported, allowing the use of the method in practical applications.

Author Contributions: Andrey E. Krauklis conceived of and designed the experiments. Andrey E. Krauklis and Abedin I. Gagani prepared the samples for experiments. Andrey E. Krauklis performed the experiments. Andrey E. Krauklis analyzed the data. Andrey E. Krauklis wrote the paper. Andreas T. Echtermeyer initiated the project. Abedin I. Gagani and Andreas T. Echtermeyer revised the work.

Conflicts of Interest: The authors declare no conflict of interest.

References

1. Li, L.; Yu, Y.; Wu, Q.; Zhan, G.; Li, S. Effect of Chemical Structure on the Water Sorption of Amine-Cured Epoxy Resins. *Corros. Sci.* **2009**, *51*, 3000. [CrossRef]
2. Lee, M.C.; Peppas, N.A. Water Transport in Epoxy-Resins. *Prog. Polym. Sci.* **1993**, *18*, 947.
3. Wang, J.; Gong, J.; Gong, Z.; Yan, X.; Wang, B.; Wu, Q.; Li, S. Effect of Curing Agent Polarity on Water Absorption and Free Volume in Epoxy Resin Studied by PALS. *Nucl. Instrum. Methods Phys. Res. B* **2010**, *268*, 2355. [CrossRef]
4. Morel, E.; Bellenger, V.; Verdu, J. Structure-Water Absorption Relationships for Amine-Cured Epoxy Resins. *Polymer* **1985**, *26*, 1719. [CrossRef]
5. Echtermeyer, A.T. Integrating Durability in Marine Composite Certification. In *Durability of Composites in a Marine Environment*; Davies, P., Rajapakse, Y.D.S., Eds.; Springer: Dordrecht, The Netherlands, 2014; pp. 179–194.
6. Weitsman, Y. Coupled Damage and Moisture-Transport in Fiber-Reinforced, Polymeric Composites. *Int. J. Solids Struct.* **1987**, *23*, 1003. [CrossRef]
7. Weitsman, Y.J.; Elahi, M. Effects of Fluids on the Deformation, Strength and Durability of Polymeric Composites—An Overview. *Mech. Time-Depend. Mater.* **2000**, *4*, 107. [CrossRef]
8. Roy, S. *Moisture-Induced Degradation in Long-Term Durability of Polymeric Matrix Composites*; Pochiraju, V.K., Tandon, P.G., Schoeppner, A.G., Eds.; Springer: Boston, MA, USA, 2012; pp. 181–236.

9.　Apicella, A.; Nicolais, L. Effect of Water on the Properties of Epoxy Matrix and Composite. *Adv. Polym. Sci.* **1985**, *72*, 69.

10.　Lefebvre, D.R.; Elliker, P.R.; Takahashi, K.M.; Raju, V.R.; Kaplan, M.L. The Critical Humidity Effect in the Adhesion of Epoxy to Glass: Role of Hydrogen Bonding. *J. Adhes. Sci. Technol.* **2000**, *14*, 925. [CrossRef]

11.　Guermazi, N.; Elleuch, K.; Ayedi, H.F. The Effect of Time and Aging Temperature on Structural and Mechanical Properties of Pipeline Coating. *Mater. Des.* **2009**, *30*, 2006. [CrossRef]

12.　Wu, C.F.; Xu, W.J. Atomistic Simulation Study of Absorbed Water Influence on Structure and Properties of Crosslinked Epoxy Resin. *Polymer* **2007**, *48*, 5440. [CrossRef]

13.　Bertolino, V.; Cavallaro, G.; Lazzara, G.; Merli, M.; Milioto, S.; Parisi, F.; Sciascia, L. Effect of the Biopolymer Charge and the Nanoclay Morphology on Nanocomposite Materials. *Ind. Eng. Chem. Res.* **2016**, *55*, 7373. [CrossRef]

14.　Ciprioti, S.V.; Tuffi, R.; Dell'Era, A.; Poggetto, F.D.; Bollino, F. Thermal Behavior and Structural Study of SiO_2/Poly(ε-caprolactone) Hybrids Synthesized via Sol-Gel Method. *Materials* **2018**, *11*, 275. [CrossRef]

15.　Mijović, J.; Zhang, H. Local Dynamics and Molecular Origin of Polymer Network−Water Interactions as Studied by Broadband Dielectric Relaxation Spectroscopy, FTIR, and Molecular Simulations. *Macromolecules* **2003**, *36*, 1279. [CrossRef]

16.　Philippe, L.V.S.; Lyon, S.B.; Sammon, C.; Yarwood, J. Validation of Electrochemical Impedance Measurements for Water Sorption into Epoxy Coatings Using Gravimetry and Infra-Red Spectroscopy. *Corros. Sci.* **2008**, *50*, 887. [CrossRef]

17.　Cotugno, S.; Mensitieri, G.; Musto, P.; Sanguigno, L. Molecular Interactions in and Transport Properties of Densely Crosslinked Networks: A Time-Resolved FT-IR Spectroscopy Investigation of the Epoxy/H_2O System. *Macromolecules* **2005**, *38*, 801. [CrossRef]

18.　Weir, M.D.; Bastide, C.; Sung, C.S.P. Characterization of Interaction of Water in Epoxy by UV Reflection Spectroscopy. *Macromolecules* **2001**, *34*, 4923. [CrossRef]

19.　Mijović, J.; Zhang, H. Molecular Dynamics Simulation Study of Motions and Interactions of Water in a Polymer Network. *J. Phys. Chem. B* **2004**, *108*, 2557. [CrossRef]

20.　MacQueen, R.C.; Granata, R.D. A Positron Annihilation Lifetime Spectroscopic Study of the Corrosion Protective Properties of Epoxy Coatings. *Prog. Org. Coat.* **1996**, *28*, 97. [CrossRef]

21.　Muroga, S.; Hikima, Y.; Ohshima, M. Near-Infrared Spectroscopic Evaluation of the Water Content of Molded Polylactide under the Effect of Crystallization. *Appl. Spectrosc.* **2017**, *71*, 1300. [CrossRef] [PubMed]

22.　Genkawa, T.; Watari, M.; Nishii, T.; Ozaki, Y. Development of a Near-Infrared/Mid-Infrared Dual-Region Spectrometer for Online Process Analysis. *Appl. Spectrosc.* **2012**, *66*, 773. [CrossRef] [PubMed]

23.　Ozaki, Y. Near-Infrared Spectroscopy—Its Versatility in Analytical Chemistry. *Anal. Sci.* **2012**, *28*, 545. [CrossRef] [PubMed]

24.　Krauklis, A.E.; Gagani, A.I.; Echtermeyer, A.T. Hygrothermal Aging of Amine Epoxy: Reversible Static and Fatigue Properties. *Polym. Test.* **2018**, submitted.

25.　Rocha, I.B.C.M.; Raijmaekers, S.; Nijssen, R.P.L.; van der Meer, F.P.; Sluys, L.J. Hygrothermal ageing behaviour of a glass/epoxy composite used in wind turbine blades. *Compos. Struct.* **2017**, *174*, 110. [CrossRef]

26.　Camacho, W.; Valles-Lluch, A.; Ribes-Greus, A.; Karksson, S. Determination of Moisture Content in Nylon 6,6 by Near-Infrared Spectroscopy and Chemometrics. *J. Appl. Polym. Sci.* **2003**, *87*, 2165. [CrossRef]

27.　Kuda-Malwathumullage, C.P.S.; Small, G.W. Determination of Moisture Content of Polyamide 66 Directly from Combination Region Near-Infrared Spectra. *J. Appl. Polym. Sci.* **2014**, *131*, 40645. [CrossRef]

28.　Zhou, G.X.; Ge, Z.; Dorwart, J.; Izzo, B.; Kukura, J.; Bicker, G.; Wyvratt, J. Determination and Differentiation of Surface and Bound Water in Drug Substances by Near Infrared Spectroscopy. *J. Pharm. Sci.* **2003**, *92*, 1058. [CrossRef] [PubMed]

29.　Cavallaro, G.; Lazzara, G.; Konnova, S.; Fakhrullin, R.; Lvov, Y. Composite films of natural clay nanotubes with cellulose and chitosan. *Green Mater.* **2014**, *2*, 232. [CrossRef]

30.　De Rodriguez, N.G.; Thielemans, W.; Dufresne, A. Sisal cellulose whiskers reinforced polyvinyl acetate nanocomposites. *Cellulose* **2006**, *13*, 261. [CrossRef]

31.　Musto, P.; Ragosta, G.; Mascia, L. Vibrational Spectroscopy Evidence for the Dual Nature of Water Sorbed into Epoxy Resins. *Chem. Mater.* **2000**, *12*, 1331. [CrossRef]

32.　Moy, P.; Karasz, F.E. Epoxy-Water Interactions. *Polym. Eng. Sci.* **1980**, *20*, 315. [CrossRef]

33. Zhou, J.M.; Lucas, J.P. Hygrothermal Effects of Epoxy Resin. Part I: The Nature of Water in Epoxy. *Polymer* **1999**, *40*, 5505. [CrossRef]

34. Barrie, J.A.; Sagoo, P.S.; Johncock, P. The Sorption and Diffusion of Water in Epoxy Resins. *J. Membr. Sci.* **1984**, *18*, 197. [CrossRef]

35. Falk, M.; Ford, T.A. Infrared Spectrum and Structure of Liquid Water. *Can. J. Chem.* **1966**, *44*, 1699. [CrossRef]

36. Wiedemair, V.; Mayr, S.; Wimmer, D.S.; Köck, E.M.; Penner, S.; Kerstan, A.; Steinmassl, P.-A.; Dumfahrt, H.; Huck, C.W. Novel Molecular Spectroscopic Multimethod Approach for Monitoring Water Absorption/Desorption Kinetics of CAD/CAM Poly(Methyl Methacrylate) Prosthodontics. *Appl. Spectrosc.* **2017**, *71*, 1600. [CrossRef] [PubMed]

37. Ramirez, F.A.; Carlsson, L.A.; Acha, B.A. Evaluation of Water Degradation of Vinylester and Epoxy Matrix Composites by Single Fiber and Composite Tests. *J. Mater. Sci.* **2008**, *43*, 5230. [CrossRef]

Appendix B

Paper II

Paper II

Article

Mechanism of Yellowing: Carbonyl Formation during Hygrothermal Aging in a Common Amine Epoxy

Andrey E. Krauklis * [ID] **and Andreas T. Echtermeyer**

Department of Mechanical and Industrial Engineering, Norwegian University of Science and Technology,
7491 Trondheim, Norway; andreas.echtermeyer@ntnu.no
* Correspondence: andrejs.krauklis@ntnu.no; Tel.: +371-26-810-288

check for
updates

Abstract: Epoxies are often exposed to water due to rain and humid air environments. Epoxy yellows during its service time under these conditions, even when protected from UV radiation. The material's color is not regained upon redrying, indicating irreversible aging mechanisms. Understanding what causes a discoloration is of importance for applications where the visual aspect of the material is significant. In this work, irreversible aging mechanisms and the cause of yellowing were identified. Experiments were performed using a combination of FT-NIR, ATR-FT-IR, EDX, HR-ICP-MS, pH measurements, optical microscopy, SEM, and DMTA. Such extensive material characterization and structured logic of investigation, provided the necessary evidence to investigate the long-term changes. No chain scission (hydrolysis or oxidation-induced) was present in the studied common DGEBA/HDDGE/IPDA/POPA epoxy, whilst it was found that thermo-oxidation and leaching occurred. Thermo-oxidation involved evolution of carbonyl groups in the polymeric carbon–carbon backbone, via nucleophilic radical attack and minor crosslinking of the HDDGE segments. Four probable reactive sites were identified, and respective reactions were proposed. Compounds involved in leaching were identified to be epichlorohydrin and inorganic impurities but were found to be unrelated to yellowing. Carbonyl formation in the epoxy backbone due to thermo-oxidation was the cause for the yellowing of the material.

Keywords: epoxy; yellowing; mechanism; thermo-oxidation; carbonyl formation; leaching

1. Introduction

Epoxy resins are used worldwide as adhesives, as matrices in composites, as surface coatings, as casting materials, and as laminating agents for artwork, longboards, and guitars [1–4]. Epoxies are also used extensively for glass conservation [5,6], as adhesives and gap-fillers [7,8], and in preservation of outdoor architectural and monumental stone as adhesives and as injection grouts for filling cracks, as well as consolidants for porous, fragile deteriorated stone [9]. In most of these applications, stability of color is of importance.

Epoxies are two-component systems consisting of an epoxy compound and a hardener, which react to form the cured network [8]. In this study, the network of interest contains two epoxy compounds (DGEBA and HDDGE) and two hardeners (IPDA and POPA). After reaction, a three-dimensional amine epoxy network is obtained [10]. Epoxy resin family covers a large diversity of polymer networks by the type of the epoxy compound and hardener employed. All these variations lead to a different final network formed, and affect its physical and chemical properties [8,11]. In addition, commercial products often contain such components as plasticizers, diluents, accelerators, and trace impurities, which can affect the final properties and the yellowing [8,9]. Whilst DGEBA constitutes more than 75% of the market [12], the number of articles concerning aging of this particular resin

(DGEBA/HDDGE/IPDA/POPA) is very limited [13,14]. Furthermore, yellowing is not investigated in any of them.

Epoxy resins are often exposed to water due to rain, humidity of the air, and in subsea and offshore applications [13,15]. In such conditions, water molecules can migrate into the polymer and may affect its properties, and lead to leaching [1,16]. Epoxies tend to yellow even at room temperature, even at medium humidity levels, with or without light exposure; it is a common observation [5,6,9]. However, light exposure can cause yellowing too, due to photo-yellowing (via photo-oxidation mechanism) [5,6,8,9,17]. In one study, it was observed that when exposed to high temperatures epoxy does not change its color in vacuum, while it does in air [18]. The yellowing phenomenon has often precluded wider use of epoxies in the various aforementioned applications [5,9]. However, studies on the yellowing of epoxy resins are few [5]. Furthermore, the identification of the mechanism of epoxy yellowing would be valuable in choosing suitable conditions, compounds or additives, for increasing service life of epoxies, i.e., in conservation [5,6].

Experimental evidence in this work was obtained using a combination of FT-NIR, ATR-FT-IR, EDX, HR-ICP-MS, pH measurements, optical microscopy, SEM, and DMTA. Such extensive material characterization, following the structured logic of investigation presented in this work, was novel and provided the necessary evidence to investigate the long-term changes in chemical structure of the studied resin.

The aim of this paper is to investigate the mechanistic origin of yellowing in a commonly used DGEBA/HDDGE/IPDA/POPA amine epoxy resin.

2. Theory

2.1. Irreversible Degradation Mechanisms

The hygrothermal process may involve both reversible and irreversible processes [19,20]. Irreversible changes persist even after redrying the material [13]. The resin yellows irreversibly, indicating that the mechanistic origin of the color change lies among irreversible degradation pathways.

The phenomenon of epoxy yellowing has been attributed to the photo-degradation of the amine hardener, to the degradation of the amine epoxy network itself via various pathways, to the degradation of additives or accelerators, and to the presence of impurities [9]. Degradation of the amine epoxy network may follow such pathways as chain scission, crosslinking between segments, and thermal and photo-oxidation of the main chains or sidegroups [18,21].

Irreversible aging mechanisms, which have been reported in the literature to occur during hygrothermal influence on general epoxies are [13,20,22,23]:

1.　Hydrolysis (involves chain scission)
2.　Thermo-oxidation (might involve chain scission, backbone modifications or crosslinking)
3.　Photo-oxidation (might involve chain scission, backbone modifications or crosslinking)
4.　Residual curing (additional crosslinking)
5.　Leaching (initially present additives, impurities or degradation products)

In this work, photo-oxidative effects were avoided by conducting experiments in the absence of high-intensity light sources [5,6]. For the studied material, no hydrolysis occurred [14]. To avoid residual curing, the material was fully cured as was indicated by the total disappearance of exothermal signal via differential scanning calorimetry (DSC) [4,24]. Two runs were performed: The first run was at 80 °C for 16 h, and the second heating cycle was performed at 80 °C for 1 h, showing that no further hardening occurs. Based on this, hydrolysis, photo-oxidation, and residual curing were excluded, whilst thermo-oxidation and leaching were investigated further, in respect to the yellowing.

2.2. Thermo-Oxidation and Leaching

The chemical mechanism of epoxy thermo-oxidation is convoluted, and the exact degradation chemistry remains the subject of ongoing work [25]. The process is complex as it involves oxygen diffusion and consumption, and a radical chain mechanism initiated by hydroperoxide decomposition [26]. The process seems to obey Arrhenius law, with activation energies around 60–80 kJ/mol, for various epoxies [25,26]. Thermo-oxidation may proceed differently for epoxies with different structures and flexibility of the chains [27].

Thermo-oxidation of amine epoxies follows a general autoxidation mechanism, in which the main source of radicals is the decomposition of hydroperoxides [4,25]. Processes often involved during oxidation are chain scission, carbonyl formation, double bond formation, and amide formation [4,11,23,28,29].

There is a limited number of articles regarding epoxy leaching [30–34]. Moreover, leaching behavior of DGEBA/HDDGE/IPDA/POPA epoxy is not investigated in any of them. The leaching phenomenon may occur due to initially present additives, impurities, or degradation products diffusing out from the epoxy network into the water environment, which is in contact with the polymer. Often but not always, it follows Fickian type diffusion [30]. Commonly reported epoxy leaching compounds are bisphenol A or epichlorohydrin [30–33]. The driving force of this process is expected to be due to the difference in concentration of these chemicals inside the resin, and in the aqueous environment.

3. Materials and Methods

3.1. Materials

Amine-cured epoxy resin was prepared by mixing reagents Epikote Resin RIMR 135 (Hexion, Columbus, OH, USA) and Epikure Curing Agent MGS RIMH 137 (Hexion, Columbus, OH, USA) stoichiometrically, in a ratio of 100:30 by weight. The mixture was degassed in a vacuum chamber for 0.5 h to remove bubbles. The samples were cured at room temperature for 24 h, and post-cured in an air oven (Lehmkuhls Verksteder, Oslo, Norway) at 80 °C for 16 h. Full cure was achieved as described above in Reference [24]. The samples were cast into rectangular moulds and then cut into $40 \times 7 \times 2$ mm^3 rectangular samples with a vertical bandsaw. Sample preparation was followed by grinding with sandpaper (FEPA P60, grain size 269 µm). The sample geometry was chosen in accordance with standard practice for glass transition temperature determination, as described in Reference [35]. The dimensions were achieved within 5% tolerance.

Resin and hardener (the epoxy system) consist of the following compounds: 0.63 wt % Bisphenol A diglycidyl ether (DGEBA; CAS 1675-54-3; number average molecular weight ≤ 700); 0.14 wt % 1,6-hexanediol diglycidyl ether (HDDGE; CAS 16096-31-4); 0.14 wt % poly(oxypropylene)diamine (POPA; CAS 9046-10-0; molecular weight 230); and 0.09 wt % isophorondiamine (IPDA; CAS 2855-13-2). Chemical structures of these compounds are shown in Figure 1.
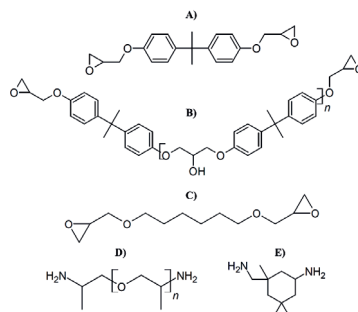

Figure 1. Molecular structures of epoxy and hardener components: (**A**) DGEBA monomer; (**B**) DGEBA oligomer (n = 1–2); (**C**) HDDGE; (**D**) POPA; (**E**) IPDA.

The distilled water (resistivity 0.5–1.0 mΩ·cm) was used for conditioning, produced via the water purification system Aquatron A4000 (Cole-Parmer, Vernon Hills, IL, USA). pH of distilled water was determined to be 5.65, being slightly acidic as water is equilibrated with the atmospheric CO_2.

3.2. Experimental Methods

3.2.1. Overview

The hygrothermal conditions provide means to the accelerated aging, to study the effect of thermo-oxidation and leaching on the yellowing of epoxy. As was mentioned elsewhere in Reference [36], aging studies are intended to accelerate the degradation chemistry. The experimental evidence on the irreversible degradation mechanisms was obtained and reported in this work.

The analysis of yellowing and morphological characterization was performed using a combination of visual inspection, optical microscopy, and scanning electron microscopy (SEM, Tescan, Brno, Czech Republic). Chemical composition and macromolecular changes were studied using a combination of FT-NIR, ATR-FT-IR, EDX, HR-ICP-MS, pH measurements, and DMTA.

3.2.2. Conditioning of Resin Samples in Distilled Water

Water uptake experiments were conducted using a batch system. A heated distilled water (60 ± 1 °C) bath was used for conditioning the samples. Samples were weighed using analytical scales AG204 (± 0.1 mg; Mettler Toledo, Columbus, OH, USA). Samples were conditioned for a period of two months. Samples were taken out of the water bath, weighed, and analyzed using a FT-NIR method [37].

3.2.3. Drying of Conditioned Resin Samples

The drying of saturated samples was performed in a drying cabinet PK-410 (ESAB, London, UK), at 60 ± 1 °C in air atmosphere, with natural convection and relative humidity of 13 RH%. After that, samples were reconditioned at ambient conditions in the air to regain their initial water content.

3.2.4. Optical Microscopy

Optical microscopy was performed using a digital microscope RH-2000 (Hirox, Tokyo, Japan), equipped with lens MXB-2500REZ, with a magnification of 140, and resolution of 1.06 μm.

3.2.5. SEM and EDX

Scanning electron microscopy (SEM) and Energy-dispersive X-ray spectroscopy (EDX) experiments were performed using Mira/LMU (Tescan, Brno, Czech Republic) in backscattered electron regime, with working voltage of 15 kV.

3.2.6. FT-NIR

Near-infrared (NIR) spectra were obtained using a Fourier transform spectrophotometer NIRSystems 6500 (Foss, Eden Prairie, MN, USA) operated in a transmission mode; an optical fiber probe and spectral analysis software Vision (Foss, Eden Prairie, MN, USA) was used. Spectra were taken in Vis-NIR wavenumber range of 4000–25,000 cm^{-1}, using 32 scans per spectrum with a resolution of 4 cm^{-1}.

FT-NIR spectroscopy was used to determine that the initial and redried epoxy has the same water content [37].

3.2.7. ATR-FT-IR

Fourier transform infrared (FT-IR) spectra were recorded using Scimitar 800 FT-IR (Varian, Inc., Palo Alto, CA, USA) in the Attenuated Total Reflectance (ATR) mode via GladiATR^{TM} (Pike

Technologies, Fitchburg, WI, USA). Spectra were obtained at 4 cm^{-1} resolution, co-adding 50 scans over a range of wavenumbers from 400 to 4000 cm^{-1}.

3.2.8. HR-ICP-MS

High resolution inductively coupled plasma mass spectrometry (HR-ICP-MS) analyses were performed using a double focusing magnetic sector field HR-ICP-MS Finnigan ELEMENT 2 (Thermo Fisher Scientific, International, Waltham, MA USA). A sample introduction system PrepFAST (ESI/Elemental Scientific, Omaha, NE, USA) was used. Pretreatment/digestion was done using UltraClave (Milestone, Milan, Italy). Acidification of samples was performed using ultra-pure grade HNO$_3$ SubPur (Milestone, Milan, Italy), to avoid adsorption of ions to the wall of the vial.

3.2.9. pH Measurements

pH measurements were performed using standard pH-meter MeterLab PHM210 (Radiometer analytical, Lyon, France) (pH $\pm$ 0.01). IUPAC standard buffer solutions (Radiometer analytical, Lyon, France) were used for calibration of pH meter.

3.2.10. DMTA

Dynamic Mechanical Thermal Analysis (DMTA) tests, for determination of glass transition temperature, storage, and loss moduli were conducted using a Netzsch GABO qualimeter Eplexor, equipped with a 1.5 kN load cell (Netzsch GABO Instruments, Ahlden, Germany) operated in displacement control with a constant static strain of 0.4%, and a cyclic strain of 0.1% applied with a frequency of 1 Hz. The temperature sweep range was from 20 up to 120 °C, with a heating rate of 1 °C/min. The glass transition temperature (T_g) was determined using DMTA as the crossing of tangents to the inflection points in the storage modulus curves [13,35].

4. Results

4.1. Discoloration and Changes in Morphology

A difference in color of unaged versus aged epoxy is shown in Figure 2. The discoloration persists even after drying and reconditioning in air. Thus, the change in color was irreversible.

Figure 2. Visual inspection of an epoxy resin showing discoloration due to hygrothermal aging. **Top**: initial (blueish grey); **bottom**: redried after conditioning (yellow).

Yellowing was not a surface phenomenon, since change in color occurred homogeneously in the bulk, as was suggested by uniform color in the cross-section of the sample cut in the middle. This agreed with an observation made in another study [5].

Digital optical and SEM micrographs indicated that there was no observable change in morphology after hygrothermal aging and reconditioning to the initial water content, as shown in Figure 3. Surface morphology was studied for both aged and unaged material. It showed no significant changes. No pores or cavities were observed, suggesting no loss of polymer from the surface.
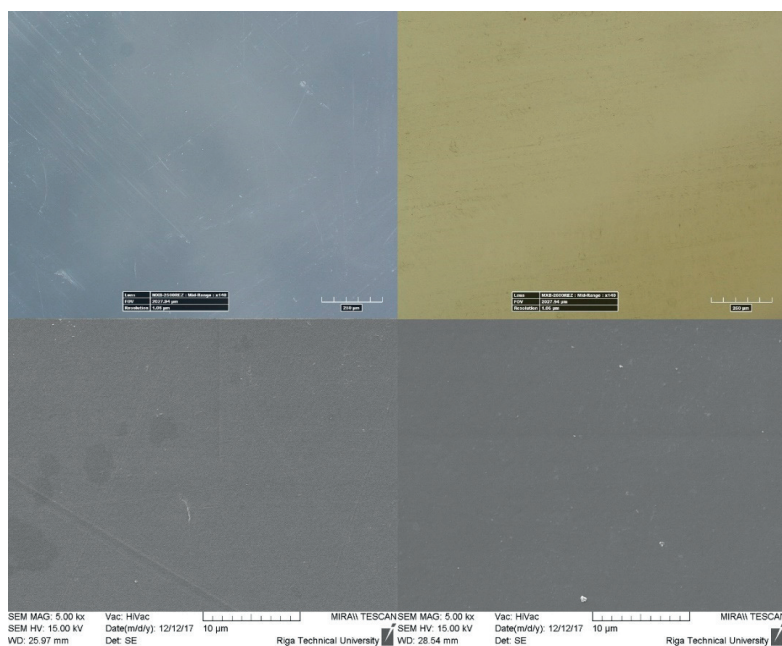
Figure 3. Digital optical (**top**) and SEM (**bottom**) micrographs of initial dry (**left**) and redried after hygrothermal aging (**right**).

4.2. Changes in Chemical Composition

Obtained FT-NIR spectra of initial epoxy and resin redried to initial water content are shown in Figure 4.
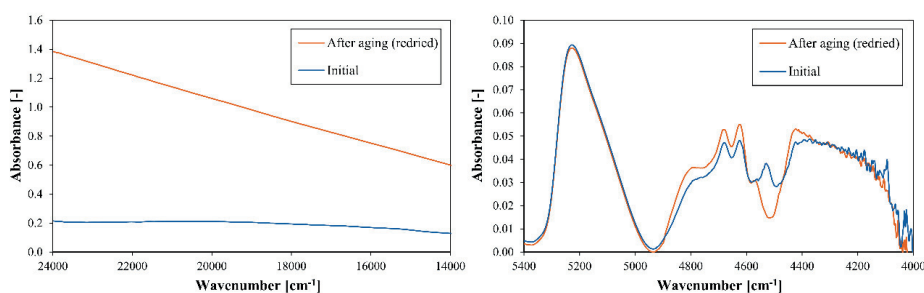
Figure 4. FT-NIR spectra of initial resin and redried epoxy after hygrothermal aging. (**Left**): visible light region. (**Right**): NIR region.

Visible light region spectra indicated clearly, the yellowing and reduced transparency of the aged epoxy. In the NIR region of the spectra, both initial and redried epoxy after aging were similar with an exception of the peak at around 4535 cm^{-1}, which corresponds to the epoxy ring [38]. It was observed that after hygrothermal aging, this peak had reduced dramatically, indicating that

a compound, containing an epoxy ring, either leached or reacted. Since the resin was fully cured, the authors believe this peak corresponded to the leached unreacted epichlorohydrin, which contained an epoxy ring in its chemical structure. This claim was further supported with EDX and HR-ICP-MS.

Obtained ATR-FT-IR spectra of the initial dry epoxy and epoxy after hygrothermal process, drying and conditioning in air to initial water content, are shown in Figure 5.
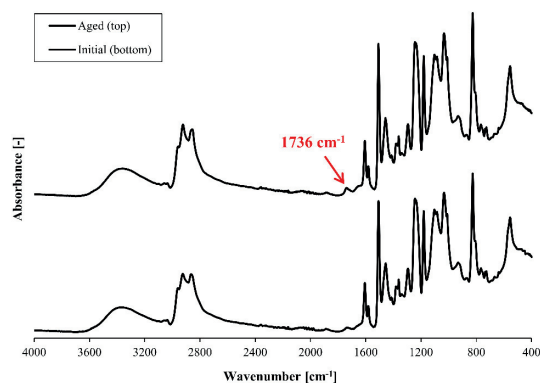
Figure 5. ATR-FT-IR spectra of initial (**bottom**) and redried after hygrothermal process resin (**top**).

Obtained spectra indicated that there was no significant difference observed in chemical structure of the initial and dried samples, except for the peak at 1736 cm^{-1}, corresponding to carbonyl groups (νC=O) [4,8,10,28,39,40].

Elemental analysis via EDX indicated that initial dry epoxy had a higher content of Cl (0.99 $\pm$ 0.08 Cl%) than epoxy, after hygrothermal aging (0.73 $\pm$ 0.05 Cl%). This suggested leaching of chlorine-containing compounds from the resin into water during hygrothermal aging. This could be due to unreacted epichlorohydrin being released, which comes from the epoxy component. Moreover, oxygen content in the aged epoxy (23.59 $\pm$ 0.42 O%) was lower than in the initial one (24.35 $\pm$ 0.45 O%), indicating most likely a leaching of an epoxy ring-containing compound, such as unreacted epichlorohydrin.

Elements (Ca, K, Na, Cl, S) were identified to be leached by the resin into contacting water during hygrothermal aging using HR-ICP-MS. The element release curves are shown in Figure 6, with Cl release being dominant.
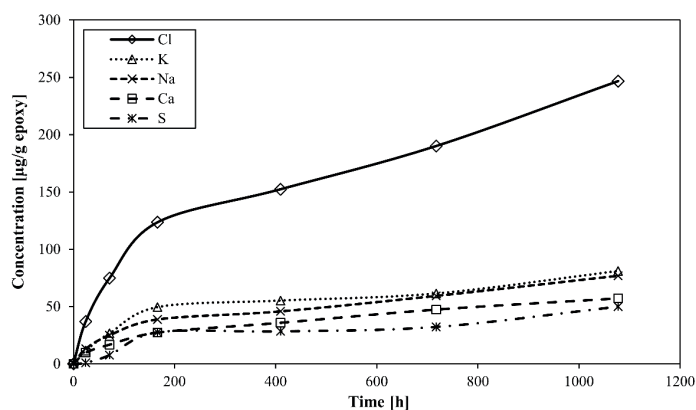
Figure 6. Ca, Cl, K, Na and S release from neat resin during hygrothermal aging at 60 °C.

pH measurement results of the water (50 mL samples) in contact with the resin during hygrothermal aging are shown in Figure 7. There was a strong initial decrease in pH upon contact of the dry resin with distilled water. The authors believe this could be related to a release of acidic impurities from the resin, i.e., HCl.
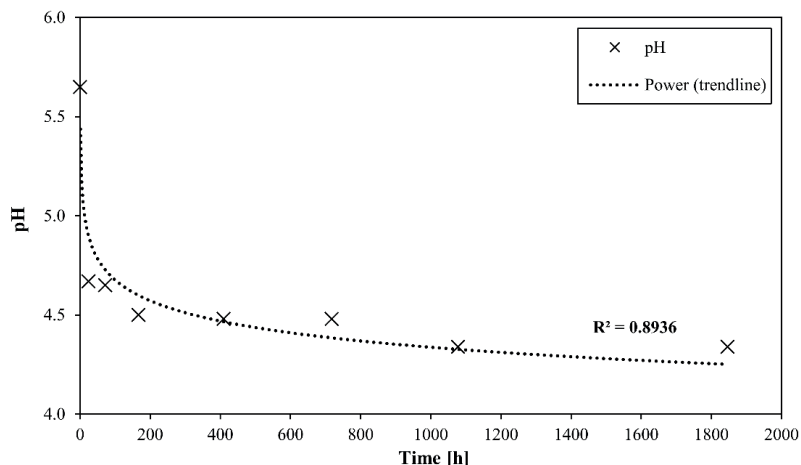
Figure 7. pH measurements of distilled water samples after contact with the resin.

The changes at macromolecular scale have been investigated by T_g change. The glass transition temperature (T_g) of the initial, saturated, and redried epoxy was 81.7, 59.1, and 84.7 °C, respectively. T_g for saturated epoxy was much lower than for the dry and dried resin, due to plasticization [14]. The T_g of a redried epoxy was slightly higher than that of initial resin. In case of chain scission, a T_g value would have decreased [41], which was not observed. A slight increase in T_g of the dried material was likely due to polymer relaxation [13], minor thermo-oxidative crosslinking [7,27], or leaching of plasticizing compounds. The tensile storage and loss moduli in a temperature sweep range from 20 to 120 °C are presented in Figure 8.
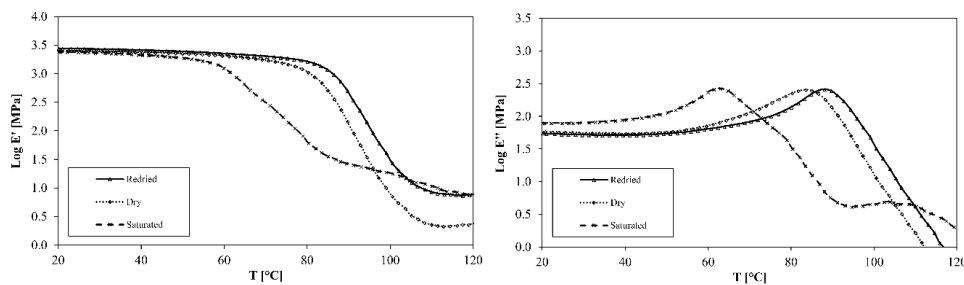
Figure 8. Temperature sweep for glass transition temperature determination for initial (dry); saturated; and redried. (**Left**): temperature sweep of tensile storage modulus. (**Right**): temperature sweep of tensile loss modulus.

5. Discussion

5.1. Logic of the Investigation

The logic which is followed in this study is shown schematically in Figure 9.
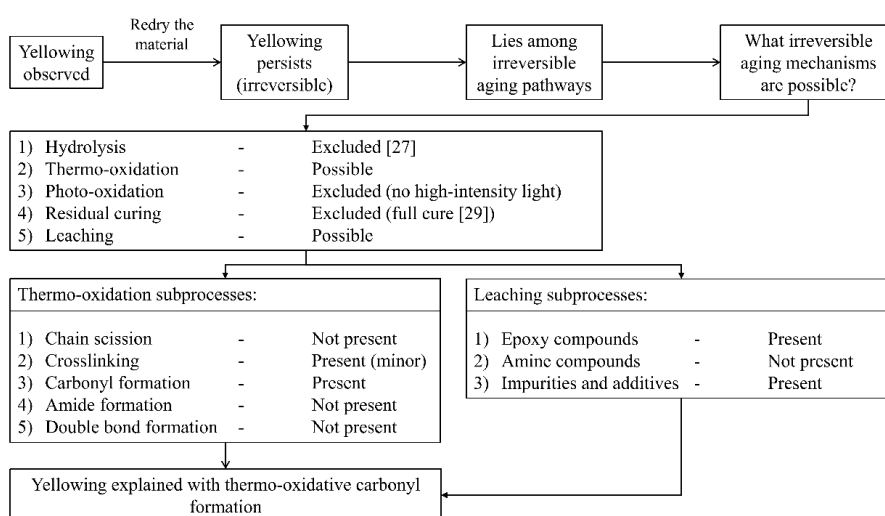
Figure 9. Schematic representation of the logic during investigation.

5.2. Leaching

There are three types of leaching that are potentially possible: (1) Leaching of hardener; (2) leaching of epoxy compounds; and (3) leaching of impurities or additives.

In theory, it is possible that some amount of unreacted hardener (blue in color), since soluble in water, would be washed out from crosslinked polymer network, or would be used up in additional crosslinking. The initial uncured epoxy resin is yellowish in color, which could explain the yellowing of the product over time [42]. The residual crosslinking, can also cause the decrease in unreacted amine group concentration causing the change in color [13], but this was not the case since the material was fully cured. Hardener leaching was not present, as supported by ATR-FT-IR. If the hardener washout or residual crosslinking was the case, it would show a decrease in peak intensity at wavenumber corresponding to unreacted amine groups at 3200–3500 cm^{-1} [43], which was not observed in the ATR-FT-IR spectra. It should also be noted that any changes to the epoxy material below IR sensitivity cannot be detected.

Whilst it was found that leaching of hardener is improbable, leaching of chemicals that are initially present in epoxy resin, such as epichlorohydrin, was found likely, using a combination of EDX, HR-ICP-MS, and FT-NIR. Based on the HR-ICP-MS data and FT-NIR intensity of the corresponding peak at 4535 cm^{-1}, the leached amount of epichlorohydrin was estimated to be 75 μg/g of resin, and the initial concentration of epichlorohydrin in the resin was estimated to be 137 μg/g.

HR-ICP-MS showed leaching of Cl-containing compounds or chloride ions. It should be noted that the DGEBA epoxy component itself, is a product of O-alkylation of Bisphenol A and epichlorohydrin. Upon such reaction, HCl is released. However, the reaction is conducted in the presence of sodium hydroxide NaOH, meaning that HCl is being neutralized [44]. It is possible that some of the Cl compounds, i.e., NaCl, unneutralized HCl or unreacted epichlorohydrin, were present in the initial dry resin. It is likely that these compounds were washed out from the epoxy system during hygrothermal aging. Furthermore, the pH measurements (Figure 7) indicate a release of acidic compounds from the resin, i.e., HCl.

To sum up, the leaching of hardener was not observed, whilst the leaching of epoxy compounds, such as epichlorohydrin, and leaching of impurities, such as HCl and NaCl, was present.

5.3. Thermo-Oxidation

Thermo-oxidation is highly selective [45], and the main source of radicals is the decomposition of the most thermally unstable chemical species [26]. Each carbon atom in α position of an electronegative atom, such as O and N, has a decreased dissociation energy and increased reactivity in the radical chain propagation, thus resulting in "weak points" in the network structure [4,28].

Increase in the intensity of the carbonyl group peak (νC=O; 1730–1740 cm^{-1}) [4,8,10,28,39,40], for aged epoxy, is related to an oxidation process taking place. Carbonyl formation can result from various pathways [28]. Thermo-oxidation involving chain scission and appearance of double bonds; carbonyl and amide species have been reported in DGEBA/IPDA and DGEBA/POPA systems [4,21,41]. Appearance of diphenylketones was reported in another work [46]. In this work, the appearance of amide species (C=O; 1644 cm^{-1} and N-H; 3325 cm^{-1}) [8,43] and diphenylketones (C=O; 1660 cm^{-1}) [46] due to thermo-oxidation was not observed. Double bond formation was not observed, as indicated by C=C bands close to 1600 cm^{-1} (1624 cm^{-1} and 1593 cm^{-1}) [28].

Chemical structure of a cured amine epoxy network (not considering the mixing proportions), is shown in Figure 10. "Weak points" for radical attack in the network were identified and are shown in Figure 10. In the network, 12 unique sites potentially involved in thermo-oxidation were found. Furthermore, 8 of these sites were excluded based on experimental evidence and literature. Sites marked in green were the identified main reactive sites (δ^+DGEBA-II, δ^+POPA-I, δ^+HDDGE-III, and δ^+HDDGE-IV).
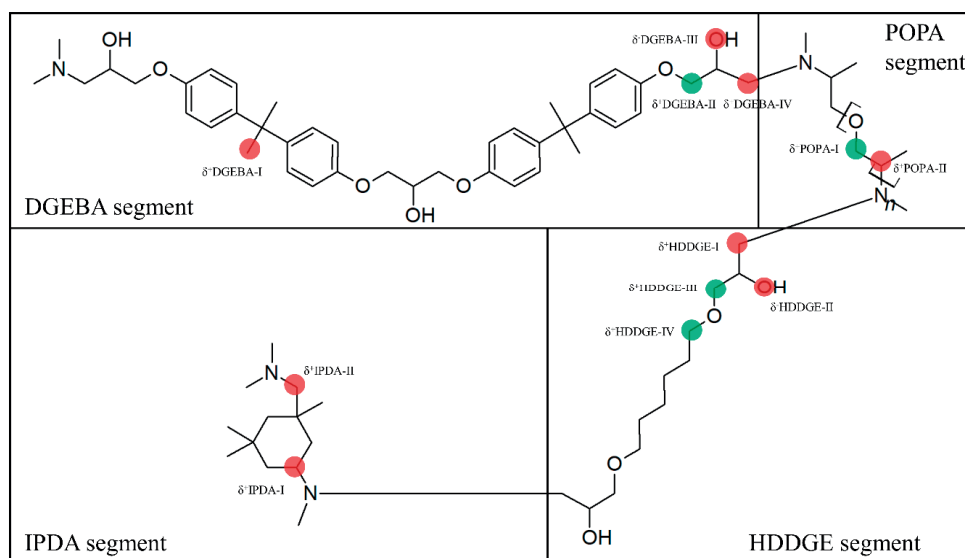
Figure 10. Chemical structure of the studied DGEBA/HDDGE/IPDA/POPA amine epoxy network (mixing ratios are not considered). Marked sites represent "weak points" for radical attack in the network. Sites marked in red are excluded based on experimental evidence and literature. Sites marked in green are the main reactive sites.

T_g can be regarded as a useful parameter revealing chemical changes for polymers [47]. The T_g of a redried epoxy (84.7 °C) was slightly higher than for the initial material (81.7 °C), indicating that no chain scission occurred [7,41]. A likely reason of a T_g increase was a combination of polymer relaxation [13], anti-plasticizing effect of leaching, and a minor crosslinking [7,27] of the HDDGE segments (site δ^+HDDGE-IV). The thermo-oxidative crosslinking mechanism has been reported for

an amine epoxy with a curing agent DGEBU similar to HDDGE in another work [27]. An analogous crosslinking mechanism of HDDGE segments is proposed in Scheme 1, involving sites δ^+HDDGE-IV.
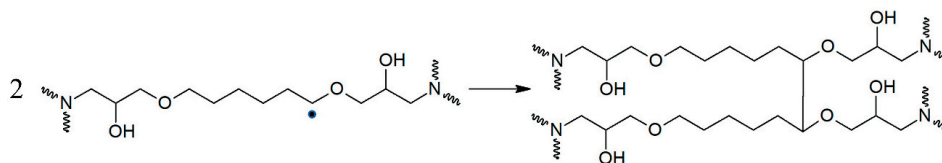
Scheme 1. Crosslinking reaction of the HDDGE segments via reactive sites δ^+HDDGE-IV.

The only way to form amides is an oxidation of amino methylenes near to network nodes [28]. There was no increase in intensity of the bands corresponding to amide species (C=O; 1644 cm^{-1} and N-H; 3325 cm^{-1}) [8,43]. This excluded the following "weak points" as potential reactive sites: δ^+DGEBA-IV, δ^+POPA-II, δ^+HDDGE-I, δ^+IPDA-I, and δ^+IPDA-II. Moreover, the formation of amide species is linked to chain scission, which was not present, as indicated by T_g measurements.

The linkage between the aromatic rings may also be sensitive to oxidation [10,25]. Carbonyl formation via acetophenone groups due to radical attack on δ^+DGEBA-I site was not observed, as indicated by the absence of the increase of the acetophenone "in-chain" group band (1684 cm^{-1}) [10] and diphenylketones (C=O; 1660 cm^{-1}) [46].

The formation of carbonyl groups may result from oxidation of the secondary alcohol groups in cured resin [28,46]. This oxidation process is accompanied by the decrease of the band at 1237 cm^{-1}, representing the characteristic C-O band in secondary alcohol groups [46]. No changes to this band were observed, which excluded the following "weak points" as potential reactive sites: δ^-DGEBA-III and δ^-HDDGE-II. Furthermore, in the hydroxyl domain ($\approx$3800–2500 cm^{-1}) [10] no changes were observed, which further supported this conclusion.

Noteworthy that all three reactive sites (δ^+DGEBA-II, δ^+POPA-I, and δ^+HDDGE-III) involved in carbonyl formation have similar structures. Whilst δ^+POPA-I contains the polyoxypropylene moiety, the other two sites (δ^+DGEBA-II and δ^+HDDGE-III) are identical and contain the *i*-propanol moiety.

δ^+POPA-I site as a polyoxypropylene moiety-containing segment is very susceptible to radical attack under oxidation, due to low stability of the tertiary C-H bond and the destabilizing effect of the neighboring ether group [10,41]. The proposed carbonyl formation reaction on this site is shown in Scheme 2.
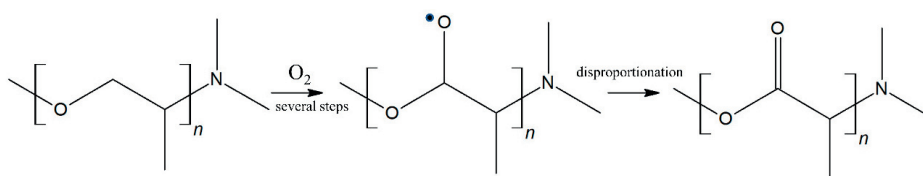
Scheme 2. Carbonyl formation involving polyoxypropylene moiety on reactive site δ^+POPA-I.

The δ^+DGEBA-II and δ^+HDDGE-III sites as *i*-propanol moiety-containing segments are also highly susceptible to oxidation [4,28]. The carbonyl formation on these two sites follows the same reaction, as shown in Scheme 3 [28].

Contrary to the DGEBA/IPDA and DGEBA/POPA binary amine epoxies [4,21,42], the results suggest that a combination of DGEBA/HDDGE/IPDA/POPA stops the oxidative chain scission and amide formation. It is not clear what exactly causes such change, but it is possible that some of the identified reactive sites operate as weak "sacrificial" centers, as suggested in another work [17], thus protecting the remaining structure.

To sum up, the results indicated that there was no chain scission, double bonds and amide groups were not formed, whilst the evolution of carbonyl groups in the macromolecular backbone and minor crosslinking of HDDGE segments occurred.
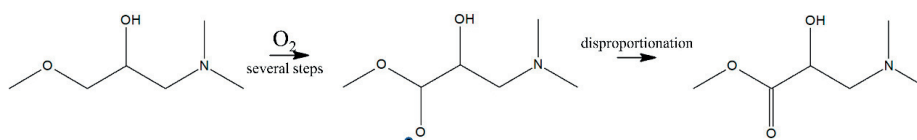
Scheme 3. Carbonyl formation reaction involving *i*-propanol moiety on reactive sites δ^+DGEBA-II and δ^+HDDGE-III.

5.4. The Cause of Yellowing

The change in color is irreversible, and is related to the irreversible aging mechanism. Two irreversible phenomena were identified: (1) Leaching of an epoxy compound epichlorohydrin and impurities, i.e., HCl and NaCl; (2) Formation of carbonyl groups C=O in the polymeric backbone due to thermo-oxidation (sites δ^+DGEBA-II, δ^+POPA-I, and δ^+HDDGE-III, shown in Figure 10). Both impurities and epichlorohydrin are colorless and do not cause discoloration. The oxidative evolution of carbonyl groups in the resin was the reason for the yellowing. It has been reported for other polymers that carbonyl formation can cause a change in color [48,49]. Furthermore, the yellowing phenomenon of a polyurethane resin was found to be linked to the mechanism of carbonyl formation in the macromolecular backbone, caused by oxidation [49].

5.5. Increasing Epoxy Service Life

Yellowing of the studied epoxy was linked to the formation of carbonyl groups in the macromolecular backbone. Based on other studies [25,50,51], conclusion can be drawn that carbonyl formation can be slowed down by using phenolic antioxidants, such as hindered phenols, which are used as stabilizers for various plastics and rubbers [50,51]. These compounds act as radical scavengers and can prevent thermo-oxidative yellowing. An effective way of introducing stabilization for epoxies, when mechanical properties are not concerned, is a co-curing procedure of epoxy with resole, which has hindered phenol moieties [50,51].

5.6. On the Similarity of Yellowing and Thermo-Oxidation Kinetics

Kinetics of epoxy yellowing and thermo-oxidative carbonyl formation found in literature, undoubtedly show common trends [6,25,28,41].

Yellowing of epoxies is not linear in time and is characterized by three stages [6]: (1) The induction period with little or no yellowing [6]; oxidation kinetics also display an induction period with a strongly auto-accelerated character [28]; (2) The steady state period, during which yellowing is high and constant [6]; (3) The declining rate period, during which the increase in yellowing is occurring at a slower rate [6], which is in agreement with another study on thermo-oxidation, stating that high oxidation levels can result in reduced sensitivity to further oxidation [25]. In the long term, in some cases, there is a horizontal asymptote in carbonyl formation kinetics, indicating equilibrium or a saturation phase, but it is not systematically observed [41]. The kinetics have a strong dependence on temperature and presence of antioxidants [28]; the kinetics follow the Arrhenius principle over a wide temperature range [25,26].

6. Conclusions

This work discussed the mechanism of yellowing of a DGEBA/HDDGE/IPDA/POPA amine epoxy. Based on the results of FT-NIR, ATR-FT-IR, EDX, HR-ICP-MS, pH measurements, optical microscopy, SEM, and DMTA, the following conclusions have been made:

1. Yellowing occurred due to the thermo-oxidative carbonyl formation in the epoxy carbon-carbon backbone via nucleophilic radical attack. The change in color was irreversible. Morphology was found to be unaffected.
2. No chain scission (hydrolysis or oxidation-induced) was present, whilst thermo-oxidation and leaching occurred.
3. Compounds involved in leaching were identified to be epichlorohydrin and inorganic impurities but were unrelated to yellowing.
4. Four unique reactive sites responsible for thermo-oxidation were found. One reactive site was involved in minor thermo-oxidative crosslinking of the HDDGE segments, while three other sites were linked to carbonyl formation. Noteworthy that all three sites involved in carbonyl formation had similar structures, containing highly reactive polyoxypropylene and *i*-propanol moieties. Respective reactions were proposed.
5. It is speculated that yellowing could be prevented or delayed by adding phenolic antioxidants, such as hindered phenols.

Conflicts of Interest: The authors declare no conflict of interest.

References

1. Maggana, C.; Pissis, P. Water sorption and diffusion studies in an epoxy resin system. *J. Polym. Sci. Part B* **1999**, *37*, 1165–1182. [CrossRef]
2. Popineau, S.; Rondeau-Mouro, C.; Sulpice-Gaillet, C.; Shanahan, M.E.R. Free/Bound water absorption in an epoxy adhesive. *Polymer* **2005**, *46*, 10733–10740. [CrossRef]
3. Chiang, C.-L.; Ma, C.-C.M.; Wang, F.-Y.; Kuan, H.-C. Thermo-oxidative degradation of novel epoxy containing silicon and phosphorous nanocomposites. *Eur. Polym. J.* **2003**, *39*, 825–830. [CrossRef]
4. Ernault, E.; Richaud, E.; Fayolle, B. Thermal oxidation of epoxies: Influence of diamine hardener. *Polym. Degrad. Stab.* **2016**, *134*, 76–86. [CrossRef]
5. Down, J.L. The Yellowing of Epoxy Resin Adhesives: Report on High-Intensity Light Aging. *Stud. Conserv.* **1986**, *31*, 159–170. [CrossRef]
6. Down, J.L. The yellowing of epoxy resin adhesives: Report on natural dark aging. *Stud. Conserv.* **1984**, *29*, 63–76.
7. Coutinho, I.; Ramos, A.M.; Lima, A.M.; Fernandes, F.B. Studies of the degradation of epoxy resins used for the conservation of glass. In Proceedings of the Holding it all together, Ancient and Modern Approaches to Joining, Repair and Consolidation, London, UK, 21–22 February 2008. [CrossRef]
8. Tennent, N.H. Clear and Pigmented Epoxy Resins for Stained Glass Conservation: Light Ageing Studies. *Stud. Conserv.* **1979**, *24*, 153–164.
9. Ginell, W.S.; Coffman, R. Epoxy resin-consolidated stone: Appearance change on aging. *Stud. Conserv.* **1998**, *43*, 242–248.
10. Mailhot, B.; Morlat-Thérias, S.; Ouahioune, M.; Gardette, J.-L. Study of the Degradation of an Epoxy/Amine Resin, 1 Photo- and Thermo-Chemical Mechanisms. *Macromol. Chem. Phys.* **2005**, *206*, 575–584. [CrossRef]

11. Ernault, E.; Richaud, E.; Fayolle, B. Origin of epoxies embrittlement during oxidative ageing. *Polym. Test.* **2017**, *63*, 448–454. [CrossRef]

12. Pham, H.Q.; Marks, M.J. Epoxy resins. In *Ullmann's Encyclopedia of Industrial Chemistry*; Wiley-VCH: Weinheim, Germany, 2005; pp. 155–244.

13. Rocha, I.B.C.M.; Raijmaekers, S.; Nijssen, R.P.L.; van der Meer, F.P.; Sluys, L.J. Hygrothermal ageing behaviour of a glass/epoxy composite used in wind turbine blades. *J. Compos. Struct.* **2017**, *174*, 110–122. [CrossRef]

14. Krauklis, A.E.; Gagani, A.I.; Echtermeyer, A.T. Hygrothermal Aging of Amine Epoxy: Reversible Static and Fatigue Properties. *Open Eng.* **2018**. under review.

15. Startsev, V.O.; Lebedev, M.P.; Khrulev, K.A.; Molokov, M.V.; Frolov, A.S.; Nizina, T.A. Effect of outdoor exposure on the moisture diffusion and mechanical properties of epoxy polymers. *Polym. Test.* **2018**, *65*, 281–296. [CrossRef]

16. Toscano, A.; Pitarresi, G.; Scafidi, M.; Di Filippo, M.; Spadaro, G.; Alessi, S. Water diffusion and swelling stresses in highly crosslinked epoxy matrices. *Polym. Degrad. Stab.* **2016**, *133*, 255–263. [CrossRef]

17. Allen, N.S.; Robinson, P.J.; White, N.J.; Swales, D.W. Photo-oxidative Stability of Electron Beam and UV Cured Acrylated Epoxy and Urethane Acrylate Resin Films. *Polym. Degrad. Stab.* **1987**, *19*, 147–160. [CrossRef]

18. Buch, X.; Shanahan, M.E.R. Thermal and thermo-oxidative ageing of an epoxy adhesive. *Polym. Degrad. Stab.* **2000**, *68*, 403–411. [CrossRef]

19. Wang, M. The hygrothermal aging process and mechanism of the novolac epoxy resin. *Compos. Part B* **2016**, *107*, 1–8. [CrossRef]

20. Clancy, T.C.; Frankland, S.J.V.; Hinkley, J.A.; Gates, T.S. Molecular modeling for calculation of mechanical properties of epoxies with moisture ingress. *Polymer* **2009**, *50*, 2736–2742. [CrossRef]

21. López-Ballester, E.; Doménech-Carbó, M.T.; Gimeno-Adelantado, J.V.; Bosch-Reig, F. Study of FT-IR spectroscopy of ageing of adhesives used in restoration of archaeological glass objects. *J. Mol. Struct.* **1999**, *482*, 525–531. [CrossRef]

22. Xiao, G.Z.; Shanahan, M.E.R. Irreversible effects of hygrothermal aging on DGEBA/DDA epoxy resin. *J. Appl. Polym. Sci.* **1998**, *69*, 363–369. [CrossRef]

23. Belec, L.; Nguyen, T.H.; Nguyen, D.L.; Chailan, J.F. Comparative effects of humid tropical weathering and artificial ageing on a model composite properties from nano- to macro-scale. *Compos. Part A Appl. Sci. Manuf.* **2015**, *68*, 235–241. [CrossRef]

24. Heinze, S.; NTNU, Trondheim, Norway. Personal communication, 2017.

25. Celina, M.C.; Dayile, A.R.; Quintana, A. A perspective on the inherent oxidation sensitivity of epoxy materials. *Polymer* **2013**, *54*, 3290–3296. [CrossRef]

26. Colin, X.; Verdu, J. Thermal ageing and lifetime prediction for organic matrix composites. *Plast. Rubber Compos.* **2003**, *32*, 349–356. [CrossRef]

27. Ernault, E.; Richaud, E.; Fayolle, B. Thermal-oxidation of epoxy/amine followed by glass transition temperature changes. *Polym. Degrad. Stab.* **2017**, *138*, 82–90. [CrossRef]

28. Galant, C.; Fayolle, B.; Kuntz, M.; Verdu, J. Thermal and radio-oxidation of epoxy coatings. *Prog. Org. Coat.* **2010**, *69*, 322–329. [CrossRef]

29. Bellenger, V.; Verdu, J.; Francilette, J.; Hoarau, P.; Morel, E. Infra-red study of hydrogen bonding in amine-crosslinked epoxies. *Polymer* **1987**, *28*, 1079–1086. [CrossRef]

30. Bruchet, A.; Elyasmino, N.; Decottignies, V.; Noyon, N. Leaching of bisphenol A and F from new and old epoxy coatings: Laboratory and field studies. *Water Sci. Technol.* **2014**, *14*, 383–389. [CrossRef]

31. Rajasärkkä, J.; Pernica, M.; Kuta, J.; Lašňák, J.; Šimek, Z.; Bláha, L. Drinking water contaminants from epoxy resin-coated pipes: A field study. *Water Res.* **2016**, *103*, 133–140. [CrossRef] [PubMed]

32. Lipke, U.; Haverkamp, J.B.; Zapf, T.; Lipperheide, C. Matrix effect on leaching of Bisphenol A diglycidyl ether (BADGE) from epoxy resin based inner lacquer of aluminium tubes into semi-solid dosage forms. *Eur. J. Pharm. Biopharm.* **2016**, *101*, 1–8. [CrossRef] [PubMed]

33. Vermeirssen, E.L.M.; Dietschweiler, C.; Werner, I.; Burkhardt, M. Corrosion protection products as a source of bisphenol A and toxicity to the aquatic environment. *Water Res.* **2017**, *123*, 586–593. [CrossRef] [PubMed]

34. Xiao, G.Z.; Delamar, M.; Shanahan, M.E.R. Irreversible interactions between water and DGEBA/DDA epoxy resin during hygrothermal aging. *J. Appl. Polym. Sci.* **1997**, *65*, 449–458. [CrossRef]

35. *Plastics in the Determination of Dynamic Mechanical Properties–Part 11: Glass Transition Temperature*; International Standard ISO 6721-11:2012(E); ISO: Geneva, Switzerland, 2012.

36. Celina, M.C. Review of polymer oxidation and its relationship with materials performance and lifetime prediction. *Polym. Degrad. Stab.* **2013**, *98*, 2419–2429. [CrossRef]

37. Krauklis, A.E.; Gagani, A.I.; Echtermeyer, A.T. Near-infrared spectroscopic method for monitoring water content in epoxy resins and fiber-reinforced composites. *Materials* **2018**, *11*, 586. [CrossRef] [PubMed]

38. Lyon, R.E.; Chike, K.E.; Angel, S.M. In situ Cure Monitoring of Epoxy Resins Using Fiber-Optic Raman Spectroscopy. *J. Appl. Polym. Sci.* **1994**, *53*, 1805–1812. [CrossRef]

39. De'Néve, B.; Shanahan, M.E.R. Water absorption by an epoxy resin and its effect on the mechanical properties and infra-red spectra. *Polymer* **1993**, *34*, 5099–5105. [CrossRef]

40. Larché, J.-F.; Bussiére, P.-O.; Thérias, S.; Gardette, J.-L. Photooxidation of polymers: Relating material properties to chemical changes. *Polym. Degrad. Stab.* **2012**, *97*, 25–34. [CrossRef]

41. Zahra, Y.; Djouani, F.; Fayolle, B.; Kuntz, M.; Verdu, J. Thermo-oxidative aging of epoxy coating systems. *Prog. Org. Coat.* **2014**, *77*, 380–387. [CrossRef]

42. Hexion Technical Data Sheet: EPIKOTE RIMR 135 and EPIKURE RIMH 134–137. 2006. Available online: http://www.hexion.com/en-us/chemistry/epoxy-resins-curing-agents-modifiers/epoxy-tds (accessed on 1 August 2018).

43. Deng, T.; Liu, Y.; Cui, X.; Yang, Y.; Jia, S.; Wang, Y.; Lu, C.; Li, D.; Cai, R.; Hou, X. Cleavage of C–N bonds in carbon fiber/epoxy resin composites. *Green Chem.* **2015**, *17*, 2141–2145. [CrossRef]

44. Unnikrishnan, K.P. Studies on the Toughening of Epoxy Resins. Ph.D. Thesis, Cochin University of Science and Technology, Kochi, India, 2006.

45. Rasoldier, N.; Colin, X.; Verdu, J.; Bocquet, M.; Olivier, L.; Chocinski-Arnault, L.; Lafarie-Frenot, M.C. Model systems for thermo-oxidised epoxy composite matrices. *Compos. Part A Appl. Sci. Manuf.* **2008**, *39*, 1522–1529. [CrossRef]

46. Li, K.; Wang, K.; Zhan, M.-S.; Xu, W. The change of thermal-mechanical properties and chemical structure of ambient cured DGEBA/TEPA under accelerated thermo-oxidative aging. *Polym. Degrad. Stab.* **2013**, *98*, 2340–2346. [CrossRef]

47. Sauvant-Moynot, V.; Duval, S.; Grenier, J. Innovative pipe coating material and process for high temperature fields. *Oil Gas Sci. Technol.* **2002**, *57*, 269–279. [CrossRef]

48. Yousif, E.; Haddad, R. Photodegradation and photostabilization of polymers, especially polystyrene: Review. *SpringerPlus* **2013**, *2*, 398–429. [CrossRef] [PubMed]

49. Rosu, D.; Rosu, L.; Cascaval, C.N. IR-change and yellowing of polyurethane as a result of UV irradiation. *Polym. Degrad. Stab.* **2009**, *94*, 591–596. [CrossRef]

50. Lin, M.-S.; Chiu, C.-C. Protection of epoxy resin against thermo-oxidation via co-curing epoxy/resole (I). *Polym. Degrad. Stab.* **2000**, *69*, 251–253. [CrossRef]

51. Lin, M.-S.; Chiu, C.-C. Protection of epoxy resin against thermo-oxidation via co-curing epoxy/resole (II). *Polym. Degrad. Stab.* **2001**, *71*, 327–329. [CrossRef]

APPENDIX C

PAPER III

KRAUKLIS A.E., GAGANI A.I., ECHTERMEYER A.T.

HYGROTHERMAL AGING OF AMINE EPOXY: REVERSIBLE STATIC AND FATIGUE PROPERTIES.

PAPER III

Research Article   **Open Access**

Andrey E. Krauklis*, Abedin I. Gagani, and Andreas T. Echtermeyer

Hygrothermal Aging of Amine Epoxy: Reversible Static and Fatigue Properties

Abstract: Fiber-reinforced polymers (FRP) are widely used in structural applications. Long-term properties of such materials exposed to water are of high concern and interest, especially for subsea and offshore applications. The objective of this study is to identify the mechanisms and to identify whether drop in properties of diamine-cured mixed DGEBA-HDDGE is reversible upon drying the material to its initial water content. The properties of interest are mechanical strength, elastic properties and fatigue performance, as well as changes in chemical structure. The effect of absorbed water on the properties of the resin is evaluated, and hygrothermal effects and aging mechanisms are discussed. Furthermore, it is shown experimentally that the tension fatigue S-N curve of a wet epoxy resin can be estimated by shifting the S-N curve of a dry material proportionally to a reduction in static tensile strength due to hygrothermal effects.

Keywords: epoxy; hygrothermal aging; plasticization; strength; fatigue

1 Introduction

Epoxy resins are well known for their relatively high strength, stiffness, low volatility, chemical resistance, and low shrinkage on curing [1, 2]. Glycidyl ether derivatives of bisphenol A, i.e. DGEBA, are the most widely used epoxy resins in structural applications and constitute more than 75% of epoxy resins sold worldwide [3]. These epoxy resins

are widely used as matrices for composite materials, i.e. fiber-reinforced polymers (FRP), as well as adhesives, organic surface coatings and encapsulating agents [1, 4]. FRPs are often exposed to water or humid air environments, where water molecules can migrate in the polymeric matrix and modify their physical and mechanical properties [1]. Highly crosslinked amine-cured epoxy resins are hydrophilic and their properties can significantly deteriorate upon water uptake [2, 5–13]. A degradation of the matrix-dominated properties of epoxy-based glass fiber composites is also expected when they are exposed to and saturated with water [14, 15]. Such effects are of special interest for offshore and marine industries, but also for many other industries, such as the renewable energy sector, i.e. wind turbines, where FRPs are widely used [16, 17]. The number of articles concerning aging of this particular mixed resin (DGEBA/HDDGE/IPDA/POPA) is very limited [17].

Water has a double effect on the polymer networks depending on its concentration [12]. At the beginning of the hygrothermal process, absorbed water causes the relaxation of residual stress and the acceleration of additional crosslinking, both of which may be responsible for the increase of the mechanical properties [12, 14, 18]. T_g can be regarded as the most useful parameter revealing material degradation [19]. The more flexible the polymer chains, the lower the T_g [12]. A decrease in T_g is generally attributed to plasticization and deterioration (i.e. chain scission), while an increase in T_g is derived from additional crosslinking [14]. The degradation of the tensile strength can be attributed to the plasticization and deterioration of the resin [14, 20]. The percentage reduction in the tensile strength of epoxies is related to the hydrophilicity of the resin blend, which may be measured by Hoy's solubility parameter for hydrogen bonding [21]. Fatigue life reduction is still not completely understood, and while some authors report significant degradation, others do not observe noticeable changes after water absorption [17].

Hygrothermal process may induce both reversible and irreversible changes in the epoxy [14, 22]. Irreversible changes persist after re-drying the material [17]. It seems that chemical processes involved in hygrothermal aging of

*Corresponding Author: Andrey E. Krauklis: Department of Mechanical and Industrial Engineering (past: Department of Engineering Design and Materials), Norwegian University of Science and Technology, 7491 Trondheim, Norway, Tel: +371 26 810 288, E-mail: andrejs.krauklis@ntnu.no
Abedin I. Gagani, Andreas T. Echtermeyer: Department of Mechanical and Industrial Engineering (past: Department of Engineering Design and Materials), Norwegian University of Science and Technology, 7491 Trondheim, Norway

epoxies are generally irreversible and persist even after the material is dried [17]. Irreversible damage in epoxies may occur due to susceptibility of the polymer to hydrolysis, oxidation, and change of the effective average crosslinked molecular weight. For some epoxy systems, water at elevated temperatures can attack the crosslinked network, causing chain scission and the leaching of segments [23]. Crosslinking reactions can also continue in an epoxy over time resulting in increased stiffness, since water causes an acceleration of the resin-hardener reaction [22, 24].

V.O. Startsev et al studied the effect of outdoor exposure on epoxies and assessed reversible effects of moisture. They have found that strength of the studied epoxies decreased by 20-40% due to plasticization [25].

Plasticization, due to water uptake, is commonly placed in the physical aging category. Authors believe that this is not fully correct, and, instead, offer a distinction between hygrothermal aging and hygrothermal effects. Aging can be defined as processes which cause changes in material properties and that are directly time-dependent. Processes which are also dependent on other terms, such as concentration (e.g. related to mass transport phenomena), are termed as hygrothermal effects, where other terms might or might not be time-dependent themselves.

The aim of this paper is to investigate whether static and fatigue properties of a commonly used DGEBA/HDDGE/IPDA/POPA amine epoxy resin are reversible or not after re-drying the material.

2 Materials

Amine-cured epoxy resin was prepared using reagents Epikote Resin RIMR 135 (Hexion) and Epikure Curing Agent MGS RIMH 137 (Hexion) in a ratio of 100:30 by weight (stoichiometrically). The epoxy value of the resin is 0.54-0.60 equivalent/100 g. The amine value of the hardener is 400-600 mg KOH/g [24]. The mixture was degassed in a vacuum chamber for 0.5 h in order to remove bubbles. The epoxy system consists of the following compounds: bisphenol A diglycidyl ether (DGEBA), 1,6-hexanediol diglycidyl ether (HDDGE), poly(oxypropylene)diamine (POPA) and isophorondiamine (IPDA).

The resin was casted into moulds to make rectangular DMTA ($40 \times 7 \times 2$ mm^3) and dogbone-shaped ($200 \times 30 \times 2$ mm^3 with 20 mm width in the most narrow part) specimens according to ISO 6721 and ISO 527 [26, 27]. The geometry of dogbone specimens equipped with strain gauges (gauge length 6 mm; Tokyo Sokki Kenkyujo Co., Ltd., Japan) is shown in Figure 1. The resin was degassed

before pouring. The specimens were cured at room temperature for 24 h and post-cured in an air oven (Lehmkuhls Verksteder, Norway) at 80 °C for 16 h. The specimens were removed from the moulds' grooves and cut into the desired length with a vertical bandsaw. After cutting the epoxy specimens were ground using sandpaper (FEPA P60, grain size 269 μm). The specified dimensions from ISO 6721 and ISO 527 [26, 27] were achieved within 5% tolerance.
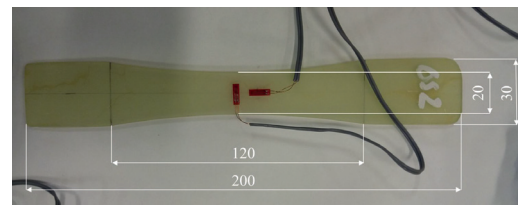
Figure 1: Geometry of dogbone specimens used for static tensile and fatigue tests. The placement of strain gauges is indicated.

The placement of strain gauges as shown in Figure 1 allowed to measure strains in both the direction of the applied load and the direction normal to it, thus enabling the calculation of Poisson's ratio.

3 Experimental

3.1 Conditioning of resin specimens in distilled water and drying

The epoxy specimens were tested dry, saturated in water and re-dried. Specimens were conditioned in a heated distilled water (60 ± 1 °C) bath for a period of two months (equilibrium was achieved after a few weeks; see Figure 2). The water content was measured by FT-NIR spectroscopy [28] and by the more widely used weight gain method [29]. Specimens were weighed using analytical scales AG204 (± 0.1 mg; Mettler Toledo, USA). Both methods gave about the same results, but the FT-NIR method has the advantage of providing a true water content using the method described in another paper [28]. The true water content shows the amount of water in respect to the absolutely dry material and is defined in Equation 1.

$$W^{\star}(t) \equiv \frac{m_{water}(t)}{m_{absolutely\ dry}} \cdot 100\%$$
$$= \left(\frac{m(t) - m_{absolutely\ dry}}{m_{absolutely\ dry}} \right) \cdot 100\% \quad (1)$$

where m_{water} is a moisture mass, $m_{absolutely\ dry}$ is a mass of resin with 0% moisture content, m is a total mass of resin with moisture.

Already at the initial stage, the 'dry' material has a true water content of about 0.63% [28], meaning that it has some initial water present being in equilibrium with water vapour in the air. The evolution of true water content in time during hygrothermal conditioning, drying and reconditioning in air atmosphere to initial water content is presented in Figure 2.
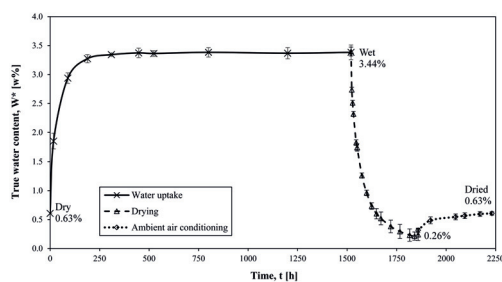
Figure 2: Evolution of true water content of amine-cured epoxy resin during water uptake, drying and conditioning in air.

The drying of saturated specimens was performed in a drying cabinet PK-410 (ESAB, UK) at 60 ± 1 °C in air atmosphere with natural convection and relative humidity of 13 RH%.

3.2 Glass transition temperature determination

Dynamic Mechanical Thermal Analysis (DMTA) tests for determination of glass transition temperature (T_g) were conducted using Netzsch GABO qualimeter Eplexor equipped with a 1.5 kN load cell (Netzsch GABO Instruments, Germany) operated in tension in displacement control with a constant static strain of 0.4% and a cyclic strain of 0.1% applied with a frequency of 1 Hz. The temperature sweep range was from 20 up to 120 °C with a heating rate of 1 °C/min. T_g is determined as the point of inflection in the temperature sweep of the storage modulus plot [26]. Evaporation of water for the wet specimens was avoided by conducting measurements in the water environment, ensuring that the specimens have been saturated during the whole process.

3.3 Mechanical testing

Tensile tests were conducted using a servo hydraulic test machine Instron model 1342 (Instron, International: USA/UK). the displacement rate was set to 1 mm/min. Fatigue tests were done using the same equipment. The testing frequency was chosen in order to keep a constant strain rate of 0.05%/min. Tests were performed at R ratio of 0.1. The temperature during the tests was about 23 °C (room temperature). Tensile tests were performed with 4 specimens for each configuration (dry, wet and dried). Average values and experimental scatter were reported for ultimate tensile strength, Young's modulus and Poisson's ratio for each group. In fatigue, between 11 and 13 dogbone specimens were used for obtaining S-N curves for each case (dry, wet and dried).

4 Results and discussion

4.1 Change of mechanical properties due to water uptake

In order to investigate the influence of the hygrothermal process and water content on the mechanical properties, static tensile and tension fatigue tests were performed.

4.1.1 Reversibility of mechanical properties in static tension

Static tensile test results are illustrated in stress-strain curves shown in Figure 3. The dry material has an ultimate tensile strength (UTS) of 60.5 ± 2.7 MPa. All scatter is given as one standard deviation. After the hygrothermal aging process, the UTS decreased to 48.5 ± 3.3 MPa, resulting in a relative decrease of about 20% on average. Results indicate that the material regained its initial strength and Young's modulus after redrying (and conditioning in air to its initial water content). It should be noted, that dried material has a slightly higher strength (66.4 ± 3.0 MPa) than the initial (60.5 ± 2.7 MPa), although the effect is within the standard deviations. A possible explanation to this phenomenon could be residual crosslinking or polymer relaxation [17]. It should be noted that not only the UTS of the dry and re-dried specimens were the same, but also the entire shape of the stress strain curve was very similar.

Poisson's ratios are reported in Figure 5. The Poisson's ratio was calculated as the ratio of strains measured via strain gauges in directions normal to applied load and in
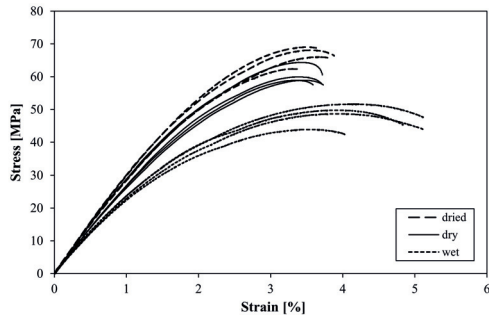
Figure 3: Stress-strain curves of dry, conditioned and dried epoxy specimens.

Figure 4: Placement and failure of the specimen in the test machine.

the direction of tension. Results show that Poisson's ratio increases for saturated epoxy but returns to the initial values after drying to the initial water content, indicating that this effect is reversible. An increase in Poisson's ratio of epoxy due to absorbed water is consistent with literature [30]. The authors believe that such increase in Poisson's ratio might be due to the absorbed almost incompressible water or the reduction of glass transition temperature (T_g) due to the plasticizing action [30,31]. Theocaris has shown that the Poisson's ratio of epoxy increases with higher plasticizer content even at room temperature below T_g [30]. The T_g of dry, saturated and re-dried epoxy was 81.7, 59.1 and 84.7 °C, respectively.

The strain to failure (ϵ_{max}) is identical for dry and dried epoxy, being 3.71 ± 0.10% and 3.69 ± 0.22% respectively, while being much higher for saturated epoxy (4.78 ± 0.51%). Dogbone specimens failed in the middle as shown in Figure 4. It was a brittle fracture and shattering often occurred for dry and re-dried specimens, while failure was less brittle for saturated epoxy. On the micro level failure is believed to occur due to a combination of crosslink bond breakage and disentanglement of macromolecular chains. The specimen placement in the machine along with the failure are shown in Figure 4.

Mechanical and elastic properties of dry, wet and dried epoxy are shown in Table 1. The average values of ultimate tensile strength (UTS), Young's modulus (E), strain to failure (ϵ_{max}) and Poisson's ratios are reported along with the statistics indicating experimental scatter (Table 1).

Figure 5: Poisson's ratio of initial (dry), wet and dried epoxy specimens.
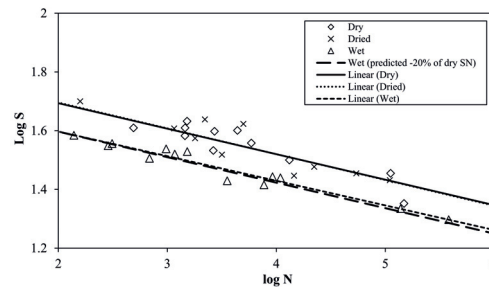
Figure 6: S-N curves of initial (dry), saturated and dried epoxy specimens in log-log scales.

4.1.2 Reversibility of mechanical properties in tension fatigue

Tension fatigue results are shown in Figure 6 and Figure 7 in log S-log N and linear S-N scales, respectively, where maximum stress S is in MPa and number of cycles to failure N is unitless. The R ratio was 0.1. The results of the fatigue

Table 1: Mechanical and elastic properties of dry, wet and dried epoxy.

Material	UTS [MPa]	E [MPa]	ϵ_{max} [%]	Poisson's ratio [-]
Dry	60.5 ± 2.7	2908.8 ± 126.6	3.71 ± 0.10	0.35 ± 0.02
Dried	66.4 ± 3.0	3237.5 ± 126.3	3.69 ± 0.22	0.36 ± 0.01
Wet	48.5 ± 3.3	2588.9 ± 252.3	4.78 ± 0.51	0.39 ± 0.01
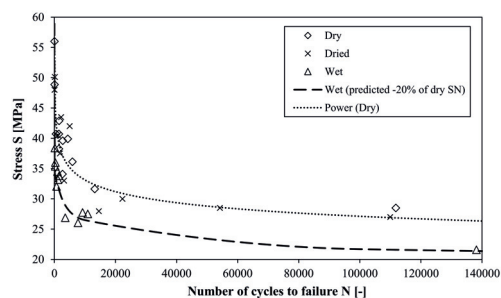
Figure 7: S-N curves of initial (dry), saturated and dried epoxy specimens in linear scales.

tests show that the S-N curve of the wet epoxy shifted down by 20% without a change in slope. The slope was obtained by linear regression of the log-log curve with the number of cycles being the dependent variable. Regression equations are shown in Table 2.

The fact that the slope of the S-N curve did not change, and the drop is the same as for the static data indicates that fatigue of wet epoxy can be simply predicted by measuring static strength changes of wet specimens.

The S-N curve of the re-dried epoxy was the same (within experimental scatter) as the original S-N curve of the dry material. This effect indicates reversibility, as was already observed for the static data.

5 Aging mechanisms and hygrothermal effects

For epoxy-amine networks [17], two possible major hygrothermal degradation mechanisms might occur: plasticization (hygrothermal effect) and chain scission (hygrothermal aging). Other failure mechanisms may also happen [14, 15, 17, 22, 32–34], but are considered of minor importance to this study, such as thermo-oxidation, photo-oxidation, additional crosslinking (residual curing), secondary crosslinking between the epoxy and water molecules, leaching of additives, polymer relaxation,

swelling-induced microcracking and formation of microcracks through absorption/desorption cycles. Multiple aging mechanisms and hygrothermal effects may also combine.

Results of this study indicate that plasticization (hygrothermal effect) is fully reversible for the studied epoxy.

No chain scission was observed. The T_g of dry, saturated and re-dried epoxy was 81.7, 59.1 and 84.7 °C, respectively. The T_g of saturated specimen decreased due to plasticization. There was only a slight increase in T_g after re-drying compared to the dry epoxy, indicating that no major changes in chemical structure have occurred during hygrothermal aging. In case of chemical degradation (chain scission) a T_g value would have decreased, which is opposite to what was observed. A slight increase in T_g of the dried material can be explained due to additional crosslinking taking place or polymer relaxation [14, 17].

6 Conclusions

Exposure of the amine-cured epoxy to water caused the material to swell. The absorption of water had detrimental, but reversible effects on static strength and cyclic fatigue properties. Similar values of dry and re-dried specimen T_g serve as an indicator that no chemical degradation (chain scission) has occurred.

The ultimate tensile strength of the resin decreased by 20% relative to the initial dry value due to plasticization by water. The strength of dried epoxy is comparable to that of the initial dry epoxy, indicating the reversibility in mechanical properties.

Poisson's ratio increased for conditioned epoxy, but returned to the initial values after drying, also indicating that the effect of water conditioning is reversible. The increase of Poisson's ratio is believed to be due to the absorbed almost incompressible water or due to the reduction of glass transition temperature (T_g) due to the plasticizing action. The results of fatigue tests indicated that the S-N curve of a wet epoxy also shifted by 20% without a change in slope. The S-N curves of dry and dried material

Table 2: Linear regression of fatigue data.

Linear models	Regression equation	Determination coefficient R^2
Dry (linear)	log N = -11.5207 log S + 21.5115	0.89
Dried (linear)	log N = -11.3895 log S + 21.3121	0.82
Wet (linear)	log N = -11.9332 log S + 21.0585	0.95
Wet (linear predicted from static data)	log N = -11.5207 log S + 20.3952	0.90

were identical, further proving the reversibility in mechanical properties.

It is shown experimentally that the tension fatigue S-N curve of a wet epoxy resin can be estimated by shifting the S-N curve of a dry material proportionally to a reduction in static tensile strength due to hygrothermal effects.

List of symbols

W*	Moisture content in the resin (w%)
m_{water}	Moisture mass in the resin (g)
$m_{absolutelydry}$	Mass of an absolutely dry resin specimen (g)
m	Measured mass of a resin specimen (g)
T_g	Glass transition temperature (°C)
t	Time (s)
ϵ_{max}	Linear strain to failure (%)
E	Young's modulus (MPa)
S	Stress (MPa)
N	Number of cycles before specimen fails in fatigue (-)
UTS	Ultimate tensile strength (MPa)
DMTA	Dynamic mechanical testing analysis
FT-NIR	Fourier transform near infrared spectroscopy

References

[1] Maggana C., Pissis P., Water sorption and diffusion studies in an epoxy resin system, J. Polym. Sci., Part B: Polym. Phys., 1999, 37(11), 1165–1182.

[2] Lee M.C., Peppas N.A., Water transport in epoxy-resins, Prog. Polym. Sci., 1993, 18(5), 947–961.

[3] Pham H.Q., Marks M.J., Epoxy resins, in Ullmann's encyclopedia of industrial chemistry, 2005, Wiley-VCH.

[4] Popineau S., Rondeau-Mouro C., Sulpice-Gaillet C., Shanahan M.E.R., Free/bound water absorption in an epoxy adhesive, Polymer, 2005, 46(24), 10733–10740.

[5] Wang J., Gong J., Gong Z., Yan X., Wang B., Wu Q., Li S., Effect of curing agent polarity on water absorption and free volume in epoxy resin studied by PALS, Nucl. Instrum. Methods Phys. Res. B., 2010, 268(14), 2355–2361.

[6] Weitsman Y., Coupled damage and moisture-transport in fiber-reinforced, polymeric composites, Int. J. Solid Struct., 1987, 23(7), 1003–1025.

[7] Weitsman Y.J., Elahi M., Effects of fluids on the deformation, strength and durability of polymeric composites – an overview, Mech. Time-Depend. Mater., 2000, 4(2), 107–126.

[8] Roy S., Moisture-induced degradation, in Long-Term Durability of Polymeric Matrix Composites, 2012, Eds.: Pochiraju K., Tandon G., Schoeppner G., Springer: Boston, MA.

[9] Apicella A., Nicolais L., Effect of water on the properties of epoxy matrix and composite, Adv. Polym. Sci., 1985, 72, 69–77.

[10] Lefebvre D.R., Elliker P.R., Takahashi K.M., Raju V.R., Kaplan M.L., The critical humidity effect in the adhesion of epoxy to glass: role of hydrogen bonding, J. Adhes. Sci. Technol., 2000, 14, 925–937.

[11] Guermazi N., Elleuch K., Ayedi H.F., The effect of time and aging temperature on structural and mechanical properties of pipeline coating, Mater. Design., 2009, 30, 2006–2010.

[12] Wu C.F., Xu W.J., Atomistic simulation study of absorbed water influence on structure and properties of crosslinked epoxy resin, Polymer, 2007, 48, 5440–5448.

[13] Li L., Yu Y., Wu Q., Zhan G., Li S., Effect of chemical structure on the water sorption of amine-cured epoxy resins, Corros. Sci., 2009, 51, 3000–3006.

[14] Wang M., The hygrothermal aging process and mechanism of the novolac epoxy resin, Composites Part B, 2016, 107, 1–8.

[15] Halpin J.C., Effects of environmental factors on composite materials, Technical Report AFML-TR67-423, 1969, Air Force Materials Laboratory, US, Ohio.

[16] Echtermeyer A.T., Integrating durability, in Durability of Composites in a Marine Environment, 2014, Eds.: Davies P., Rajapakse Y.D.S., Springer: Dordrecht.

[17] Rocha I.B.C.M., Raijmaekers S., Nijssen R.P.L., van der Meer F.P., Sluys L.J., Hygrothermal ageing behaviour of a glass/epoxy composite used in wind turbine blades, J. Compos. Struct., 2017, 174, 110–122.

[18] Xian G., Karbhari V.M., Segmental relaxation of water-aged ambient cured epoxy, Polym. Degrad. Stab., 2007, 92(9), 1650–1659.

[19] Sauvant-Moynot V., Duval S., Grenier J., Innovative pipe coating material and process for high temperature fields, Oil Gas Sci. Technol., 2002, 57(3), 269–279.

[20] Chen Y., Davalos J.F., Ray I., Kim H.-Y., Accelerated aging tests for

evaluations of durability performance of FRP reinforcing bars for concrete structures, Compos. Struct., 2007, 78(1), 101–111.

[21] Yiu C.K.Y., King N.M., Pashley D.H., Suh B.I., Carvalho R.M., Carrilho M.R.O., Tay F.R., Effect of resin hydrophilicity and water storage on resin strength, Biomaterials, 2004, 25(26), 5789–5796.

[22] Clancy T.C., Frankland S.J.V., Hinkley J.A., Gates T.S., Molecular modeling for calculation of mechanical properties of epoxies with moisture ingress, Polymer, 2009, 50(12), 2736–2742.

[23] Xiao G.Z., Shanahan M.E.R., Irreversible effects of hygrothermal aging on DGEBA/DDA epoxy resin, J. Appl. Polym. Sci., 1998, 69(2), 363–369.

[24] Technical data sheet, EPIKOTE RIMR 135 and EPIKURE RIMH 134–137, 2006, Hexion.

[25] Startsev V.O., Lebedev M.P., Khrulev K.A., Molokov M.V., Frolov A.S., Nizina T.A., Effect of outdoor exposure on the moisture diffusion and mechanical properties of epoxy polymers, Polym. Test., 2018, 65, 281-296.

[26] International Standard ISO 6721-11:2012(E), Plastics – Determination of dynamic mechanical properties – Part 11: Glass transition temperature, 2012.

[27] International Standard ISO 527-1:2012(E), Plastics – Determination of tensile properties – Part 1: General principles, 2012.

[28] Krauklis A.E., Gagani A.I., Echtermeyer A.T., Near-infrared spectroscopic method for monitoring water content in epoxy resins and fiber-reinforced composites, Materials, 2018, 11(4), 586-599.

[29] International Standard ISO 62-2008(E), Plastics – Determination of water absorption, 2008.

[30] Theocaris P.S., Influence of plasticizer on Poisson's ratio of epoxy polymers, Polymer, 1979, 20, 1149-1154.

[31] Fine R.A., Millero F.J., Compressibility of water as a function of temperature and pressure, J. Chem. Phys., 1973, 59(10), 5529-5536.

[32] Xiao G.Z., Shanahan M.E.R., Swelling of DGEBA/DDA epoxy resin during hygrothermal ageing, Polymer, 1998, 39(14), 3253–3260.

[33] Belec L., Nguyen T.H., Nguyen D.L., Chailan J.F., Comparative effects of humid tropical weathering and artificial ageing on a model composite properties from nano- to macro-scale, Composites Part A, 2015, 68, 235–241.

[34] Alfrey, Jr. T., Gurnee E.F., Lloyd W.G., Diffusion in glass polymers, J. Polym. Sci. Part C, 1966, 12(1), 249–261.

A Appendix Fatigue raw data

Table 3: Fatigue raw data. S represents maximum stress in MPa. The R ratio was 0.1.

	DRY			DRIED			WET	
Specimen	N [-]	S [MPa]	Specimen	N [-]	S [MPa]	Specimen	N [-]	S [MPa]
1	21	56.0	1	158	50.1	1	139	38.4
2	53	48.9	2	53	48.0	2	311	36.0
3	1515	42.9	3	2210	43.5	3	286	35.4
4	489	40.7	4	4986	42.0	4	974	34.5
5	1455	40.7	5	1155	40.5	5	1524	33.8
6	4392	39.9	6	1798	37.5	6	1169	33.2
7	2711	39.6	7	3171	33.0	7	686	32.1
8	1451	38.3	8	22265	30.0	8	9219	27.8
9	5896	36.1	9	54185	28.5	9	10911	27.5
10	2643	34.1	10	14538	28.0	10	3543	26.9
11	13183	31.6	11	109947	27.0	11	7710	26.0
12	111785	28.5				12	138162	21.6
13	148408	22.5				13	381758	19.8

APPENDIX D

PAPER IV

KRAUKLIS A.E., GAGANI A.I., ECHTERMEYER A.T.

PREDICTION OF ORTHOTROPIC HYGROSCOPIC SWELLING OF FIBER-REINFORCED COMPOSITES FROM ISOTROPIC SWELLING OF MATRIX POLYMER.

PAPER IV

Article

Prediction of Orthotropic Hygroscopic Swelling of Fiber-Reinforced Composites from Isotropic Swelling of Matrix Polymer

Andrey E. Krauklis * , **Abedin I. Gagani and Andreas T. Echtermeyer**

Department of Mechanical and Industrial Engineering (past: Department of Engineering Design and Materials), Norwegian University of Science and Technology, 7491 Trondheim, Norway; abedin.gagani@ntnu.no (A.I.G.); andreas.echtermeyer@ntnu.no (A.T.E.)

* Correspondence: andrejs.krauklis@ntnu.no or andykrauklis@gmail.com; Tel.: +371-268-10288

check for
updates

Abstract: Swelling in fiber-reinforced composites is anisotropic. In this work, dealing with glass fiber epoxy composite immersed in distilled water, swelling coefficients are obtained in each direction experimentally. Swelling behaviour in the fiber direction was constrained by the non-swelling fibers and was close to null, while swelling in the transverse directions was found to occur freely—similar to the unconstrained polymer. An analytical method for predicting anisotropic swelling in composites from the swelling of the matrix polymer is reported in this work. The method has an advantage that it is simple to use in practice and requires only a swelling coefficient of the matrix polymer, elastic constants of the matrix and fibers, and a known fiber volume fraction of the composite. The method was validated using finite element analysis. Good agreement was obtained and is reported between experimental hygroscopic swelling data, analytical and numerical results for composite laminates, indicating the validity of this predictive approach.

1. Introduction

Fiber-reinforced composite (fiber-reinforced polymer; FRP) laminates are used for structural applications in marine, offshore and oil and gas industries due to their light weight and corrosion resistance [1–3]. Composites offshore have been implemented in such applications as risers, tethers, repair patches and ship hulls [4–8]. In these applications, FRPs are exposed to water and experience subsequent water-induced or hygroscopic swelling [1–3].

One of the main effects of water on the mechanical property deterioration of polymers is swelling, even more so if the polymer is not affected by hydrolysis or chain scission, such as the epoxy in this study [1,9]. Swelling is a specific response accompanying moisture diffusion in polymers and polymer-based composites [2]. Susceptibility of polymers to swelling results in a two-fold effect on FRPs: on the one hand, it causes a decrease in mechanical strength of the polymeric matrix [9], while on the other, it results in swelling stresses when the hygroscopic swelling is restrained [10].

In FRPs, the matrix is constricted by fibers, and as a result, this affects the swelling behaviour. What complicates the phenomenon even more is the orthotropic nature of swelling of composites—fibers, such as glass or carbon, do not swell, while the polymer does [3,10]. Such incompatible swelling behaviour in FRPs leads to swelling stresses at the interfaces, which may lead to microcrack formation, especially under transient conditions (non-uniform moisture content distribution) [3,11]. Hygroscopic swelling may affect the mechanical properties of FRPs significantly [2,9,12,13]. Thus, it is important to know not only the moisture diffusion behaviour,

but also the swelling behaviour, in order to properly characterize the FRP material property change, i.e., strength or modulus, resulting from moisture absorption. The focus of this work is on swelling and its orthotropic nature in FRPs.

The amount of hygroscopic strain found from dimensional change is normally assumed to be linearly proportional to the moisture concentration as follows (Equation (1)) [14]:

$$\varepsilon_h = \beta W \tag{1}$$

where ε_h is the hygroscopic strain, β is the coefficient of hygroscopic expansion (CHE), and W is the moisture concentration.

Linear strain behaviour has been observed experimentally with increasing moisture concentration for both composites and polymers [13,14]. For orthotropic laminates, three CHEs ($\beta_x, \beta_y, \beta_z$) are needed in order to predict swelling. Strains in longitudinal (along-the-fibers) direction are often assumed to be null for composites with moisture-insensitive fibers, i.e., glass or carbon [15].

Quantification of the orthotropic CHEs can be performed experimentally using samples with different fiber orientations. However, it is a time-consuming and tedious process that also tends to involve quite high experimental scatters. The industrial interest lies in the reduction of testing time and testing-related expenses. Thus, a modelling approach to swelling of FRPs due to the effects of water (and also other liquids, such as oil) is of interest [16].

Various studies have been performed on swelling of FRPs [10,13,17–25] and, more recently, on hygroscopic swelling in textile composites [26,27]. The works available in the literature have addressed several aspects of hygroscopic swelling in composites, from the nature of swelling in polymeric matrix [3,10,28,29], to the influence of swelling on the fluid diffusion in polymers [13,16,23, 30,31], to the development of micromechanical models to predict transverse swelling [17,26,27].

Ashton et al. [18] suggested the use of thermal expansion theory when dealing with hygroscopic swelling: in particular the Halpin-Tsai equation [19] for fluid diffusion and Schapery equation [20] for hygroscopic swelling of composites. Coran et al. [21] and Daniels [22] analyzed swelling of reinforced rubbers by means of thermodynamic theory of elasticity, confirming an orthotropic swelling behaviour and relating the elastic constants to the swelling constants of the rubber composite. Fan et al. [23] modelled a coupled diffusion and swelling of fiber-reinforced composites. Meng et al. [25] developed a multiscale model for coupled moisture diffusion and swelling in FRPs by means of finite element (FE) analysis. The model enabled evaluation of the fiber-matrix interfacial stresses [25]. Sinchuk et al. [26] developed a realistic voxel-model simulating fluid diffusion and hygroscopic swelling in a textile composite using a mesoscale approach of modelling the orthotropic tows and the resin-rich areas. In a later work, Sinchuk et al. [27] developed a hierarchical multiscale model for the prediction of hygroscopic swelling-induced stresses in textile composites.

An interesting opportunity would be the possibility to predict the orthotropic swelling constants (CHEs) of the composite from the CHE of the matrix polymer, which is isotropic. The matrix properties are easy to measure. Furthermore, they also may be found in literature for various polymers [28,32]. However, in some cases, the interfacial effects may not be negligible [33], many of the moisture-related properties of composites are known to be traceable to those of the matrix material [12,13]. Swelling strains of a composite and a matrix polymer should also be related to each other through a proper analysis [13,34]. Since swelling in polymers does not follow the ideal mixing law [2], i.e., the volume increase of the polymer is not equal to the volume of the absorbed water, and it is necessary to perform swelling experiments for the matrix polymer itself, or to find polymer CHE in the literature [28,32]. The composite swelling can then be analytically or numerically predicted from the swelling of the matrix polymer, as shown in this work.

Few works have investigated the anisotropic nature of swelling in unidirectional FRPs. In this work, the authors developed an analytical model based on linear elasticity. Both the analytical model and a finite element analysis employing a periodic representative volume element (RVE) were able to predict the orthotropic hygroscopic swelling of fiber-reinforced composites from the isotropic swelling

of the polymer used as a matrix. The model was validated with experiments on glass fiber-reinforced epoxy composites, using the matrix isotropic CHE to predict directional swelling of the composite, and yielded a good agreement. To the best knowledge of the authors, this is the first micromechanical model that predicts the anisotropic swelling of composites from isotropic swelling of the polymer.

2. Materials and Methods

2.1. Materials

A typical glass fiber epoxy used for marine and oil and gas applications was selected for this study. HiPer-Tex^{TM} fabrics weaved by 3B Fibreglass (Birkeland, Norway) were used as a glass fiber reinforcement with an average fiber diameter of 17 μm. The density of glass (ρ_f) was 2.54 g/cm^3. Hexion^{TM} (Columbus, OH, USA) epoxy resin RIMR135^{TM} and amine hardener RIMH137^{TM} were used for preparing the matrix polymer by mixing in a stoichiometric ratio of 100:30 by weight. The resin and the curing agent consisted of the following compounds: bisphenol A diglycidyl ether (DGEBA), 1,6-hexanediol diglycidyl ether (HDDGE), poly(oxypropylene)diamine (POPA) and isophorondiamine (IPDA). The density of the polymer (ρ_m) was 1.1 g/cm^3. Before pouring, the mixture was degassed in a vacuum chamber for 0.5 h in order to remove bubbles. Degassed resin was moulded into rectangular-shaped moulds, followed by curing at room temperature for 24 h and post-curing in an air oven (Lehmkuhls Verksteder, Norway) at 80 °C for 16 h. After samples were post-cured, the polymer was cut into rectangular bars and then further cut into plates using a vertical bandsaw. The final dimensions of plates were 25 mm × 25 mm × 2 mm. The desired thickness was obtained using PHOENIX 2000 (Jean Wirtz, Germany) and SiC grinding discs (Struers, Cleveland, OH, USA; FEPA P500, grain size 30 μm). The sufficient thickness control, correct length and width was ensured within a 5% tolerance.

Glass fiber-reinforced epoxy composite laminates were prepared using vacuum assisted resin transfer moulding (VARTM). The same epoxy resin was used as for preparation of polymer samples. The composite laminate was cut into rectangular bars and subsequently into plates with different fiber orientations (C1 and C3 as shown in Figure 1). The dimensions of plates were 25 mm × 25 mm × 2 mm. The thickness was adjusted to 2 mm within 5% tolerance via grinding with a super fine sandpaper (FEPA P800, grain size 21.8 μm). The specified dimensions were achieved within 5% tolerance.
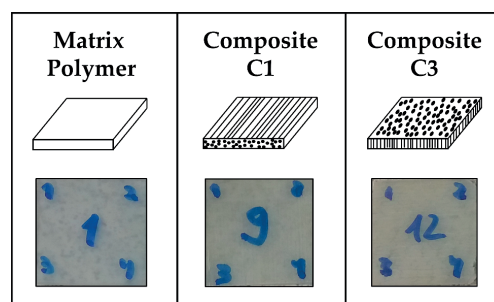
Figure 1. Matrix polymer and composite plates used for swelling measurements.

Distilled water (0.5–1.0 MΩ·cm) was used for conditioning matrix polymer and composite samples, produced via water purification system Aquatron A4000 (Cole-Parmer, Vernon Hills, IL, USA).

2.2. Methods

Fiber volume fractions were obtained by density measurements. The polymer and composite plates were exposed to water. The resulting changes in plate dimensions were measured using digital

microscopy, allowing swelling-induced linear strains to be obtained at various water contents for matrix polymers (ε_m) and for composites in 3 different directions (ε_x, ε_y, ε_z).

The density of matrix polymer (ρ_m) and glass fiber (ρ_f) was 1.1 g/cm^3 and 2.54 g/cm^3, respectively. The density of the composite ($\rho_{composite}$) was determined to be 1.97 g/cm^3 by measuring mass and dimensions of a large composite block. The volume and mass fractions of matrix polymer were calculated using Equations (2) and (3), respectively.

$$V_f = \frac{\rho_{composite} - \rho_m}{\rho_f - \rho_m} \tag{2}$$

$$m_f = \frac{\rho_f \cdot V_f}{\rho_m \cdot \left(1 - V_f\right) + \rho_f \cdot V_f} \tag{3}$$

The volume and mass fraction of the fibers were V_f = 0.606 and m_f = 0.780, respectively. The void content is ignored, because it was very low (less than 0.02 %—calculated from true water content [12]) and could be neglected. The true water content of a composite should be calculated according to [12]. If the void content is high, it should be considered.

Water uptake experiments were conducted using a batch system. A heated distilled water ($60 \pm 1\,^{\circ}$C) bath was used for conditioning the polymer and composite plates. Samples were conditioned for a period of about two months up to reaching equilibrium. During this time, samples were taken out of the water bath at various times and weighed using analytical scales AG204 ($\pm$ 0.1 mg; Mettler Toledo, Columbus, OH, USA). The moisture content (true water content) was calculated from experimental gravimetric data using a method described in more detail in another work that allows to obtain the mass of an absolutely dry plate [12]. The definition of moisture content used in this work is given in Equation (4):

$$W = \frac{m_{water}}{m_{dry\ plate}} \cdot 100\% = \frac{m_{plate} - m_{dry\ plate}}{m_{dry\ plate}} \cdot 100\% \tag{4}$$

where m_{plate} is the mass of epoxy or composite plate sample; $m_{dry\ plate}$ is the mass of an absolutely dry epoxy or composite plate sample; m_{water} is the mass of moisture uptaken by the plate.

The moisture content in composite plates was scaled by the mass matrix fraction as shown in Equation (5), since fibers do not take up moisture:

$$W_m = \frac{W}{1 - m_f} \tag{5}$$

This operation is useful for easier comparison of swelling-induced strains between the matrix polymer and the composite laminates, since it is only the polymer part which is affected by swelling in composites.

Optical microscopy was performed using a digital microscope RH-2000 (Hirox, Tokyo, Japan) equipped with lens MXB-2500REZ with a magnification of 140 and resolution of 1.06 μm. Changes in the length and width of the plates were measured using the edge dimensions of the plates. The strains and swelling coefficients were obtained using Equations (6) and (7) for matrix polymer and composites, respectively:

$$\varepsilon_m = \frac{l - l_0}{l_0} = \beta_m W \tag{6}$$

$$\varepsilon_i = \frac{l - l_0}{l_0} = \beta_i W_m \tag{7}$$

where i stands for x, y and z for respective swelling directions. Composite C1 was used to obtain swelling coefficients in the direction parallel to fibers (β_x) and transverse to fibers (β_y), while composite C3 also provided transverse-to-fibers swelling (β_z) which was similar to and consistent with β_y.

3. Model

3.1. Swelling Analytical Model

The swelling behaviour of a fiber-reinforced polymer composite can be estimated using a simple scheme where fiber and matrix are schematized as rectangular, in a cubic cell having unit dimensions $1 \times 1 \times 1$, shown in Figure 2.
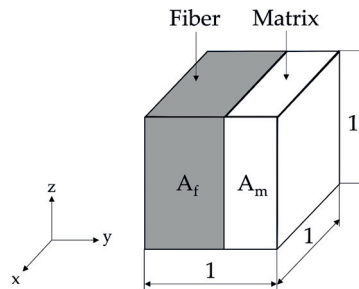
Figure 2. Schematic fiber-reinforced composite (cubic unit cell with dimensions $1 \times 1 \times 1$).

The RVE represented in Figure 2 is the result of periodicity and symmetry considerations. In fact, the RVE can be imagined as half model of a RVE comprised by matrix surrounded by fibers. Consequently, localized differential deformations and strains may arise in the RVE, but the global deformed shape does not bend, due to the symmetry along its lateral plane.

Composite transverse swelling, which occurs in direction y in Figure 2, can be predicted as a serial connection of fiber and matrix, hence:

$$\varepsilon_y = V_f \varepsilon_f + \left(1 - V_f\right) \varepsilon_m \tag{8}$$

where ε_y is the composite transverse swelling strain, V_f the fiber volume fraction, ε_f is the fiber swelling strain and ε_m is the matrix swelling strain. For many engineering reinforcements (carbon fibers, glass fibers, etc.) the swelling is null, $\varepsilon_f = 0$. In these cases, Equation (8) can be simplified as follows:

$$\varepsilon_y = \left(1 - V_f\right) \varepsilon_m \tag{9}$$

The transverse swelling coefficient is defined in Equation (10) [35]:

$$\beta_y = \frac{\varepsilon_y}{W_c} = \frac{\left(1 - V_f\right) \varepsilon_m}{W_c} = \left(1 - V_f\right) \frac{W}{W_c} \beta_m \tag{10}$$

where W is the moisture content in the matrix and W_c the moisture content in the composite.

Composite axial swelling, which occurs in direction x in Figure 2, can be predicted employing a parallel connection model of fiber and matrix. The swelling of the matrix in this case is strongly constrained by the stiffness of the fibers. The constrained swelling strain in the matrix ε_m generates a stress equal to:

$$\sigma_m = E_m \varepsilon_m \tag{11}$$

where σ_m is the stress in the matrix and E_m is the stiffness of the matrix.

The load transferred from the matrix to the fibers, L can be estimated as:

$$L = \sigma_m A_m = \sigma_m A(1 - V_f) = \sigma_f A_f = \sigma_f A V_f \tag{12}$$

where A is the cubic cell lateral surface area (in the $x - z$ plane), $A_m = A(1 - V_f)$ is the matrix part of the cubic cell lateral surface area and $A_f = AV_f$ is the fiber part of the cubic cell lateral surface area, as shown in Figure 2.

From Equation (12) it is possible to estimate the stress transferred to the fiber, σ_f:

$$\sigma_f = \sigma_m \frac{1 - V_f}{V_f} \tag{13}$$

Finally, the composite axial strain, ε_x, can be predicted as equal to the fiber axial strain, ε_f, as the axial swelling of the cubic cell is governed by its behaviour:

$$\varepsilon_x = \varepsilon_f = \frac{\sigma_f}{E_f} = \frac{\sigma_m}{E_f} \frac{1 - V_f}{V_f} \tag{14}$$

where E_f is the fiber stiffness.

The transverse swelling coefficient is defined as [35]:

$$\beta_x = \frac{\varepsilon_x}{W_c} = \frac{\sigma_m}{W_c E_f} \frac{1 - V_f}{V_f} = \frac{E_m \varepsilon_m}{W_c E_f} \frac{1 - V_f}{V_f} = \frac{E_m \beta_m}{E_f} \frac{W}{W_c} \frac{1 - V_f}{V_f} \tag{15}$$

3.2. Finite Element Model

The swelling behaviour of a fiber-reinforced polymer composite can be estimated using a three-dimensional periodic RVE comprised of matrix and randomly placed fibers.

An RVE was modelled in Abaqus^{TM}, (Abaqus Inc., Johnston, RI, USA) having dimensions 110 μm × 110 μm × 10 μm. The fibers radius is 9 μm, as measured experimentally. These RVE dimensions enable having several fibers in the RVE, predicting the composite properties with a good fidelity [36,37]. The thickness of the RVE enables axial swelling to be captured accurately while reducing the total number of elements required for the analysis. A sensitivity analysis was performed employing a thicker RVE (110 μm × 110 μm × 55 μm), the results deviation was below 1%. The elements used are C3D6 for the fibers (6-node linear triangular prism) and C3D8R for the matrix (8-node linear brick, reduced integration). The element size chosen was 1.5 μm. A mesh sensitivity analysis was also performed in order to verify the convergence of the results.

The mesh of the model is shown in Figure 3. The constituents of the composite are modelled as linear elastic. The elastic constants of the matrix polymer are E_m = 2.908 GPa and ν_m = 0.35 [9]. The elastic constants of the fibers are E_f = 72.4 GPa and ν_f = 0.22 [35].

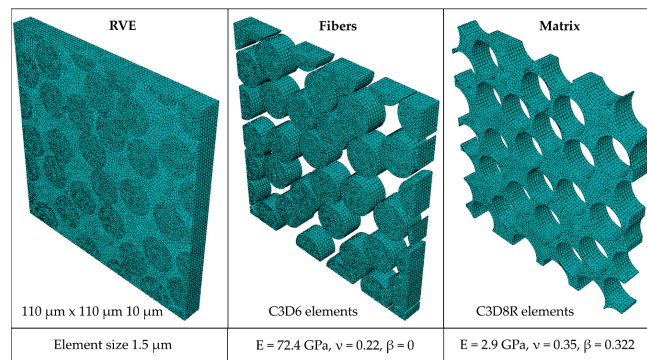| RVE	Fibers	Matrix
110 μm x 110 μm 10 μm	C3D6 elements	C3D8R elements
Element size 1.5 μm	E = 72.4 GPa, ν = 0.22, β = 0	E = 2.9 GPa, ν = 0.35, β = 0.322

Figure 3. Finite element model of the representative volume element (RVE): fiber and matrix properties are also shown.

In order to account for the deviations in the swelling coefficients due to the random fiber distribution in the RVE, five RVEs having the same fiber volume fraction were modelled, as shown in Figure 4. This allows the deviation in swelling coefficient due to the fiber random arrangement to be quantified.
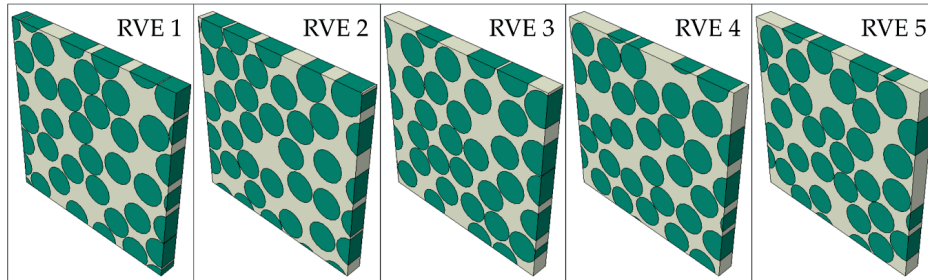
Figure 4. Finite element model of the RVE.

Hygrothermal swelling was simulated in Abaqus[TM] using a heat-mass transfer laws analogy, defining a coefficient of hygrothermal expansion β instead of the thermal expansion coefficient α and a concentration field $W(x, y, z)$ instead of the temperature field $T(x, y, z)$.

$$\varepsilon = \alpha \Delta T \leftrightarrow \varepsilon = \beta \Delta W \tag{16}$$

During the simulation, periodic boundary conditions were applied on the surfaces of the RVE. These are applied as relative displacements of opposite faces of the RVE, vectors $\vec{u_x}$, $\vec{u_y}$ and $\vec{u_z}$.

$$\begin{aligned}
\vec{u}\,(L_x,\, y,\, z) - \vec{u}\,(0,\, y,\, z) &= \vec{u_x} \\
\vec{u}\,(x,\, L_y,\, z) - \vec{u}\,(x,\, 0,\, z) &= \vec{u_y} \\
\vec{u}\,(x,\, y,\, L_z) - \vec{u}\,(x,\, y,\, 0) &= \vec{u_z}
\end{aligned} \tag{17}$$

where x, y and z are Cartesian coordinates, $\vec{u}(x,\, y,\, z)$ the displacement vector at a point having coordinates $(x,\, y,\, z)$ and L_x, L_y and L_z the dimensions of the RVE in directions x, y and z, respectively. Displacements on one node of the RVE were constrained in order to avoid rigid translations. Fluid saturation was modelled using a predefined field of initially dry and later saturated material.

The homogenized strain components of the RVE were obtained as:

$$\overline{\varepsilon_{ij}} = \frac{1}{V} \int_V \varepsilon_{ij}\, dV \tag{18}$$

where $\overline{\varepsilon_{ij}}$ is the homogenized strain component of the RVE and ε_{ij} and V are the strain component and the volume of each point in the RVE, respectively.

The swelling coefficients are defined as [35]:

$$\beta_{ij} = \frac{\overline{\varepsilon_{ij}}}{\Delta W} \tag{19}$$

where W is the moisture content.

4. Results

4.1. Swelling Measurements

Hygroscopic strains were measured after various exposure times to water for both matrix polymer and composite samples (C1 and C3). The experimentally obtained evolution of linear strains with increasing water contents for the polymer and composites, is shown in Figures 5 and 6, respectively.
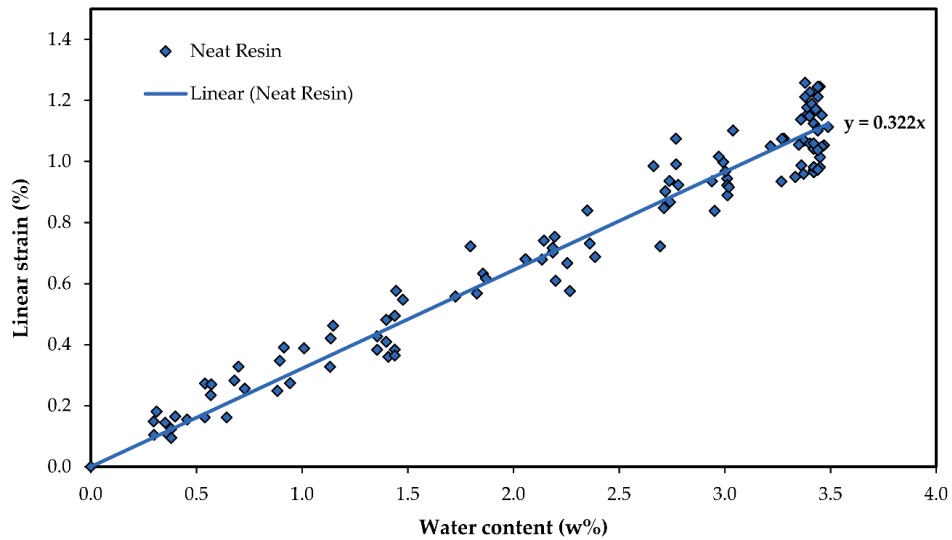
Figure 5. Experimental data and linear regression of hygroscopic swelling of epoxy polymer.
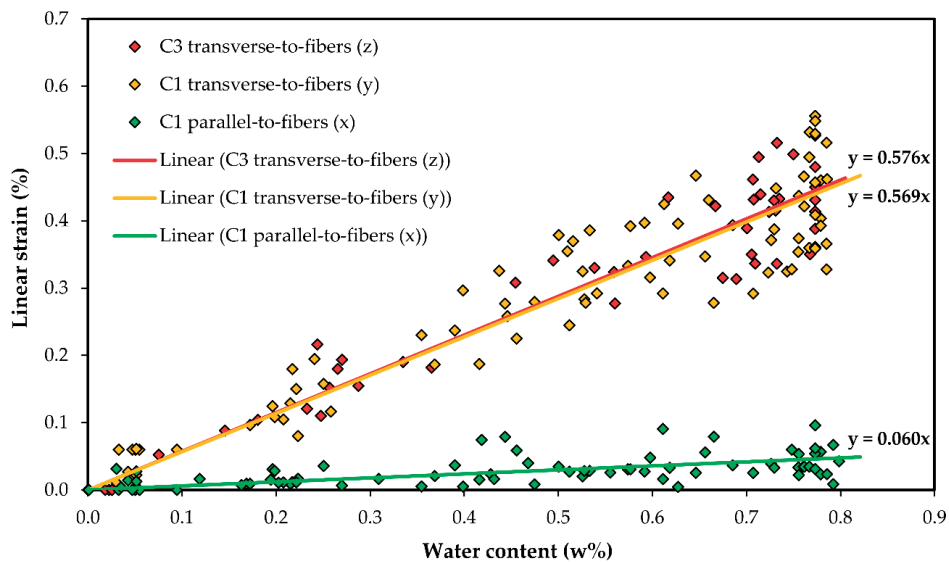
Figure 6. Experimental data and linear regression of orthotropic swelling for composites.

Linear regression of experimental data was performed via the least squares approach to obtain a coefficient of hygroscopic expansion of the matrix polymer β_m and for composite plates in directions transverse (β_y, β_z) and parallel to fibers (β_x). The determination coefficient R^2 obtained for the matrix

polymer via linear regression of experimental data was 0.9534 with an average β_m of 0.332. The linear regression included 112 observations with a standard deviation of 0.021 for the β_m. The average slope for composite experimental data in the transverse-to-fibers directions was found to be 0.571 with a determination coefficient of $R^2 = 0.9750$. A similar value of 0.6 was reported by Tsai for Kevlar/epoxy composite [15]. The linear regression included 129 observations with a standard deviation of 0.063 for the slope. The average slope β_x for experimental data obtained in the parallel-to-fibers direction was found to be non-zero and equal to 0.060 with a determination coefficient of $R^2 = 0.3110$. The linear regression included 77 observations with a standard deviation of 0.018 for the slope. The experimental scatter is reported with one standard deviation in Table 1.

4.2. Analytical and Finite Element Predictions

Experiments validate both analytical and numerical models. Both numerical and analytical results are shown in Figure 7. They show a good fit with the experimental swelling data of composites. The analytically predicted coefficient 0.546 (both β_y and β_z) of hygroscopic swelling in transverse-to-fibers directions (y and z) is close to the numerically predicted values of 0.552 and 0.573 for β_y and β_z, respectively, and all predicted values fall within the experimental scatter of 0.571 ± 0.063 (both β_y and β_z).

In the fiber direction, both analytically and numerically obtained coefficients of hygroscopic swelling β_x are close, 0.036 and 0.044, respectively. Both values are slightly higher than the experimental value obtained via linear regression 0.060 ± 0.018. Such discrepancy is reasonable considering the low determination coefficient in the linear regression of experimental data (0.3110) and low strains involved resulting in larger experimental data scatter.

Numerical FE and analytical prediction as well as experimental results are shown in Table 1 and Figure 7.
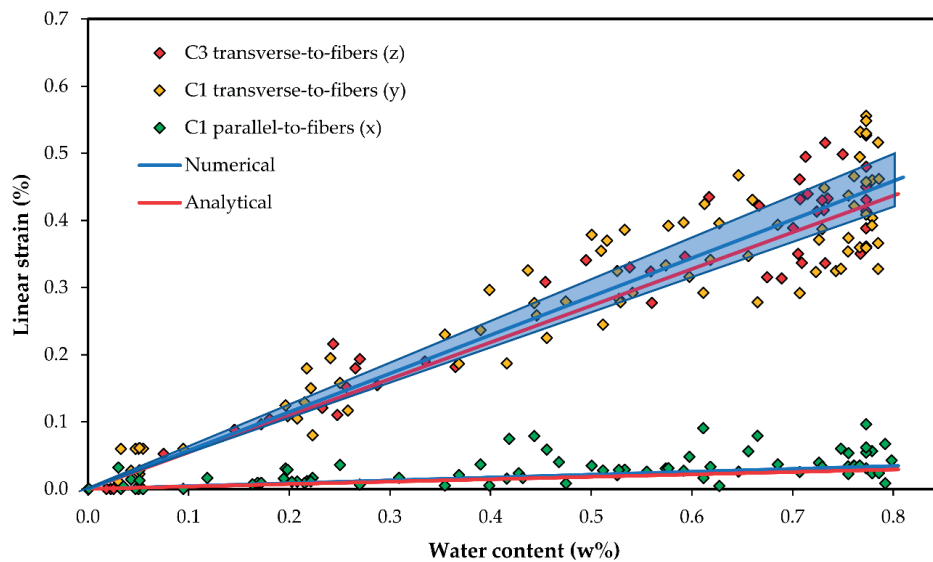
Figure 7. Numerical and analytical fit of swelling with the experimental data for composites. Analytical results are shown in red lines; global averaged out numerical results are shown in blue lines, while a numerical scatter is shown with blue sectors indicating scatter on the local scale due to various fiber arrangements.

Table 1. Coefficients of hygroscopic expansion. Experimental scatter is reported with one standard deviation for the coefficient of hygroscopic expansion (CHE). * indicates an input parameter for the models.

CHE	Experimental	Analytical	Numerical
β_m	0.332 ± 0.021	0.332 *	0.332 *
β_X	0.060 ± 0.018	0.036	0.044
β_Y	0.569 ± 0.066	0.546	0.552
β_Z	0.576 ± 0.059	0.546	0.573

The numerical scatter was obtained using five RVEs of the same fiber volume fraction with random fiber distribution to assess swelling on the local scale. On the global scale, these effects are averaged out. The predicted numerical scatter 0.552 ± 0.036 and 0.573 ± 0.049 for numerically obtained β_y and β_z, respectively.

It is possible to notice that axial swelling coefficients obtained numerically, β_x, have quite low scatters on a local scale due to various fiber arrangements, while transverse coefficients, β_y and β_z, have higher scatters. This suggests that axial swelling is not strongly influenced by the fiber arrangement, while transverse swelling is sensible to the fiber distribution.

Variability of numerically predicted CHE values due to random fiber orientation is shown in Figures 8 and 9.

Figure 8. Swelling coefficients in transverse directions y and x for the five RVEs used in the simulations.

Figure 9. Swelling coefficient in axial direction, z, for the five RVEs used in the simulations.

Figure 10 shows the hygrothermal strains in RVE1. For the transverse directions, y and z, the swelling strains arise mainly in the matrix and are negligible in the fibers, since these do not swell. For the axial directio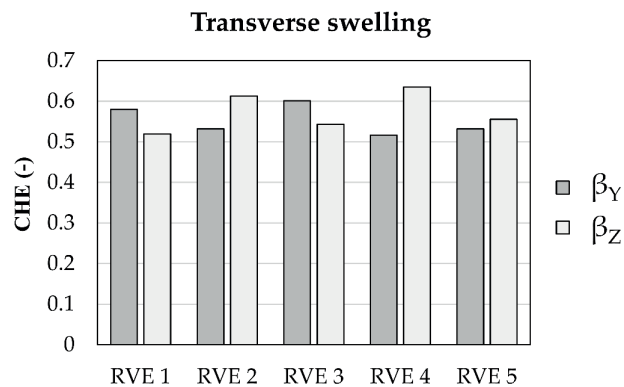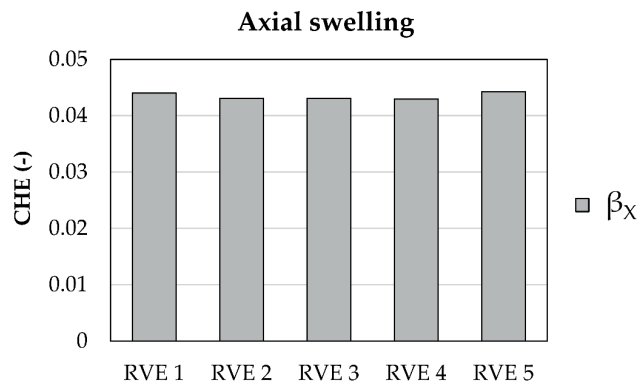n, however, it is possible to notice a very homogeneous strain field in the whole RVE, matrix and fibers are displaced together. This observation shows the validity of the assumption in the analytical section, where axial swelling is modelled as a parallel connection of fiber and matrix.
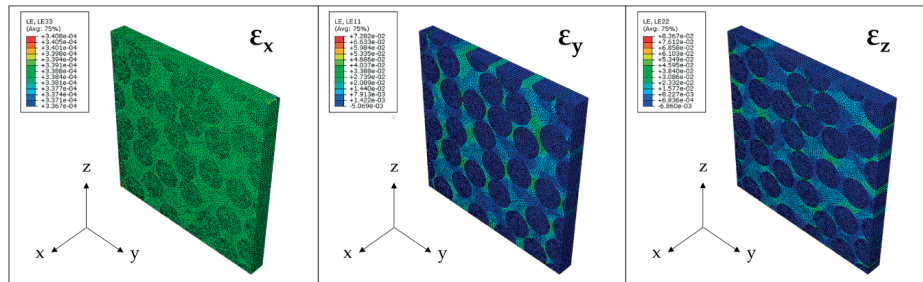

Figure 10. Swelling coefficient in axial direction, z, for the five RVEs used in the simulations.

5. Discussion

From the experimentally obtained hygroscopic swelling data (Figure 5), it can be deduced that the isotropic coefficient of hygroscopic swelling of the polymer matrix β_m is 0.322. For composite plates hygroscopic swelling occurred freely in the transverse-to-the-fibers direction. As expected, obtained values of β_y (0.569 ± 0.066) and β_z (0.576 ± 0.059) for both composite plates C1 and C3 were very similar. These values can be predicted from the matrix polymer (β_m = 0.322), considering that fibers are not affected by swelling and the volume fraction of the matrix in these composites was 0.394. Hygroscopic strains determined in the direction of the fibers are considered to be consistent with the hypothesis that hygroscopic strains in the fiber direction in composites are very low, but nevertheless they were found to be non-zero.

Furthermore, analytical and numerical approaches show a good agreement. The analytical model predicts the coefficient of hygroscopic swelling well within the experimental scatter. The experimental scatter includes errors due to (1) weighing, (2) determination of dimensional change and (3) variations between the samples. The experimental fit curve is a mean of all these considerations. Analytical results are based on the mean values of V_f, β_m, E_f, E_m. It fits the experimental mean curve fairly well, and is clearly within the experimental scatter.

The analytical model, however, does not consider the effect of fiber distribution for a known fiber fraction. The effect of fiber distribution on the coefficient of hygroscopic swelling can be accessed via FE simulations and the numerical scatter can be obtained. However, when a simplified and faster approach is needed, the analytical model is able provide a good prediction of hygroscopic swelling of composites using the properties of the polymer (β_m and E_m) and fibers (E_f). The observation that the simple analytical model gives practically the same results on swelling strains as experiments and more sophisticated FE analysis shows as a first approximation that the stiff fibers do not restrain expansion of the matrix transverse to the fibers. Furthermore, the effect of fiber distribution is important mostly on the local scale and would average out on the global scale. Such global results along with local numerical scatters are shown and compared with the experimental and analytical results in Figure 7. FE results were very similar to experimental and analytical results.

To the best understanding of the authors, there is no limitation to apply the model at various humidity levels. This is due to the fact that swelling behaviour is predicted from the microconstituent properties. The water uptake behaviour of a polymer matrix may be affected by different humidity levels. This would affect the concentration of water in the polymer, but to the best knowledge of the

authors this does not change the method of predicting the swelling of the composite from the swelling of the polymer.

The imperfections of the fiber–matrix interface are neglected in this model. While this is an assumption, the good agreement between experimental, numerical and analytical results indicates that this effect is negligible for the material system studied. For a more advanced model, there should be additional studies concerning this aspect.

In addition, the authors believe that it would be of interest to develop analytical models based on the same approach shown here not only for the fiber-reinforced composites, but also for other novel material systems such as polymer/clay composites [38] and multilayer nanocomposites of halloysite and biopolymers [39], that also possess a high mismatch in elastic properties of constituent materials.

6. Conclusions

Orthotropic water-induced or hygroscopic swelling of fiber-reinforced composite laminates can be predicted from the isotropic swelling data of the polymer (the matrix material of a composite). Swelling in composites shows a strong anisotropy, where swelling in the fiber direction is close to null, being constricted by non-expanding fibers, while swelling transverse to fibers behaves similarly to that of the unconstrained polymer. Good agreement was obtained and is reported between experimental swelling data, and analytical and numerical results for composite laminates, indicating the validity of this predictive approach. The analytical approach for predictions is the simplest to use, and good agreement with finite element analysis validates the use of this analytical tool for applications.

References

1. Krauklis, A.; Echtermeyer, A. Mechanism of yellowing: Carbonyl formation during hygrothermal aging in a common amine epoxy. *Polymers* **2018**, *10*, 1017. [CrossRef]
2. Xiao, G.Z.; Shanahan, M.E.R. Swelling of DGEBA/DDA epoxy resin during hygrothermal ageing. *Polymer* **1998**, *39*, 3253–3260. [CrossRef]
3. Toscano, A.; Pitarresi, G.; Scafidi, M.; Di Filippo, M.; Spadaro, G.; Alessi, S. Water diffusion and swelling stresses in highly crosslinked epoxy matrices. *Polym. Degrad. STable* **2016**, *133*, 255–263. [CrossRef]
4. Grabovac, I.; Whittaker, D. Application of bonded composites in the repair of ships structures—A 15-year service experience. *Compos. Part A* **2009**, *40*, 1381–1398. [CrossRef]
5. McGeorge, D.; Echtermeyer, A.T.; Leong, K.H.; Melve, B.; Robinson, M.; Fischer, K.P. Repair of floating offshore units using bonded fibre composite materials. *Compos. Part A* **2009**, *40*, 1364–1380. [CrossRef]
6. Gustafson, C.G.; Echtermeyer, A. Long-term properties of carbon fibre composite tethers. *Int. J. Fatigue.* **2006**, *28*, 1353–1362. [CrossRef]
7. Salama, M.M.; Stjern, G.; Storhaug, T.; Spencer, B.; Echtermeyer, A. The First Offshore Field Installation for a Composite Riser Joint. OTC-14018-MS. In Proceedings of the Offshore Technology Conference, Houston, TX, USA, 6–9 May 2002; Offshore Technology Conference: Houston, TX, USA, 2002. [CrossRef]

8. Echtermeyer, A.T.; Gagani, A.I.; Krauklis, A.E.; Mazan, T. Multiscale Modelling of Environmental Degradation—First Steps. In *Durability of Composites in a Marine Environment 2. Solid Mechanics and Its Applications*; Davies, P., Rajapakse, Y.D.S., Eds.; Springer: Cham, Switzerland, 2018; Volume 245, pp. 135–149, ISBN 978-3-319-65145-3.

9. Krauklis, A.E.; Gagani, A.I.; Echtermeyer, A.T. Hygrothermal aging of amine epoxy: Reversible static and fatigue properties. *Open Eng.* **2018**, *8*, 447–454. [CrossRef]

10. Ibarra, L.; Chamorro, C. Short fiber–elastomer composites. Effects of matrix and fiber level on swelling and mechanical and dynamic properties. *J. Appl. Polym. Sci.* **1991**, *43*, 1805–1819. [CrossRef]

11. Zhou, J. Transient analysis on hygroscopic swelling characterization using sequentially coupled moisture diffusion and hygroscopic stress modeling method. *Microelectron. Reliab.* **2008**, *48*, 805–810. [CrossRef]

12. Krauklis, A.E.; Gagani, A.I.; Echtermeyer, A.T. Near-Infrared spectroscopic method for monitoring water content in epoxy resins and fiber-reinforced composites. *Materials* **2018**, *11*, 586. [CrossRef]

13. Hahn, H.T.; Kim, R.Y. Swelling of Composite Laminates. In *Advanced Composite Materials: Environmental Effects*; ASTM STP 658; American Society for Testing and Materials: Philadelphia, PA, USA, 1978; pp. 98–120.

14. Shirangi, M.H.; Michel, B. Mechanism of moisture diffusion, hygroscopic swelling, and adhesion degradation in epoxy molding compounds. In *Moisture Sensitivity of Plastic Packages of IC Devices*; Fan, X.J., Suhir, E., Eds.; Springer: New York, NY, USA, 2010; pp. 29–69, ISBN 978-1-4419-5719-1.

15. Tsai, S.W. *Composites Design*, 4th ed.; Think Composites: Dayton, OH, USA, 1988; ISBN 0-9618090-2-7.

16. Obeid, H.; Clément, A.; Fréour, S.; Jacquemin, F.; Casari, P. On the identification of the coefficient of moisture expansion of polyamide-6: Accounting differential swelling strains and plasticization. *Mech. Mater.* **2018**, *118*, 1–10. [CrossRef]

17. Cairns, D.S.; Adams, D.F. Moisture and thermal expansion properties of unidirectional composite materials and the epoxy matrix. *J. Reinf. Plast. Compos.* **1983**, *2*, 239–255. [CrossRef]

18. Ashton, J.E.; Halpin, J.C.; Petit, P.H. *Primer on Composite Materials Analysis*; Technomic Pub. Co.: Stamford, CT, USA, 1969; ISBN 978-0-8776-2754-8.

19. Halpin, J.C. *Effects of Environmental Factors on Composite Materials*; Technical report AFML-TR-67–423; Air Force Materials Laboratory: Dayton, OH, USA, 1969.

20. Schapery, R.A. Thermal expansion coefficients of composite materials based on energy principles. *J. Compos. Mater.* **1968**, *2*, 380–404. [CrossRef]

21. Coran, A.Y.; Boustany, K.; Hamed, P. Unidirectional fiber-polymer composites: Swelling and modulus anisotropy. *J. Appl. Polym. Sci.* **1971**, *15*, 2471–2485. [CrossRef]

22. Daniels, B.K. Orthotropic swelling and simplified elasticity laws with special reference to cord-reinforced rubber. *J. Appl. Polym. Sci.* **1973**, *17*, 2847–2853. [CrossRef]

23. Fan, Y.; Gomez, A.; Ferraro, S.; Pinto, B.; Muliana, A.; La Saponara, V. Diffusion of water in glass fiber reinforced polymer composites at different temperatures. *J. Compos. Mater.* **2018**, 1–14. [CrossRef]

24. Jacquemin, F.; Fréour, S.; Guillén, R. Analytical modeling of transient hygro-elastic stress concentration—Application to embedded optical fiber in a non-uniform transient strain field. *Compos. Sci. Technol.* **2006**, *66*, 397–406. [CrossRef]

25. Meng, M.; Rizvi, M.J.; Le, H.R.; Grove, S.M. Multi-scale modelling of moisture diffusion coupled with stress distribution in CFRP laminated composites. *Compos. Struct.* **2016**, *138*, 295–304. [CrossRef]

26. Sinchuk, Y.; Pannier, Y.; Gueguen, M.; Tandiang, D.; Gigliotti, M. Computed-tomography based modeling and simulation of moisture diffusion and induced swelling in textile composite materials. *Int. J. Solids Struct.* **2018**, *154*, 88–96. [CrossRef]

27. Sinchuk, Y.; Pannier, Y.; Gueguen, M.; Gigliotti, M. Image-based modeling of moisture-induced swelling nd stress in 2D textile composite materials using a global-local approach. *Proc. Inst. Mech. Eng. Part C J. Mech. Eng. Sci.* **2018**, *232*, 1505–1519. [CrossRef]

28. Weitsman, Y.J. *Fluid Effects in Polymers and Polymeric Composites*; Springer: New York, NY, USA, 2012; ISBN 978-1-4614-1059-1.

29. Weitsman, Y.J.; Elahi, M. Effects of fluids on the deformation, strength and durability of polymeric composites—An overview. *Mech. Time-Depend. Mater.* **2000**, *4*, 107–126. [CrossRef]

30. Sar, B.E.; Fréour, S.; Davies, P.; Jacquemin, F. Accounting for differential swelling in the multi-physics modelling of the diffusive behaviour of polymers. *J. Appl. Math. Mech.* **2014**, *94*, 452–460. [CrossRef]

31. Fan, Y.; Gomez, A.; Ferraro, S.; Pinto, B.; Muliana, A.; La Saponara, V. The effects of temperatures and volumetric expansion on the diffusion of fluids through solid polymers. *J. Appl. Polym. Sci.* **2017**, *134*, 45151–45165. [CrossRef]

32. Kappert, E.J.; Raaijmakers, M.J.T.; Tempelman, K.; Cuperus, F.P.; Ogieglo, W.; Benes, N.E. Swelling of 9 polymers commonly employed for solvent-resistant nanofiltration membranes: A comprehensive dataset. *J. Membr. Sci.* **2019**, *569*, 177–199. [CrossRef]

33. Ramirez, F.A.; Carlsson, L.A.; Acha, B.A. Evaluation of water degradation of vinylester and epoxy matrix composites by single fiber and composite tests. *J. Mater. Sci.* **2008**, *43*, 5230–5242. [CrossRef]

34. Shirell, C.D.; Halpin, J. Moisture Absorption in Epoxy Composite Materials. In Proceedings of the Composite Materials: Testing and Design (Fourth Conference), ASTM STP617, Valley Forge, PA, USA, 3–4 May 1977; American Society for Testing and Materials: Philadelphia, PA, USA, 1979; pp. 514–528. [CrossRef]

35. Agarwal, B.D.; Broutman, L.J. *Analysis and Performance of Fiber Composites*, 2nd ed.; John Wiley & Sons, Inc.: Hoboken, NJ, USA, 1990; ISBN 978-0-4715-1152-6.

36. González, C.; Llorca, J. Mechanical behavior of unidirectional fiber-reinforced polymers under transverse compression: Microscopic mechanisms and modeling. *Compos. Sci. Technol.* **2007**, *67*, 2795–2806. [CrossRef]

37. Yang, L.; Yan, Y.; Ma, J.; Liu, B. Effects of inter-fiber spacing and thermal residual stress on transverse failure of fiber-reinforced polymer–matrix composites. *Comput. Mater. Sci.* **2013**, *68*, 255–262. [CrossRef]

38. Yamabe, K.; Goto, H. Synthesis and surface observation of montmorillonite/polyaniline composites. *J. Comp. Sci.* **2018**, *2*, 15. [CrossRef]

39. Bertolino, V.; Cavallaro, G.; Milioto, S.; Parisi, F.; Lazzara, G. Thermal properties of multilayer nanocomposites based on halloysite nanotubes and biopolymers. *J. Comp. Sci.* **2018**, *2*, 41. [CrossRef]

PAPER V

KRAUKLIS A.E., ECHTERMEYER A.T.

LONG-TERM DISSOLUTION OF GLASS FIBERS IN WATER DESCRIBED BY DISSOLVING CYLINDER ZERO-ORDER KINETIC MODEL: MASS LOSS AND RADIUS REDUCTION.

PAPER V

Andrey E. Krauklis* Andreas T. Echtermeyer

Long-Term Dissolution of Glass Fibers in Water Described by Dissolving Cylinder Zero-Order Kinetic Model: Mass Loss and Radius Reduction

Abstract: Glass fibers are degraded when they are exposed to water. In this work, a model is developed that uses zero-order kinetics for predicting a decreasing glass fiber radius. The model is used to describe experimental test results of almost half a year long-term dissolution of R-glass fibers. The model is able to predict both mass loss and radius reduction kinetics using the same four parameters: initial fiber radius (r_o), rate constants for both short-term degradation (K_0^I) and steady-state degradation (K_0^{II}) and the time when steady-state kinetics are reached (t_{st}). All parameters can be easily determined from initial radius measurements and mass loss evolution in time. Elements released and detected during degradation were Na, K, Ca, Mg, Fe, Al, Si and Cl. Rate constants were obtained for individual ion release and for the total mass loss. The contribution of Si to the total mass loss was the largest (56.1% by mass). It governed the dissolution process. The kinetics of radius reduction are also reported. The radius reduction was found to be linear with time during the steady-state dissolution. The zero-order kinetic constant and the density of the glass describe the rate (proportionality) of the dissolution.

Keywords: glass fibers; model; dissolution; kinetics; ion release.

1 Introduction

Glass fibers are widely used as reinforcement in structural composite materials. They are produced from raw materials, which are virtually unlimited in supply [1]. The fibers have high hardness and such desirable reinforcement properties as high strength and stiffness in fiber direction [1,2]. It is known that, glass fibers are hydrophilic and are susceptible to a relatively slow degradation when exposed to water environments [3]. Hydrolytic degradation of glass fibers can significantly reduce mechanical strength and leads to corrosion-induced defects [4].

The term degradation is used in the present work to denote all processes which lead to or affect the mass loss of the glass material by interacting with water. This includes the complex nature of several processes occurring in parallel, such as dissolution of glass matrix constituents, gel layer formation, neoformation of solid reaction products, alkaline and alkaline earth ion exchange. Some of these reactions occur while maintaining the glassy state, while others lead to leaching of the reaction products into the water environment [5].

The long-term environmental degradation of glass materials, described by chemical kinetics, has been extensively studied with respect to nuclear waste applications [5,6]. More recently, there has been an increasing interest in environmental degradation of composite laminates, where R-glass is often used as reinforcement [7-10]. However, studies on environmental degradation of composites are usually concerned with deterioration of the mechanical properties, and the kinetics of chemical degradation tend to be overlooked [8,10]. A number of studies exist that explain general mechanisms of environmental degradation of glass materials using various approaches that are based on surface reactions, chemical affinity and diffusion [3,11-14]. A process-driven approach was described by Geisler-Wierwille et al., involving the congruent dissolution of the glass coupled to the precipitation and growth of an

---

*Corresponding author: Andrey E. Krauklis, Department of Mechanical and Industrial Engineering, Norwegian University of Science and Technology, 7491 Trondheim, Norway, E-mail: andrejs.krauklis@ntnu.no
Andreas T. Echtermeyer: Department of Mechanical and Industrial Engineering, Norwegian University of Science and Technology, 7491 Trondheim, Norway

amorphous silica layer at an inwardly moving reaction interface [12]. More recently, a combination of chemical affinity for controlling the distribution of Si among different alteration phases and the diffusion barrier for the release rate of glass modifiers was implemented by Ma et al. [14]. Dissolution experiments in existing studies are mainly performed with bulk silicate glasses, and fibers are not studied often.

Few studies exist on the kinetics of glass fiber dissolution. Mišíková et al. have studied the E-glass fiber leaching kinetics in distilled water at different temperatures [15]. Bashir et al. studied the kinetics of the dissolution of E-glass fibres in alkaline solutions by immersing single fibers and measuring the diameter change [16]. They concluded that the rate limiting step was either the diffusion of hydroxide ions through the solution or the glass fibre etching itself [16]. Krauklis and Echtermeyer presented a model that predicts Si loss kinetics during long-term hygrothermal aging of fiber-reinforced composites [17]. Glass fibers formulated with significant amounts of various metal oxides, such as R-glass (often used in composites), are rarely studied [16]. Thus, this work is concerned with the dissolution kinetics of R-glass fibers in water.

The degradation is divided into two distinct kinetic regions: (1) short-term non-steady-state and (2) long-term steady-state degradation. In the short-term region, the degradation is complex and involves such processes as ion exchange, gel formation and dissolution [5]. When the long-term steady-state is reached, the dissolution becomes dominant [5,18] and the degradation follows zero-order reaction kinetics. Such kinetics depend on the glass surface area in contact with water, which is proportional to the fiber radius. As the dissolution continues, the radius decreases resulting in the mass loss deceleration.

The aim of this work is twofold: (1) to study the long-term dissolution behaviour of R-glass fibers in water and (2) to develop a model that describes the mass loss and fiber radius reduction kinetics during dissolution.

2 Theory – dissolution kinetic models

Different models are used for describing dissolution kinetics of various materials such as zero-order, first-order, advection/dispersion/reaction, GRAAL (Glass Reactivity with Allowance for the Alteration Levels), Noyes-Whitney, Hixson-Crowell, Hopfenberg and Korsmeyer-Peppas models, as well as similar in concept shrinking or contracting cylinder models [5,16,18-20]. Much of the confusion related to the modelling of degradation of glass fibers is due to the fact that dissolution is not the only process involved in degradation. The discrepancies between models are, however, mostly dominant in the short-term [5]. The whole degradation versus time curve is not linear as long as the complex processes take place. The model reported in this work is similar in concept to an existing solid-state model called the contracting cylinder [20] or shrinking cylinder [16], which relates the evolution of conversion to time. However, the novel model presented in this work differentiates between the complex short-term and dissolution-dominated long-term processes. Furthermore, the novel model describes both dissolution and radius reduction kinetics without the necessity for introducing additional terms such as a conversion factor. Rate constants are often given in relation to the surface area of a material, thus describing dissolution behaviour from a unit of the material's surface area [14]. Surface area-based constants are used throughout this work.

3 Experimental

3.1 Materials

Boron-free and fluorine-free HiPer-tex W2020 glass fiber (GF) bundles were used. These are classified as high strength, high modulus R-glass (defined by an international standard [21]). The density is 2.54 g/cm³; the mean filament diameter is 17 ± 2 μm [22].

Deionized water (0.5-1.0 MΩ·cm) was used for conditioning of the glass fibers. It was produced by using the water purification system Aquatron A4000 (Cole-Parmer, USA). The pH of the deionized water was determined to be 5.65, which is lower than neutral due to dissolved CO_2 (in equilibrium).

3.2 Determination of number of fibers in the sample

The amount of fibers is denoted as n. The length of fibers is $l = 0.1$ m; the initial mass of a fiber bundle is m_0=5.8 g; the mean initial radius is r_0=8.5• 10^{-6} m. The amount of fibers was calculated using Equation 1:

$$n = \frac{m_0}{\rho_{glass}\pi l r_0^2} \tag{1}$$

The amount of fibers in the sample n was determined to be 100602.

3.3 Determination of surface area of the sample

Since a surface reaction is of interest, it is important to identify the specific surface area of the glass material. The external surface area of glass fibers was evaluated from geometrical considerations as a product of number, circumference and length of fibers. The specific surface area of a studied sample can be calculated using Equation 2:

$$S_0^{specific} = \frac{S_0}{m_0} = \frac{2\pi n l r_0}{m_0} \qquad (2)$$

Specific surface area $S_0^{specific}$ was determined to be 0.09 (m^2/g).

3.4 Dissolution experiments

Dissolution in water experiments of glass fibers were conducted using a batch system. Basically, infinite water availablity conditions were ensured by using fresh deionized water for each separate measurement. The ion release with time (dissolution) was obtained as the cumulative result of the individual ion release measurements.

The dissolution of ions was accelerated by conditioning the fibers at an elevated temperature of 60 °C, since the dissolution reaction is an exothermic reaction [5,6,18]. The temperature of 60°C is often used for conditioning fiber-reinforced composites, and this fact provided an additional justification for choosing this particular temperature. The water´s temperature was controlled via PID-controlled heating, giving an accuracy of ± 1°C. Two-stage heating system was used in order to ensure that there is no contact of the sample water with other potential ion release sources, such as the heating element itself.

Samples were weighed using analytical scales AG204 (± 0.1 mg; Mettler Toledo, USA) before the experiments. Experiments were performed with 3 parallels.

The concentration of the dissolved ions in the water bach was measured by high resolution inductively coupled plasma mass spectrometry (HR-ICP-MS). Analyses were performed using a double focusing magnetic sector field ICP-MS Finnigan ELEMENT 2 (Thermo-Scientific), equipped with a sample introduction system PrepFAST (ESI/Elemental Scientific) and a pretreatment/digestion UltraClave (Milestone). Acidification of samples was performed using ultra-pure grade HNO_3 SubPur (Milestone) to avoid adsorption of ions to the wall of the sample vials.

The benefit of HR-ICP-MS versus gravimetric analysis is that the model can be applied to obtain the rate constant (K_0) of each ion separately, as well as for the total mass loss ($m_{dissolved}$). The data obtained from the HR-ICP-MS experiments are in the form of mass concentration at each time point (non-cumulative) c (g/L) and need to be converted to the $m_{dissolved}$ form by using Equation 3:

$$m_{dissolved} = V_{water} \int_0^t c \, dt \qquad (3)$$

where V_{water} is the volume of a water sample in the HR-ICP-MS measurement. V_{water} used for experiments was 50 mL. Equation 3 is valid for each individual ion release and for the total mass loss.

3.5 Radius reduction measurements.

R-glass fibers were immersed in deionized water for prolonged periods of time, carefully dried with a paper tissue, and the fiber diameter was measured using a digital microscope RH-2000 (Hirox, Japan). The radii of around five fibers were measured at each time, and for each fiber, measurements of radii were made at three different locations, similarly as was done in another work [16].

Ethical approval: The conducted research is not related to either human or animal use.

4 Results and Discussion

4.1 Elements released and respective chemical reactions

The HR-ICP-MS method identified the following elements as being released during glass fiber degradation in deionized water: Na, K, Ca, Mg, Fe, Al, Si, Cl. Release of B and Zn was found to be insignificant at less than 0.8 ppm, if the elements were present at all.
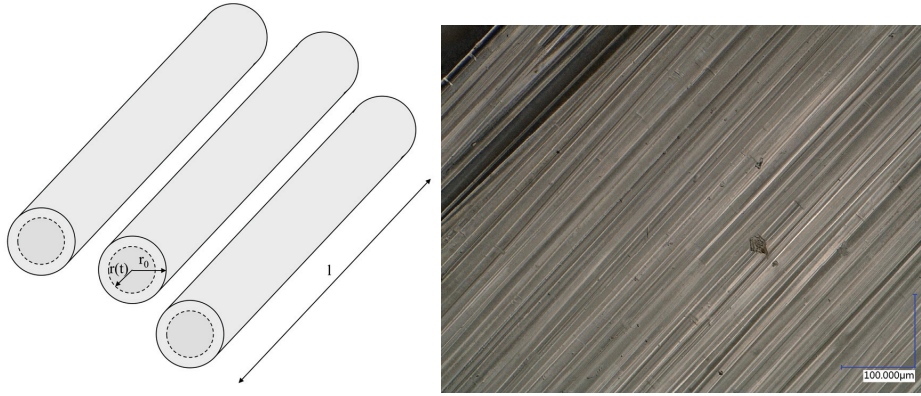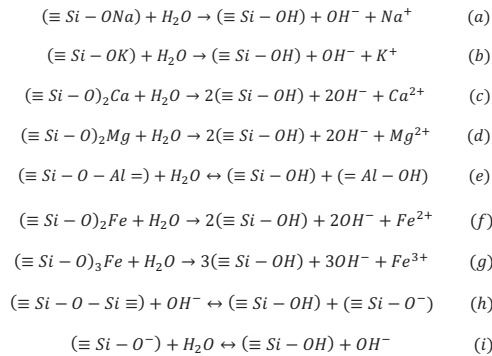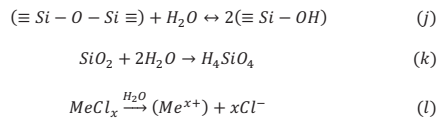
Figure 1: Left: Schematic representation of a fiber bundle and geometrical dimensions. Right: micrograph of a fiber bundle.

Chemical reactions involved in the degradation of the studied glass fibers for the identified released elements are shown in Chemical reactions (a)-(l) [5,18,23]:

$$(\equiv Si - ONa) + H_2O \rightarrow (\equiv Si - OH) + OH^- + Na^+ \qquad (a)$$

$$(\equiv Si - OK) + H_2O \rightarrow (\equiv Si - OH) + OH^- + K^+ \qquad (b)$$

$$(\equiv Si - O)_2Ca + H_2O \rightarrow 2(\equiv Si - OH) + 2OH^- + Ca^{2+} \qquad (c)$$

$$(\equiv Si - O)_2Mg + H_2O \rightarrow 2(\equiv Si - OH) + 2OH^- + Mg^{2+} \qquad (d)$$

$$(\equiv Si - O - Al =) + H_2O \leftrightarrow (\equiv Si - OH) + (= Al - OH) \qquad (e)$$

$$(\equiv Si - O)_2Fe + H_2O \rightarrow 2(\equiv Si - OH) + 2OH^- + Fe^{2+} \qquad (f)$$

$$(\equiv Si - O)_3Fe + H_2O \rightarrow 3(\equiv Si - OH) + 3OH^- + Fe^{3+} \qquad (g)$$

$$(\equiv Si - O - Si \equiv) + OH^- \leftrightarrow (\equiv Si - OH) + (\equiv Si - O^-) \qquad (h)$$

$$(\equiv Si - O^-) + H_2O \leftrightarrow (\equiv Si - OH) + OH^- \qquad (i)$$

Combining chemical reactions (h) and (i), a summary reaction can be written as Chemical reaction (j):

$$(\equiv Si - O - Si \equiv) + H_2O \leftrightarrow 2(\equiv Si - OH) \qquad (j)$$

$$SiO_2 + 2H_2O \rightarrow H_4SiO_4 \qquad (k)$$

$$MeCl_x \xrightarrow{H_2O} (Me^{x+}) + xCl^- \qquad (l)$$

4.2 Zero-order kinetic model of a dissolving cylinder

A schematic representation of a fiber bundle and important dimensions for the model are shown in Figure 1.

The number of fibers is n (-); the initial radius of the fibers is r_0 (m); the length of fibers is l (m).

The model involves the following assumptions. As a simplification, this model is deterministic and all fibers are assumed to have the same initial radius, which is r_0; and the cross-sectional surface area at the end of the fibres is assumed to be negligible in calculations of the surface area. The length of the long fibers l is assumed to be constant during the whole dissolution process. During the whole degradation process, the density of the glass material stays constant (ρ_{glass}).

Dissolution is a surface reaction. In a general case, the rate of the dissolution is dependent on the constant describing the rate of the reaction (K_0), the glass surface area exposed to water (S), the availability of water (C_{H_2O}) and the order of the reaction ($n_{reaction}$). The global model (general case) can then be mathematically expressed as Equation 4.

$$\frac{\partial m}{\partial t} = K_0 S C_{H_2O}^{n_{reaction}} \qquad (4)$$

In case of infinite availability of water, the rate of reaction becomes independent of the reactant (water) concentration, and the reaction order $n_{reaction}$ becomes 0. In infinite water availability conditions, the surface reaction can be well-described with zero-order kinetics [16,24], which can then be represented by a differential Equation 5:

$$\frac{\partial m}{\partial t} = K_0 S \qquad (5)$$

where m(g) is a total cumulative mass dissolved after time t (s), K_0 (g/m²•s) is a zero-order reaction kinetic constant and S (m²) is the glass surface area in contact with water.

As the reaction proceeds, the radius of the fibers is reduced and the total surface area (S) is decreased, thus leading to a decrease in the rate of mass loss as seen in Equation 5. The overall ion release rate decreases proportionally to the decrease in total surface area or a decrease in fiber radius.

$$\frac{S(t)}{S_0} = \frac{2\pi n l r(t)}{2\pi n l r_0} = \frac{r(t)}{r_0} \tag{6}$$

It can be seen that $\frac{S(t)}{S_0} = \frac{r(t)}{r_0}$. Thus, the ion release rate decelerates linearly with a decrease in fiber radius. The mass loss has to slow down as the available surface area is reduced. Thus, the cumulative mass loss kinetic curve deviates from a linear dissolution.

The volume of a single fiber is $\pi r^2 l$, where l is the cylinder length and r is the cylinder radius. For n fibers, the volume is $\pi r^2 l$ and mass is $\rho_{glass} n \pi r^2 l$. The surface area of a single fiber is $2n\pi r l$. For n fibers it is $2n\pi r l$. Substituting mass and surface area expressed in such terms into Equation 5,

$$\frac{\partial \rho_{glass} n \pi r^2 l}{\partial t} = K_0 \cdot 2n\pi r l \tag{7}$$

$$\frac{\partial r^2}{\partial t} = \frac{2K_0}{\rho_{glass}} r \tag{8}$$

Substituting then r^2 with the following $z = r^2$,

$$\frac{\partial z}{\partial t} = \frac{2K_0}{\rho_{glass}} \sqrt{z} \tag{9}$$

where $\frac{2K_0}{\rho_{glass}}$ is a constant. Dividing both sides by $\sqrt{z}$,

$$\frac{\frac{\partial z}{\partial t}}{\sqrt{z}} = \frac{2K_0}{\rho_{glass}} \tag{10}$$

Both sides are then integrated with respect to t,

$$\int \frac{\frac{\partial z}{\partial t}}{\sqrt{z}} dt = \int \frac{2K_0}{\rho_{glass}} dt \tag{11}$$

Integrating and solving for $\sqrt{z}$,

$$\sqrt{z} = \frac{1}{2}\left(\frac{2K_0}{\rho_{glass}} t + c'\right) \tag{12}$$

$$\sqrt{z} = \frac{K_0}{\rho_{glass}} t + c'' \tag{13}$$

where c' and c'' are arbitrary constants after integration. Substituting r^2 back into the equation:

$$\sqrt{r^2} = \frac{K_0}{\rho_{glass}} t + c'' \tag{14}$$

$$\pm r = \frac{K_0}{\rho_{glass}} t + c'' \tag{15}$$

It can be seen that the radius reduction is linear with time, where the proportionality is given by the zero-order kinetic constant K_0 (g/m²•s) and the density of the glass (g/m³). A linear radius reduction of fibers with time was previously experimentally observed in another work [16]. Since the radius reduction depends on the initial radius r_0 of the fibers (m), the arbitrary constant c'' (m) is equal to the initial radius.

The kinetic model equation for fiber radius reduction then becomes as shown in Equation 16:

$$r = r_0 - \frac{K_0}{\rho_{glass}} t \tag{16}$$

Returning to the mass loss kinetics (Equation 5),

$$\frac{\partial m}{\partial t} = K_0 S = K_0 \cdot 2n\pi r l \tag{5}$$

Substituting r for the radius reduction kinetic Equation 28, the final mass loss kinetic model equation in differential form is obtained (Equation 17):

$$\frac{\partial m}{\partial t} = 2n\pi l \left(r_0 K_0 - \frac{K_0^2}{\rho_{glass}} t\right) \tag{17}$$

Integrating the obtained Equation 17 over time t, the integral model equation is obtained, describing the cumulative mass loss (ion release):

$$m_{dissolved} = \int_0^t 2n\pi l \left(r_0 K_0 - \frac{K_0^2}{\rho_{glass}} t\right) dt \tag{18}$$
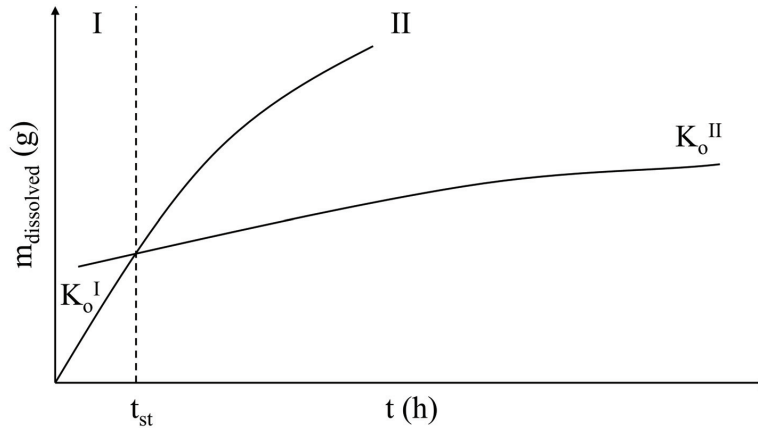
Figure 2: Separation of mass loss or cumulative ion release curves into (I) short-term non-steady-state and (II) long-term steady-state regions.

Definite integral solution is then the following (Equation 19):

$$m_{dissolved} = -\frac{1}{2} \cdot 2n\pi l \cdot t \left(\frac{K_0^2}{\rho_{glass}} t - 2r_0 K_0 \right) \quad (19)$$

The final mass loss model kinetic equation in the integral form is then the following (Equation 20):

$$m_{dissolved} = n\pi l \left(2r_0 K_0 t - \frac{K_0^2}{\rho_{glass}} t^2 \right) \quad (20)$$

The solution of Equation 20 is then checked using an alternative approach. Based on the mass conservation principle, mass loss in integral form can be also written as Equation 21:

$$m_{dissolved} = m_0 - m = \rho_{glass}\, n\pi l (r_0^2 - r^2) \quad (21)$$

Combining Equations 16 and 21,

$$m_{dissolved} = \rho_{glass}\, n\pi l \left(r_0^2 - \left(r_0 - \frac{K_0}{\rho_{glass}} t \right)^2 \right) =$$
$$= n\pi l \left(2r_0 K_0 t - \frac{K_0^2}{\rho_{glass}} t^2 \right) \quad (22)$$

The obtained Equation 22 is the same mass loss kinetic equation in the integral form as Equation 20. The use of two alternative mathematical ways to obtain

Equations 20 and 22 by the integration and by the mass conservation principle, respectively, has proven the mathematical consistency of the model. The fact that the model is adequate and physical was demonstrated by its ability to explain the experimentally observed dissolution phenomena as described later.

4.3 The model extended to short-term and long-term degradation.

The reaction kinetics described above apply for a dissolution-dominated process. As shown in the Chemical reactions (a)-(l), various competing reactions happen simultaneously. Initially these reactions happen at independent rates, later one process becomes limiting and dominates the behaviour. Therefore, the degradation process should be divided into a short-term non-steady-state process and a long-term steady-state process since the subprocesses involved follow individual kinetics and are likely interdependent contributing to the complexity of the short-term region. In the non-steady-state region the process is rather complex, involving in addition to dissolution also other competing leaching mechanisms such as ion exchange and gel formation, and thus cannot be properly described with only one kinetic equation [5,18]. The complexity and varying rates of the competing processes in the short-term make this stage of the degradation to be non-linear non-steady-state. In the long-term hygrothermal degradation of glass fibers, however, dissolution kinetics become dominant [5,18] and the process becomes then steady-state following the

Table 1: Model parameters and fit to experimental data (total mass loss $m_{dissolved}$).

K_0^I (g/m²•s)	K_0^{II} (g/m²•s)	t_{st} (h)	R² (t ≤ t_{st})	R² (t > t_{st})
3.00•10⁻⁹	6.68•10⁻¹⁰	166	0.8069	0.9653

Table 2: Model parameters for individual released ions and fit to experimental data.

	K_0^I (g/m²•s)	K_0^{II} (g/m²•s)	R² (t ≤ t_{st})	R² (t > t_{st})
Na	6.80•10⁻¹¹	1.80•10⁻¹¹	0.5326	0.9578
K	4.85•10⁻¹¹	9.80•10⁻¹²	0.5583	0.9211
Ca	8.72•10⁻¹⁰	9.70•10⁻¹¹	0.7256	0.9310
Mg	4.85•10⁻¹⁰	1.02•10⁻¹⁰	0.7164	0.9898
Fe	2.20•10⁻¹²	4.40•10⁻¹³	0.9261	0.8963
Al	1.45•10⁻¹⁰	4.68•10⁻¹¹	0.7596	0.9272
Si	1.10•10⁻⁹	3.80•10⁻¹⁰	0.9177	0.9781
Cl	7.80•10⁻¹¹	2.28•10⁻¹¹	0.6605	0.9572
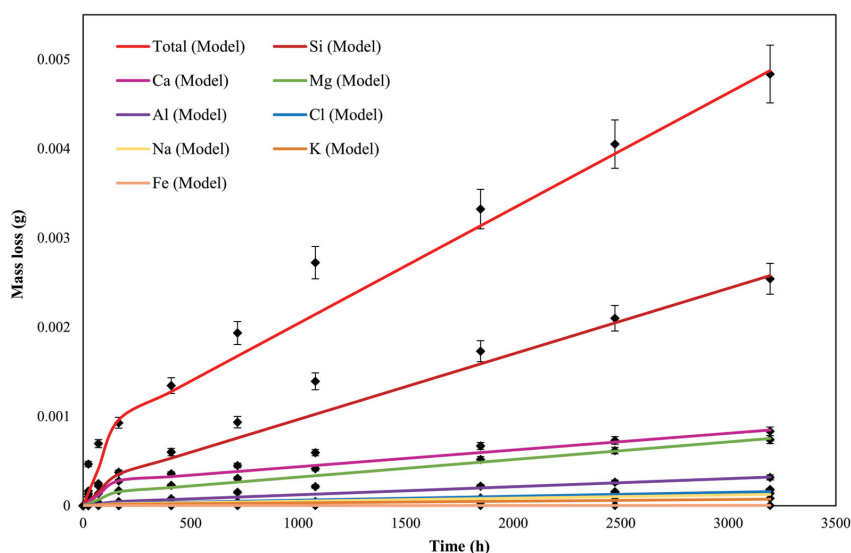
Figure 3: Experimental data and predicted ion release and total mass loss kinetics.

zero-order kinetics. In the long-term degradation, kinetic equations described above become physical.

When long-term degradation is of most interest, such as in this work, the shape of the non-linear short-term part is not important, an approximate solution can then be used to describe also the short-term non-steady-state stage with dissolving cylinder zero-order kinetic model. In case when short-term degradation is of most importance, kinetic models for each individual subprocesses (dissolution, ion exchange, gel formation) taking place in the short-term non-steady-state should be studied and implemented, and their influence on each other should be understood.

The fiber radius decreases at a constant rate (linearly) in time. However, the induction period before the linear regime is often observed [16], which can be explained with the complexity of the short-term non-steady-state process and, to the best knowledge of the authors, was not explained before.
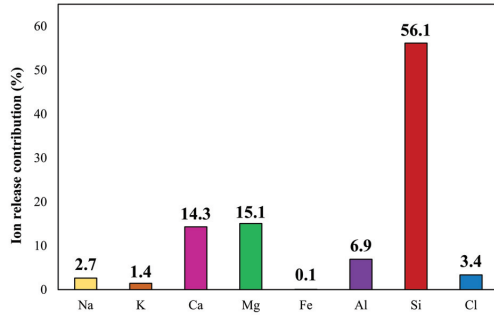
Figure 4: Comparison of ion release rates in the steady-state (values have been calculated from the rate constants in the steady-state).
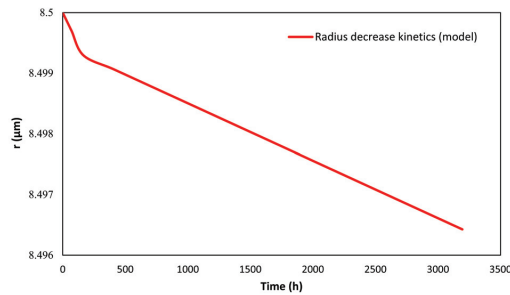

Figure 5: Modelled radius reduction in R-glass fibers after treatment in water at various times at 60°C.
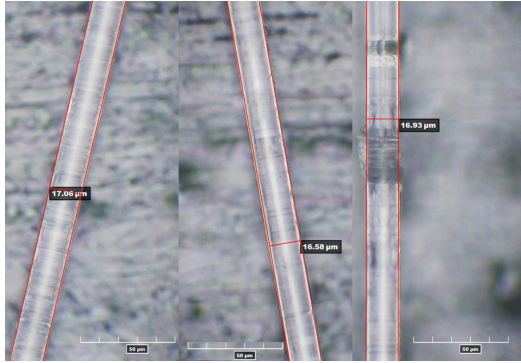
Figure 6: Digital microscope images of R-glass fibers from left to right: untreated; after 69 h in water at 60°C; after 3194 h in water at 60°C.

The whole process can be divided into two regions as shown in Figure 2 and can be described via four parameters: $r_0, t_{st}, K_0^I, K_0^{II}$.

Table 3: Predicted dissolution times for various mass and radius loss values at 60°C.

Time in water (years)	Mass loss (%)	Radius loss (%)
0.5	0.10	0.05
2.5	0.50	0.25
5.1	1.00	0.50
25.9	5.00	2.53
52.5	10.00	5.13
300.2	50.00	29.30
512.6	75.00	50.02
1025.1	100.00	100.00

The final model equations combining approximated non-steady-state short-term and physically-correct steady-state long-term dissolution kinetics are proposed.

The radius reduction kinetic model based on Equation 16 is shown in Equation 23:

$$\begin{cases} t \leq t_{st}: \quad r = r_0 - \dfrac{K_0^I}{\rho_{glass}} t \\ t > t_{st}: \quad r = r_{t_{st}} - \dfrac{K_0^{II}}{\rho_{glass}} (t - t_{st}) \end{cases} \quad (23)$$

The mass loss kinetic model based on Equation 20 is shown in Equation 24:

$$\begin{cases} t \leq t_{st}: \quad m_{dissolved} = n\pi l \left(2r_0 K_0^I t - \dfrac{K_0^{I\,2}}{\rho_{glass}} t^2 \right) \\ t > t_{st}: \quad m_{dissolved} = m_{dissolved_{t_{st}}} + n\pi l \left(2r_{t_{st}} K_0^{II} (t - t_{st}) - \dfrac{K_0^{II\,2}}{\rho_{glass}} (t - t_{st})^2 \right) \end{cases}$$

$$(24)$$

where K_0^I and K_0^{II} are the rate constants (g/m²•s) for the short-term non-steady-state and long-term steady-state regions, respectively; $r_{t_{st}}$(m) and $m_{dissolved_{t_{st}}}$ (g) are the fiber radius and lost mass after time t_{st} (s), when steady-state is reached.

4.4 Dissolution of R-glass fibers explained with the model

Experimentally $m_{dissolved}$ was measured as a sum of all ions' release quantified with HR-ICP-MS cumulatively over time. Alternatively, a gravimetric analysis over time can be used to obtain $m_{dissolved}$. Both kinetic parameters K_0^I and K_0^{II} are determined from obtained $m_{dissolved} - t$ curves by using the

described methodology in this work for each individual element, as well as for the total mass loss.

Ions released from the studied glass material are the following: Na, K, Ca, Mg, Fe, Al, Si, Cl. The total mass of all ions released is the cumulative mass loss, as shown by Equation 25:

$$m_{dissolved} = m_{dissolved_{Na}} + m_{dissolved_K} + m_{dissolved_{Ca}} + m_{dissolved_{Mg}} + m_{dissolved_{Fe}}$$
$$+ m_{dissolved_{Al}} + m_{dissolved_{Si}} + m_{dissolved_{Cl}} \tag{25}$$

The total mass loss is described by four parameters $(r_0, t_{st}, K_0^I, K_0^{II})$. For each ion, individual K_0^I and K_0^{II} values have to be obtained, while t_{st} and r_0 for each individual ion release are the same and are equivalent to that for the total mass loss.

From the cumulative data of ions released altogether $(m_{dissolved})$, the kinetic model parameters $(K_0^I$ and $K_0^{II})$ were obtained using non-linear regression for each separate ion as well as for the total mass loss curve. The Generalized Reduced Gradient (GRG) non-linear regression method was used by minimizing the sum of squares of the differences between modelled and experimental values. The obtained parameters and model fit to experimental data are systematized in Table 1. Obtained values are reasonable (similar order of magnitude) compared with dissolution rates of other glass fibers studied in literature [25].

Using the obtained t_{st}, these parameters are included in the model for each individual ion release (Na, K, Ca, Mg, Fe, Al, Si, Cl). K_0^I and K_0^{II} are obtained for each ion by regression of experimental data for each individual ion cumulative release curve. The same method of non-linear regression as described above was used in each case. The rate constants K_0^I and K_0^{II} for the identified released ions are systematized in Table 2. It should be noted that the R^2 values in the non-steady-state ($t \leq t_{st}$) are fairly low, while the fit is good in the steady-state region ($t > t_{st}$). As was mentioned earlier, this is because the model can only be used as a mathematical approximation in the non-steady-state, while it is physical in the steady-state long-term.

Experimental data and modelled curves for individual ion release and total mass loss are shown in Figure 3. Experimentally mass loss was obtained from HR-ICP-MS measurements for separate ions being released.

Rates of ion release during steady-state for the studied material are compared in Figure 4.

The contribution from Si to the total mass loss is the largest (56.1% by mass) and seems to govern the dissolution process. Ca and Mg are released at approximately similar rates to each other and contribute 14.3 and 15.1% to the

total mass loss, respectively, while all other elements contribute less than 7% individually. Once the steady-state is reached, it can be assumed that the reactions do not have any effect on each other and proceed at constant independent rates. It can be speculated that in the steady-state some equilibrium composition of glass (different from the bulk composition) is obtained in the outer layers that are contact with water, allowing elements to dissolve at some limiting rate and proportionally to their content in the outer layers of the glass.

Radius reduction in R-glass fibers after treatment in water at various times at 60°C predicted with the model is shown in Figure 5. The fiber radius decrease could not be captured with a digital microscope. Digital micrographs of fibers, untreated and treated in water are shown in Figure 6.

The lack of accuracy is reasonable, taking into account that the radius reduction predicted by the model in 3194 h time is only 0.0036 μm (0.04% radius loss) as seen in Figure 5, and the microscope resolution is 0.16 μm. Furthermore, a statistical error has to be considered since the radius is not perfectly equal in different locations of the fibers (as seen by discrepancy in measurements reported in Figure 6).

With the reaction rates obtained in this work, the full dissolution of the studied R-glass fibers would take 8.98•10⁶ h or 1025.1 years as reported in Table 3. The radius loss after 25 years, a typical design lifetime, would be 2.45%. These values are for 60°C. For lower temperatures, the radius reduction would be even less [5,6,18]. The effect of temperature on dissolution kinetics and the effect of cracks in the fibers of this particular glass material will be studied in the future.

5 Conclusions

In this study, the long-term (3194 h) dissolution of R-glass fibers in water was studied experimentally. A dissolving cylinder zero-order kinetic model was developed and successfully used to describe the kinetics of mass loss and the fiber's radius reduction during dissolution in water.

Elements released during degradation were determined to be Na, K, Ca, Mg, Fe, Al, Si and Cl. The total material loss and release of each separate ion was modelled using the developed kinetic equations, and rate constants were obtained and reported. The contribution of Si to the total mass loss was the largest (56.1% by mass) and governed the dissolution process.

The model differentiates between the complex short-term and dissolution-dominated long-term processes.

Furthermore, the novelty of the model is the ability to describe both dissolution and radius reduction kinetics without the necessity for introducing additional terms such as a conversion factor. The model is able to predict both mass loss and radius reduction kinetics using the same four parameters, which can be determined experimentally. The methodology provided in this work offers the guidelines to obtain the required parameters to use the model in practice. The developed model is useful for both monitoring the radius of degrading fibers and for monitoring the time evolution of the loss of material.

The radius reduction was found to be linear with time during dissolution when a steady-state is reached. The zero-order kinetic constant and the density of the glass describe the rate (proportionality) of the dissolution. Radius reduction predicted by the model in 3194 h time was only 0.0036 μm (0.04% radius loss) at 60°C and could not be captured with a microscope. The full dissolution of the studied R-glass fibers would take $8.98 \cdot 10^6$ h or 1025.1 years. The radius loss after 25 years, a typical design lifetime, would be 2.45%.

Conflict of interest: Authors declare no conflict of interest.

References

[1] Wallenberger F.T., Commercial and Experimental Glass Fibers, in: Fiberglass and Glass Technology, Eds: Wallenberger F.T., Bingham P.A., Springer, US, 2010.

[2] Steinmann W., Saelhoff A.-K., Essential Properties of Fibres for Composite Applications, in: Fibrous and Textile Materials for Composite Applications, Textile Science and Clothing Technology, Eds.: Rana S., Fangueiro R., Springer, Singapore, 2016.

[3] Tournié A., Ricciardi P., Colomban P., Glass Corrosion Mechanisms: A Multiscale Analysis, Solid State Ionics, 2008, 179(38), 2142-2154.

[4] Brown E.N., Davis A.K., Jonnalagadda K.D., Sottos N.R., Effect of surface treatment on the hydrolytic stability of E-glass fiber

bundle tensile strength, Compos. Sci. Technol., 2005, 65, 129–136.

[5] Grambow B., Müller R., First-order dissolution rate law and the role of surface layers in glass performance assessment, J. Nucl. Mater., 2001, 298(1-2), 112-124.

[6] Grambow B., A General Rate Equation for Nuclear Waste Glass Corrosion, Mat. Res. Soc. Symp. Proc., 1985, 44, 15-27.

[7] Krauklis A.E., Gagani A.I., Echtermeyer A.T., Near-Infrared Spectroscopic Method for Monitoring Water Content in Epoxy Resins and Fiber-Reinforced Composites, Materials, 2018, 11(4), 586-599.

[8] Stamenović M.R., Putić S.S., Rakin M.B., Medjo B., Čikara D., Effect of alkaline and acidic solutions on the tensile properties of glass–polyester pipes, Mater. Des., 2011, 32(4), 2456-2461.

[9] Krauklis A.E., Echtermeyer A.T., Mechanism of Yellowing: Carbonyl Formation during Hygrothermal Aging in a Common Amine Epoxy, Polymers, 2018, 10(9), 1017-1031.

[10] Amaro A.M., Reis P.N.B., Neto M.A., Louro C., Effects of alkaline and acid solutions on glass/epoxy composites, Polym. Degrad. Stab., 2013, 98(4), 853-862.

[11] Delage F., Ghaleb D., Dussossoy J.L., Chevallier O., Vernaz E., A mechanistic model for understanding nuclear waste glass dissolution, J. Nucl. Mater., 1992, 190, 191-197.

[12] Geisler-Wierwille T., Nagel T.J., Kilburn M.R., Janssen A., Icenhower J., Fonseca R.O.C., Grange M.L., Nemchin A.A., The Mechanism of Borosilicate Glass Corrosion Revisited, Geochim. Cosmochim. Acta, 2015, 158, 112-129.

[13] Icenhower J., Steefel C.I., Dissolution Rate of Borosilicate Glass SON68: A Method of Quantification Based upon Interferometry and Implications for Experimental and Natural Weathering Rates of Glass, Geochim. Cosmochim. Acta, 2015, 157, 147-163.

[14] Ma T., Jivkov A.P., Li W., Liang W., Wang Y., Xu H., Han X., A mechanistic model for long-term nuclear waste glass dissolution integrating chemical affinity and interfacial diffusion barrier, J. Nucl. Mater., 2017, 486, 70-85.

[15] Mišíková L., Liška M., Galusková D., CORROSION OF E-GLASS FIBERS IN DISTILLED WATER, Ceram. Silikaty, 2007, 51(3), 131-135.

[16] Bashir S.T., Yang L., Liggat J.J., Thomason J.L., Kinetics of dissolution of glass fibre in hot alkaline solution, J. Mater. Sci., 2018, 53(3), 1710-1722.

[17] Krauklis A.E., Echtermeyer A.T., Dissolving Cylinder Zero-Order Kinetic Model for Predicting Hygrothermal Aging of Glass Fiber Bundles and Fiber-Reinforced Composites, International Glass Fiber Symposium, 2018.

[18] Report RWM005105, AMEC/103498/02 Issue 2: Review of glass dissolution models and application to UK glasses, Didcot, 2015.

[19] Costa P., Sousa Lobo J.M., Review: Modeling and comparison of dissolution profiles, Eur. J. Pharm. Sci., 2001, 13, 123-133.

[20] Khawam A., Flanagan D.R., Solid-State Kinetic Models: Basics and Mathematical Fundamentals, J. Phys. Chem. B, 2006, 110, 17315-17328.

[21] International Standard ISO 2078:1993 (revised in 2014), Textile glass – Yarns – Designation, 2014.

[22] 3B Fibreglass technical data sheet. HiPer-tex W2020 rovings, Belgium, 2012.

[23] Li H., Gu P., Watson J., Meng J., Acid corrosion resistance and mechanism of E-glass fibers: boron factor, J. Mater. Sci., 2013, 48(8), 3075-3087.

[24] Čornaja S., Fizikālā ķīmija. Elektroķīmija. Kinētika, RTU
       Izdevniecība, Rīga, 2008, (in Latvian).
[25] Eastes W., Potter R.M., Hadley J.G., Estimating in-vitro glass
       fiber dissolution rate from composition, Inhal. Toxicol., 2000,
       12, 269-280.

PAPER VI

KRAUKLIS A.E., ECHTERMEYER A.T.

DISSOLVING CYLINDER ZERO-ORDER KINETIC MODEL FOR PREDICTING HYGROTHERMAL AGING OF GLASS FIBER BUNDLES AND FIBER-REINFORCED COMPOSITES.

Not included due to copyright restrictions

PAPER VI

Appendix G

Paper VII

Krauklis A.E., Gagani A.I., Vegere K., Kalnina I., Klavins M., Echtermeyer A.T.

Dissolution Kinetics of R-Glass Fibres: Influence of Water Acidity, Temperature, and Stress Corrosion.

Dissolution Kinetics of R-Glass Fibres: Influence of Water Acidity, Temperature, and Stress Corrosion

Andrey E. Krauklis [1,*] [ID], **Abedin I. Gagani** [1], **Kristine Vegere** [2], **Ilze Kalnina** [2], **Maris Klavins** [3] **and Andreas T. Echtermeyer** [1]

[1] Department of Mechanical and Industrial Engineering (past: Department of Engineering Design and Materials), Norwegian University of Science and Technology, 7491 Trondheim, Norway; abedin.gagani@ntnu.no (A.I.G.); andreas.echtermeyer@ntnu.no (A.T.E.)

[2] Institute of General Chemical Engineering, Faculty of Materials Science and Applied Chemistry, Riga Technical University, P. Valdena str. 3/7, Riga LV-1048, Latvia; kristine.rugele@rtu.lv (K.V.); ilzekalnina0@gmail.com (I.K.)

[3] Department of Environmental Science, University of Latvia, Riga LV-1004, Latvia; maris.klavins@lu.lv

* Correspondence: andrejs.krauklis@ntnu.no or andykrauklis@gmail.com; Tel.: +371-268-10288

![check for updates]

Abstract: Glass fibres slowly degrade due to dissolution when exposed to water. Such environmental aging results in the deterioration of the mechanical properties. In structural offshore and marine applications, as well as in the wind energy sector, R-glass fibre composites are continuously exposed to water and humid environments for decades, with a typical design lifetime being around 25 years or more. During this lifetime, these materials are affected by various temperatures, acidity levels, and mechanical loads. A Dissolving Cylinder Zero-Order Kinetic (DCZOK) model was able to explain the long-term dissolution of R-glass fibres, considering the influence of the pH, temperature, and stress corrosion. The effects of these environmental conditions on the dissolution rate constants and activation energies of dissolution were obtained. Experimentally, dissolution was measured using High Resolution Inductively Coupled Plasma Mass Spectrometry (HR-ICP-MS). For stress corrosion, a custom rig was designed and used. The temperature showed an Arrhenius-type influence on the kinetics, increasing the rate of dissolution exponentially with increasing temperature. In comparison with neutral conditions, basic and acidic aqueous environments showed an increase in the dissolution rates, affecting the lifetime of glass fibres negatively. External loads also increased glass dissolution rates due to stress corrosion. The model was able to capture all of these effects.

Keywords: glass; fibres; model; dissolution; kinetics; water; environmental; aging; stress corrosion

1. Introduction

Glass fibres (GFs) are the most common fibrous reinforcement material used in fibre-reinforced composites (fibre-reinforced polymers; FRPs) [1]. The GFs possess desirable reinforcement material properties, such as high hardness, strength, and stiffness [2,3]. Various types of GFs exist, such as E, ECR, R, and S-glass, listed in the order of their increasing mechanical strength. Glass fibre-reinforced composites (GFRPs) are often used in structural applications in marine and offshore industries, as well as in the wind energy sector [4–11]. In these applications, GFRPs are continuously exposed to water and humid environments for decades, with a typical design lifetime being around 25 years or more [8]. When exposed to such environments, hydrolytic degradation of the glass material occurs [12,13], leading to a reduction of the mechanical strength and the initiation of corrosion-induced defects in fibres and composites [14]. The degradation of glass fibres due to environmental attacks can severely affect the performance of GFRPs [1]. Aqueous environments clearly have a negative effect on the

fatigue properties of GFRPs and such environments act primarily to reduce the fibre strength [15]. The fact that even water may corrode glass fibres has been known for many years [15]. In the long-term, hydrolytic degradation occurs mainly via the glass dissolution mechanism [12]. Thus, understanding the dissolution behaviour of glass is necessary to predict the deterioration of the composite's physical and mechanical properties [16].

The long-term environmental degradation of glass materials has been previously studied, mainly with respect to nuclear waste applications [17,18]. Most of the existing works on glass dissolution have been performed with bulk silicate glass and fibres are not studied often [12]. Recently, there has been an increasing interest in the environmental aging of FRPs, where R-glass and E-glass are often used as reinforcement [4,12,16,19–21]. Even so, very few studies exist on the kinetics of GF dissolution (mostly on E-glass) [22,23] and even less on R-glass [12,16].

The degradation of GFs in water can be divided into two kinetic regions (Phases I and II). Phase I is the short-term non-steady-state. Phase II is the long-term steady-state [12,16]. Phase I is complex and involves such processes as ion exchange, gel formation, and dissolution [12,17]. However, once the long-term kinetic region is reached, glass dissolution becomes a dominant process [12,17,24]. For the studied GFs, this transition to steady-state occurs in about a week (166 h) [12,16]. This time is very negligible compared to the typical design lifetime of about 25 years or more for the structures in which these materials are implemented [8]. Thus, as in the case of structural applications, when the long-term degradation is mainly of interest, dissolution is the governing process, which has to be understood and well-predictable.

During glass-water interactions, several chemical reactions may occur, shown in the chemical reactions (1)–(11) [12,17,24,25]:

$$(\equiv Si - ONa) + H_2O \rightarrow (\equiv Si - OH) + OH^- + Na^+ \tag{1}$$

$$(\equiv Si - OK) + H_2O \rightarrow (\equiv Si - OH) + OH^- + K^+ \tag{2}$$

$$(\equiv Si - O)_2Ca + H_2O \rightarrow 2(\equiv Si - OH) + 2OH^- + Ca^{2+} \tag{3}$$

$$(\equiv Si - O)_2Mg + H_2O \rightarrow 2(\equiv Si - OH) + 2OH^- + Mg^{2+} \tag{4}$$

$$(\equiv Si - O - Al =) + H_2O \leftrightarrow (\equiv Si - OH) + (= Al - OH) \tag{5}$$

$$(\equiv Si - O)_2Fe + H_2O \rightarrow 2(\equiv Si - OH) + 2OH^- + Fe^{2+} \tag{6}$$

$$(\equiv Si - O)_3Fe + H_2O \rightarrow 3(\equiv Si - OH) + 3OH^- + Fe^{3+} \tag{7}$$

$$(\equiv Si - O - Si \equiv) + OH^- \leftrightarrow (\equiv Si - OH) + (\equiv Si - O^-) \tag{8}$$

$$(\equiv Si - O^-) + H_2O \leftrightarrow (\equiv Si - OH) + OH^- \tag{9}$$

$$SiO_2 + 2H_2O \leftrightarrow H_4SiO_4 \tag{10}$$

$$MeCl_x \overset{H_2O}{\Rightarrow} (Me^{x+}) + xCl^- \tag{11}$$
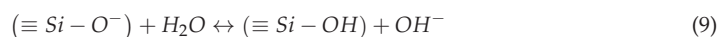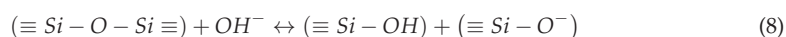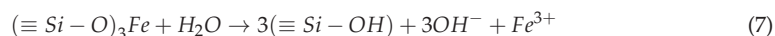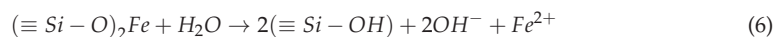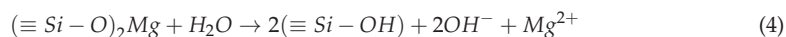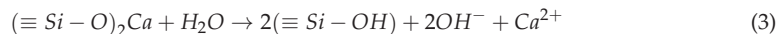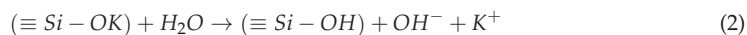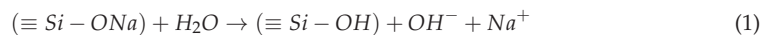
The chemical reaction (10) can also be written as a combination of the subsequent reactions (12) and (13), meaning that initially H_2SiO_3 is formed, which dissociates weakly and further reacts with water to form silicic acid:

$$SiO_2 + H_2O \leftrightarrow H_2SiO_3 \tag{12}$$

$$H_2SiO_3 + H_2O \leftrightarrow H_4SiO_4 \tag{13}$$

The elements that are released during the degradation of R-glass are Na, K, Ca, Mg, Fe, Al, Si, and Cl [12]. The cumulative mass loss is the summary mass of all of the ions released [12]. The total mass loss is what causes the radius reduction [12]. As shown in the chemical reactions (1)–(11), various competing reactions happen in parallel. During Phase I, these reactions happen at independent rates,

then one process later becomes limiting and dominates the behaviour (Phase II). Thus, the degradation process should be divided into two aforementioned stages. Furthermore, the sub-processes may follow individual kinetics and may be interdependent during Phase I [12]. During Phase I, the process is rather complex. It involves competing leaching mechanisms in addition to the dissolution reactions, i.e., ion exchange and gel formation. Therefore, it cannot be fully described with just one kinetic equation [12,17,24]. The complexity and varying rates of the competing processes during Phase I turn this stage of the glass degradation into a non-linear and non-steady-state process.

During Phase II, however, dissolution becomes dominant [17,24] and the process becomes steady-state, governed by the dissolution kinetics [12,16]. For R-glass, the contribution from Si to the total mass loss is the largest (56.1% by mass) and governs the long-term steady-state dissolution [12]. Once the steady-state is reached, the reactions proceed at constant independent rates [12]. It may be speculated that, during Phase II, an equilibrium composition of glass (likely different from the bulk composition) is obtained in the outer layers in contact with water. This allows elements to dissolve at a limiting rate and proportionally to their content in the outer layers of the glass, being indicative of the glass outer layer composition [12]. In other words, the long-term dissolution is dominated by the slowest dissolving element and the other elements following proportionally, at some equilibrium composition [12].

The non-linear non-steady-state stage of degradation can be approximated using the Dissolving Cylinder Zero-Order Kinetic (DCZOK) model, when the exact shape of the non-linear short-term part is not important, i.e., when the long-term degradation is of the most interest, such as in cases of the long service life of structures implementing GFs [8,12].

Glass dissolution kinetics depend on the surface area of the glass in contact with water. This surface area is proportional to the glass fibre radius. As the dissolution proceeds, the radius decreases and results in the deceleration of the mass loss; the DCZOK model accounts for this effect [12,16]. Glass dissolution kinetics are affected by the pH, temperature, glass composition (i.e., E, ECR, R, S-glass), solution composition (distilled water or seawater), surface area of the glass, the protective effect of the sizing, and the ionic strength of the solution, to a lesser extent. The temperature and pH are considered to be key parameters for the long-term glass dissolution [16,17,20,24,26,27]. Elevated temperatures accelerate the dissolution since the dissolution is exothermic [17,20,26]. The activity of the water is dependent on the composition of the aqueous environment, notably, on the, as well as ionic concentration of some species in the glass composition [28]. Interestingly enough, for R-glass, the sizing was found to slow down the dissolution kinetics of the GFs by almost an order of magnitude [16]. In addition, external loads may have an influence on glass dissolution kinetics, due to stress corrosion [27,28].

Humid and water environments reduce the strength of silicate glasses due to the growth of flaws, such as surface cracks, under the combination of stress and chemical attacks, known as stress corrosion [1,15]. The glass corrosion (dissolution) rate is accelerated by this stress [1].

The classical theory of stress corrosion involves the chemical reaction of a water molecule with silica, and was described elsewhere [27]. A model and the details of the chemical interaction between the adsorbed water and the Si–O bond was described by Michalske and Freiman [29]. Their model showed that water is efficient in the stress-activated corrosion of glass [27]. The basic mechanism of the stress corrosion reaction was related to the stress-enhanced thermal activation of a dissociative hydrolysis reaction, presented in Figure 1 [28,29].
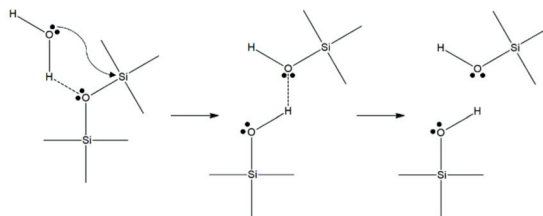
Figure 1. The chemical mechanism of stress corrosion in glass, proposed by Michalske and Freiman [29].

Any molecule that is able to donate a proton (hydrogen ion and has a lone pair of electrons, such as water, can react with the strained Si–O bond at the tip of a crack, provided that the molecular diameter is smaller than 0.5 nm [30]. The first property is necessary for the harmonized reaction of adsorption and the chemical scission of the siloxane bridges of the glass network. The small diameter is necessary to avoid steric problems, so that the reactive water molecules can reach the strained bonds at the crack tip [28]. The constrained Si–O bonds have an enhanced chemical reactivity with water due to the intensity of the strain, as was shown via hydrolysis experiments for different siloxane ring structures, after [31]. Michalske and Bunker [32] also supported the effect of stress on the stress corrosion reaction rate. They proved this hypothesis by conducting molecular-orbital simulations of the stress corrosion reaction on distorted siloxane bonds. Several other reactions are possible for other glass compositions, but they all share the feature of being stress-enhanced and thermally activated, therefore explaining the exponential (Arrhenius type) relationship [28]. In addition, it is believed that the interaction of water with cations in the flaws leads to hydrolysis and a local increase in the concentration of hydroxyl ions, leading to an increase in the pH locally [33].

Various approaches have been proposed on how to model the kinetics of glass degradation. Grambow has developed a general rate equation for the reaction of glass in nuclear wastewater solutions with different pH levels, surface areas, times, temperatures, and compositions of the reagents [18]. Delage et al. described the dissolution of borosilicate glass in aqueous media using a combination of surface reaction kinetics and diffusion [34]. Mišíková et al. have studied the kinetics of the leaching of E-glass fibres in distilled water at various temperatures, linking the glass fibre dissolution to the temperature using statistical methods [22]. Tournié et al. presented an extensive experimental study of the glass corrosion mechanism in both acidic and basic solutions. They reported that a strong acid attack was dependent on the composition of the glass [13]. Ma et al. presented a model for the glass dissolution, based on the combination of the chemical affinity and diffusion [35]. Bashir et al. studied the kinetics of the dissolution of E-glass fibres in hot alkaline solutions using zero-order and shrinking cylinder models [23,36]. They reported that both an increased temperature and increased alkalinity (higher pH) accelerated the dissolution reaction rates [23]. Bashir et al. concluded that the rate-limiting step was either the glass dissolution itself or the diffusion of hydroxide ions [23]. Krauklis and Echtermeyer developed and presented a Dissolving Cylinder Zero-Order Kinetic (DCZOK) model that explained the long-term dissolution of R-glass in water for both fibres [12,16] and GFRPs [16]. The DCZOK model is able to predict both the mass loss and the radius reduction kinetics due to dissolution [12].

Glasses formulated with significant amounts of various metal oxides, such as R-glass, have rarely been studied, but they are becoming popular for structural applications [12,18]. Thus, this work focuses on the dissolution kinetics of R-glass in water at various environmental conditions (pH, temperature, stress corrosion). However, the model should be applicable to other types of glass as well, as SiO_2 is the major component in virtually all types of glass [23].

The aim of this work is to study the effects of the pH, temperature, and stress corrosion on the R-glass fibre dissolution kinetics, in terms of the rate constants and activation energies, and to capture these effects using the Dissolving Cylinder Zero-Order Kinetics (DCZOK) model.

2. Materials and Methods

2.1. Materials

A typical glass fibre used for marine, oil, and gas applications was selected for this study. Boron-free and fluorine-free high strength, high modulus 3B HiPer-Tex™ W2020 R-glass fibre bundles were used. These were classified as high-strength, high modulus R-glass (defined by an international standard [37]). The average fibre diameter was 17 ± 2 µm [12,38]. The density of the glass (ρ_f) was 2.54 g/cm^3 [12,38]. The authors estimated that a bundle had about 4098 fibres [12]. The specific surface area of the glass fibres was determined to be 0.09 m^2/g from the geometrical considerations, as a product of the number, circumference, and length of the fibres [12]. All of the fibres used during this work were sized, whereas the dissolution of unsized R-glass fibres was previously studied in another study by Krauklis and Echtermeyer [16]. A micrograph of R-glass fibre bundles is shown in Figure 2.
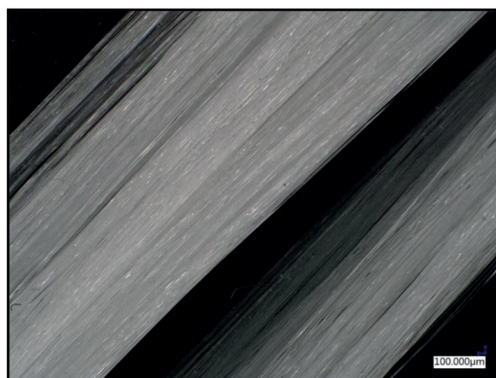
Figure 2. A micrograph of R-glass fibre bundles taken with a digital microscope, the Keyence VHX6000 (Osaka, Japan).

Distilled water (0.5–1.0 MΩ·cm) was used for the conditioning of the GF bundles, produced using a water purification system, the Aquatron A4000 (Cole-Parmer, Vernon Hills, IL, USA). The *pH* of the distilled water was 5.650 ± 0.010, being lower than neutral due to the dissolved CO_2 from the atmosphere in equilibrium. IUPAC standard buffer solutions (Radiometer analytical, Lyon, France) were used for studying the effect of the *pH* on the kinetics of the GF dissolution. The solutions of *pH* 1.679 ± 0.010, 4.005 ± 0.010, 5.650 ± 0.010, 7.000 ± 0.010, and 10.012 ± 0.010 were used.

2.2. Methods

Glass Dissolution Experiments:

Aqueous dissolution experiments of GF samples were performed using a batch system. The samples for the dissolution study were weighed using AG204 analytical scales (± 0.1 mg; Mettler Toledo, OH, USA) before the experiments. The samples were placed in inert closed vessels filled with 50 mL of distilled water or *pH* buffer solutions. The tight sealing of samples was ensured. The water-tight vessels, with the samples and water solutions in them, were placed into the water bath.

The water's temperature (25, 40, 60, 80 °C) in the bath was controlled via proportional–integral–derivative (PID)-controlled heating, giving an accuracy of ± 1 °C. A two-stage heating system was used in order to make sure that there is no contact of the sample water with potential contaminating ion release sources, i.e., the heating element.

pH measurements were performed using a standard MeterLab PHM210 *pH*-meter (Radiometer analytical, France) calibrated with IUPAC standard buffer solutions, providing an accuracy of ± 0.010 *pH*.

The concentration of the dissolved ions in the water from the vessels was analysed over time via high resolution inductively coupled plasma mass spectrometry (HR-ICP-MS), providing glass dissolution kinetics. Experimentally, the total mass loss of glass material was measured as a sum of all of the ions' release, quantified with HR-ICP-MS. Analyses were performed using a double focusing magnetic sector field ICP-MS Finnigan ELEMENT 2 (Thermo-Scientific, Waltham, MA, USA), equipped with a PrepFAST sample introduction system (ESI/Elemental Scientific) and an UltraClave pre-treatment/digestion machine (Milestone, Brøndby Kommune, Denmark). The acidification of samples was performed using an ultra-pure grade HNO_3 SubPur (Milestone) in order to avoid the adsorption of ions into the wall of the sample vials that would otherwise give erroneous results.

The benefit of HR-ICP-MS versus gravimetric analysis is that it allows the measurement of the dissolution kinetics of each separate ion, as well as the total mass loss [12]. The data obtained from the HR-ICP-MS experiments are in the form of the non-cumulative mass concentration at each point in time (g/L) and need to be converted to the cumulative $m_{dissolved}$ form by using Equation (14):

$$m_{dissolved} = V_{water} \int_0^t c\,dt \qquad (14)$$

where V_{water} is the volume of a water sample using the HR-ICP-MS measurement. The V_{water} used for the experiments was 50 mL. Equation (14) is valid for each individual ion release and for the total mass loss.

For studying the influence of the external loads on the dissolution kinetics, a stress corrosion rig was designed, built, and used during the experiments. The experimental rig is shown in Figure 3 and the design schematics of the stress corrosion setup are attached in Appendix A. The principle is that glass fibres are inside an inert cylinder pushed by an inert rod, which transfers the stress from the weights to the fibres. The water samples for the HR-ICP-MS analyses were taken from the main cylinder, where the distilled water was in contact with the stressed glass fibres. The temperature was PID-controlled by using a two-stage heating system, ensuring a temperature of $60 \pm 1\,^\circ$C. Polymeric spheres, seen in Figure 3, were used to reduce the evaporation rate of the heating water.

Figure 3. The glass fibre stress corrosion experimental setup.

3. Dissolving Cylinder Zero-Order Kinetic (DCZOK) Model

3.1. The Model and Its Assumptions

An approach used to describe the glass dissolution kinetics in the fibres was proposed and explained in works by Krauklis and Echtermeyer [12,16]. This approach is used as a basis for this study. In this work, the kinetic constants are obtained for the Dissolving Cylinder Zero-Order Kinetic (DCZOK) model for various pH and temperature conditions, as well as for different stress levels. The protective effect of sizing is accounted for in this model [16].

The rate of the dissolution is dependent on the glass dissolution rate constant (K_0), the glass surface area exposed to water (S), and the effect of sizing (ξ_{sizing}) [12]. For fibres, in infinite water availability conditions, the dissolution, being a surface reaction, can be well-described with zero-order kinetics [23], but the decrease in the fibre radius, and thus in the surface area over time, should be accounted for [12]. For sizeless fibres, Equation (15) should be used [16]:

$$\frac{\partial m}{\partial t} = K_0 S(t) \tag{15}$$

For sized fibres, the effect of sizing, ξ_{sizing}, should also be accounted for, as shown in Equation (16) [16]:

$$\frac{\partial m}{\partial t} = K_0 \xi_{sizing} S(t) \tag{16}$$

where m is the total cumulative mass dissolved after time t, K_0 is a material/environment interaction property, and ξ_{sizing} is the protective effect of sizing. K_0 is affected by environmental effects [12].

In this Equation (16), K_0 and ξ_{sizing} are the time-independent parameters, whereas S changes with time. As the dissolution continues, the fibre's radius is reduced and the total surface area (S) is decreased. This leads to a decrease in the dissolution rate. The ion release rate slows down linearly with a decrease in the fibre's radius [12]. The glass fibre's radius reduction is linear with time. The proportionality is given by the dissolution rate constant (K_0 (g/(m^2·s))) and the density of the glass (ρ_{glass}(g/m^3)) [12]. A linear radius decrease of the glass fibres over time was previously experimentally observed elsewhere [23] and is accounted for in the DCZOK model [12].

The effect of sizing on the glass dissolution (ξ_{sizing}) for the studied R-glass is 0.165, protecting the fibres from water by almost an order of magnitude, in terms of dissolution rates. The effect of sizing (ξ_{sizing}) is assumed to be time-independent [16]. ξ_{sizing} goes into the model linearly, since fibres are covered in "islands" or patches of sizing, meaning not the whole surface is coated [39]. These areas of the bare unsized glass dominate the dissolution behaviour (the difference being roughly an order of magnitude) [16].

Taking into account the geometry of the fibres, the mass loss kinetic DCZOK model equation in its differential form is the following, as shown in Equation (17) [12]:

$$\frac{\partial m}{\partial t} = 2n\pi l \left(r_0 K_0 \xi_{sizing} - \frac{K_0^2 \xi_{sizing}^2}{\rho_{glass}} t \right) \tag{17}$$

where n is the number of fibres (-), l is the length of the fibres (m), r_0 is the initial fibre radius (m), and ρ_{glass} is the density of the glass (g/m^3).

The model shows the rate of mass loss due to dissolution. It can be used for the total mass loss $\left(\frac{\partial m}{\partial t} \right)$, as well as for Si $\left(\frac{\partial m_{Si}}{\partial t} \right)$ or another ion's release.

As can be seen from the differential expression of the DCZOK model in Equation (17), the radius reduction over time is accounted for in the model. The pH, temperature, and stress corrosion affect the material-environment energy-activated interactions, thus affecting the dissolution rate constants (K_0), as represented by Equation (18).

$$K_0 = f(pH, T, \sigma) \tag{18}$$

where pH is the acidity of the environment (-), T is the temperature (K), and σ is the stress (MPa).

The model involves the following assumptions: the model is deterministic and all of the glass fibres are assumed to have the same initial fibre radius (r_0); the cross-sectional surface area at the ends of the fibres is assumed negligible in the surface area calculations; the length of the fibres (l) is assumed to be constant during the whole dissolution process. During the whole degradation process, the density of the glass material is assumed to be constant (ρ_{glass}). The effect of sizing (ξ_{sizing}) is assumed to be independent of the environmental conditions and time [12,16]. For free fibre bundles (not embedded in the composite), the condition of the infinite availability of water is ensured by using large volumes of water, thus making the rate of the reaction independent of the water concentration [12,16].

3.2. The Effect of the Environment on the Dissolution Rate Constant

It has been reported that the temperature dependence of the rate of the glass fibre radius reduction follows an exponential trend and the diameter reduction is linearly related to the loss of material in fibres due to dissolution [12,23]. The fact that the temperature dependence of a dissolution rate constant is described by the Arrhenius equation is also confirmed by the evidence reported further in this manuscript. The temperature dependence of a dissolution rate constant can be described using the Arrhenius equation (Equation (19)), being an exponential function:

$$K_0 = Ae^{-\frac{E_A(pH,\sigma)}{RT}} \tag{19}$$

where A is the pre-exponential factor (g/(m^2·s)), R is the gas constant being 8.314 J/(mol·K), T is the absolute temperature (K), and E_A is the activation energy (J/mol). Both the pH and stress corrosion are thought to affect the activation energy term in the Arrhenius equation [31,40].

The activation energy can be obtained through the graphing of the constant pH and σ, using Equation (20) [18]:

$$lnK_0 = -\frac{E_A}{R}\frac{1}{T} + lnA \tag{20}$$

The rate constant can be calculated for each temperature from the general differential mass loss DCZOK model equation. To obtain the E_A, the lnK_0 is plotted against $\frac{1}{T}$. The pre-exponential factor (A) is assumed to be constant. The DCZOK model can be expanded (Equation (21)):

$$
\begin{aligned}
\frac{\partial m}{\partial t} &= 2n\pi l\left(r_0 K_0 \xi_{sizing} - \frac{(K_0\xi_{sizing})^2}{\rho_{glass}}t\right) \\
&= 2n\pi l\left(r_0 Ae^{-\frac{E_A(pH,\sigma)}{RT}}\xi_{sizing} - \frac{\left(Ae^{-\frac{E_A(pH,\sigma)}{RT}}\xi_{sizing}\right)^2}{\rho_{glass}}t\right)
\end{aligned}
\tag{21}
$$

3.3. Modelling of the Two Distinct Stages of Glass Degradation

Mass loss curves made during the aging of glass over time can be divided into two parts: Short-term non-steady-state degradation and long-term steady-state dissolution [12]. When the long-term dissolution (Phase II) is of the most interest, the shape of the non-linear short-term stage (Phase I) is not important. In such case, an approximate solution can then be used to describe the Phase I of degradation as well, using the DCZOK model. In the case when the short-term degradation (Phase i) is of the most interest, the kinetic models for each of the individual sub-processes, i.e., ion exchange, gel formation, and dissolution, should be implemented.

The model can also predict the fibre radius reduction kinetics during the dissolution, using the same four parameters that can be determined experimentally [12]. The DCZOK model can be used to describe the dissolution for each element separately, as well as for the total mass loss. The glass mass loss (all elements included) is described by four parameters (r_0, t_{st}, K_0^I, K_0^{II}). For each ion, the individual K_0^I and K_0^{II} values have to be obtained, while the the t_{st} and r_0 for each individual ion

release are the same and are equivalent to that for the total mass loss [12]. K_0^I and K_0^{II} are the dissolution rate constants (g/(m^2·s)) for the Phase I and Phase II regions, respectively.

For each material, the activation energy function $(E_A(pH, \sigma))$ of the pH and stress has to be established experimentally for both the short-term and long-term stages of glass degradation.

The total material loss and the release of Si at various environmental conditions were modelled using the DCZOK model Equation (21) and the rate constants were obtained and reported.

4. Results

From the measured cumulative concentration data of the ions released during the dissolution of glass, the dissolution rate constants were obtained using non-linear regression for Si ($K_{0_{Si}}^I$ and $K_{0_{Si}}^{II}$) and for the total mass loss ($K_{0_{total}}^I$ and $K_{0_{total}}^{II}$). The Generalized Reduced Gradient (GRG) non-linear regression method was used. It involved minimization of the sum of the squares of the differences between the modelled values and the experimental values. The obtained parameters are systematized in Tables 1–3 for the effect of the pH, temperature, and stress, respectively. The values obtained are comparable with the dissolution rates of other glass fibres, reported in the literature [12,16,41].

In Figure 4, and further also for the glass dissolution kinetics at various stress levels and temperatures, the points represent the experimental data, whereas the lines represent the DCZOK modelled curves using the rate constants reported in Tables 1–3, respectively. In figures of the glass dissolution kinetics at various environmental conditions, the glass mass loss is reported as normalized per the initial surface area of the fibres (S_0), as is common for surface reaction kinetics [12,16,42]. The effect of sizing on the glass dissolution (ξ_{sizing}) for the studied R-glass was 0.165 [16].

4.1. Effect of pH on the Glass Dissolution Kinetics

The dissolution rate constants for the glass dissolution from fibres in water at various pH levels at 60 ± 1 °C are shown in Table 1. This steady-state was achieved after about a week.

Table 1. The glass dissolution rate constants obtained via the regression of the experimental data of the R-glass fibre bundles using the Dissolving Cylinder Zero-Order Kinetic (DCZOK) model for Si and the total mass loss at 60 °C and various pH levels. $K_{0_{Si}}^I$, $K_{0_{Si}}^{II}$, $K_{0_{total}}^I$ and $K_{0_{total}}^{II}$ are dissolution rate constants for Phase I and II for Si and total glass dissolution, as indicated by indices.

pH	$K_{0_{Si}}^I$ (g/(m^2·s))	$K_{0_{Si}}^{II}$ (g/(m^2·s))	$K_{0_{total}}^I$ (g/(m^2·s))	$K_{0_{total}}^{II}$ (g/(m^2·s))	Reference
1.679 ± 0.010	$(3.10 \pm 0.44) \cdot 10^{-7}$	$(1.25 \pm 0.09) \cdot 10^{-7}$	$(1.70 \pm 0.19) \cdot 10^{-6}$	$(1.16 \pm 0.08) \cdot 10^{-6}$	This work
4.005 ± 0.010	$(2.59 \pm 0.33) \cdot 10^{-8}$	$(1.70 \pm 0.11) \cdot 10^{-8}$	$(8.48 \pm 1.21) \cdot 10^{-8}$	$(6.24 \pm 0.36) \cdot 10^{-8}$	This work
5.650 ± 0.010	$(6.67 \pm 1.03) \cdot 10^{-9}$	$(2.30 \pm 0.16) \cdot 10^{-9}$	$(1.82 \pm 0.29) \cdot 10^{-8}$	$(4.05 \pm 0.29) \cdot 10^{-9}$	This work, [12,16]
7.000 ± 0.010	$(3.64 \pm 0.53) \cdot 10^{-8}$	$(2.55 \pm 0.19) \cdot 10^{-8}$	$(5.46 \pm 0.82) \cdot 10^{-8}$	$(4.85 \pm 0.38) \cdot 10^{-8}$	This work
10.012 ± 0.010	$(8.97 \pm 1.27) \cdot 10^{-8}$	$(4.56 \pm 0.32) \cdot 10^{-8}$	$(1.39 \pm 0.16) \cdot 10^{-7}$	$(1.11 \pm 0.07) \cdot 10^{-7}$	This work

The experimental glass dissolution data and the modelled DCZOK dissolution curves for various pH levels are shown in Figure 4.

It is possible to obtain a pH influence on the activation energies of dissolution by rearranging Equation (19) into the following form (Equation (22)):

$$E_A = RT(lnA - lnK_0) \tag{22}$$

A pH function of the activation energy of dissolution $\left(E_A^{II} = f(pH)\right)$ is shown in Figure 5. It is fine to approximate the kinetic pH dependency as a polynomial function, being a parabolic function in this case [43–46].

Figure 4. The glass dissolution kinetics at various *pH* levels: The experimental data and modelled Dissolving Cylinder Zero-Order Kinetic (DCZOK) dissolution curves for the R-glass fibre bundles. GF: Glass fibre.
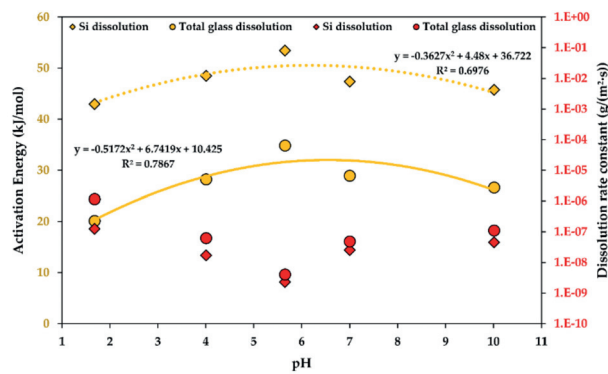
Figure 5. The activation energy (yellow) and the rate constants (red) of the steady-state R-glass dissolution as a function of the *pH*. Determination coefficients R^2 are shown. 1.E-10 stands for "1×10^{-10}".

Both the glass and the Si dissolution rate constant trends are similar, with an exception at low *pH* levels, i.e., at a *pH* of 1, the rates of Si dissolution increase more dramatically than the total glass dissolution rates, indicating a higher contribution of Si to the material loss during the dissolution in strongly acidic environments. Thus, GFRPs should not be used in strongly acidic conditions. This is in agreement with an observation in another study, stating that many GFRPs fail catastrophically after a critical time when exposed to acids [1].

4.2. The Effect of Temperature on Glass Dissolution Kinetics

The dissolution rate constants for glass dissolution from the fibres in water at various temperatures at a *pH* of 5.650 ± 0.010 are shown in Table 2. The steady-state was achieved after about a week.

Table 2. The glass dissolution rate constants obtained via the regression of the experimental data using the Dissolving Cylinder Zero-Order Kinetic (DCZOK) model for Si and the total mass loss at a pH of 5.65 and at various temperatures. $K_{0_{Si}}^{I}$, $K_{0_{Si}}^{II}$, $K_{0_{total}}^{I}$ and $K_{0_{total}}^{II}$ are dissolution rate constants for Phase I and II for Si and total glass dissolution, as indicated by indices.

Temperature (°C)	$K_{0_{Si}}^{I}$ (g/(m²·s))	$K_{0_{Si}}^{II}$ (g/(m²·s))	$K_{0_{total}}^{I}$ (g/(m²·s))	$K_{0_{total}}^{II}$ (g/(m²·s))	Reference
25 ± 1	$(1.46 \pm 0.23) \cdot 10^{-9}$	$(2.60 \pm 0.18) \cdot 10^{-10}$	$(1.04 \pm 0.12) \cdot 10^{-8}$	$(1.42 \pm 0.11) \cdot 10^{-9}$	This work
40 ± 1	$(2.62 \pm 0.37) \cdot 10^{-9}$	$(1.08 \pm 0.08) \cdot 10^{-9}$	$(1.37 \pm 0.19) \cdot 10^{-8}$	$(2.72 \pm 0.19) \cdot 10^{-9}$	This work
60 ± 1	$(6.67 \pm 1.03) \cdot 10^{-9}$	$(2.30 \pm 0.16) \cdot 10^{-9}$	$(1.82 \pm 0.29) \cdot 10^{-8}$	$(4.05 \pm 0.29) \cdot 10^{-9}$	This work, [12,16]
80 ± 1	$(2.19 \pm 0.31) \cdot 10^{-8}$	$(8.91 \pm 0.73) \cdot 10^{-9}$	$(4.24 \pm 0.59) \cdot 10^{-8}$	$(1.47 \pm 0.11) \cdot 10^{-8}$	This work

The Arrhenius approach was used to obtain the activation energy of the steady-state Si and glass dissolution. The activation energy was obtained through graphing at a constant pH and σ, similar to what was done in another study, using Equation (23) [23]:

$$lnK_0 = -\frac{E_A}{R}\frac{1}{T} + lnA \qquad (23)$$

The graphing approach is shown in Figure 6. The obtained activation energy (E_A) of Si dissolution is 53.46 kJ/mol (using $K_{0_{Si}}^{II}$ values). The pre-exponential factor (A) for Si dissolution is $6.82 \cdot 10^{-1}$ g/(m²·s). The obtained activation energy (E_A) of the total glass dissolution is 34.84 kJ/mol (using $K_{0_{total}}^{II}$ values). The pre-exponential factor for the glass dissolution (A) is $1.67 \cdot 10^{-3}$ g/(m²·s).

The obtained values are consistent with the values reported in the literature, being slightly lower than for E-glass (58–79 kJ/mol in alkaline solutions [23]). The activation energy for the Si dissolution of various silica-based materials may be around 60 kJ/mol [47].
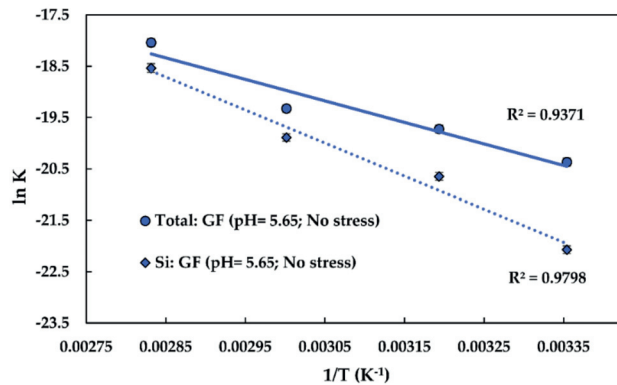
Figure 6. The graphing approach used to obtain the pre-exponential factors, the activation energies of Si, and the total glass dissolution of the fibres at a pH of 5.65 and under no stress. GF: Glass fibre. 1/T stands for reciprocal temperature; R^2 is the determination coefficient.

The experimental glass dissolution data and the modelled DCZOK dissolution curves for various temperatures are shown in Figure 7.
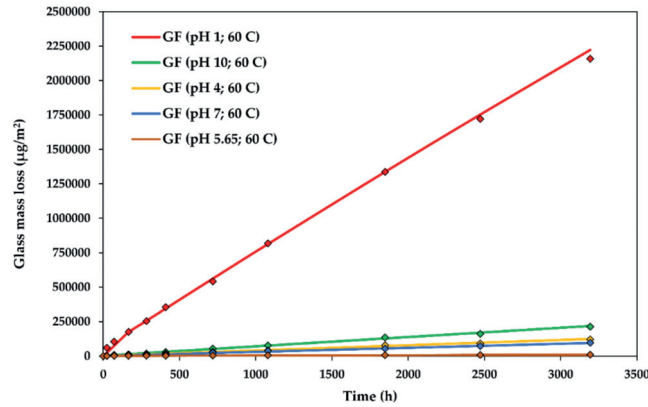
Figure 7. The glass dissolution kinetics at various temperatures: The experimental data and the modelled Dissolving Cylinder Zero-Order Kinetic (DCZOK) dissolution curves for R-glass fibre bundles. GF: Glass fibre.
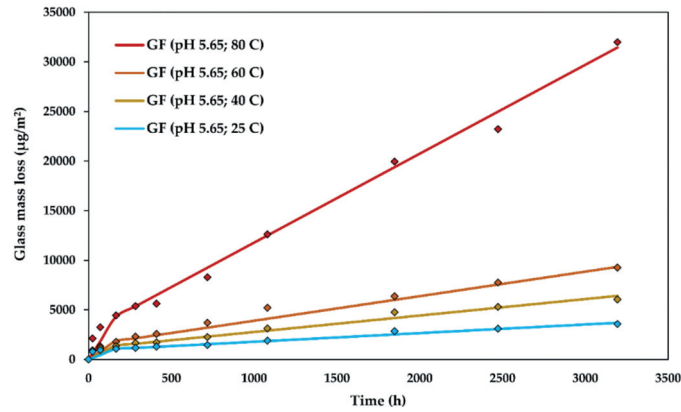
4.3. The Effect of Stress Corrosion on Glass Dissolution Kinetics

The dissolution rate constants for glass dissolution from fibres in water loaded with various weights (0.03, 5, 8, and 10 kg) at a pH of 5.650 ± 0.010 and at $60 \pm 1\,^{\circ}$C are shown in Table 3. The stress was calculated as half of the weight divided by the cross-sectional area of the glass fibre bundles (0.93 mm^2). The division by two is due to the fact that the weight is carried by a bundle which goes from each side of the rig, meaning that the total area is that of two bundles. In order to visualize the setup and the fibre arrangement, the experimental rig in action is shown in Figure 3. The steady-state was achieved after about 5 days (120 h), sooner than in all of the unstressed cases, indicating that stress may slightly accelerate the transition towards the steady-state dissolution.

Table 3. The glass dissolution rate constants obtained via the regression of the experimental data using the Dissolving Cylinder Zero-Order Kinetic (DCZOK) model for Si and the total mass loss at 60 $^{\circ}$C and at a pH of 5.65 at various stress levels. σ stands for stress; $K^I_{0_{Si}}$, $K^{II}_{0_{Si}}$, $K^I_{0_{total}}$ and $K^{II}_{0_{total}}$ are dissolution rate constants for Phase I and II for Si and total glass dissolution, as indicated by indices.

Weight (kg)	σ	$K^I_{0_{Si}}$ (g/(m$^2\cdot$s))	$K^{II}_{0_{Si}}$ (g/(m$^2\cdot$s))	$K^I_{0_{total}}$ (g/(m$^2\cdot$s))	$K^{II}_{0_{total}}$ (g/(m$^2\cdot$s))	Reference
0	0.0	$(6.67 \pm 1.03)\cdot10^{-9}$	$(2.30 \pm 0.16)\cdot10^{-9}$	$(1.82 \pm 0.29)\cdot10^{-8}$	$(4.05 \pm 0.29)\cdot10^{-9}$	This work, [12]
0.03	0.2	$(7.27 \pm 1.15)\cdot10^{-9}$	$(2.38 \pm 0.21)\cdot10^{-9}$	$(2.08 \pm 0.42)\cdot10^{-8}$	$(4.12 \pm 0.33)\cdot10^{-9}$	This work
5	26.4	$(7.45 \pm 1.03)\cdot10^{-9}$	$(2.58 \pm 0.19)\cdot10^{-9}$	$(2.04 \pm 0.33)\cdot10^{-8}$	$(4.35 \pm 0.35)\cdot10^{-9}$	This work
8	42.2	$(8.30 \pm 1.33)\cdot10^{-9}$	$(3.47 \pm 0.25)\cdot10^{-9}$	$(2.01 \pm 0.41)\cdot10^{-8}$	$(5.56 \pm 0.44)\cdot10^{-9}$	This work
10	52.7	$(9.21 \pm 1.33)\cdot10^{-9}$	$(4.73 \pm 0.33)\cdot10^{-9}$	$(1.65 \pm 0.44)\cdot10^{-8}$	$(8.12 \pm 0.67)\cdot10^{-9}$	This work

The experimental glass dissolution data and the modelled DCZOK dissolution curves for various stress levels are shown in Figure 8.
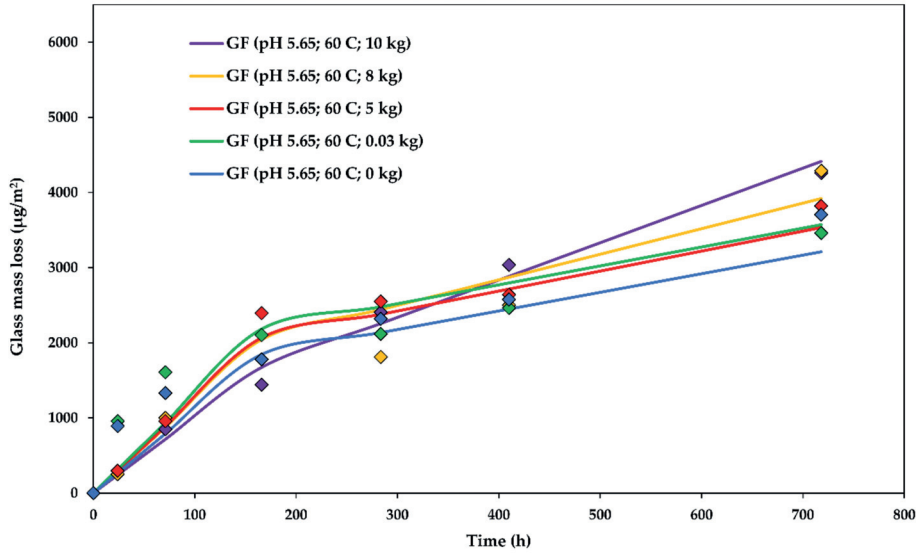
Figure 8. The glass dissolution kinetics at various stress levels: The experimental data and the modelled Dissolving Cylinder Zero-Order Kinetic (DCZOK) dissolution curves for glass fibre bundles. GF: Glass fibre.

A stress function of the activation energy of dissolution $\left(E_A^{II} = f(\sigma)\right)$ for R-glass fibre bundles is shown in Figure 9. An increase in the stress seems to accelerate glass dissolution, showing a similar trend for both Si and the total mass loss kinetics. The increase in the stress reduces the activation energy of dissolution linearly and accelerates the glass dissolution rates exponentially. Additional studies involving higher stresses are recommended to establish this influence in more detail.
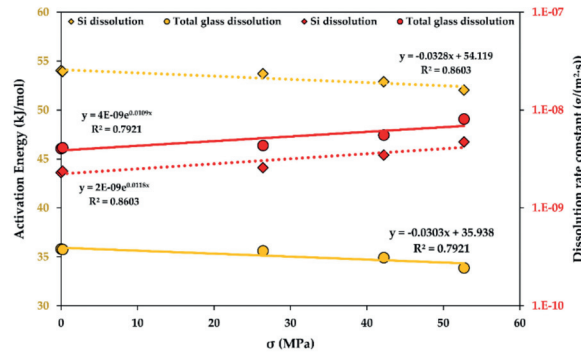
Figure 9. The activation energy of dissolution (yellow) and the dissolution rate constants (red), functions of the stress (σ) for the glass fibre bundles at the steady-state. Determination coefficients R^2 are shown. 4E-9 stands for "4×10^{-9}".

5. Discussion

R-glass fibres were studied in this work. However, there should be no limitations to applying the DCZOK model to other types of glass fibres. Validation of the model with various types of glass fibres, such as E, ECR, and S, is advised. The processes for all of these fibres are expected to follow similar trends, whereas only the values of the terms in the model have to be assessed for each material individually.

The industry is interested in the pH, temperature, and stress corrosion for environmental effects. Temperatures are also interesting to the industry for accelerated testing purposes. As the industry is concerned with lowering the testing time for the fibre-dominated property deterioration in GFRPs, the model allows the prediction of the loss of glass material. While it takes time to obtain the parameters, the most significant time saving comes from using the kinetic constants and the model.

The influence of the pH, temperature, and stress corrosion on the rate constants and dissolution activation energies was obtained, however, the influence of each parameter was studied once at a time. Thus, a suggestion for future work includes a cross-parametric study of the pH, temperature, and stress corrosion, in order to deduce a general analytical solution for the environmental influence on the activation energy of dissolution and to study whether there is a coupled effect. The DCZOK model should be extendable to include the effect of the ionic strength and, finally, to be further used in linking the reduction in the mechanical strength of the fibres with the dissolution kinetics.

The authors think that validating the DCZOK model for seawater conditions (about 1.84–12.62 mg SiO_2/kg water; pH of seawater at 7.8) would be highly beneficial, especially for the marine and offshore industries, since the real-life structures most often operate in the seawater environment. When GFs are used in seawater, the dissolution of glass occurs at a slower rate, due to the presence of silica in the seawater, which is in seawater from the contact with sand and minerals [48–51]. The approach in distilled water is conservative with regards to seawater, meaning that structures implementing glass fibres designed for distilled water conditions should not encounter penalties to their service time in the seawater.

The model should be applicable to other types of glass as well, as SiO_2 is the major component in virtually all types of glass [23], but it would be beneficial to validate this model experimentally with other types of glass fibres. Information on the exact composition of the studied R-glass was not available from the manufacturer, supplier, or technical data sheets. However, it may be possible to speculate that the composition of the dissolving ions during steady-state Phase II is somewhat representative of the glass composition, since all ions follow the slowest dissolving element, as was reported elsewhere for the same material [12]. The ion composition during the steady-state was the following: 2.7 wt% Na, 1.4 wt% K, 14.3 wt% Ca, 15.1 wt% Mg, 0.1 wt% Fe, 6.9 wt% Al, 56.1 wt% Si, and 3.4 wt% Cl [12].

Another aspect that should be investigated is the effect of the sizing on the glass fibre dissolution, i.e., its chemical composition, amount, and distribution on the fibres. For the studied R-glass, it is known that the sizing is epoxy-compatible and its loss on ignition (LOI) value is 0.64 wt%. The protective effect of sizing for the studied R-glass fibres was reported in another study [16].

It was previously observed by Scheffler et al. [52] that strong alkaline solutions can significantly damage glass fibres due to the chemical attack [52]. This observation is consistent with the results in this work, indicating much higher dissolution rates at a pH of 10 (at least an order of magnitude higher) compared to the neutral conditions.

6. Conclusions

The analytical model, termed the Dissolving Cylinder Zero-Order Kinetic model, was successfully used to explain the long-term glass dissolution experiments of R-glass fibres with various environmental conditions:

$$\begin{aligned}
\frac{\partial m}{\partial t} &= 2n\pi l\left(r_0 K_0 \xi_{sizing} - \frac{\left(K_0 \xi_{sizing}\right)^2}{\rho_{glass}}t\right) \\
&= 2n\pi l\left(r_0 A e^{-\frac{E_A(pH,\sigma)}{RT}}\xi_{sizing} - \frac{\left(A e^{-\frac{E_A(pH,\sigma)}{RT}}\xi_{sizing}\right)^2}{\rho_{glass}}t\right)
\end{aligned} \tag{21}$$

The model accounts for the influence of the *pH*, temperature, and stress, as well as the effects of sizing protection (ξ_{sizing} for the studied R-glass is 0.165). The glass dissolution rate constants were obtained and reported for various *pH* levels and temperatures, as well as for various stress corrosion conditions.

The temperature showed an Arrhenius-type influence on the kinetics, increasing the rate of dissolution exponentially with an increasing temperature. The activation energy of the steady-state glass dissolution was obtained and reported at a *pH* of 5.65 and with no stress (53.46 and 34.84 kJ/mol for Si and the total glass dissolution, respectively). The activation energy of dissolution is affected by the *pH* and stress. The activation energy decreases linearly as the stress increases. The influence of the *pH* is more complicated and may be described by a parabolic polynomial function; the activation energy peaks at a *pH* of 5.65 and decreases towards more basic, as well as more acidic, conditions.

In comparison with neutral conditions, basic and acidic aqueous environments showed an increase in the dissolution rates, affecting the lifetime of the glass fibres negatively.

External loads also increased the glass dissolution rates due to stress corrosion. The stress seems to accelerate the glass dissolution rates exponentially. The model was able to capture all of these effects.

Abbreviations

r	Fibre radius (m)
r_0	Initial fibre radius (m)
K_0	Dissolution rate constant (g/(m^2·s))
$K^I_{0_{Si}}$	Dissolution rate constant for Si only (non-steady-state) (g/(m^2·s))
$K^{II}_{0_{Si}}$	Dissolution rate constant for Si only (steady-state) (g/(m^2·s))
$K^I_{0_{total}}$	Dissolution rate constant for glass (non-steady state) (g/(m^2·s))
$K^{II}_{0_{total}}$	Dissolution rate constant for glass (steady-state) (g/(m^2·s))
t_{st}	Time when long-term steady state is reached (s)
n	Number of fibres (-)
l	Length of fibres (m)
S	Glass fibre surface area (m^2)
S_0	Initial glass fibre surface area (m^2)
pH	Acidity of the environment (-)
A	Pre-exponential factor (g/(m^2·s))
R	Universal gas constant (8.314 J/(mol·K))
T	Absolute temperature (K)
E_A	Dissolution activation energy (J/mol)
ρ_{glass}	Density of the glass (g/m^3)
t	Time (s)
σ	Stress (MPa)
$m; m_{dissolved}$	Total mass loss due to dissolution (g)

m_{Si}	Si mass loss due to dissolution (g)
ξ_{sizing}	Protective effect of sizing against glass dissolution (-)
c	Non-cumulative ion mass concentration measured with HR-ICP-MS (g/L)
V_{water}	Volume of a water sample used for the HR-ICP-MS (L)
GF	Glass Fibre
GFRP	Glass Fibre-Reinforced Polymer; same as Glass Fibre-Reinforced Composite
DCZOK	Dissolving Cylinder Zero-Order Kinetic (model)
$E-glass$	"Electrical" glass
$ECR-glass$	"Electrical/Chemical Resistance" glass
$R-glass$	"Reinforcement" glass
$S-glass$	"Strength" glass
FRP	Fibre-Reinforced Polymer, same as fibre-reinforced composite
HR-ICP-MS	High Resolution Inductively Coupled Plasma Mass Spectrometry

Appendix A. The Schematics of the Stress Corrosion Rig.
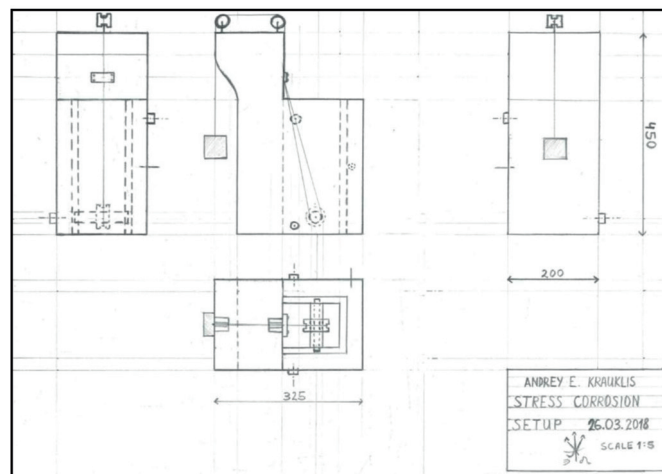
Figure A1. The design schematics of the stress corrosion rig for the glass fibre bundles, indicating the placement of the fibres and the weights.

References

1. Agarwal, B.D.; Broutman, L.J. *Analysis and Performance of Fibre Composites*, 2nd ed.; John Wiley and Sons, Inc.: Hoboken, NJ, USA, 1990; pp. 339–359, ISBN 978-0-471-51152-6.
2. Wallenberger, F.T. Commercial and Experimental Glass Fibres. In *Fibreglass and Glass Technology*; Wallenberger, F.T., Bingham, P.A., Eds.; Springer: New York, NY, USA, 2010; ISBN 978-1-4419-0735-6.
3. Steinmann, W.; Saelhoff, A.-K. Essential Properties of Fibres for Composite Applications. In *Fibrous and Textile Materials for Composite Applications, Textile Science and Clothing Technology*; Rana, S., Fangueiro, R., Eds.; Springer: Singapore, 2016; ISBN 978-981-10-0232-8.
4. Krauklis, A.E.; Echtermeyer, A.T. Mechanism of Yellowing: Carbonyl Formation during Hygrothermal Aging in a Common Amine Epoxy. *Polymers* **2018**, *10*, 1017. [CrossRef]
5. Xiao, G.Z.; Shanahan, M.E.R. Swelling of DGEBA/DDA epoxy resin during hygrothermal ageing. *Polymer* **1998**, *39*, 3253–3260. [CrossRef]
6. Toscano, A.; Pitarresi, G.; Scafidi, M.; Di Filippo, M.; Spadaro, G.; Alessi, S. Water diffusion and swelling stresses in highly crosslinked epoxy matrices. *Polym. Degrad. Stab.* **2016**, *133*, 255–263. [CrossRef]
7. Grabovac, I.; Whittaker, D. Application of bonded composites in the repair of ships structures—A 15-year service experience. *Compos. Part A* **2009**, *40*, 1381–1398. [CrossRef]

8. McGeorge, D.; Echtermeyer, A.T.; Leong, K.H.; Melve, B.; Robinson, M.; Fischer, K.P. Repair of floating offshore units using bonded fibre composite materials. *Compos. Part A* **2009**, *40*, 1364–1380. [CrossRef]

9. Gustafson, C.-G.; Echtermeyer, A. Long-term properties of carbon fibre composite tethers. *Int. J. Fatigue* **2006**, *28*, 1353–1362. [CrossRef]

10. Salama, M.M.; Stjern, G.; Storhaug, T.; Spencer, B.; Echtermeyer, A. *The First Offshore Field Installation for a Composite Riser Joint*; OTC-14018-MS; Offshore Technology Conference: Houston, TX, USA, 2002.

11. Echtermeyer, A.T.; Gagani, A.I.; Krauklis, A.E.; Mazan, T. Multiscale Modelling of Environmental Degradation—First Steps. In *Durability of Composites in a Marine Environment 2. Solid Mechanics and Its Applications*; Davies, P., Rajapakse, Y.D.S., Eds.; Springer: Cham, Switzerland, 2018; Volume 245, pp. 135–149, ISBN 978-3-319-65145-3.

12. Krauklis, A.E.; Echtermeyer, A.T. Long-Term Dissolution of Glass Fibres in Water Described by Dissolving Cylinder Zero-Order Kinetic Model: Mass Loss and Radius Reduction. *Open Chem.* **2018**, *16*, 1189–1199. [CrossRef]

13. Tournié, A.; Ricciardi, P.; Colomban, Ph. Glass Corrosion Mechanisms: A Multiscale Analysis. *Solid State Ionics* **2008**, *179*, 2142–2154. [CrossRef]

14. Brown, E.N.; Davis, A.K.; Jonnalagadda, K.D.; Sottos, N.R. Effect of surface treatment on the hydrolytic stability of E-glass fibre bundle tensile strength. *Compos. Sci. Technol.* **2005**, *65*, 129–136. [CrossRef]

15. Bledzki, A.; Spaude, R.; Ehrenstein, G.W. Corrosion Phenomena in Glass Fibres and Glass Fibre Reinforced Thermosetting Resins. *Compos. Sci. Technol.* **1985**, *23*, 263–285. [CrossRef]

16. Krauklis, A.E.; Echtermeyer, A.T. Dissolving Cylinder Zero-Order Kinetic Model for Predicting Hygrothermal Aging of Glass Fibre Bundles and Fibre-Reinforced Composites. In *4th International Glass Fibre Symposium*; Gries, T., Pico, D., Lüking, A., Becker, T., Eds.; Mainz, G (Verlag): Aachen, Germany, 2018; pp. 66–72, ISBN 978-3-95886-249-4.

17. Grambow, B.; Müller, R. First-order dissolution rate law and the role of surface layers in glass performance assessment. *J. Nucl. Mater.* **2001**, *298*, 112–124. [CrossRef]

18. Grambow, B. A General Rate Equation for Nuclear Waste Glass Corrosion. *MRS Symp. Proc. Libr. Arch.* **1985**, *44*, 15–27. [CrossRef]

19. Krauklis, A.E.; Gagani, A.I.; Echtermeyer, A.T. Near-Infrared Spectroscopic Method for Monitoring Water Content in Epoxy Resins and Fibre-Reinforced Composites. *Materials* **2018**, *11*, 586. [CrossRef]

20. Stamenović, M.R.; Putić, S.S.; Rakin, M.B.; Medjo, B.; Čikara, D. Effect of alkaline and acidic solutions on the tensile properties of glass–polyester pipes. *Mater. Des.* **2011**, *32*, 2456–2461. [CrossRef]

21. Amaro, A.M.; Reis, P.N.B.; Neto, M.A.; Louro, C. Effects of alkaline and acid solutions on glass/epoxy composites. *Polym. Degrad. Stab.* **2013**, *98*, 853–862. [CrossRef]

22. Mišíková, L.; Liška, M.; Galusková, D. Corrosion of e-glass fibres in distilled water. *Ceram. Silik.* **2007**, *51*, 131–135.

23. Bashir, S.T.; Yang, L.; Liggat, J.J.; Thomason, J.L. Kinetics of dissolution of glass fibre in hot alkaline solution. *J. Mater. Sci.* **2018**, *53*, 1710–1722. [CrossRef]

24. Hunter, F.M.I.; Hoch, A.R.; Heath, T.G.; Baston, G.M.N. *Report RWM005105, AMEC/103498/02 Issue 2: Review of Glass Dissolution Models and Application to UK Glasses*; AMEC: Didcot, Oxfordshire, UK, 2015.

25. Li, H.; Gu, P.; Watson, J.; Meng, J. Acid corrosion resistance and mechanism of E-glass fibres: Boron factor. *J. Mater. Sci.* **2013**, *48*, 3075–3087. [CrossRef]

26. Icenhower, J.; Steefel, C.I. Dissolution Rate of Borosilicate Glass SON68: A Method of Quantification Based upon Interferometry and Implications for Experimental and Natural Weathering Rates of Glass. *Geochim. Cosmochim. Acta* **2015**, *157*, 147–163. [CrossRef]

27. Gy, R. Stress corrosion of silicate glass: A review. *J. Non-Cryst. Solids* **2003**, *316*, 1–11. [CrossRef]

28. Ciccotti, M. Stress-corrosion mechanisms in silicate glasses. *J. Phys. D Appl. Phys.* **2009**, *42*, 214006–214039. [CrossRef]

29. Michalske, T.A.; Freiman, S.W. A Molecular Mechanism for Stress Corrosion in Vitreous Silica. *J. Am. Ceram. Soc.* **1983**, *66*, 284–288. [CrossRef]

30. Michalske, T.A.; Bunker, B.C. Steric Effects in Stress Corrosion Fracture of Glass. *J. Am. Ceram. Soc.* **1987**, *70*, 780–784. [CrossRef]

31. Michalske, T.A.; Bunker, B.C. A Chemical Kinetics Model for Glass Fracture. *J. Am. Ceram. Soc.* **1993**, *76*, 2613–2618. [CrossRef]

32. Michalske, T.A.; Bunker, B.C. Slow fracture model based on strained silicate structures. *J. Appl. Phys.* **1984**, *56*, 2686–2693. [CrossRef]

33. Schmitz, G.K.; Metcalfe, A.G. Stress Corrosion of E-Glass Fibres. *Ind. Eng. Chem. Prod. Res. Dev.* **1966**, *5*, 1–8. [CrossRef]

34. Delage, F.; Ghaleb, D.; Dussossoy, J.L.; Chevallier, O.; Vernaz, E. A mechanistic model for understanding nuclear waste glass dissolution. *J. Nucl. Mater.* **1992**, *190*, 191–197. [CrossRef]

35. Ma, T.; Jivkov, A.P.; Li, W.; Liang, W.; Wang, Y.; Xu, H.; Han, X. A mechanistic model for long-term nuclear waste glass dissolution integrating chemical affinity and interfacial diffusion barrier. *J. Nucl. Mater.* **2017**, *486*, 70–85. [CrossRef]

36. Khawam, A.; Flanagan, D.R. Solid-State Kinetic Models: Basics and Mathematical Fundamentals. *J. Phys. Chem. B* **2006**, *110*, 17315–17328. [CrossRef]

37. International Standard ISO 2078:1993 (revised in 2014), Textile Glass—Yarns—Designation. 2014. Available online: https://www.iso.org/standard/6865.html (accessed on 11 February 2019).

38. 3B Fibreglass technical data sheet. HiPer-tex W2020 rovings, Belgium. 2012. Available online: https://www.3b-fibreglass.com/ (accessed on 24 July 2018).

39. Thomason, J.L. *Glass Fiber Sizings: A Review of the Scientific Literature*; J.L. Thomason: Middletown, DE, USA, 2012; p. 127, ISBN 978-0-9573814-1-4.

40. Shiue, Y.S.; Matthewson, M.J. Stress dependent activation entropy for dynamic fatigue of pristine silica optical fibres. *J. Appl. Phys.* **2001**, *89*, 4787–4793. [CrossRef]

41. Eastes, W.; Potter, R.M.; Hadley, J.G. Estimating in-vitro glass fibre dissolution rate from composition. *Inhal. Toxicol.* **2000**, *12*, 269–280. [CrossRef] [PubMed]

42. Papadimitriou, S.; Kennedy, H.; Kennedy, P.; Thomas, D.N. Kinetics of ikaite precipitation and dissolution in seawater-derived brines at sub-zero temperatures to 265 K. *Geochim. Cosmochim. Acta* **2014**, *140*, 199–211. [CrossRef]

43. Ozola, R.; Krauklis, A.E.; Leitietis, M.; Burlakovs, J.; Vircava, I.; Ansone-Bertina, L.; Bhatnagar, A.; Klavins, M. FeOOH-modified clay sorbents for arsenic removal from aqueous solutions. *Environ. Technol. Innov.* **2016**. [CrossRef]

44. Krauklis, A.E.; Ozola, R.; Burlakovs, J.; Rugele, K.; Kirillov, K.; Trubaca-Boginska, A.; Rubenis, K.; Stepanova, V.; Klavins, M. FeOOH and $Mn_8O_{10}Cl_3$ Modified Zeolites for As(V) Removal in Aqueous Medium. *J. Chem. Technol. Biotechnol.* **2017**, *92*, 1948–1960. [CrossRef]

45. Anxolabéhère-Mallart, E.; Costentin, C.; Policar, C.; Robert, M.; Savéant, J.M.; Teillout, A.L. Proton-coupled electron transfers in biomimetic water bound metal complexes. The electrochemical approach. *Faraday Discuss.* **2011**, *148*, 83–95. [CrossRef]

46. Secula, M.S.; Crețescu, I.; Petrescu, S. An experimental study of indigo carmine removal from aqueous solution by electrocoagulation. *Desalination* **2011**, *277*, 227–235. [CrossRef]

47. Criscenti, L.J.; Kubicki, J.D.; Brantley, S.L. Silicate Glass and Mineral Dissolution: Calculated Reaction Paths and Activation Energies for Hydrolysis of a Q^3 Si by H_3O^+ Using Ab Initio Methods. *J. Phys. Chem. A* **2006**, *110*, 198–206. [CrossRef]

48. Fournier, R.O.; Rowe, J.J. The solubility of amorphous silica in water at high temperatures and high pressures. *Am. Miner.* **1977**, *62*, 1052–1056.

49. Crundwell, F.K. On the Mechanism of the Dissolution of Quartz and Silica in Aqueous Solutions. *ACS Omega* **2017**, *2*, 1116–1127. [CrossRef]

50. Von Damm, K.L.; Edmond, J.M.; Grant, B.; Measures, C.I.; Walden, B.; Weiss, R.F. Chemistry of submarine hydrothermal solutions at 21°N, East Pacific Rise. *Geochim. Cosmochim. Acta* **1985**, *49*, 2197–2220. [CrossRef]

51. Holland, H.D. *The Chemistry of the Atmosphere and Oceans*; Wiley: New York, NY, USA, 1978; p. 351, ISBN 978-0471035091.

52. Scheffler, C.; Förster, T.; Mäder, E.; Heinrich, G.; Hempel, S.; Mechtcherine, V. Aging of alkali-resistant glass and basalt fibers in alkaline solutions: Evaluation of the failure stress by Weibull distribution function. *J. Non-Cryst. Solids* **2009**, *355*, 2588–2595. [CrossRef]

KRAUKLIS A.E., GAGANI A.I., ECHTERMEYER A.T.

LONG-TERM HYDROLYTIC DEGRADATION OF THE SIZING-RICH COMPOSITE INTERPHASE.

Long-Term Hydrolytic Degradation of the Sizing-Rich Composite Interphase

Andrey E. Krauklis * , **Abedin I. Gagani and Andreas T. Echtermeyer**

Department of Mechanical and Industrial Engineering, Norwegian University of Science and Technology, 7491 Trondheim, Norway; abedin.gagani@ntnu.no (A.I.G.); andreas.echtermeyer@ntnu.no (A.T.E.)
* Correspondence: andrejs.krauklis@ntnu.no or andykrauklis@gmail.com; Tel.: +371-268-10-288

check for updates

Abstract: Glass fiber-reinforced composites are exposed to hydrolytic degradation in subsea and offshore applications. Fiber-matrix interphase degradation was observed after the matrix was fully saturated with water and typical water absorption tests according to ASTM D5229 were stopped. Due to water-induced dissolution, fiber-matrix interphase flaws were formed, which then lead to increased water uptake. Cutting sample plates from a larger laminate, where the fibers were running parallel to the 1.5 mm long short edge, allowed the hydrolytic degradation process to be studied. The analysis is based on a full mechanistic mass balance approach considering all the composite's constituents: water uptake and leaching of the matrix, dissolution of the glass fibers, and dissolution of the composite interphase. These processes were modeled using a combination of Fickian diffusion and zero-order kinetics. For the composite laminate studied here with a saturated epoxy matrix, the fiber matrix interphase is predicted to be fully degraded after 22 to 30 years.

Keywords: composites; sizing; interphase; glass fibers; environmental degradation; aging; model; kinetics; durability; hydrolysis

1. Introduction

Fiber-reinforced polymer (FRP) composites have experienced a rapid rise in use in the past 50 years due to their high strength, stiffness, relatively light weight and good corrosion resistance, especially when compared with more traditional structural materials such as steel and aluminum [1]. The reason for such superior performance is the synergistic interaction between the constituent materials inside the composite [1]. One such material is the sizing, which is a multi-component coating on the surface of the fibers. During the manufacture of FRPs, this results in the formation of a sizing-rich composite interphase between the reinforcing fibers and the matrix polymer [2]. This composite interphase is of vital importance since the mechanical properties of composite materials are often determined by whether the mechanical stresses can be efficiently transferred from the matrix to the reinforcing fibers [3–5]. The quality of the interfacial interaction is strongly dependent on the adhesional contact and the presence of flaws in the interphase [6]. It is generally agreed that the composite interphase is often the mechanical weak link and a potential source for the initiation of defects in fiber-reinforced composite structures [5].

Composite laminates are often exposed to aqueous and humid environments. Environmental aging is especially interesting for marine, offshore and deep-water applications of composites, such as oil risers and tethers [7–12]. It has been reported that water and humid environments negatively impact the mechanical properties of FRPs partially because of a loss of the interfacial bonding [5,12–15]. Flaws in the interphase can be introduced due to the interaction of the interphase with water taken up from the environment [6]. The removal of the sizing material can also lead to a microcrack initiation at

the surface of glass fibers. Furthermore, various sizing components can be extracted by water, resulting in the loss of the material [16–20]. Quantifying the water-induced aging is especially important for glass fiber-reinforced composites since the glass fibers are highly hygroscopic [5]. The environmental durability is one of the limiting factors in the structural applications [21], since the superior strength and stiffness of such materials are often compromised by the uncertainty of the material's interaction with the environment [22]. Durability is a primary issue because environmental factors such as moisture, temperature and the state of stress to which the material is exposed can degrade interfacial adhesion as well as the properties of the constituent phases. Environmental aging is mainly important at high temperatures, since the dissolution reactions are accelerated at higher temperatures. Therefore, it is of great importance to understand the environmental aging and dissolution kinetics of a sizing-rich composite interphase.

1.1. Sizing and its Composition

The sizing which forms the interphase, has typically a proprietary composition. Available information about commercial glass fibers tends to contain only one or two sizing-related details. The first is an indication of the chemical compatibility of the sizing with the matrix polymer, e.g., epoxy, as in this case. The second is a value for the loss on ignition (LOI), which indicates the amount of sizing [23]. The key functions of the sizing are: (1) to protect the glass fibers during handling and production; (2) to ensure a high level of stress transfer capability across the fiber-matrix interphase; and (3) to protect the composite matrix interphase against environmental degradation [12].

A typical sizing consists of about 20 chemicals. The most important chemical is an organofunctional silane commonly referred to as a coupling agent [24–26], which is the main component that promotes adhesion and stress-transfer between the polymer matrix and the fiber [12]. It also provides improvements in the interphase strength and hygrothermal resistance of the composite interphase [26–28]. The silane coupling agents have the general structure $[X–Si(–O–R)_3]$ where R is a methyl or ethyl group and X is a reactive group towards the polymer, in this case, an amine group. When applied to fibers, a silane coupling agent is first hydrolyzed to a silanol in presence of water. It is unstable and further condenses onto the fibers by producing a siloxane/poly(siloxane) network, which then partially becomes covalently bonded to the glass fiber surface. During the composite manufacture, the X reactive groups of the silane may react with the thermosetting matrix polymer, leading to a strong network bridging between the fiber and the matrix [12].

Although there are many different silane molecules available, the aminosilanes form the largest proportion of silanes employed in the composites industry [12]. The most common coupling agent is an aminosilane compound called γ-aminopropyltriethoxysilane (γ-APS), also known as APTES, which is the coupling agent in the studied sizing [16]. Usually sizings contain about 10 wt % of the coupling agent [29].

The composition of the sizing also consists of a number of multi-purpose components, such as a film former which holds the filaments together in a strand and protects the filaments from damage through fiber–fiber contact. Film formers are as closely compatible to the polymer matrix as possible. Epoxies, such as in this case, are very common film formers [12]. Usually sizings contain about 70–80 wt % of the film former [12,29].

Much less is known about the other chemicals in the sizing [12]. The sizing may also contain other compounds such as cationic or non-ionic lubricants, antistatic agents, emulsifiers, chopping aids, wetting agents or surfactants, and antioxidants [2,12,30]. Poly(propylene oxide) (PPO) or its co-polymer with poly(ethylene oxide) (PEO) is often used as a surfactant in sizings [2]. Polydimethylsiloxane (PDMS) is a common adhesion promoter, wetting agent, or surface tension reducer [2].

The exact composition of the sizing used in this study was not known to the authors, but based on technical details on the given R-glass fibers elsewhere [16], it is assumed that the sizing is based on the general characteristics described above. The results obtained are compatible with this assumption.

1.2. The Structure of the Sizing-Rich Composite Interphase

The structure of the sizing-rich composite interphase is very complex [12], as the sizing itself is heterogeneous and not uniform [12,31,32]. Furthermore, it has been observed by various researchers, that sizing is coated on fibers in "islands", "islets" or in patches, meaning that the fiber surface is only partially covered by the sizing, also giving some roughness to the surface [12,33–38]. Thomason and Dwight have concluded that epoxy-compatible sizings cover at least 90% of the glass fiber surface [39]. Mai et al. investigated APTES sizings using atomic force microscopy (AFM) and concluded that sized fibers are rougher than unsized fibers [38]. Also, similar conclusions were drawn by a few other researchers, including Turrión et al., who have shown that thickness of the sizing on the glass fibers varies from some nanometers up to a few hundred nanometers due to roughness [6,31,37].

With regards to the molecular structure of the interphase, APTES forms chemical covalent and physico-chemical hydrogen bonds and van der Waals interactions with the glass fibers and the amine epoxy [12,40]. The majority of APTES molecules which react with the glass surface can only form single Si–O–Si bonds with the glass due to steric limitations, while the vast majority of Si–O–Si bond formation in the silane interphase is due to polymerization—formation of the poly(siloxane) network [12]. A multilayer is formed on the glass fiber surfaces where the amino groups form intramolecular ring structures [32,41].

The concept of a composite interphase can be represented by a matrix polymer/poly(siloxane)/glass fiber model (shown in Figure 1) [5].

The siloxanes and poly(siloxanes) form covalent bonds with the glass fiber surface, resulting in a two-dimensional interface, the thickness of which is governed by the length of the chemical bonds, and is of an ångstrøm-scale (one tenth of a nanometer) [5].

The composite interphase is a gradient-type blend of the sizing compounds and the bulk matrix polymer, usually being about a micrometer in thickness [5,12,29,42,43]. It was observed, that an interfacial failure occurs at 0.5–4 nm from the glass surface in glass/γ-APS/epoxy interphase, indicating that the interphase region, rather than the two-dimensional interface is the weak link [5].
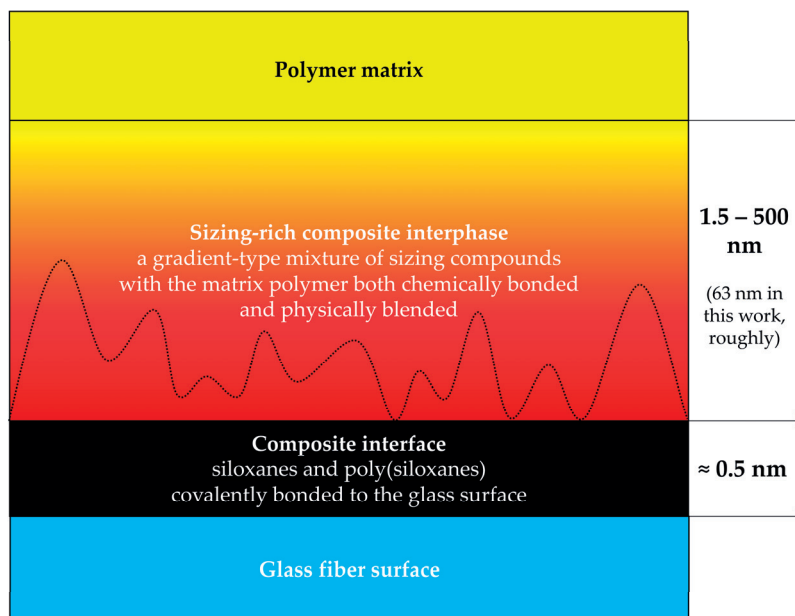

Figure 1. The concept of a polymer–siloxane–glass interphase, after [5]. The dotted line indicates that the sizing is rough [6,31,38].

1.3. The Aim of This Work

Composites take up water from their surroundings and may release some molecules into the surrounding water. Water uptake curves for composites are not straightforward to interpret since each constituent (matrix, fibers, sizing-rich interphase) interacts differently with the absorbed water. The mass uptake curve presents the combined effect of all these individual interactions.

Testing of water absorption is usually stopped when the composite material's water uptake has reached a maximum. The typical test procedures follow ASTM D5229 [44], where testing is stopped when two subsequent measurements do not differ by more than 0.5% [44]. However, when exposure to water is extended for longer periods, experiments performed in this work showed that degradation of the composite continues and additional mass gain and loss processes are involved. A similar observation was made by Perreux et al. [45], who studied immersion in water of 2.7 mm thick glass fiber epoxy composite plates for up to 10 years. They found that the weight gain of plates aged at 60 °C increased strongly after saturation. After about five years in water at 60 °C, a composite plate started to continuously lose mass with time [45]. This study will show that these effects can be related to the hydrolytic degradation of the fiber/matrix interphase.

The aim of this manuscript is to describe the degradation of the fiber/matrix interphase with special emphasis on the reaction kinetics.

2. Materials and Methods

2.1. Materials

Composite laminates were made with an amine-cured epoxy. The epoxy was prepared by mixing reagents Epikote Resin RIMR135^{TM} (Hexion, Columbus, OH, USA) and amine based Epikure Curing Agent RIMH137^{TM} (Hexion), stoichiometrically, in a ratio of 100:30 by weight. The mixture was degassed in a vacuum chamber for 30 min in order to remove bubbles. The density of the polymer (ρ_m) was 1.1 g/cm^3. Resin and hardener system consisted of the following compounds by composition: 0.63 wt % bisphenol A diglycidyl ether (DGEBA), 0.14 wt % 1,6-hexanediol diglycidyl ether (HDDGE), 0.14 wt % poly(oxypropylene)diamine (POPA) and 0.09 wt % isophorondiamine (IPDA) [46].

A typical glass fiber used for marine and oil and gas applications was selected: boron-free and fluorine-free high-strength, high-modulus 3B HiPer-Tex^{TM} W2020 R-glass (3B-the fiberglass company, Hoeilaart, Belgium). Stitch-bonded mats were used. The average fiber diameter was 17 ± 2 μm [47,48]. The density of glass (ρ_f) was 2.54 g/cm^3 [47,48].

Composite laminates 50 mm thick were prepared via vacuum-assisted resin transfer molding (VARTM). Laminates were manufactured using the aforementioned fabrics and epoxy resin. The curing was performed at room temperature for 24 h, continued by post-curing in an air oven (Lehmkuhls Verksteder, Oslo, Norway) at 80 °C for 16 h. Full cure was achieved [46,49]. The composite laminates were cut into specimens with dimensions of 50 mm × 50 mm × 1.5 mm. The geometry of the samples and cross section of the fibers is shown in Figure 2. Two configurations C1 and C3 were cut, as shown in Figure 2. Configurations. C1 is representative of a typical composite where fibers are parallel to one of the long sides. The surface area of cut fibers with exposed cross sections is 50 mm × 1.5 mm. Configuration C3 was cut in a way that a maximum number of cut fibers were obtained having exposed cross sections (50 mm × 50 mm). The length of the fibers was just 1.5 mm. This unusual specimen was made to obtain maximum fiber exposure towards the water. The same specimens were also used to measure anisotropic diffusivity in a separate study [49]. The specified dimensions were achieved within 5% tolerance. The thickness was adjusted using a grinding and polishing machine Jean Wirtz PHOENIX 2000 (Jean Wirtz, Dusseldorf, Germany) and SiC discs (Struers, Cleveland, OH, USA; FEPA P500, grain size 30 μm).

Figure 2 also shows a micrograph of a surface with visible cross sections of cut fibers from a specimen with C3 configuration. The micrograph was taken with a confocal microscope InfiniteFocus G4 (Alicona, Graz, Austria).
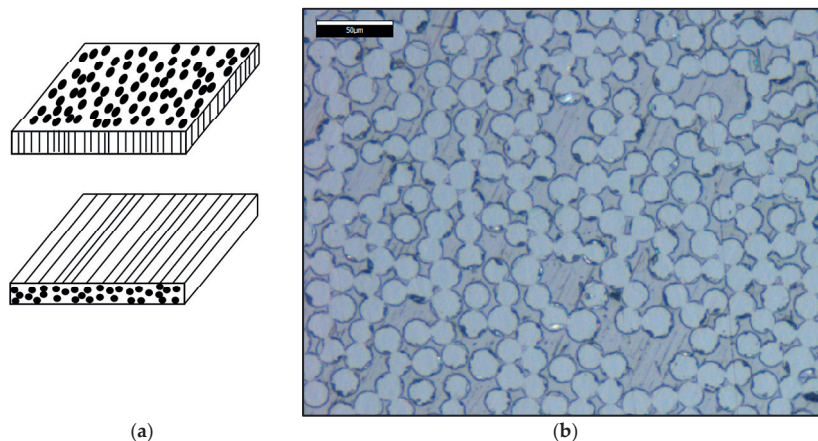
Figure 2. Glass fiber-reinforced epoxy composite plates: (**a**) sample configuration indicating alignment of the fibers in the plate: C3 at the top; C1 at the bottom; (**b**) micrograph of the largest face of the composite plate showing the cross section of the fibers at the surface.

Distilled water (resistivity 0.5–1.0 MΩ·cm) was used for conditioning of the composite samples. It was produced using the water purification system Aquatron A4000 (Cole-Parmer, Vernon Hills, IL, USA). The pH of the distilled water was 5.650 ± 0.010, being lower than neutral due to dissolved CO_2 from atmosphere in equilibrium.

2.2. Experimental Methods

2.2.1. Loss on Ignition

The loss on ignition (LOI) value of the fiber bundles was determined according to the standard practice ASTM D4963 [23]. This technique allows measurement of the weight loss of a sized glass sample. Since the weight loss is due to the burning off of the sizing, the method can be used to determine the amount of sizing on the fiber [12]. According to the LOI measurements, the sizing was 0.64 wt % of the sized fibers. The temperature during the LOI measurement was about 565 °C applied for about 5–5.5 h.

The obtained LOI is consistent with literature. LOI of most glass fiber reinforcement products is below 1.2 wt % [12]. For instance, Zinck and Gerard [50] also studied an APTES-based sizing which had a similar LOI value of 0.77 wt %.

2.2.2. Constituent Volume and Mass Fractions of the Composite

The fiber volume fraction of the composite was 59.5% and was determined using the burn-off test, after the ASTM Standard D3171 [51]. The void volume fraction of the composite was 0.44% and was measured by image analysis of optical microscope images, as was described elsewhere by Gagani et al. [49]. Fiber, matrix, interphase and voids volume fractions were 59.5%, 39.2%, 0.9% and 0.44%, respectively. The interphase volume fraction was obtained using the LOI value (0.64 wt %), the mass of sized glass fibers (about 5.6 g), the density of the interphase (1.1 g/cm^3) and the mass of the composite (about 7.2 g). Fiber, matrix and interphase mass fractions were 77.2%, 22.3% and 0.5%, respectively. The fiber surface area of one plate was about 0.5 m^2 on average. The composite interphase mass fraction (m_{f_i}) was calculated as:

$$m_{f_i} = \frac{\text{LOI} \cdot m_{\text{fibers}}}{m_{\text{comp}}}$$

(1)

where m_{fibers} is the mass of the sized fibers; m_{comp} is the mass of the composite.

2.2.3. Conditioning of Composite Plates

Water uptake and hygrothermal aging of the composite laminates was conducted using a batch system. A heated bath with distilled water (60 ± 1 °C) was used for conditioning the samples. Samples were weighed using analytical scales AG204 (±0.1 mg; Mettler Toledo, Columbus, OH, USA). Samples were conditioned for a period of about a year. Three parallels were performed.

2.2.4. Specific Surface Area of the Fibers Obtained by N_2 Sorption/Desorption and Brunauer–Emmett–Teller (BET) Theory

The specific surface area of the sized and unsized glass fibers was obtained via N_2 sorption and desorption. The method uses physical adsorption and desorption of gas molecules based on the Brunauer–Emmett–Teller (BET) theory [52]. The specific surface area was measured using QUADRASORB SI (Quantachrome Instruments, Boynton Beach, FL, USA) equipment. BET tests for specific surface area determination were performed according to the international standard ISO 9277:2010(E) [53]. The method is based on the determination of the amount of adsorptive gas molecules covering the external surface of the solid [53].

Since the sizing's surface is rough [12], the BET tests can provide the specific surface area. The BET theory explains the physical adsorption of gas molecules on a solid surface of a material, and it is the basis for the specific surface area determination.

Due to the roughness of the sizing on the fiber surface, the specific surface area of sized glass fibers measured with BET was 0.180 m^2/g (see Figure 3), being higher than the specific surface area of unsized glass fibers of 0.09 m^2/g (geometrical considerations as described in Section 2.1) or 0.084 m^2/g using the BET method. For the unsized and sized glass fibers, the data with the BET model fit was with a determination coefficient R^2 of 0.968 and 0.994, respectively.
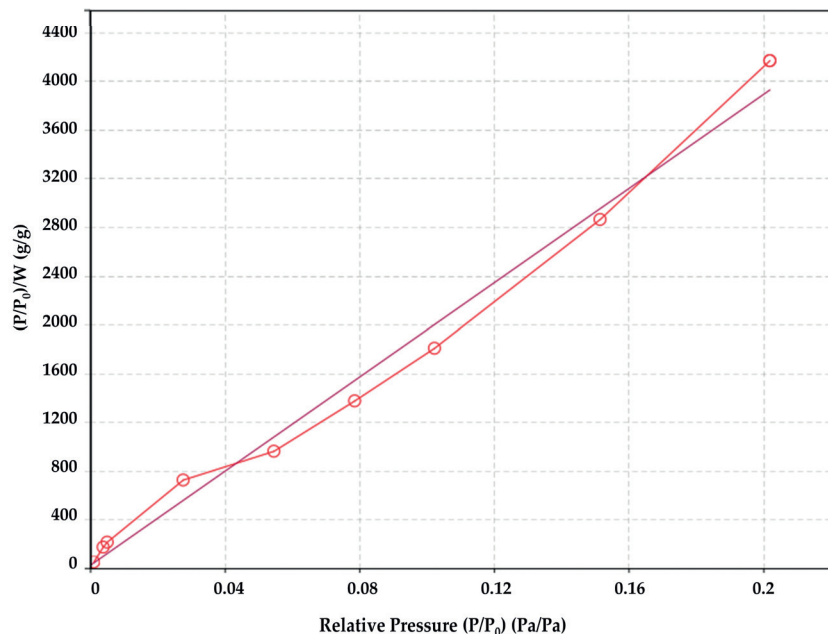

Figure 3. Brunauer–Emmett–Teller (BET) analysis of the specific surface area of the sized fibers.

3. Analytical Model

3.1. Mass Balance

When polymers take up water from the environment, their mass is affected by the water uptake itself, leaching and aging mechanisms such as hydrolysis, chain scission or oxidation [46,54]. For the studied epoxy, there is no significant mass loss due to chemical bond scission, since hydrolysis and chain scission are not occurring [46,55].

The combination of the phenomenological perspective and mass balance approach provide a useful tool for analyzing mass uptake/loss processes in composites during hygrothermal aging by breaking down a complex process into constituent-related processes. The processes that affect weight gain or loss of composites are summarized in Table 1.

Table 1. Summary of the processes during hygrothermal aging of composites that affect the mass balance.

Process	Sign	Reference
Water uptake of the polymer matrix	+	[49]
Water uptake by the composite interphase	+	[56]
Water uptake by the voids	+	[12,49,57]
Thermo-oxidation of the polymer matrix	+	[46]
Leaching from polymer matrix	−	[46]
Glass fiber dissolution	−	[28,47]
Sizing-rich interphase dissolution	−	This work

Gravimetric measurements determine the sample's mass over time during conditioning in water. The mass consists of the following terms:

$$m_{\text{gravimetric}}(t) = \begin{aligned} & m_{\text{dry}} + m_{\text{water uptake}}(t) + m_{\text{oxidation}}(t) - m_{\text{leaching}}(t) \\ & -m_{\text{glass dissolution}}(t) - m_{\text{interphase dissolution}}(t) \end{aligned} \tag{2}$$

The dissolution of the interphase is then simply given by:

$$m_{\text{interphase dissolution}}(t) = \begin{aligned} & m_{\text{dry}} + m_{\text{water uptake}}(t) + m_{\text{oxidation}}(t) - m_{\text{leaching}}(t) \\ & - m_{\text{glass dissolution}}(t) - m_{\text{gravimetric}}(t) \end{aligned} \tag{3}$$

The proposed model equation should be a phenomenologically full representation of the interaction between the composite material and the water environment. More details will now be given for each of the terms.

3.2. Water Uptake

The water uptake for composites includes three sub-processes: the uptake by the polymer matrix, by the interphase, and by the voids [49]. The glass fibers themselves do not absorb any water.

The water taken up by the polymer matrix at any point of time is limited by the diffusivity and the water saturation level [49,54]. The Fickian diffusion model can be used to model the water uptake by the polymer and the interphase [49]. In addition, the effect of voids being filled with water has to be considered [12,49]. The water content at saturation of the studied epoxy is 3.44 wt % if no voids are present [56]. Saturation has been defined as the moment when the difference in two consecutive water absorption measurements is lower than 0.5%, as defined by ASTM D5229 [44]. The composite's saturation water content M_∞ was determined to be 0.96 wt % [49]. It can be calculated by Equation (4) [49]:

$$M_\infty = \frac{M_\infty^m (v_{\text{m}} + v_{\text{i}})\rho_{\text{m}} + M_\infty^v v_{\text{v}}\rho_{\text{water}}}{v_{\text{f}}\rho_{\text{f}} + (v_{\text{m}} + v_{\text{i}})\rho_{\text{m}}} \tag{4}$$

where ρ_m is the matrix density, ρ_f is the fiber density, ρ_{water} is the water density, v_f is the fiber volume fraction, v_m is the matrix volume fraction, v_i is the interphase volume fraction, v_v is the void volume fraction ($v_f + v_m + v_i + v_v = 1$), M_∞^m is the matrix saturation water content (3.44 wt %) and M_∞^v is the void saturation water content (100 wt %). Fiber, matrix, interphase and voids volume fractions are 59.5%, 39.2%, 0.9% and 0.44%, respectively.

The sizing-rich interphase is assumed to have the same saturation water content as the epoxy matrix, since it contains about 70–80 wt % epoxy film-former [12,29,56]. Since the volume of the sizing is very small compared to the composite's volume any deviation from this assumption would have a minimal effect on the water uptake.

It is assumed here that the small voids will be completely filled with water $M_\infty^v = 1$, as was measured experimentally for the composite described here [49].

The water diffusivity of the studied epoxy polymer and the composites C1 and C3 in the thickness direction (with the fibers running transverse and parallel to the thickness direction for C1 and C3, respectively; see Figure 2) are systematized in Table 2 [49]. The higher diffusivity of the composite C3 is due to the fact that the diffusivity of the interphase in the direction parallel to the fibers is almost an order of magnitude higher than that of the polymer, after [49].

Table 2. Diffusivities in the through-the-thickness direction, after [49].

Specimen	D (mm²/h)
Epoxy	0.0068
C1	0.0051
C3	0.0210

The following equation links the mass uptake to diffusivity from solving the 1-D Fickian diffusion equation, as described by Crank [58]:

$$M(t) = M_\infty \left[1 - \left(\frac{8}{\pi^2} \right) \sum_{i=0}^{\infty} \frac{e^{-(2i+1)\left(\frac{\pi}{h}\right)^2 Dt}}{(2i+1)^2} \right] \tag{5}$$

By fitting the exact solution of the diffusion equation to an exponential function, the ASTM standard simplified equation is the following [44]:

$$M(t) = M_\infty \left[1 - e^{-7.3\left(\frac{Dt}{h^2}\right)^{0.75}} \right] \tag{6}$$

where $M(t)$ is the water content, M_∞ is the water saturation content, t is time, h is the thickness and D is the diffusivity in the thickness direction of the plate.

More details and 3-D Fickian model calculations can be found elsewhere [49]. 1-D and 3-D Fickian models gave the same result. Thus, for the sake of simplicity, the 1-D diffusion model for water uptake is used in this work.

Experimental gravimetric measurements and modeled water uptake curves using Equation (6) are shown in Figure 4 for a composite C3 with and without voids. It can be clearly seen that the absorption of water in the voids needs to be modeled to get a good fit with the experimental data.
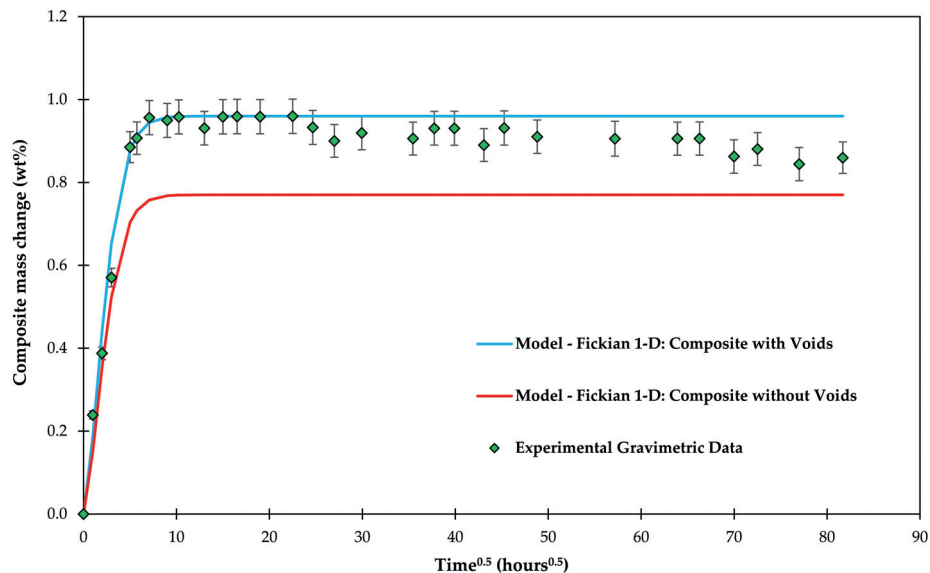
Figure 4. Experimental gravimetric measurements of composite C3 plates conditioned in water and modeled water uptake curves using the Fickian 1-D model.

3.3. Oxidation of the Epoxy Matrix

Photo-oxidation is not present as the material is not exposed to high-energy irradiation [46]. The effect of thermo-oxidation on mass gain due to water uptake is negligible. Thermo-oxidation for the studied epoxy polymer occurs via the carbonyl formation mechanism in the carbon-carbon backbone via nucleophilic radical attack, as is described elsewhere [46].

3.4. Leaching of Molecules out of the Epoxy Matrix

Water molecules can migrate into the epoxy polymer while at the same time small molecules may leach out of the matrix [59,60]. The leaching phenomenon may occur due to initially present additives, impurities, unreacted hardener or degradation products diffusing out of the epoxy network into the water environment, which is in contact with the polymer. Often leaching follows Fickian-type diffusion [61]. The driving force of this process is due to the difference in concentration of these chemicals inside the polymer, and in the surrounding aqueous environment.

Leaching was determined experimentally using HR-ICP-MS up to about 1100 h in another work for the same epoxy material as used for making the composites in this study [46]. Krauklis and Echtermeyer [46] found that for the studied epoxy polymer there was no leaching of hardener, whilst the leaching occurred of epoxy compounds and impurities, such as epichlorohydrin and inorganic compounds. Based on Fourier transform–near infrared (FT-NIR) spectra (reported in [46]) the leached amount after about 1100 h of conditioning was estimated to be at 54.74 wt % of the initial leachable compounds present in the material. This indicates that more than a half of the small molecules were leached out after the relatively short time of 1100 h. The initial leachable compound content M^0_{leaching} was found to be 0.092 wt % (about 1.5 mg) defined as the mass loss due to leaching divided by the initial mass of the polymer (about 1.6 g).

The diffusivity of leached compounds through the epoxy polymer was determined according to 1-D Fickian diffusion [44,61]:

$$M_{\text{leaching}}(t) = M_{\text{leaching}}^0 \left[1 - e^{-7.3 \left(\frac{D_{\text{leaching}} t}{h^2} \right)^{0.75}} \right] \tag{7}$$

The diffusivity was obtained by regression analysis of the data performing non-linear Generalized Reduced Gradient (GRG) algorithm, while minimizing the residual sum of squares. The leaching diffusivity D_{leaching} obtained in this study was 6.0×10^{-5} mm²/h.

The leached-out compounds were experimentally measured with High-resolution inductively coupled plasma mass spectrometry (HR-ICP-MS) (data from [46]). The modeled leaching behavior from the matrix polymer is shown in Figure 5.
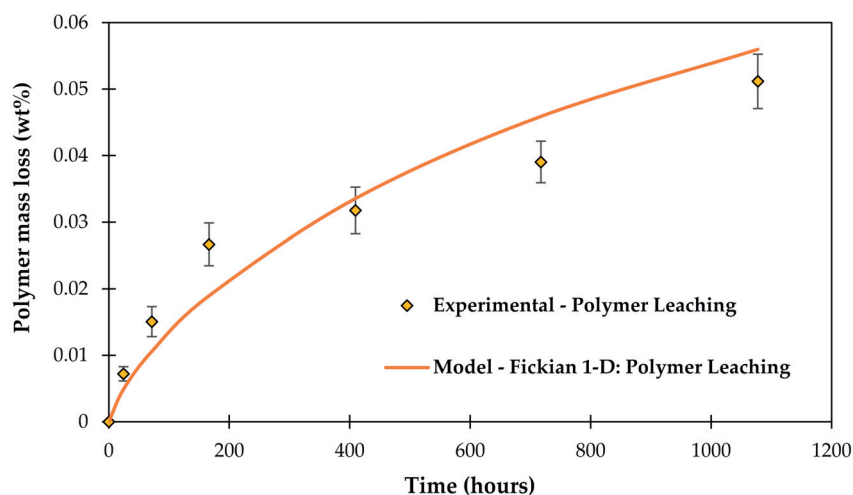

Figure 5. Polymer leaching determined experimentally with HR-ICP-MS, after [46], and modeled using Fickian 1-D model, after [61].

3.5. Glass Dissolution

Glass fibers slowly degrade in water environments via dissolution reactions resulting in a mass loss [47,62,63]. The degradation of glass fibers follows two distinct kinetic regions: short-term non-steady-state (Phase I) and long-term steady-state degradation (Phase II), as described in the dissolving cylinder zero-order kinetic (DCZOK) model for prediction of long-term dissolution of glass from both fiber bundles [47]. During Phase I, the degradation is complex and involves such processes as ion exchange, gel formation and dissolution. When Phase II is reached, the dissolution becomes dominant and the degradation follows zero-order reaction kinetics. For the studied R-glass, the transition from Phase I into Phase II occurs in about a week (166 h) at 60 °C and pH 5.65 [28,47]. Elements that are released during degradation of R-glass are Na, K, Ca, Mg, Fe, Al, Si and Cl [47]. The glass mass loss is the cumulative mass loss of all these ions [47]. Si contribution to the total mass loss of the studied R-glass is the largest (56.1 wt %) and seems to govern the dissolution process [47].

The rate of the dissolution depends on the apparent glass dissolution rate constant (K_0^*) and the glass surface area exposed to water (S) [28,47]. The glass surface area is proportional to the fiber radius. As the dissolution continues, the radius decreases linearly with time resulting in the mass loss deceleration; the DCZOK model accounts for this effect [47]. Rate constants at various environmental conditions (pH, temperature and stress), as well as more details about the model can be found in other works [28,47,63].

For a thin composite with fibers parallel to the short side through-thickness direction, such as in this work, the dissolution of glass, compared to the free fiber bundles with sizing (not embedded in the composite), is slowed down by 36.84% [28]. The differential mass loss equation for thin composites can be written as [28]:

$$\frac{\partial m}{\partial t} = K_0^* S(t) \tag{8}$$

The K_0^* includes the effects of diffusion and accumulation of the degradation products inside the composite, the protective effect of the sizing and the availability of water [28,47,63]. The time-dependent parameter is the fiber surface area $S(t)$.

Considering the two distinct phases of the degradation, the full DCZOK model in the integral form is the following, after [47]:

$$
\begin{cases}
t \leq t_{\mathrm{st}} : \; m_{\mathrm{dissolved}} = n\pi l \left(2r_0 K_0^{*\,I} t - \frac{K_0^{*\,I\,2}}{\rho_{\mathrm{f}}} t^2 \right) \\
t > t_{\mathrm{st}} : \; m_{\mathrm{dissolved}} = m_{\mathrm{dissolved}_{t_{\mathrm{st}}}} + n\pi l \left(2r_{t_{\mathrm{st}}} K_0^{*\,II} (t - t_{\mathrm{st}}) - \frac{K_0^{*\,II\,2}}{\rho_{\mathrm{f}}} (t - t_{\mathrm{st}})^2 \right)
\end{cases}
\tag{9}
$$

where n is the number of fibres (6450824); l is the length of fibres (1.5 mm); r_0 is the initial fiber radius (8.5 μm), and ρ_{glass} is the density of glass (2.54 g/cm^3); $K_0^{*\,I}$ and $K_0^{*\,II}$ are the apparent dissolution rate constants (g/m^2·s) for the short-term non-steady-state (Phase I) and long-term steady-state (Phase II) regions, respectively; $r_{t_{\mathrm{st}}}$ (m) and $m_{\mathrm{dissolved}_{t_{\mathrm{st}}}}$ (g) are the fiber radius and lost mass after time t_{st} (s), when steady-state is reached (166 h [47,63]).

Using the composition of dissolving ions reported for the studied R-glass (Si contribution 56.1 wt %) [47], and the composite data after [28], $K_0^{*\,I}$ and $K_0^{*\,II}$ for the studied composite are 6.91×10^{-6} and 1.54×10^{-6} g/(m^2·h), respectively. The dissolution rate constants are systematized in Table 3. The glass mass loss was modeled using the DCZOK Equation (9) as shown in Figure 6. The glass mass loss is normalized by the composite plate's glass fiber surface area (about 0.5 m^2).

Table 3. Apparent glass dissolution rate constants.

Phase	K_0^* (g/(m^2·h))
Phase I	6.91×10^{-6}
Phase II	1.54×10^{-6}

These ions determined with HR-ICP-MS come from both glass material and the sizing-rich interphase. HR-ICP-MS can capture ions from interface and interphase (ionic products of the polysiloxane/siloxane hydrolysis), but ICP does not allow carbon detection due to CO_2 in the plasma, thus the organics from sizing-rich interphase are not captured. In other words, the predicted mass loss due to dissolution includes ions coming from the interface and interphase, but does not include organic compounds from the interphase. This is what makes the difference between the HR-ICP-MS determined mass loss and the gravimetric mass loss of the composite.
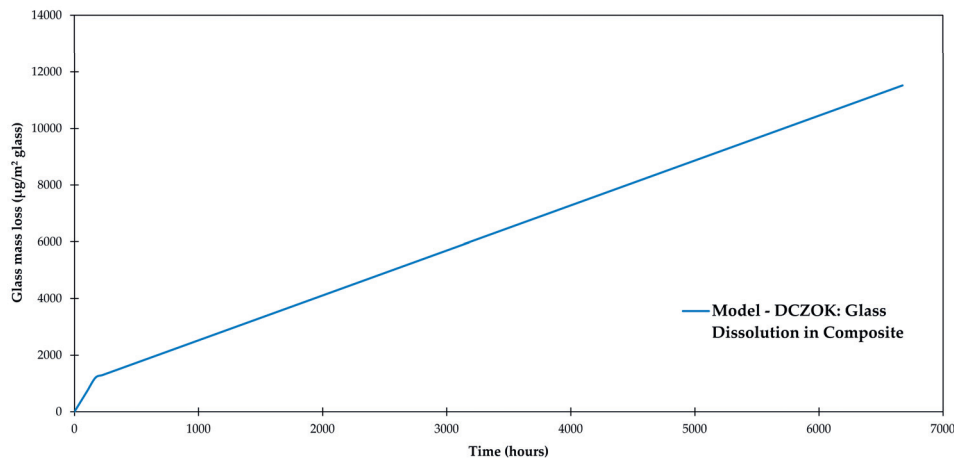
Figure 6. Glass-fiber dissolution modeled using dissolving cylinder zero-order kinetics (DCZOK) for the studied composite, after [28,47,63].

3.6. Interphase Dissolution

The aging of the sizing-rich composite interphase is the least understood constituent. The small amount of the interphase sizing compared to the composite bulk material makes analysis difficult. The proprietary nature of the sizing's composition allows only general evaluations. For typical sizing formulations, water interacting with the interphase may hydrate the Si–O–Si and Si–O–C bonds [5]. It was found that water molecules adsorbed in the epoxy matrix could migrate towards the sizing/glass fiber interface through the sizing, resulting in the dissolution/decomposition of the polysiloxane [30]. The reaction with water breaks strained Si–O–Si bonds and generates Si–OH sites [12]. Principle silane chemical bonding is reversible in the presence of water, thus the Si–O–Si bonds can be broken due to hydrolysis, as shown in Chemical Reaction (10) [12]:

$$\equiv \text{Si–O–Si} \equiv +\text{H}_2\text{O} \leftrightarrow 2 \equiv \text{Si–OH} \tag{10}$$

In this work, the sizing-rich interphase loss is modeled assuming a simple zero-order kinetic model.

4. Results and Discussion

The increase of the composite's mass with time within the first few hundred hours could be fairly well described by a standard diffusion approach, as shown in Figure 4. It was important to include the water uptake of the voids in the calculations. However, the diffusion approach would predict a constant mass over time once saturation has been reached (0.96 wt %). The data of C3 show a slight gradual drop in mass after saturation was reached, whereas the mass of C1 is clearly increasing, as shown in Figure 7.
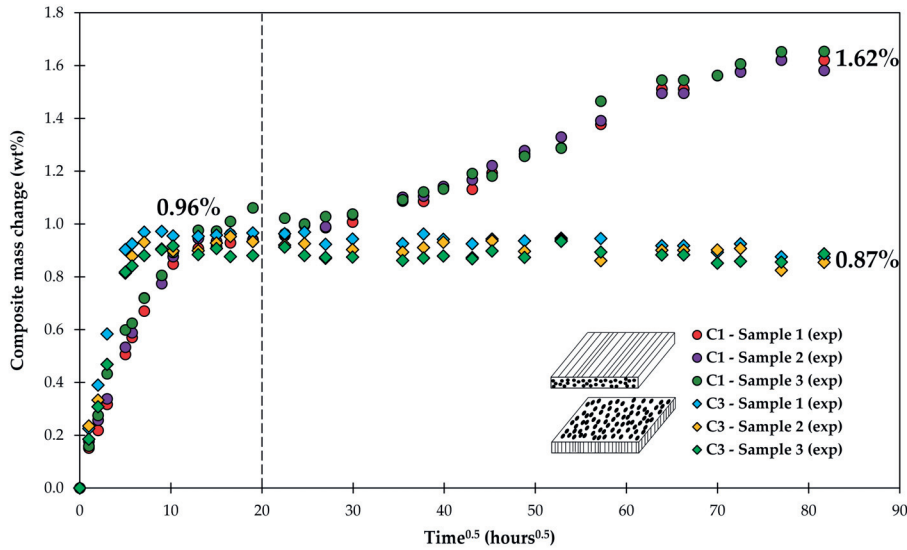
Figure 7. Long-term water uptake by composite laminates. Dashed line corresponds to a time when a test following standard practice ASTM D5229 would be stopped [44].

If the water uptake experiments are stopped as suggested by ASTM, then the long-term behavior is not captured. This observation is also consistent with the results of another study on long-term water uptake by composite plates [45]. The diverging behavior of water uptake by C1 and C3 composites can be observed starting only after about 20 h$^{0.5}$ (about 2 weeks), only after the saturation M_∞ (0.96 wt %) has been already achieved. The discussion on how the diverging behavior of C1 and C3 can be captured will follow.

4.1. Samples with Short Fibers C3

Firstly, the gravimetric behavior of C3 is addressed. As described above, a mass loss can be caused by leaching material out of the epoxy and by the glass fibers losing ions. If these effects are added to the mass vs. time curve a fairly good agreement with the experimental data is achieved, as shown in Figure 8. It could be argued that the agreement is sufficient within the experimental scatter. However, a closer look at the data can give some insight in the behavior of the sizing (interphase), although the evaluation is at the limit of what can be analyzed considering the scatter of the results.

Looking at Figure 8, a slightly better fit of the data can be obtained with a curve that has a higher mass loss with increasing time, i.e., is a bit steeper. This extra loss of material could be related to the disintegration of the interphase. The simplest approach is to model the mass loss of the interphase using the zero-order kinetics [64]:

$$\frac{\partial m_i}{\partial t} = K_i^0 S_i(t) \tag{11}$$

where m_i is the mass of the interphase, K_i^0 is the kinetic coefficient of the interphase dissolution and S_i is the surface area of the interphase. The solution of this equation for cylindrical fibers is given in Equation (9). For small mass changes and short times, the equation can be approximated by its first linear term with the sizing having a constant surface area S_i^0 to be:

$$m_i(t) = m_i^0 - K_i^0 S_i^0 t \tag{12}$$

The initial mass of the sizing m_i^0 (35.7 mg) was determined by the burn-off test to be 0.64 wt % of the sized fibers. Fitting the data in Figure 8 allows finding $K_i^0 S_i^0$, which basically describes the slightly

steeper slope compared to the previous analysis based only on matrix and glass fiber dissolution. Using linear regression, as shown in Figure 9, The best fit for $K_i^0 S_i^0 = 1.80 \times 10^{-7}$ g/h.
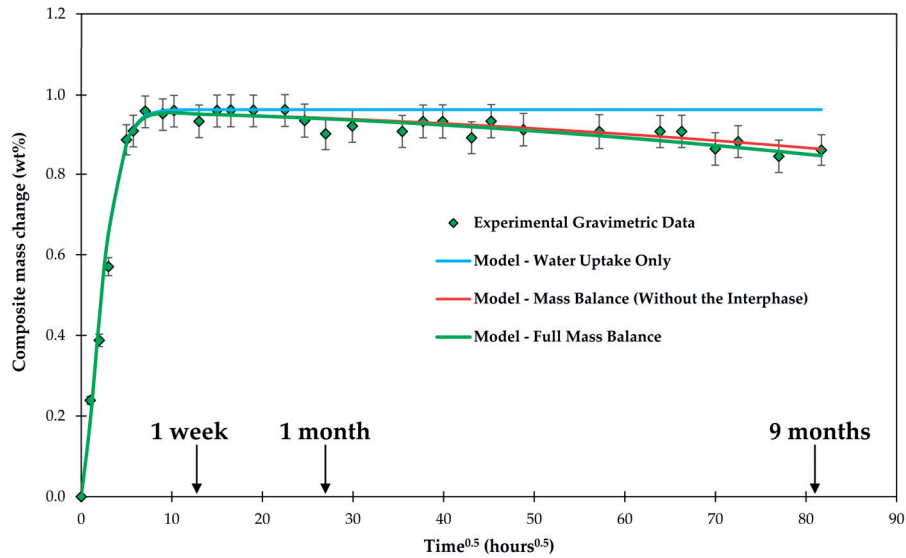

Figure 8. Experimental composite C3 plate mass change during the conditioning in water, shown over a square root of time. Water uptake and mass balance are modeled.
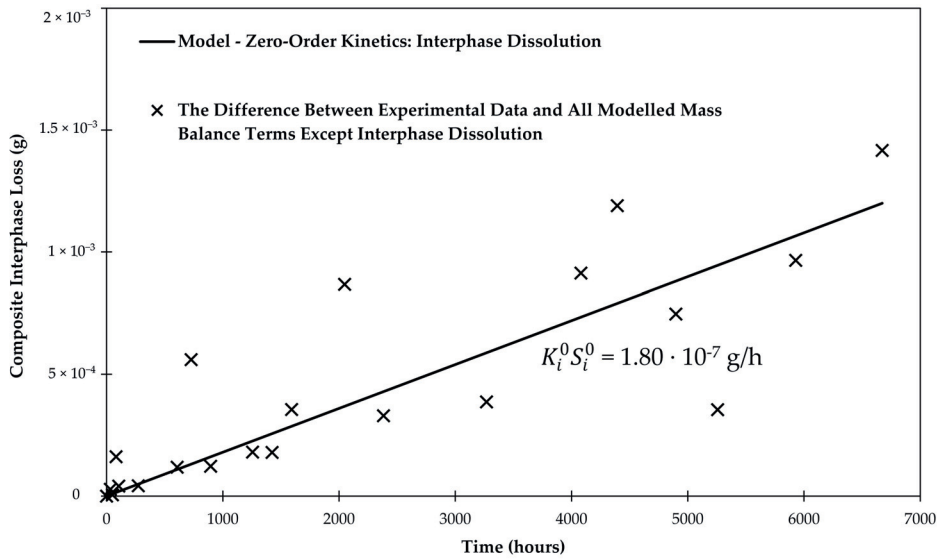

Figure 9. Linear regression of the difference between the experimental data and the all modelled terms except the interphase. The regressed line provides insight about the rate of the composite interphase dissolution in water.

Since dissolution is a surface reaction, a surface area of the sizing-rich interphase has to be obtained in order to determine the kinetics of dissolution. Unfortunately, we do not know the exact surface area of the sizing. Using the BET method, it was found that unsized fibers have a surface area of

0.084 m^2/g and sized fibers have a surface area of 0.180 m^2/g, roughly twice the value of the unsized fibers. As discussed in the introduction, the sizing is rough which creates a larger surface [6,31,37], but it also covers only parts of the fiber [12,32–37]. A typical sizing coverage of 90% of the glass fiber surface is assumed, after [39]. Furthermore, the sizing is bonded to the glass fiber on one side and the epoxy matrix on the other side, which does not create free surfaces at all. Based on the currently available information, the only possibility is to calculate K_i^0 for a number of plausible scenarios for the surface area S_i^0.

The thickness of the interphase is obtained from the volume of the interphase V_i taking geometry and known coverage (i.e., 0.9 or 1) into consideration. The volume of the interphase is known from LOI (0.64 wt %; 35.8 mg) and interphase density (1.1 g/cm^3), V_i = 0.0325 cm^3. The thickness of the interphase is then obtained as follows:

$$\delta_i = \frac{V_i}{\text{Coverage} \cdot S_{\text{glass}}} \tag{13}$$

where S_{glass} is the total glass fiber surface area in a composite plate (about 0.5 m^2). For 90% and 100% coverage, a mean interphase thickness is 72 and 65 nm, respectively.

Scenario 1. The minimum surface area S_i^0 would be just the cross-sectional area of the sizing exposed on the surface of the composite specimen. The fiber fraction was 59.5% and the area of one exposed surface of a C3 specimen was 50 mm × 50 mm. The surface area of fibers on both exposed surfaces is then 2975 mm^2. The radius of an individual fiber was 8.5 µm. Based on the burn-off method (LOI 0.64 wt %) and assuming extreme 100% coverage, the average sizing thickness was 65 nm. The ratio of exposed sizing cross sectional area to fiber cross sectional area is then 0.0149 and the exposed sizing area is 44.3 mm^2. In this scenario K_i^0 = 4.06 × 10^{-3} g/(m^2·h). The sizing would be dissolved along the axis of the fibers while the exposed cross section would remain constant until the sizing is completely dissolved. Equation (12) would accurately describe dissolution in this scenario. For these 1.5 mm-thick samples, the time to dissolve the sizing would be 22.7 years.

Scenario 2. The other extreme would be to argue that the epoxy is quickly saturated with water (after about 100 and 81 h for C1 and C3, respectively), The water can then attack and dissolve the sizing. In that case, the exposed area of the sizing would be much bigger. The BET method measured a specific surface area of sized fibers to be 0.180 m^2/g. Then, the total surface area of sized fibers (5.6 g fibers) in one plate is 1.01 m^2. Since the sizing covers only parts of the fiber, not all of this surface is from the sizing. But to obtain an outer bound K_i^0 can be calculated for this maximum surface area (assuming coverage of 100%). In this case using Equation (12), K_i^0 = 1.78 × 10^{-7} g/(m^2·h). The K_i^0 should be accurately determined by this equation for the relatively small area reduction during the measurement. However, the proper cylindrical Equation (9) taking the surface area reduction with time into account should be used to obtain the long-term dissolving of the sizing. The time to dissolve the sizing would be 30.5 years.

Scenario 3. Considering the descriptions of the literature about sizing, a typical sizing covers approximately 90% of the fiber [39]. In that case, the surface area of the sizing would be 0.91 m^2. Using the same approach of a cylindrical sizing exposed to water in the epoxy as described for Scenario 2 above the K_i^0 for this case would be 1.98 × 10^{-7} g/(m^2·h) and the time to dissolve the sizing would be 30.5 years.

The parameters of the three scenarios are systematized in Table 4.

Table 4. Systematized scenarios of the interphase dissolution kinetics.

Scenario	$K_i^0 S_i^0$ (g/h)	Sizing Coverage (%)	δ_i (nm)	S_i^0 (m^2)	K_i^0 (g/(m^2·h))	Time to Total Dissolution (years)
Scenario 1	1.80 × 10^{-7}	100	65	4.43 × 10^{-5}	4.06 × 10^{-3}	22.7
Scenario 2	1.80 × 10^{-7}	100	65	1.01	1.78 × 10^{-7}	30.5
Scenario 3	1.80 × 10^{-7}	90, after [39]	72	0.91	1.98 × 10^{-7}	30.5

The mass loss due to long-term gravimetric behavior of composite C3 could be successfully modeled, because the C3 samples did not have a significant accumulation of the degradation products. The C3 plates have a short fiber length (1.5 mm). Once the matrix is saturated with water, the water can attack and degrade the interphase. Any reduction products can be quickly transported along the interphase to the surface of the sample and will be absorbed by the surrounding water.

4.2. Samples with Long Fibers C1

The C1 samples showed a mass increase with time, see Figure 7, an additional 0.66 wt % of water was taken up after 6673 h of conditioning. Since C1 and C3 samples were made from the same laminate, just cut in a different direction, the change in behavior must be related to the sample's geometry. Compared to the C3 samples the C1 samples have much longer fibers and subsequently much longer fiber matrix interphases (1.5 mm vs. 50 mm).

The matrix of both sample types absorbs water in roughly the same period (see Table 2). The water will attack the interphase between fibers and matrix in the same way. But, it is believed that degradation products (of fibers and interphase) cannot easily move along the interphase and escape into the surrounding water at the composite's surface. Instead, the weakening of the interphase causes the formation of flaws. The degradation products and water can accumulate in these flaws. Thus, the mass of the composite does not decrease with time as for samples C3, but the mass of C1 samples increases with time. Figure 10 shows schematically what such a flaw could look like. Figure 11A shows that such flaws are, indeed, observed in the samples.
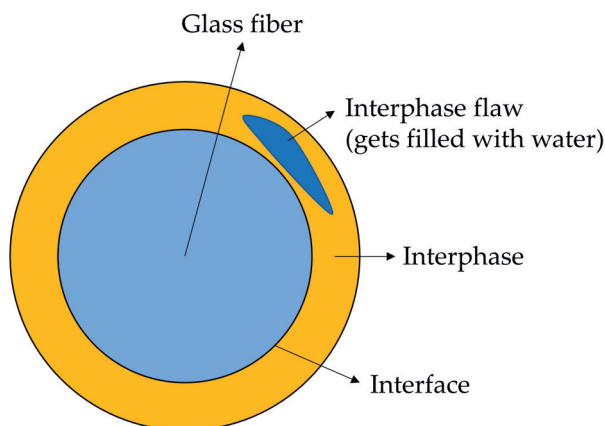

Figure 10. Interphase flaw is formed and is filled with water.

Since the laminate absorbed another 0.66 wt % of water, it is possible to estimate the size of flaws needed to accommodate this amount of water. The initial mass of the C1 plate was about 7.36 g. Water in the interphase flaws should thus weigh 48.6 mg, taking up volume of 4.86×10^{-8} m^3. Assuming for the moment that all fibers have evenly distributed flaws, the following calculations can be made. Dividing volume necessary to accommodate the extra water by the amount of fibers in a composite C1 plate (193525) and the length of a fiber (50 mm), the cross-sectional area of a water-filled interphase flaw around one fiber is found to be 5.02×10^{-12} m^2. The radius of the glass fiber is 8.5 μm, thus the cross-sectional area of the fiber is 2.27×10^{-10} m^2. By combining cross-sectional areas of the interphase flaw and the fiber, and deducting the radius of the fiber, an average thickness of a water-filled interphase flaw of 93.5 nm is obtained.

In reality, not all interphase flaws are the same size and not all fiber/matrix interphases are damaged equally, as shown in Figure 11. The weakest links will fail first. Once cracks are formed, stresses are released and more complicated processes follow. However, it is interesting that the first

fiber matrix debondings, as shown in Figure 11A, have dimensions similar to the calculated value of 93.5 nm. Fiber/matrix debondings shown in Figure 11A range from about a 100 nm to a few microns, as was observed experimentally using microscopy after 6673 h of conditioning. The thickness also matches debonding dimensions observed elsewhere for the same composite [65,66].

Three damage mechanisms were observed in the micrographs:

- Fiber/matrix debondings, shown in Figure 11A.
- Matrix transverse cracks, shown in Figure 11B. These cracks seem to be inside the bundle. This location may be also a result of the weakening of the fiber/matrix interphase, which was covered in point 1.
- Splitting along the fibers, shown in Figure 11C.

Fiber/matrix debonding appears to be the first failure mechanism, caused by hydrolysis of the interphase. This failure mechanism is described by the observations made for the C3 samples in Section 4.1 When these failure mechanisms accumulate, creating a weakened local region, they can easily combine into a longer "matrix crack" due to a release of curing, thermal and swelling stresses, resulting in a crack formation. The reason for the observed splitting along fibers is less clear. It could be related to the matrix cracks, but it could also be caused by the fibers used for stitching the reinforcing mat. All these flaws (cracks) create volume that can be filled with water and increases the mass of the composite.
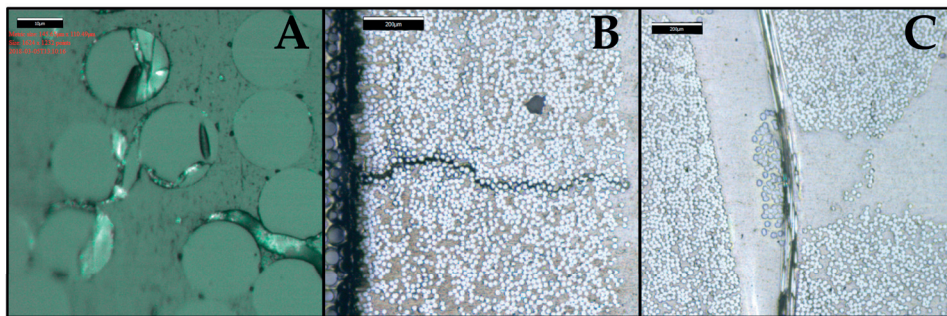

Figure 11. Micrograph of a composite sample exposed to water for 6673 h at 60 °C. The micrograph indicates the (**A**) fiber/matrix debondings; (**B**) matrix transverse cracks; (**C**) splitting along the fibers.

Perreux, Choqueuse and Davies [45] investigated long-term water uptake by 2.7 mm-thick composite plates. The plate was made with an anhydride-based curing agent while this study looked at an epoxy laminate made with an amine-based curing agent. They observed that after ASTM saturation was achieved, there was still a significant continuous mass gain up to about 5 years of conditioning in water at 60 °C. After this point, an abrupt and continuous mass loss occurred for the following 5 years until the measurements were stopped. The data is schematically shown in Figure 12.
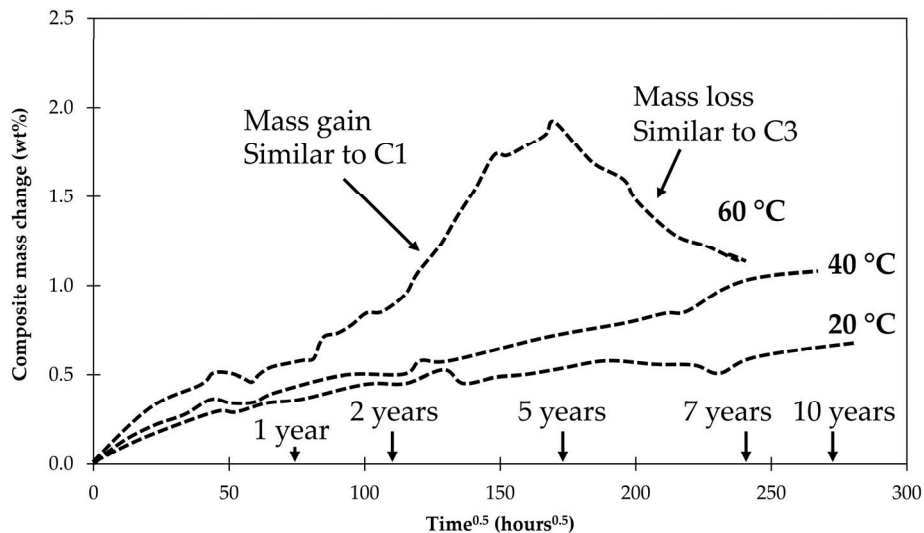
Figure 12. Schematic representation of the long-term water uptake at 20, 40 and 60 °C observed by Perreux, Choqueuse and Davies for the 2.7 mm thick composite plates [45].

The results seem to be a combination of what was found for samples C1 and C3 investigated here. An explanation for the behavior observed by Perreux et al. [45] may be given by the findings of this work. Initially flaws form in the composite interphase that is filled with water, resulting in a mass gain as found in C1 samples. At one point, so many flaws have accumulated that an open interpenetrating network with access to the surface of the laminate has formed. This network allows the degradation products and previously absorbed water to diffuse out, creating a mass loss similar to samples C3 (since fiber lengths in C3 were so small the interpenetrating network was present from the beginning). Since the observed mass reduction happened gradually, this means that the network of flaws and cracks is gradually being connected to the sample's surface. The mass drop was not observed for tests carried at lower temperatures. In that case all processes are slower and the samples only increased their mass, indicating the formation of flaws and cracks. But a network of the cracks reaching the surface was not created yet. It should be noted that the matrix of anhydride-based epoxies studied by Perreux et al. [45] is also prone to hydrolysis, so the hydrolysis in their samples may have affected the matrix and the fiber–matrix interphase.

4.3. General Aspects

For the composite laminates studied here, about 3.5 wt % of the interphase was dissolved in a year's time. The expected total dissolution for the geometry of the C3 sample would occur between 22.7 and 30.5 years, according to the three scenarios at 60 °C. At lower temperatures, the processes would be significantly slower, because diffusivities and dissolution rates follow Arrhenius-type temperature dependence [63,67]. Activation energies of these individual processes differ. Thus, it is likely not a straightforward Arrhenius-type influence on the process rate as a whole (summary mass uptake or loss).

The degradation time (22.7 to 30.5 years) should be independent of sample geometry and should be applicable once the matrix has reached saturation. For thick composite laminates the fiber–matrix interphase may only degrade in the surface region, because the matrix in the inside may remain dry. Degradation may also be stopped or slowed down by an accumulation of reaction product, if the degradation reaction is reversible, such as reaction (a). The mass uptake data obtained here showed a slight slowdown of the reaction after 9 months, close to the point when experiments were stopped, see

Figure 7. But it is unclear whether the data really flatten out. The test results from Perreux et al. [45] run over 10 years indicate that the degradation continues all the time.

Damage caused by the hydrolytic aging of the sizing-rich composite interphase very likely leads to a decrease in interfacial strength. For instance, Gagani et al. [68] and Rocha et al. [42] have reported the composite interphase-related deterioration of the mechanical properties due to aging in water. It is likely that the formation of the interphase flaws described in this work is the mechanistic origin of the interfacial strength deterioration of composites.

The authors think that studying the effect of seawater on the hydrolysis of the interphase would be useful, since the composite marine structures are most often used in the seawater environments. The dissolution in seawater conditions is expected to occur slower than in distilled water due to the presence of silica (dissolved from sand and other minerals). The reason for an expected aging rate slowdown in seawater is that the degradation products are already present in the surrounding environment, thus decreasing the driving force—a concentration gradient.

The length of glass fibers should not affect the molecular structure or morphology of the interphase per se. However, it should be added that what is affected by the fiber length is the path (or length) that the hydrolytic degradation products have to travel in order to escape the composite material and diffuse out into the surrounding water. It was shown in this work that water interaction with composites with very short interphase leads to mass loss, whereas for a typical composite an interpenetrating flaw network takes a relatively long time to form in order for degradation products to leave the composite. This leads to another aspect that needs to be studied in more detail: a diffusion of degradation products through the interphase. It is important to understand whether there is a diffusion-controlled aspect.

This paper covers hydrolysis of the composite interphase, but the same approach should be applicable for all other environmental agents and solvents (in general, solvolysis).

5. Conclusions

Glass fiber composites absorb water with time and the mass of the composites increase subsequently. When measuring diffusivity and saturation level of water according to ASTM D5229 [44] testing is stopped when the mass increase with time stops, i.e., it is reaching a plateau, in this case at about 200 h. However, continuing the tests exposing the laminates to water for longer, the mass of the composite increases again, measured up to 9 months. This additional water uptake was found to be due to the hydrolytic degradation of the sizing-rich fiber matrix interphase. Due to water-induced dissolution interphase flaws being formed which developed further into matrix cracks. The internal volume created by the flaws and cracks can be filled with water leading to the observed mass increase. The microscopically measured size of the flaws matches the order of magnitude of the volume required for obtaining the measured additional mass increase.

The hydrolytic degradation of the fiber matrix interphase could be investigated directly by cutting non-typical specimens from a thick composite laminate. The test specimens were 50 mm $\times$ 50 mm $\times$ 1.5 mm coupons where all the fibers were running parallel to the short edge. This created specimens with a short fiber–matrix interface length and the interphases being connected to the large sample's surface. When these specimens were conditioned in water, their mass increased during the first 200 h as the typical specimens described above. Continuing the test for longer times leads, however, to a mass loss. For these specimens, the flaws created by the fiber matrix interphase hydrolysis were open towards the surface of the test specimen, since the interphase length (and fiber length) was so short, 1.5 mm. The reaction products of the hydrolysis could migrate into the surrounding water bath leading to a mass drop. This mass loss allowed the product of the dissolution rate constant and the surface area of the interphase $K_i^0 S_i^0$ to be determined. The small specimens tested here would degrade the entire interphase within 22 to 30 years at 60 °C. The calculation is based on a full mechanistic mass balance approach considering all the composite's constituents: water uptake and leaching of the matrix, dissolution of the glass fibers, and dissolution of the composite interphase. These processes were modeled using a combination of Fickian diffusion and zero-order kinetics.

Based on long-term test data from the literature tested for close to 10 years, it seems that composites will initially absorb extra water in the flaws and cracks created by interphase hydrolysis. Eventually these cracks will create a network that is connected to the surface of the composite laminate. When this network is formed reaction products can leave the laminate and the mass will be reduced.

The possible strength degradation due to the flaws in the fiber matrix interface forming within 22 to 30 years (for the tested type of epoxy laminate) in saturated laminates should be taken into account in designs for long lifetimes.

Abbreviations

ρ_f	Density of the glass fibers (g/m^3)
ρ_m	Density of the matrix polymer (g/m^3)
ρ_i	Density of the sizing-rich composite interphase (g/m^3)
ρ_{water}	Density of the water (g/m^3)
h	Thickness of a material plate (m)
v_f	Volume fraction of the fibers (m^3/m^3)
v_m	Volume fraction of the matrix polymer (m^3/m^3)
v_i	Volume fraction of the composite interphase (m^3/m^3)
v_v	Volume fraction of the voids (m^3/m^3)
$M(t)$	Time-dependent water content of the composite (wt %)
M_∞	Saturation water content of the composite (wt %)
$M^m(t)$	Time-dependent water content of the matrix polymer (wt %)
M_∞^m	Saturation water content of the matrix polymer (wt %)
M_∞^v	Saturation water content of the voids (wt %)
D	Through-thickness water diffusivity of the material (mm^2/h)
$M_{leaching}(t)$	Time-dependent content of leached compounds from the polymer (wt %)
$M_{leaching}^0$	Initial leachable compound content in the polymer (wt %)
$D_{leaching}$	Through-thickness leachable compound diffusivity of the material (mm^2/h)
$r(t)$	Time-dependent fiber radius (m)
r_0	Initial fiber radius (m)
$r_{t_{st}}$	Fiber radius when the steady-state dissolution is reached (m)
K_0	Glass dissolution rate constant (g/(m^2·s))
K_0^*	Apparent glass dissolution rate constant (g/(m^2·s))
$K_0^{*\,I}$	Apparent glass dissolution rate constant (non-steady-state; Phase I) (g/(m^2·s))
$K_0^{*\,II}$	Apparent glass dissolution rate constant (steady-state; Phase II) (g/(m^2·s))
t_{st}	Time when long-term steady-state is reached (s)
n	Number of fibers (–)
l	Length of fibers and the interphase (m)

$S(t)$	Time-dependent glass fiber surface area (m^2)
S_0	Initial glass fiber surface area (m^2)
t	Time (s)
m; $m_{\text{dissolved}}$	Glass mass loss due to dissolution (g)
$m_{\text{dissolved}_{\text{st}}}$	Dissolved glass mass when the steady-state is reached (g)
ξ_{sizing}	Protective effect of sizing against glass dissolution (–)
n_{order}	Order of the water availability term (–)
$S_i(t)$	Time-dependent surface area of the composite interphase (m^2)
S_{i0}	Initial surface area of the composite interphase (m^2)
S_i^{specific}	Specific surface area of the composite interphase (m^2)
K_i^0	Zero-order rate constant of the composite interphase dissolution (g/(m^2·s))
$m_i(t)$	Time-dependent mass of the composite interphase (g)
m_{i0}	Initial mass of the composite interphase (g)
GF	Glass fiber
GFRP	Glass fiber-reinforced polymer; same as glass fiber-reinforced composite
DCZOK	Dissolving cylinder zero-order kinetic (model)
DGEBA	Bisphenol A diglycidyl ether
HDDGE	1,6-Hexanediol diglycidyl ether
POPA	Poly(oxypropylene)diamine
IPDA	Isophorondiamine
R-glass	"Reinforcement" glass
FRP	Fiber-reinforced polymer, same as fiber-reinforced composite
HR-ICP-MS	High-resolution inductively coupled plasma mass spectrometry\
VARTM	Vacuum-assisted resin transfer molding
BET	Brunauer–Emmett–Teller theory
LOI	Loss on ignition
γ-APS APTES	γ-aminopropyltriethoxysilane
PPO	Poly(propylene oxide)
PEO	Poly(ethylene oxide)
PDMS	Polydimethylsiloxane

References

1. Berg, J.; Jones, F.R. The role of sizing resins, coupling agents and their blends on the formation of the interphase in glass fiber composites. *Compos. Part A* **1998**, *29*, 1261–1272. [CrossRef]
2. Feih, S.; Wei, J.; Kingshott, P.; Sørensen, B.F. The influence of fiber sizing on the strength and fracture toughness of glass fiber composites. *Compos. Part A* **2005**, *36*, 245–255. [CrossRef]
3. Dai, Z.; Shi, F.; Zhang, B.; Li, M.; Zhang, Z. Effect of sizing on carbon fiber surface properties and fibers/epoxy interfacial adhesion. *Appl. Surf. Sci.* **2011**, *257*, 6980–6985. [CrossRef]
4. Yuan, X.; Zhu, B.; Cai, X.; Liu, J.; Qiao, K.; Yu, J. Optimization of interfacial properties of carbon fiber/epoxy composites via a modified polyacrylate emulsion sizing. *Appl. Surf. Sci.* **2017**, *401*, 414–423. [CrossRef]
5. DiBenedetto, A.T. Tailoring of interfaces in glass fiber reinforced polymer composites: A review. *Mater. Sci. Eng. A* **2001**, *302*, 74–82. [CrossRef]
6. Plonka, R.; Mäder, E.; Gao, S.L.; Bellmann, C.; Dutschk, V.; Zhandarov, S. Adhesion of epoxy/glass fiber composites influenced by aging effects on sizings. *Compos. Part A* **2004**, *35*, 1207–1216. [CrossRef]
7. Grabovac, I.; Whittaker, D. Application of bonded composites in the repair of ships structures—A 15-year service experience. *Compos. Part A* **2009**, *40*, 1381–1398. [CrossRef]
8. McGeorge, D.; Echtermeyer, A.T.; Leong, K.H.; Melve, B.; Robinson, M.; Fischer, K.P. Repair of floating offshore units using bonded fibre composite materials. *Compos. Part A* **2009**, *40*, 1364–1380. [CrossRef]
9. Gustafson, C.-G.; Echtermeyer, A. Long-term properties of carbon fibre composite tethers. *Int. J. Fatigue* **2006**, *28*, 1353–1362. [CrossRef]
10. Salama, M.M.; Stjern, G.; Storhaug, T.; Spencer, B.; Echtermeyer, A. The first offshore field installation for a composite riser joint. OTC-14018-MS. In Proceedings of the Offshore Technology Conference, Houston, TX, USA, 6–9 May 2002. [CrossRef]

11. Echtermeyer, A.T.; Gagani, A.I.; Krauklis, A.E.; Mazan, T. Multiscale modelling of environmental degradation—First steps. In *Durability of Composites in a Marine Environment 2. Solid Mechanics and Its Applications*; Davies, P., Rajapakse, Y.D.S., Eds.; Springer: Cham, Switzerland, 2018; Volume 245, pp. 135–149. ISBN 978-3-319-65145-3.

12. Thomason, J.L. *Glass Fiber Sizings: A Review of the Scientific Literature*; James L Thomason: Middletown, DE, USA, 2012; ISBN 978-0-9573814-1-4.

13. Weitsman, Y. Coupled damage and moisture-transport in fiber-reinforced, polymeric composites. *Int. J. Solids Struct.* **1987**, *23*, 1003–1025. [CrossRef]

14. Weitsman, Y.J.; Elahi, M. Effects of fluids on the deformation, strength and durability of polymeric composites—An overview. *Mech. Time-Depend. Mater.* **2000**, *4*, 107–126. [CrossRef]

15. Roy, S. Moisture-induced degradation. In *Long-Term Durability of Polymeric Matrix Composites*; Pochiraju, V.K., Tandon, P.G., Schoppner, A.G., Eds.; Springer: Boston, MA, USA, 2012; pp. 181–236. ISBN 978-1-4419-9307-6.

16. Peters, L. Influence of glass fibre sizing and storage conditions on composite properties. In *Durability of Composites in a Marine Environment 2. Solid Mechanics and Its Applications*; Davies, P., Rajapakse, Y.D.S., Eds.; Springer: Cham, Switzerland, 2018; Volume 245, pp. 19–31. ISBN 978-3-319-65145-3.

17. Culler, S.R.; Ishida, H.; Koenig, J.L. *Hydrothermal Stability of γ-Aminopropyltriethoxysilane Coupling Agent on Ground Silicon Powder and E-Glass Fibers*; Technical Report; Department of Macromolecular Science: Cleveland, OH, USA, 1983.

18. Wang, D.; Jones, F.R.; Denison, P. TOF SIMS and XPS study of the interaction of hydrolysed γ-aminopropyltriethoxysilane with E-glass surfaces. *J. Adhes. Sci. Technol.* **1992**, *6*, 79–98. [CrossRef]

19. Wang, D.; Jones, F.R.; Denison, P. Surface analytical study of the interaction between γ-amino propyl triethoxysilane and E-glass surface. Part I Time-of-flight secondary ion mass spectrometry. *J. Mater. Sci.* **1992**, *27*, 36–48. [CrossRef]

20. Wang, D.; Jones, F.R. Surface analytical study of the interaction between γ-amino propyl triethoxysilane and E-glass surface. Part II X-ray photoelectron spectroscopy. *J. Mater. Sci.* **1993**, *28*, 2481–2488. [CrossRef]

21. Wang, M.; Xu, X.; Ji, J.; Yang, Y.; Shen, J.; Ye, M. The hygrothermal aging process and mechanism of the novolac epoxy resin. *Compos. Part B* **2016**, *107*, 1–8. [CrossRef]

22. Halpin, J.C. *Effects of Environmental Factors on Composite Materials*; Technical Report AFML-TR-67–423; Air Force Materials Laboratory: Dayton, OH, USA, 1969.

23. *ASTM D4963/D4963M-2011 Standard Test Method for Ignition Loss of Glass Strands and Fabrics*; ASTM: West Conshohocken, PA, USA, 2011.

24. Loewenstein, K.L. *Glass Science and Technology (Book 6), The Manufacturing Technology of Continuous Glass Fibres*; Elsevier: Amsterdam, The Netherlands, 1993; ISBN 978-0444893468.

25. Thomason, J.L.; Adzima, L.J. Sizing up the interphase: An insider's guide to the science of sizing. *Compos. Part A* **2001**, *32*, 313–321. [CrossRef]

26. Plueddemann, E.P. *Silane Coupling Agents*, 2nd ed.; Plenum Press: New York, NY, USA, 1991; ISBN 978-0-306-43473-0.

27. Emadipour, H.; Chiang, P.; Koenig, J.L. Interfacial strength studies of fibre-reinforced composites. *Res. Mech.* **1982**, *5*, 165–176.

28. Krauklis, A.E.; Echtermeyer, A.T. Dissolving cylinder zero-order kinetic model for predicting hygrothermal aging of glass fibre bundles and fibre-reinforced composites. In Proceedings of the 4th International Glass Fibre Symposium, Aachen, Germany, 29–31 October 2018; pp. 66–72, ISBN 978-3-95886-249-4.

29. Joliff, Y.; Belec, L.; Chailan, J.-F. Impact of the interphases on the durability of a composite in humid environment—A short review. In Proceedings of the 20th International Conference on Composite Structures ICCS20, Paris, France, 4–7 September 2017.

30. Zhuang, R.-C.; Burghardt, T.; Mäder, E. Study on interfacial adhesion strength of single glass fiber/polypropylene model composites by altering the nature of the surface of sized glass fibers. *Compos. Sci. Technol.* **2010**, *70*, 1523–1529. [CrossRef]

31. Wolff, V.; Perwuelz, A.; El Achari, A.; Caze, C.; Carlier, E. Determination of surface heterogeneity by contact angle measurements on glass fibres coated with different sizings. *J. Mater. Sci.* **1999**, *34*, 3821–3829. [CrossRef]

32. Ishida, H.; Koenig, J.L. An investigation of the coupling agent/matrix interface of fiberglass reinforced plastics by fourier transform infrared spectroscopy. *Polym. Phys. B* **1979**, *17*, 615–626. [CrossRef]

33. Watson, H.; Mikkola, P.J.; Matisons, J.G.; Rosenholm, J.B. Deposition characteristics of ureido silane ethanol solutions onto E-glass fibres. *Colloids Surf. A* **2000**, *161*, 183–192. [CrossRef]

34. Feresenbet, E.; Raghavan, D.; Holmes, G.A. Influence of silane coupling agent composition on the surface characterization of fiber and on fiber-matrix interfacial shear strength. *J. Adhes.* **2003**, *79*, 643–665. [CrossRef]

35. Fagerholm, H.M.; Lindsjö, C.; Rosenholm, J.B.; Rökman, K. Physical characterization of E-glass fibres treated with alkylphenylpoly(oxyethylene)alcohol. *Colloids Surf.* **1992**, *69*, 79–86. [CrossRef]

36. Thomason, J.L.; Dwight, D.W. The use of XPS for characterization of glass fibre coatings. *Compos. Part A* **1999**, *30*, 1401–1413. [CrossRef]

37. Turrión, S.G.; Olmos, D.; González-Benito, J. Complementary characterization by fluorescence and AFM of polyaminosiloxane glass fibers coatings. *Polym. Test.* **2005**, *24*, 301–308. [CrossRef]

38. Mai, K.; Mäder, E.; Mühle, M. Interphase characterization in composites with new non-destructive methods. *Compos. Part A* **1998**, *29*, 1111–1119. [CrossRef]

39. Thomason, J.L.; Dwight, D.W. XPS analysis of the coverage and composition of coatings on glass fibers. *J. Adhes. Sci. Technol.* **2000**, *14*, 745–764. [CrossRef]

40. Wang, D.; Jones, F.R. TOF SIMS and XPS study of the interaction of silanized E-glass with epoxy resin. *J. Mater. Sci.* **1993**, *28*, 1396–1408. [CrossRef]

41. Chiang, C.H.; Ishida, H.; Koenig, J.L. The structure of aminopropyltriethoxysilane on glass surfaces. *J. Colloid Interface Sci.* **1980**, *74*, 396–404. [CrossRef]

42. Rocha, I.B.C.M.; Raijmaekers, S.; Nijssen, R.P.L.; van der Meer, F.P.; Sluys, L.J. Hygrothermal ageing behaviour of a glass/epoxy composite used in wind turbine blades. *J. Compos. Struct.* **2017**, *174*, 110–122. [CrossRef]

43. Kim, J.K.; Sham, M.L.; Wu, J. Nanoscale characterization of interphase in silane treated glass fibre composites. *Compos. Part A* **2001**, *32*, 607–618. [CrossRef]

44. *ASTM D5229/D5229M-14 Standard Test Method for Moisture Absorption Properties and Equilibrium Conditioning of Polymer Matrix Composite Materials*; ASTM International: West Conshohocken, PA, USA, 2014.

45. Perreux, D.; Choqueuse, D.; Davies, P. Anomalies in moisture absorption of glass fibre reinforced epoxy tubes. *Compos. Part A* **2002**, *33*, 147–154. [CrossRef]

46. Krauklis, A.E.; Echtermeyer, A.T. Mechanism of yellowing: carbonyl formation during hygrothermal aging in a common amine epoxy. *Polymers* **2018**, *10*, 1017. [CrossRef] [PubMed]

47. Krauklis, A.E.; Echtermeyer, A.T. Long-term dissolution of glass fibers in water described by dissolving cylinder zero-order kinetic model: Mass loss and radius reduction. *Open Chem.* **2018**, *16*, 1189–1199. [CrossRef]

48. *3B Fibreglass Technical Data Sheet*; HiPer-Tex W2020 Rovings: Belgium, Brussel, 2012.

49. Gagani, A.I.; Fan, Y.; Muliana, A.H.; Echtermeyer, A.T. Micromechanical modeling of anisotropic water diffusion in glass fiber epoxy reinforced composites. *J. Compos. Mater.* **2017**, *52*, 2321–2335. [CrossRef]

50. Zinck, P.; Gerard, J.F. On the hybrid character of glass fibres surface networks. *J. Mater. Sci.* **2005**, *40*, 2759–2760. [CrossRef]

51. *ASTM D3171/D3171-15 Standard Test Methods for Constituent Content of Composite Materials*; ASTM International: West Conshohocken, PA, USA, 2015.

52. Brunauer, S.; Emmett, P.H.; Teller, E. Adsorption of gases in multimolecular layers. *J. Am. Chem. Soc.* **1938**, *60*, 309–319. [CrossRef]

53. *International Standard ISO 9277:2010(E) Determination of the Specific Surface Area of Solids by Gas Adsorption—BET Method*; ISO: Berlin, Germany, 2010.

54. Popineau, S.; Rondeau-Mouro, C.; Sulpice-Gaillet, C.; Shanahan, M.E.R. Free/bound water absorption in an epoxy adhesive. *Polymer* **2005**, *46*, 10733–10740. [CrossRef]

55. Krauklis, A.E.; Gagani, A.I.; Echtermeyer, A.T. Hygrothermal aging of amine epoxy: reversible static and fatigue properties. *Open Eng.* **2018**, *8*, 447–454. [CrossRef]

56. Krauklis, A.E.; Gagani, A.I.; Echtermeyer, A.T. Near-Infrared Spectroscopic Method For Monitoring Water Content In Epoxy Resins And Fiber-Reinforced Composites. *Materials* **2018**, *11*, 586. [CrossRef]

57. Thomason, J.L. The interface region in glass-fibre-reinforced epoxy resin composites: 2. Water absorption, voids and the interface. *Composites* **1995**, *26*, 477–485. [CrossRef]

58. Crank, J. *The Mathematics of Diffusion*, 2nd ed.; Clarendon Press: Oxford, UK, 1975; ISBN 978-0-19-853411-6.

59. Maggana, C.; Pissis, P. Water sorption and diffusion studies in an epoxy resin system. *J. Polym. Sci. Part B* **1999**, *37*, 1165–1182. [CrossRef]

60. Toscano, A.; Pitarresi, G.; Scafidi, M.; Di Filippo, M.; Spadaro, G.; Alessi, S. Water diffusion and swelling stresses in highly crosslinked epoxy matrices. *Polym. Degrad. Stab.* **2016**, *133*, 255–263. [CrossRef]

61. Bruchet, A.; Elyasmino, N.; Decottignies, V.; Noyon, N. Leaching of bisphenol A and F from new and old epoxy coatings: Laboratory and field studies. *Water Sci. Technol.* **2014**, *14*, 383–389. [CrossRef]

62. Schutte, C.L. Environmental durability of glass-fiber composites. *Mater. Sci. Eng. R Rep.* **1994**, *13*, 265–323. [CrossRef]

63. Krauklis, A.E.; Gagani, A.I.; Vegere, K.; Kalnina, I.; Klavins, M.; Echtermeyer, A.T. Dissolution kinetics of R-glass fibres: Influence of water acidity, temperature and stress corrosion. *Fibers* **2019**, *7*, 22. [CrossRef]

64. Khawam, A.; Flanagan, D.R. Solid-state kinetic models: basics and mathematical fundamentals. *J. Phys. Chem. B* **2006**, *110*, 17315–17328. [CrossRef] [PubMed]

65. Gagani, A.I.; Mialon, E.P.V.; Echtermeyer, A.T. Immersed interlaminar fatigue of glass fiber epoxy composites using the I-beam method. *Int. J. Fatigue* **2019**, *119*, 302–310. [CrossRef]

66. Rocha, I.B.C.M.; van der Meer, F.P.; Raijmaekers, S.; Lahuerta, F.; Nijssen, R.P.L.; Mikkelsen, L.P.; Sluys, L.J. A combined experimental/numerical investigation on hygrothermal aging of fiber-reinforced composites. *Eur. J. Mech. Sol.* **2019**, *73*, 407–419. [CrossRef]

67. Bonniau, P.; Bunsell, A.R. Water absorption by glass fibre reinforced epoxy resin. In *Composite Structures*; Marshall, I.H., Ed.; Springer: Dordrecht, The Netherlands, 1981; pp. 92–105. ISBN 978-94-009-8122-5.

68. Gagani, A.I.; Krauklis, A.E.; Sæter, E.; Vedvik, N.P.; Echtermeyer, A.T. A novel method for testing and determining ILSS for marine and offshore composites. *Comp. Struct.* **2019**, *220*, 431–440. [CrossRef]